A mantle-to-crust study of magmatic processes in the Main Ethiopian Rift

Kevin Wong
The University of Leeds
School of Earth and Environment

Submitted in accordance with the requirements for the degree of
Doctor of Philosophy
February, 2023

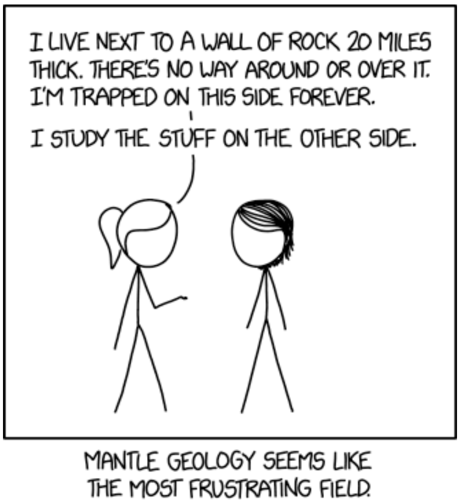

Rock Wall, by xkcd.com, used under a CC-BY-NC 2.5 licence.

Declaration

The candidate confirms that the work submitted is his own, except where work which has formed part of jointly authored publications has been included. The contribution of the candidate and the other authors to this work has been explicitly indicated below. The candidate confirms that appropriate credit has been given within the thesis where reference has been made to the work of others.

Chapters 3 and 4 have resulted in the publication of two journal articles.

- **Wong, K.**, Ferguson, D., Matthews, S., Morgan, D., Tadesse, A. Z., Sinetebeb, Y., and Yirgu, G. (2022). Exploring rift geodynamics in Ethiopia through olivine-spinel Al-exchange thermometry and rare-earth element distributions. *Earth and Planetary Science Letters*, 597, 117820. DOI: 10.1016/j.epsl.2022.117820

  Author contributions: KW, DF, DM, and GY conceived the study. KW, DF, AZT, YS, and GY performed fieldwork to collect samples used in this study. KW performed sample preparation and collected data supervised by DF, DM, and GY. KW, DF, and SM coded mantle melting models. KW, DF, and SM wrote the manuscript. All authors read and approved the final manuscript.

- Matthews S., **Wong, K.**, and Gleeson M (2022). pyMelt: An extensible Python engine for mantle melting calculations. *Volcanica*, 5(2). DOI: 10.30909/vol.05.02.469475

  Author contributions: SM conceived the study. SM and KW wrote the code for the mantle melting models, developed documentation, and drafted the manuscript. KW developed the mantle chemistry code. MG and SM developed the hydrous melting code. All authors contributed to editing the manuscript.

Chapter 5 has also been submitted as a journal article.

- **Wong, K.**, Ferguson, D. J., Wieser, P., Morgan, D. J., Edmonds, M., Tadesse, A. Z., Yirgu, G., Harvey, J., and Hammond, S., in preparation. Focused mid-crustal magma intrusion during continental break-up in Ethiopia.

Author contributions: KW, DF, DM, ME, and GY conceived the study. KW, DF, AZT, and GY performed fieldwork to collect samples used in this study. KW and JH performed sample preparation. KW and PW obtained Raman spectroscopy data. SH obtained ICP-MS data. KW obtained electron probe data and performed geochemical modelling supervised by DF, DM, and ME. All authors contributed to the writing and editing of the final manuscript.

Acknowledgements

'Give me a place to stand, and a lever long enough, and I will move the world.'

Archimedes' quote comes to mind as I write this section. While the lever is much diminished by the disruption during the COVID-19 pandemic, I must thank the many people that form the fulcrum which allows me to at least coax the Earth a little bit.

I would firstly like to thank my lead supervisor, David Ferguson, for his patience and insight over the course of this project. Over four years of supervision meetings, Dave has inspired, challenged, and argued with me; he has ultimately too forged and improved my abilities as an Earth Scientist. I would additionally like to thank Dan Morgan for his witty and reassuring remarks and expertise as a senior researcher, whose comments on work progress helped keep me sane and on-track during the course of this project. I especially thank him for his time during the write-up of Chapter 6. Finally I express my immense gratitude to Marie Edmonds. Marie has been with me on this PhD journey every step of the way, even participating as a course leader on my first-year undergraduate Arran field trip back in 2015. I would not be where I am now if it were not for her constant support and her willingness to make time even for a brief catch-up meeting. Thank you Marie.

There are many other researchers I would like to acknowledge who have contributed in some way to my research. Simon Matthews has been a fantastic mentor and collaborator on the pyMelt module, and I thank him for this encouragement and patience during the work on Chapters 3 and 4. Likewise, I thank Penny Wieser for the extensive guidance and support she has given me for Chapter 5. The training and technical support provided in Leeds by Jason Harvey, Harri Wyn Williams, Gary Keech, Lesley Neve, and Richard Walshaw, in Cambridge by Emilie Ringe, from the Open University by Samantha Hammond, and in Edinburgh by Cristina Talavera Rodriguez were invaluable over the course of this project especially given the COVID-19 pandemic. I would additionally like to emphatically thank Cristina for performing the SIMS analyses which are paramount to the completion

of Chapter 5. The Department of Earth Sciences at Addis Ababa University provided considerable support both during and after fieldwork; in particular I thank Amdemichael Zafu Tadesse, Yared Sinetebeb, and Yafet Gebrewold Birhane for assistance in the field, and Gezahegn Yirgu for the logistical support and generosity offered to me by his department. Biruk of Ethioder Cars is thanked for his exceptional driving skills on the slopes of the many scoria cones we visited.

I have received financial support from NERC via DTP grant NE/L002574/1 (Leeds-York SPHERES), and I acknowledge further support from the Geologists' Association via their New Researchers' Award. In addition, the ion probe analyses of Chapter 5 were funded through NERC grant IMF694/1119 awarded to David Ferguson as principal investigator. The work performed in this thesis would not be possible without this funding.

As for friends, there are far too many to list, but here goes. From Leeds, I thank Jack McGrath, Maeve Murphy Quinlan, Claire Orlov, Stephanie Shahrzad, and Andrew Watson for being fantastic office mates and Dungeons and Dragons players. I additionally thank Rachel Sansom, Rachel Whitty, Merin Joseph, and the other participants of the SEE badminton squad. Graham McLeod and Bob Jamieson are thanked for inviting me (and tolerating me enough) to teach on many field trips with them. And finally, the friends from elsewhere: Maria-Andreea Filip, Angus Hammond, James and Francesca Palmer, Jared Hanlon, Sarah Wilson, Roxanne Armfield, John Warburton, Cassandra Wynne, Thomas Finch, Oliver George, Ethan Lee, Rachel Fitchett, Olivia Pickup, Neil Hawkins, and many many others that I cannot squeeze into the word limit are thanked for all supporting me, especially during the long lockdown periods when I was stuck optimistically waiting alone in Leeds for labs to reopen.

Finally, I thank my mum, dad, younger brother, and grandma. I apologise to them for the many missed calls during the write-up phase of this thesis.

This work is dedicated to my grandfather, Loy Wong, who passed away during the summer of 2020.

A mantle-to-crust study of magmatic processes in the Main Ethiopian Rift

Kevin Wong

Continental rifting is the means by which strong continental lithosphere is faulted, weakened, and ruptured to form a new ocean basin. This process evolves temporally and spatially, and is accompanied by significant seismicity and often crustal intrusion of mantle-derived magmas in its penultimate stages, which facilitate further extension through crustal thermo-mechanical weakening. Understanding the relationship between magmatism and extension in rifts is paramount for developing new models of tectonic evolution that account for the effects of magmas during the rifting process.

This thesis investigates the magmatic character of the late-stage Main Ethiopian Rift (MER), the northernmost sector of the East African Rift System. A subject of intense geophysical examination, the MER hosts volcano-tectonic segments that accommodate the bulk of extensional strain. Past literature has highlighted the anomalous nature of the mantle and the presence of both solid and molten intrusions in the rifting crust under these segments. To verify geophysical evidence, new independent petrological observations of melt generation and crustal magmatic storage and transport are necessary.

I explore magmatism in the MER by analysing erupted basalts from scoria cones. Geochemical analyses of these materials, including whole rocks, olivine crystals, and olivine-hosted melt inclusions, are used to explore melt generation, crystal fractionation, and cationic diffusion within crystals.

The three principal studies outlined in this thesis demonstrate that heterogeneous melts, derived from a hot mantle that is geochemically and lithologically enriched relative to ambient mantle, are stalled and stored in a mid-crustal weak layer prior to eruption. Significant degassing of CO_2 occurs within this layer. Eruptions are triggered by the intrusion of hot mafic dykes in the months leading up to cone-forming events. These results provide new constraints on the temperature and composition of the sub-MER mantle, the storage conditions of rift magmas, and the timescales of processes that trigger eruptions.

Contents

List of Figures

List of Tables

Commonly used abbreviations

BSE	Backscatter electron
EAR(S)	East African Rift (System)
EPMA	Electron probe micro-analysis
ICP-MS	Inductively coupled plasma-mass spectrometry
LAB	lithosphere-asthenosphere boundary
MER	Main Ethiopian Rift
MOR	mid-ocean ridge
MORB	mid-ocean ridge basalt
PEC	post-entrapment crystallisation
REE	rare earth element
LREE	light REE
MREE	medium REE
HREE	heavy REE
SDFZ	Silti-Debre Zeyit Fault Zone
SIMS	Secondary ion mass spectrometry
WFB	Wonji Fault Belt
XRF	X-ray fluorescence

Chapter 1

Introduction and background

Wilson (1966) first described the genesis of ocean basins from the rifting-apart of intact continental crust. Since this seminal work, research has highlighted the necessity of continental rifting in the Earth system, including (but not limited to) tectonic evolution (e.g., Ebinger, 2005; Keir, 2014), the deep carbon cycle (e.g., Foley and Fischer, 2017; Brune et al., 2017; Wong et al., 2019), and continental modification (e.g., White and McKenzie, 1989; White et al., 2008; Thybo and Nielsen, 2009). While rifted passive margins, the remnants of ancient continental rifting events, may provide insights into the processes occurring during active continental break-up (e.g., White et al., 2008; Magee et al., 2016), they are often overprinted by the significant volcano-tectonic activity that accompanies the latest stages of rifting (Ebinger, 2005). Models illustrating the spatial and temporal development of continental rifting must therefore rely on detailed study of extant continental rift systems transitioning to oceanic crust.

The East African Rift System (EARS) is the archetypal present-day active continental rift system. Extending across East Africa, from Afar in the north to Mozambique in the south, the EARS accommodates the ongoing separation between the Somalian and Nubian plates, and hosts a complex series of rift basins, fault zones, and volcanoes (Figure 1.1). In its northernmost sector within Ethiopia (termed the Ethiopian Rift), the EARS gradually transitions into an oceanic spreading centre as part of the Afar Triple Junction, exposing several stages of rift-to-ridge development (e.g., Ebinger, 2005). This portion of the rift therefore offers an exciting opportunity to study the driving factors, geodynamics, and effects of late-stage continental rifting within the crust and mantle.

Much like its geophysical features, the volcanic features of the rift vary too along its length (e.g., Rogers, 2006; Furman, 2007). The erupted products of different stages of the

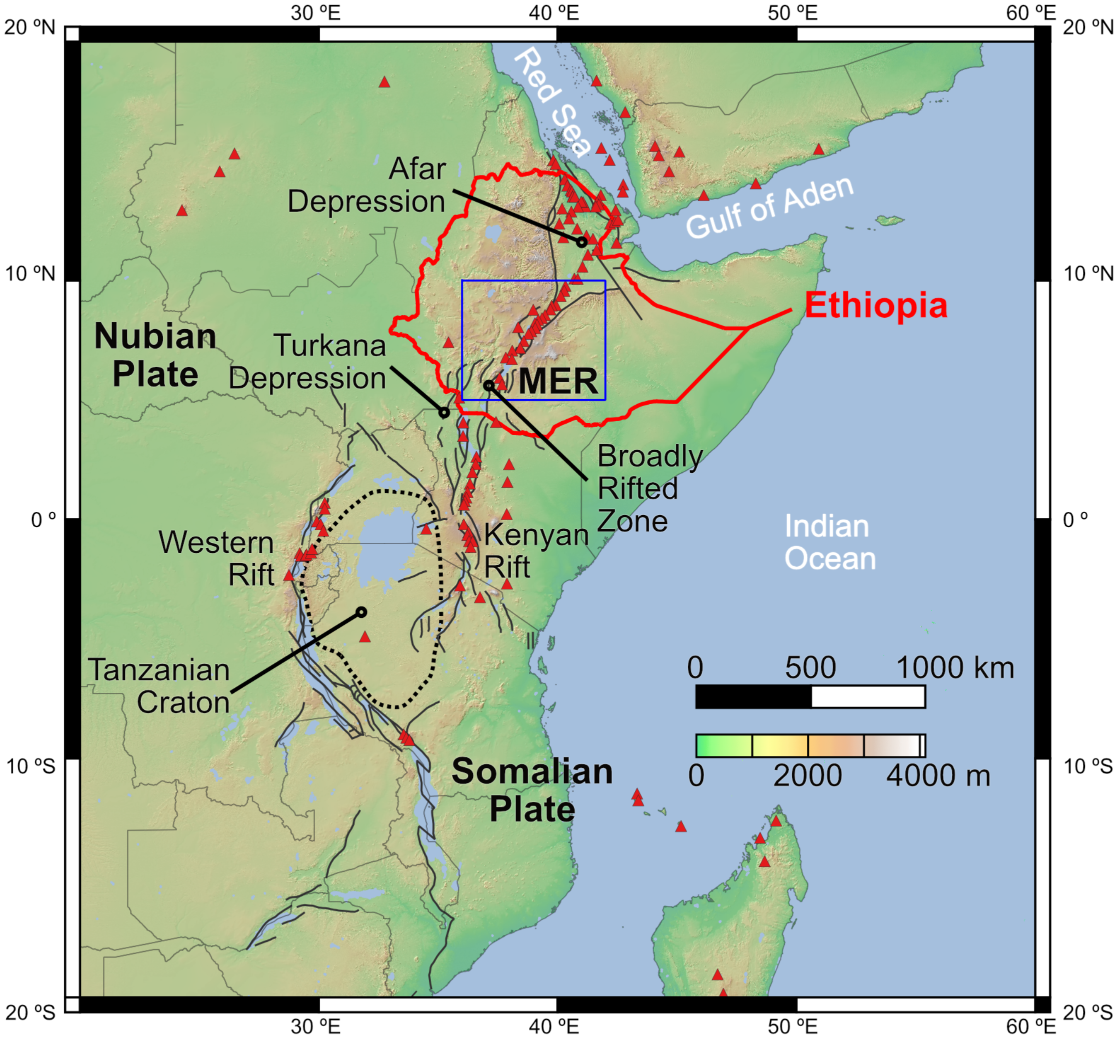

Figure 1.1: Overview elevation map of East Africa with the primary components of the East African Rift system highlighted. The black lines mark out the position of faults dividing the Nubian and Somalian subplates (redrawn after Chorowicz, 2005). The blue box shows the spatial area presented in Figure 1.2. Red triangles show volcanoes from the Global Volcanism Program (2013). The East African Rift sectors labelled include the Western Rift (WR), Kenyan Rift (KR), Main Ethiopian Rift (MER), Turkana Depression (TD), Afar Depression (AD), and Tanzania Craton (TC), which is additionally bordered by a thick, dashed, black line. The digital elevation model is GTOPO30 (completed in 1996).

rifting process harbour observable geochemical variations that can infer the conditions of their generation and transport. Scoria cones and basaltic flows occur along the length of the Ethiopian Rift, forming vast 50–100 km long and ∼20 km wide volcanic fields on the rift floor (Abebe et al., 2007). Volcanic ejecta from these scoria cones, with focus on early crystallising olivine from mantle-derived basaltic melts, form the subject matter of this thesis.

1.1 The Ethiopian Rift

The 60 km-wide Ethiopian Rift is the ∼1000 km seismically and volcanically active sector of the East African Rift system that passes through the centre of Ethiopia with a N-S trend, which rotates to NE-SW at ∼5 °N latitude (Figure 1.2). Its rift valley separates the Ethiopian and Somalian plateaux to its west and east respectively, and connects the Turkana Depression in the south to the Afar Depression in the north. At Afar, the Rift joins with the Red Sea Rift and Gulf of Aden ridge systems to form the Afar triple junction. South of the Ethiopian Rift lies the Broadly Rifted Zone, a ∼300 km-wide series of rift valleys and basins which mark the overlap between the Ethiopian Rift and the Eastern Rift of Kenya to the north of Turkana (e.g., Ebinger et al., 2000). The Ethiopian Rift is often subdivided into two near-continuous segments: the ∼600 km-long Main Ethiopian Rift (MER) and Southern Afar (e.g., Corti, 2009); the former segment is the focus of this thesis.

Traditionally, the MER is differentiated into southern, central, and northern sectors (SMER, CMER, NMER; Figure 1.2), with each sector bearing distinct rift and fault trends and architectures reflective of the complex rifting stages undergone by the rift as a whole (Hayward and Ebinger, 1996; Bonini et al., 2005; Keranen and Klemperer, 2008; Agostini et al., 2011; Keir et al., 2015). Geographically, the SMER-CMER divide is marked by the Goba-Bonga volcanic lineament, which runs parallel to Lake Awassa (Corti et al., 2018b, e.g.,), and the NMER-CMER divide by the Boru Toru structural high, the onset of the transition to the Afar depression (Bonini et al., 2005). Within Afar, the E-W extension of the NMER is separated from Arabian NE-SW extension by the Quaternary left-lateral oblique-slip Tendaho-Goba'ad Discontinuity (Acton et al., 1991).

Past research into both the MER and Afar Depression has been hampered by Ethiopian political instability, civil unrest, and conflicts with the neighbouring states of Eritrea and

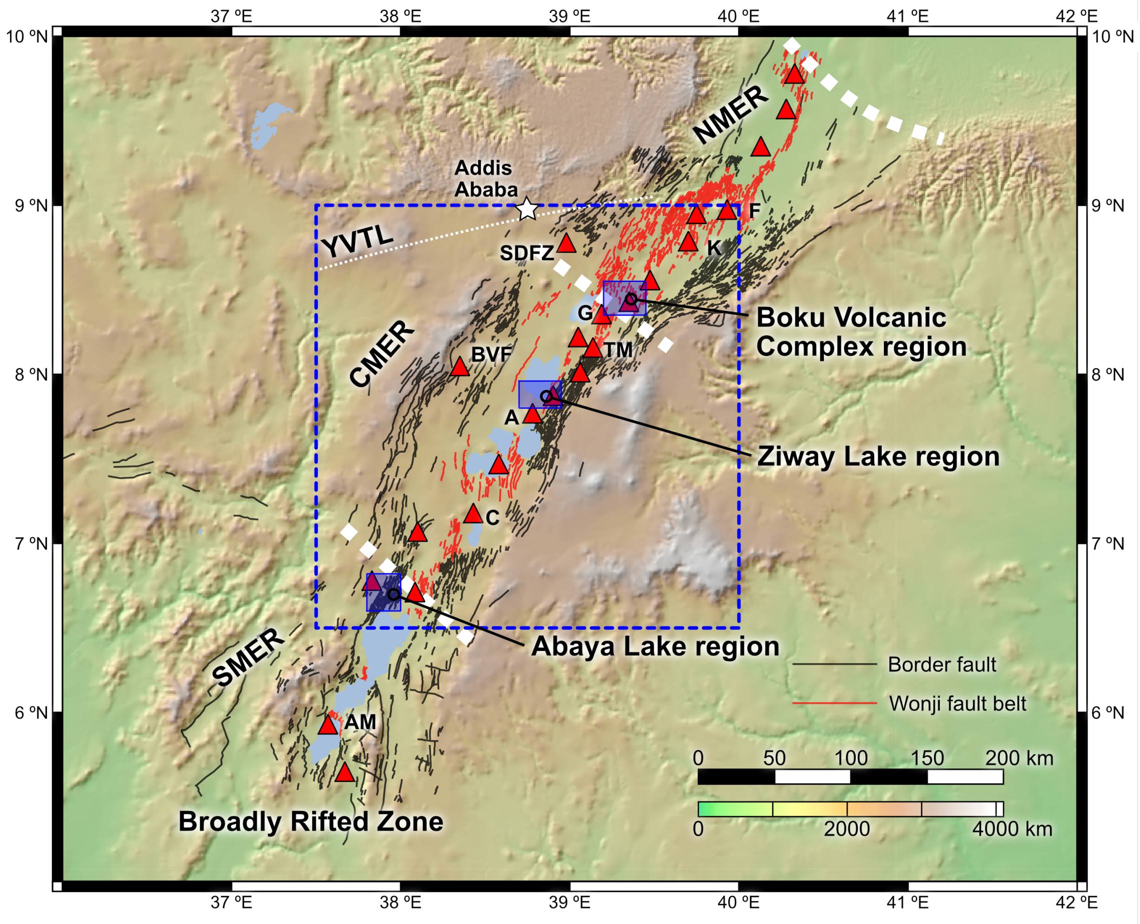

Figure 1.2: Overview elevation map of the Main Ethiopian Rift. The MER is differentiated into southern, central, and northern sectors (SMER, CMER, NMER) by thick, dashed, white lines. Border faults and faults of the Wonji Fault belt are included as grey and red lines respectively (Agostini et al., 2011). The dashed blue box shows the extents of Figure 1.4; the solid blue boxes show the sampled areas near Abaya Lake (Figure 2.1), Ziway Lake (Figure 2.3), and the Boku Volcanic Complex (Figure 2.5). The rough position of the Yerer Tullu-Wellel volcano-tectonic lineament (YTVL) is also included. Red triangles show volcanoes from the Global Volcanism Program (2013), with the following major calderas and volcanic fields labelled as follows: AM, Arba Minch; C, Corbetti; A, Aluto; BVF, Butajira volcanic field; TM, Tullu Moye; G, Gedemsa; SDFZ, Silti-Debre Zeyit Fault Zone; BB, Boset-Bericha; K, Kone; F, Fantale. The digital elevation model is GTOPO30 (completed in 1996).

Somalia. Most in-depth petrological and geophysical studies are therefore recent, and the majority are in collaboration with the Ethiopia Afar Geoscientific Lithospheric Experiment (EAGLE; 2001–2003), Afar Rift Consortium (ARC; 2007–2011), and RiftVolc (2014–2019) research groups (e.g., Yirgu et al., 2006; Bastow et al., 2011; Wright et al., 2016).

Besides its unique geophysical setting, the Ethiopian Rift is known for being the 'Cradle of Mankind' after the discovery of several early hominid fossil localities within it, including the oldest known *Homo sapiens* (e.g., White et al., 2009; Vidal et al., 2022). Uplift and volcanism in the Ethiopian Plateau during early rift development promoted the development of grasslands in the rift system, which may have spurred the evolutionary radiation of hominids within the rift valley (e.g., Gani et al., 2007; Hutchison et al., 2016b). The most recent evolution of the MER is therefore possibly entwined with that of humans, who still live among the rift volcanoes at the present day (Aspinall et al., 2011).

1.2 Regional tectonics

At the present day, the MER accommodates 4–6 mm yr^{-1} extension in a roughly east-west direction between the Nubia and Somalia subplates (Calais et al., 2006; Saria et al., 2014). Overarching rift development is migrating from the north of the MER to the south, although significant portions of the rift are oblique to the direction of extension and have an asymmetric across-strike architecture (e.g., Siegburg et al., 2020), suggesting that rift development may follow deep-set pre-existing weaknesses and heterogeneities within the underlying lithosphere (Corti et al., 2013a, 2018a). Rift formation and localisation in Ethiopia in the Tertiary have been correlated to basement deformation during the Proterozoic, and this early continental and lithospheric deformation may therefore primarily control rift location and orientation (Keranen and Klemperer, 2008; Keranen et al., 2009).

The early magmatic history of East Africa is marked by periods of extensive flood basaltic volcanism prior to continental rifting from ∼45 to ∼30 Ma (e.g., Rooney, 2017). This widespread volcanism is thought to be related to the impingement of one or more mantle plumes at the base of the lithosphere, which may linger to the present day (see Section 1.2.3). Volcanic activity initiated in southwest Ethiopia and the Turkana depression at 45–40 Ma; however little lithospheric extension accompanied these events (e.g., Ebinger et al., 1993).

Extension in the northern parts of East Africa is thought to have began in the Oligocene,

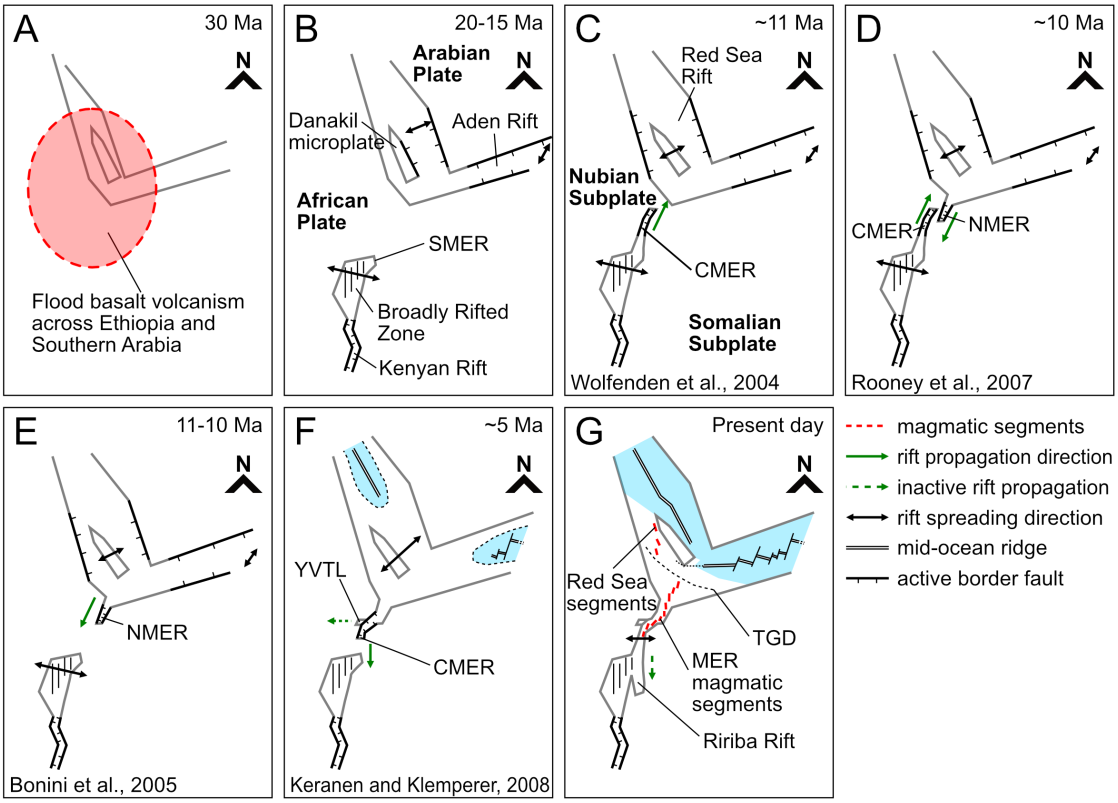

Figure 1.3: Schematic diagrams illustrating time-frames and hypotheses for MER development. A depicts flood-basalt volcanism in Afar, covering much of Ethiopia and Yemen. B illustrates the development of the SMER from the Broadly Rifted Zone. C to F highlight different development models put forward in the literature; C illustrates the northward propagation of the MER from the Broadly Rifted Zone (Wolfenden et al., 2004); D shows the bi-directional rift development model put forward by Rooney et al. (2007) to satisfy the presence of two rift-parallel volcanic fields; E depicts a southward propagation of the rift from Afar towards the Broadly Rifted Zone (Bonini et al., 2005), possibly completed with a possible diversion along the Yerer Tullu-Wellel volcano-tectonic lineament (YVTL) in the Pliocene as shown in F (Keranen and Klemperer, 2008). G depicts the current configuration of the rift at the present day.

coincident with the eruption of continental flood basalts in Afar at ∼30 Ma (Figure 1.3A; WoldeGabriel et al., 1990). Eruption of significant volumes of basaltic lava (∼350,000 km^3) heralded the onset of volcanism in Northern Ethiopia during this period (Mohr, 1983). While initial results from K-Ar dating suggested three major eruptive events from 50–20 Ma (Berhe et al., 1987), it is now generally agreed that flood-basalt volcanism was rapid: Ar-Ar dating points to the emplacement of 500–1500 m thickness of lavas over an area at least 600,000 km^2 within ∼1 Ma at ∼30 Ma (Hofmann et al., 1997). The start of rifting in the Red Sea and Gulf of Aden at 29–26 Ma is coeval with this major eruptive event, as is initial rifting in Ethiopia; however this phase of rift growth did not progress further south than 10 °N into the latitudes of the present-day MER (Wolfenden et al., 2005). Extension and related magmatism and deformation of the NMER occurred later during the Miocene, and are thought to be unrelated to the earlier Afar flood basalt volcanism (e.g., Wolfenden et al., 2004; Bonini et al., 2005).

Rifting to the south of the present-day MER starting from ∼25 Ma formed the Turkana depression, which marks the upper limit of the Kenya Rift system within the Broadly Rifted Zone (e.g., Hendrie et al., 1994; Knappe et al., 2020). Extension of the Kenya Rift to the north of Turkana established the SMER, linking the MER with the Broadly Rifted Zone (e.g., Ebinger et al., 2000). Radiometric dating of fluvial-lacustrine sediments constrain the onset of SMER deformation to the Early Miocene (21–20 Ma), with fault structures active until ∼11 Ma (Figure 1.3B; WoldeGabriel et al., 1991; Ebinger et al., 1993; Bonini et al., 2005); plate kinematic models similarly necessitate extension in the MER by 16 Ma at the latest (DeMets and Merkouriev, 2016). Initial volcanism in the SMER, synchronous with the onset of rifting, resulted in the eruption of the Getra Kele basalts near Arba Minch (Ebinger et al., 1993; George and Rogers, 2002). NMER extension began at ∼11 Ma on the NE-striking border fault system which mark the flanks of the present-day rift (WoldeGabriel et al., 1990; Wolfenden et al., 2004). While the start of silicic shield-building volcanism within the CMER is concurrent with the onset of NMER rifting (Chernet et al., 1998; Wolfenden et al., 2004), the rift development of the CMER itself is debated. WoldeGabriel et al. (1990) suggest through rift wall stratigraphy and K-Ar dating that the CMER border faults had developed by 9.7–8.3 Ma; on the other hand Bonini et al. (2005) utilise similar methods to obtain a main rifting period initiating at 6–5 Ma.

Several models for MER development have arisen as a result of its diachronous genesis. A northward-propagation model suggests that the earliest deformation of the MER initiated in the south at ∼18 Ma and migrated northwards towards the Afar depression from ∼11 Ma onwards (Figure 1.3C; Wolfenden et al., 2004). Alternatively, southward propagation of the MER from Southern Afar at 11–10 Ma towards the Kenya Rift triggered by the rotation of the Somalian Plate may have occurred (Figure 1.3E; Bonini et al., 2005), possibly initially diverting westward along the Yerer Tullu-Wellel volcano-tectonic lineament (YTVL) before resuming CMER development towards the south from 5–6 Ma onwards as the regional stress field changed, which forced the rift to continue developing along Proterozoic sutures (Figure 1.3F; Wolfenden et al., 2004; Keranen and Klemperer, 2008). While propagation along the YVTL was supplanted by the onset of CMER rifting, the lineation remains seismically active to the present day (e.g., Keir et al., 2006b). Finally, the synthesis model of Rooney et al. (2007) proposes that the MER developed from two independent rift systems: the northward-propagating EARS and the southward-propagating Red Sea rift (Figure 1.3D). Rooney et al. present the existence of two major volcano-tectonic zones on opposite sides of the CMER as evidence for two separate but interacting rift domains (see Section 1.3.2); however further geochronological work on lavas erupted within these two zones is necessary before their relationship, and the resultant implications for overarching rift development, can be assessed (Rooney, 2010).

MER propagation continued south into the Turkana depression at ∼3.7 Ma and after to form the Ririba Rift (Figure 1.3G), which ceased propagation prior to the Pleistocene (Corti et al., 2019; Franceschini et al., 2020). At the present day, the Ririba Rift accommodates most of the deformation in southern Ethiopia within pre-existing structures oblique to the direction of rifting, as opposed to structures in the MER which form perpendicular to extension direction (Franceschini et al., 2020). The Ririba Rift lithosphere has not yet been modified by extensive magmatic intrusion associated with the later stages of rifting (Franceschini et al., 2020, see following section).

1.2.1 Ethiopian Rift magmatic segments

Extensional strain within the MER is accommodated by two major fault systems: the border fault system common to all sectors of the EARS and the volcano-tectonic segments of the MER (e.g., Agostini et al., 2011). The border fault system is comprised of long, high-angle normal faults bounding the flanks of the MER that host considerable vertical throw and define its 60–100 km wide grabens. The immense length of the faults in these regions can be attributed to the substantial thickness of the seismogenic layer in unrifted continental crust, which scales with fault length (e.g., Hayward and Ebinger, 1996; Ebinger et al., 1999; Copley and Woodcock, 2016). South of the MER, border faults accommodate the majority of extension within the EARS (Ebinger, 2005; Muirhead et al., 2016). Geomorphological and seismological observations in the SMER and CMER suggest that the border fault system in these sectors remains active, albeit accommodating only a minor portion of extension (Pizzi et al., 2006; Keir et al., 2006a). In the NMER, the border faults are seismically inactive (Casey et al., 2006; Keir et al., 2006a).

Most extension in the MER is accommodated by a series of right-stepping volcano-

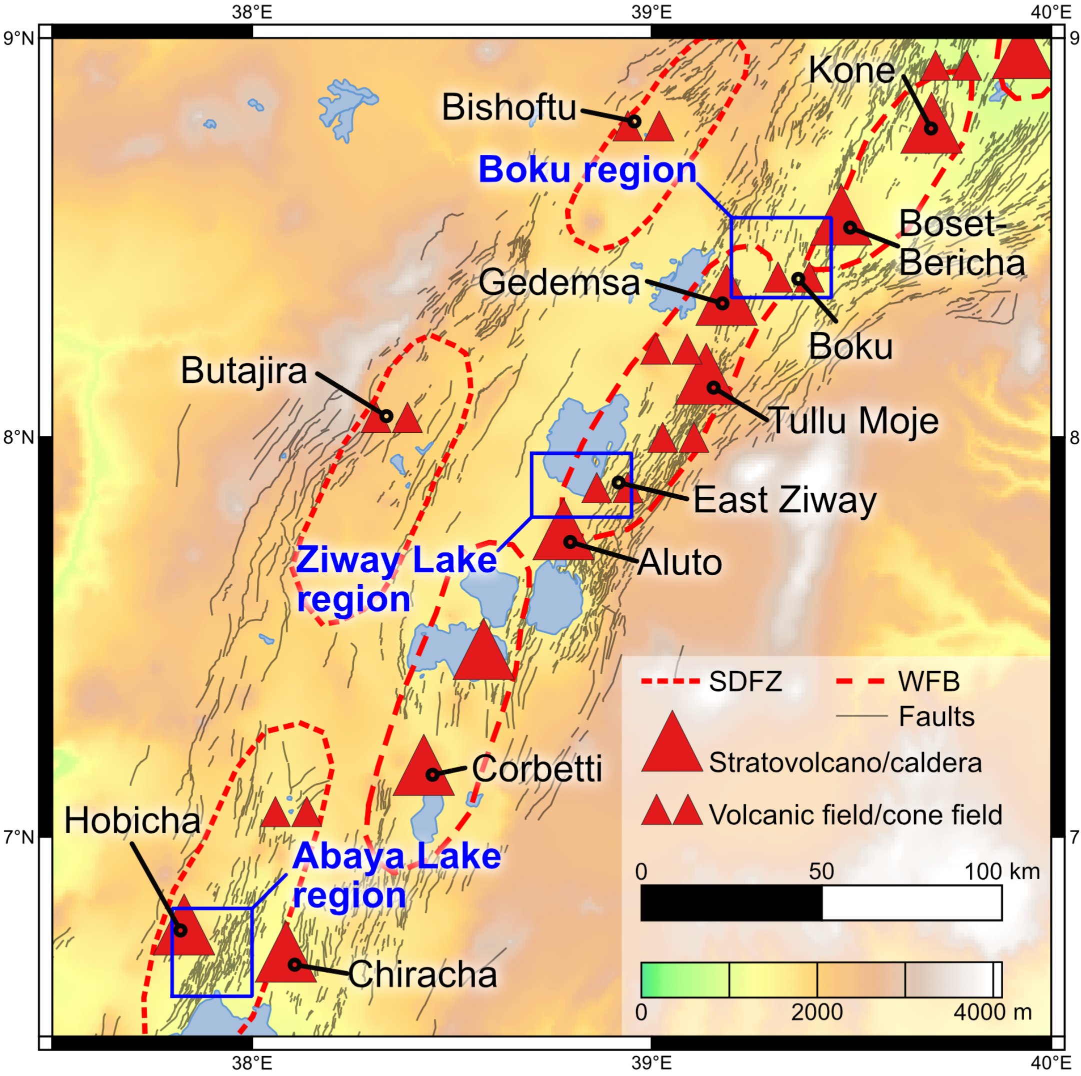

Figure 1.4: Map showing locations of major volcanoes and volcanic fields within the MER. The volcanic segments of Hayward and Ebinger (1996), including differentiation by Rooney et al. (2011), are additionally shown as the Silti-Debre Zeyit Fault Zone (SDFZ) and the Wonji Fault Belt (WFB). The blue boxes show the sampled areas near Abaya Lake (Figure 2.1), Ziway Lake (Figure 2.3), and Adama (Figure 2.5), which are described in more detail in the following chapter. Major rift faults are included as grey lines. Volcanoes and volcanic fields are recorded from the Global Volcanism Program (2013). The digital elevation model is GTOPO30 (completed in 1996).

tectonic lineations in the centre of the rift valley, sub-parallel to the direction of the rift axis. Numerous faults, fissures, and aligned volcanic fields outcrop within these lineations (Figure 1.4; e.g., Mohr, 1967; Boccaletti et al., 1999; Ebinger and Casey, 2001; Pizzi et al., 2006). Development of these volcano-tectonic segments initiated after ∼2 Ma (Ebinger and Casey, 2001), and segments of the fault belt are more evolved in the NMER and CMER than in the SMER, where surface deformation and volcanism occurs over a broader area (e.g., Keir et al., 2006a) without a well-defined southern termination (Rooney, 2010). In the north, these rift segments terminate clearly with the MER as a whole at the Tendaho-Goba'ad Discontinuity. The development of rift axis segmentation could arise from the obliquity of extension relative to the rift, which can generate fault patterns similar to those observed in the MER (Corti, 2008). This segmentation process may be facilitated by magmatic intrusion, as deformation migration is absent in the magma-poor Western Rift branch of the EARS (Muirhead et al., 2019).

In the SMER and CMER, deformation is aligned along both the eastern and western margins of the rift floor in two distinct parallel lineaments of volcano-tectonic segments (Figure 1.4). Of these two structures, only the eastern lineament of magmatic segments progresses north into the NMER and Southern Afar. Some authors use the term Wonji Fault Belt (WFB) to describe the chain along the eastern margin of the CMER (which progresses further north), and the Silti-Debre Zeyit Fault Zone (SDFZ) for the western marginal graben of the CMER (e.g., WoldeGabriel et al., 1990; Rooney et al., 2005). Others use the term WFB as a catch-all description for any magmatic segments (e.g., Pizzi et al., 2006; Corti, 2009), while several authors use 'magmatic segments' in lieu of either term (e.g., Ebinger, 2005; Kurz et al., 2007). In this thesis, I will use the term 'magmatic segments' or phrases of similar meaning when discussing the regional geophysical features, and will utilise WFB and SDFZ to further differentiate between the magmatic segments as required.

Geophysical analyses of the sub-rift lithosphere have revealed several distinct features in the crust and mantle related to extensive magmatic intrusion beneath rift segments. High P-wave velocity seismic anomalies in the mid-upper crust underlie segments, and are interpreted as cooled mafic intrusive bodies (Keranen et al., 2004; Daly et al., 2008). Additionally, the crust and uppermost mantle under magmatic segments have high magnetotelluric conductivity (Whaler and Hautot, 2006; Hübert et al., 2018) and low S-wave velocity (Keranen et al., 2009; Kim et al., 2012; Chambers et al., 2019), characteristic of the presence of partial melt. High-velocity, high-density lower crust is also common throughout the rift (Maguire et al., 2006; Cornwell et al., 2006; Mickus et al., 2007). These multiple strands of geophysical analysis therefore combine to suggest that the MER crust has been heavily intruded by basaltic magmas, which has remained partially molten to the present-day.

Seismic anisotropy can be used to resolve the orientation of intrusive fabrics in the Ethiopian crust and mantle (Ayele et al., 2004; Kendall et al., 2005; Chambers et al., 2021). The fast direction of shear wave anisotropy in the MER is aligned roughly parallel to the local trend of rifting segments, and its magnitude is co-variant with the intensity of surface deformation and magmatism (Keir et al., 2005; Kendall et al., 2006). Thin layering of seismically contrasting basaltic and sedimentary material in the uppermost crust produces surface wave anisotropy, and stress field-oriented melt pockets and dykes contribute to this anisotropy at greater crustal depths (Bastow et al., 2010). In particular, strong horizontally oriented anisotropy between 5–15 km suggests that horizontal sills dominate melt storage in the MER mid-crust in particular; the orientation of intrusions in the lower crust are more difficult to resolve (Chambers et al., 2021). Seismic anisotropy in the underlying uppermost mantle is linked to flow from the lower mantle (Kendall et al., 2006, see Section 1.2.3). However, pre-existing fabrics from Precambrian Pan-African deformation may also contribute to observed lithospheric anisotropy (Gashawbeza et al., 2004).

1.2.2 Magma-assisted rifting

The border fault system and the deforming magmatic segments represent two transitioning regimes of rift evolution in the EARS which are preserved and exhibited within the MER (Ebinger, 2005; Corti, 2009; Ebinger et al., 2017). To the south of the MER, the progressive migration of rift deformation from border faults to intra-rift faults is observed in the Magadi-Natron basin, which is thought to be a less mature rift than in the MER (e.g., Ebinger, 2005; Muirhead et al., 2016, Figure 1.5A). Within the first 3 Myr of extension in the Magadi-Natron basin, border faults accommodated most strain (69%) related to regional extension (Muirhead et al., 2016). After this period, faulting within the rift axis itself supports much more of the regional extension (67–80%; Ebinger, 2005; Muirhead et al., 2016). Strain accommodation in the Magadi-Natron basin therefore migrates from border faults to intra-rift faults as rifting progresses, a process which nears completion in the Ethiopian Rift (e.g., Ebinger, 2005).

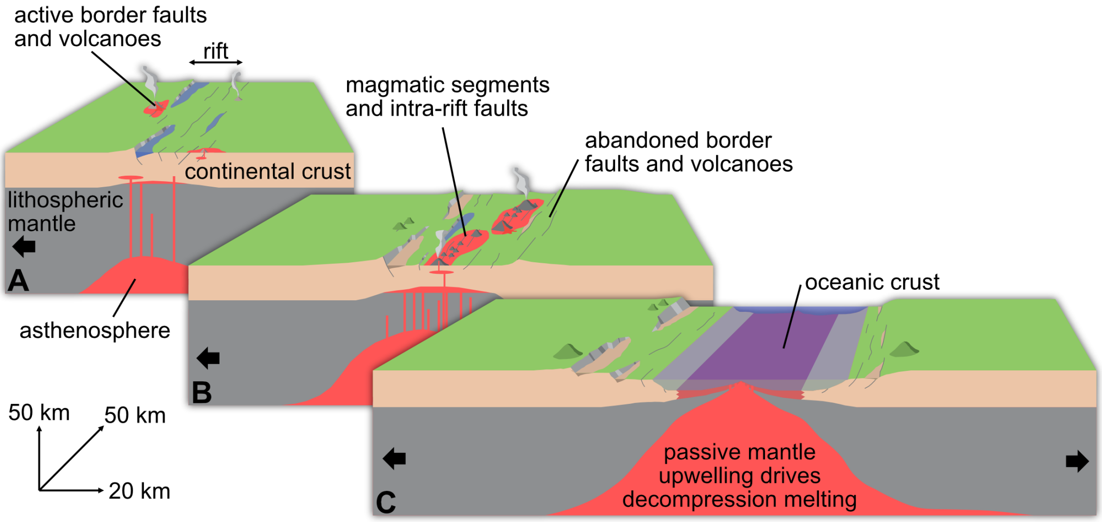

Figure 1.5: Block model illustrating the temporal evolution of continental rifts (modified after Ebinger, 2005). A. Rift border faults and associated graben and half-graben structures accommodate all extension within the rift zone within the first 5 million years of rift initiation. Early volcanism is focussed along these border faults (e.g., Kenyan Rift). B. The rift matures after 10 million years, and magmatism and deformation is now focussed within volcano-tectonic segments in the rift centre. Deformation is now mostly aseismic, and extension is accommodated by repeated dyke injection. At this stage the lithosphere is thinned, but crust remains thick (e.g., MER). C. Continental break-up reaches completion, and the rift-to-ridge transition is complete. All magmatism occurs within the ridge axis, and is fuelled by melting from a passively-upwelling asthenosphere (e.g., Gulf of Aden).

Extensional deformation in the MER has shifted to the rift floor and magmatic segments over the past ∼2 Ma (Hayward and Ebinger, 1996; Ebinger, 2005, Figure 1.5B). The migration of volcanism from the flanks of the rift to the intra-rift segments was concurrent with this change in extensional regime (e.g., Ebinger and Casey, 2001). Although the strain resulting from regional kinematics is distributed over a greater length-scale than the width of the rift valley itself, a significant proportion of strain is accommodated narrowly within the rift segments (Bendick et al., 2006; Casey et al., 2006); GPS measurements suggest that ∼80% of present-day extensional strain within the NMER is accommodated by deformation within the rift floor (Bilham et al., 1999). The majority of observed seismicity is also localised to the segments, further highlighting the comparative inactivity of the border fault system (Keir et al., 2006a,b; Daly et al., 2008). However, while seismically inactive, border faults may still control the position of mantle upwellings beneath the rift and hence the loci of melt generation, melt focusing, and volcanism at the surface (Bastow et al., 2005, 2008).

A mismatch between observed seismic moment and expected released seismic moment within the MER demonstrates that most extensional deformation occurs aseismically (Hofstetter and Beyth, 2003). Aseismic deformation is attributed to volcanic activity and episodic dyke intrusions within rift segments (Keir et al., 2006a; Daly et al., 2008). Mantle flow models suggest that the combined tectonic forces of slab pull and the gravitational collapse of plume-related dynamic topography are insufficient to rupture East African continental crust; magmatic intrusion into the crust is therefore necessary for rifting to commence (Kendall and Lithgow-Bertelloni, 2016). Hot mantle-derived magmas in continental lithosphere reduce plate strength through heat transfer during intrusion, permitting ductile behaviour at lower pressures in the crust (Ebinger, 2005; Daniels et al., 2014; Muluneh et al., 2020) while strengthening local crust via thermal metamorphism to promote dyke intrusion in place of crustal stretching (Lavecchia et al., 2016). Strain is therefore accommodated by magmatic intrusion at lower stress levels than through only seismic deformation: magma-assisted rifting promotes the abandonment of border faults in favour of volcano-tectonic zones in the rift centre (Buck, 2006). This is evident when observing the spatial distribution of rift earthquakes; earthquakes are shallower and higher-magnitude in the southern parts of the MER where extension by faulting is still prominent (Mazzarini et al., 2013a), but are lower magnitude in the CMER and NMER within rift segments (Keir et al., 2006a). Magmatic intrusion in rift segments is therefore an important factor in controlling the geodynamic regime in active continental rifts; this form of rift development is especially prevalent in the highly-evolved rift system of Afar (e.g., Wright et al., 2006; Keir et al., 2009; Ebinger et al., 2010).

Magma-assisted rifting models are in contrast to 'traditional' stretching models, which predict progressive thinning of crust and strain localisation as basin development continues (e.g., McKenzie, 1978). Traditional rifting is not observed in the MER and Afar (Bastow and Keir, 2011), or other active continental rift zones (e.g., Thybo and Nielsen, 2009). Rather than the progressive focusing of strain into a narrower zone as rifting reaches its later stages as predicted from traditional rifting, GPS velocity profiles reveal the opposite – strain becomes more distributed as rift development continues (Kogan et al., 2012). Rifted crust remains thick until the final stages of rifting, when it thins rapidly, unlike the gradual thinning expected from early basin development models (Bastow et al., 2011). The β-factor (ratio of initial thickness to thickness after rifting) of Southern Afar expected from traditional rifting models is $\sim$3 (Eagles et al., 2002); however seismic reflection studies give β of 1.1 beneath the MER and $\sim$1.7 in Southern Afar (Maguire et al., 2006).

Crustal thickness is maintained by magmatic intrusion into the crust until the final stages of continental break-up in Afar (Bastow et al., 2011). The final surface subsidence and widening of the rift occurs when seismogenically strong parts of the lithosphere lose their competence and deform in the ductile regime (Kogan et al., 2012).

Rifting to completion will result in seafloor spreading, as seen in the Red Sea and the Gulf of Aden (e.g., Ebinger et al., 2017, Figure 1.5C); this is not yet observed in the MER or Afar, as upper mantle upwellings are not yet coupled to surface features as seen at MORs (Bastow et al., 2008), and crustal thicknesses at Afar (∼15 km) are similar to that of continent-ocean transitions seen at rifted margins (e.g., White and McKenzie, 1989). It is hence appropriate to say that extension in Ethiopia has not yet evolved to seafloor spreading.

1.2.3 Mantle plume(s?) beneath the Ethiopian Rift

Flood basalt volcanism in the north of Ethiopia at ∼30 Ma is often correlated with the impingement of a mantle plume head with the base of the Afar lithosphere (e.g., Morgan, 1972; White and McKenzie, 1989; Furman et al., 2006; Pik et al., 2006). Geochemical evidence for the past and/or current presence of a mantle plume source contributing to volcanic activity is obtained through study of isotopes of lavas from the MER and Afar, which suggest that magmas are derived from a mantle source distinct from MORB-source mantle (e.g., Rogers, 2006). In particular, ^{3}He/^{4}He isotope ratios of Afar flood basalts lie over a wide compositional range, capturing values typical of MORB, continental lithospheric mantle, continental crust, and a ‘primitive’ high ^{3}He mantle source typical of plume-influenced settings (Marty et al., 1996; Pik et al., 2006). Extensive research in recent times has therefore focussed on determining the nature of mantle upwellings beneath the rifting East African region, and the role they may play in manipulating ongoing rift development.

Regional and global seismic tomography have been the primary geophysical means used to ascertain the existence and number of plumes in the mantle underlying Ethiopia and East Africa. P- and S-wave travel time tomography of the upper mantle reveals a large-scale low-velocity anomaly within the uppermost 500 km of the sub-rift mantle (Bastow et al., 2005, 2008; Benoit et al., 2006a,b; Adams et al., 2012). Within the mantle transition zone, this anomaly has been correlated to a ∼30 km topographic elevation of the 660 km mantle discontinuity, corresponding to a temperature anomaly of 300–400 °C (Benoit et al., 2006a), but no clearly resolved corresponding topographic depression of the 410 km discontinuity also expected from a positive thermal anomaly (Nyblade et al., 2000; Benoit et al., 2006a; Nyblade, 2011). Beneath the transition zone, global tomographic models show that the anomaly trends to the south-west, where a low-velocity conduit joins the anomaly to a large low-velocity province (LLVP) present at the core-mantle boundary underlying the south and west of the African continent (Ritsema et al., 1999; Montelli et al., 2004; Montelli et al., 2006; Simmons et al., 2007; French and Romanowicz, 2015). The African LLVP, often termed the ‘African superplume’, is a long-lived thermo-chemical region of uncertain origin that is distinct from the surrounding mantle on the basis of its anomalously low seismic velocity (e.g., Garnero et al., 2016). Its thermal and possibly chemical effects on dynamic surface topography are associated with the African ‘super-swell’ (Kendall and Lithgow-Bertelloni, 2016), a broad region of anomalous uplift comprising East and southern Africa (e.g., Nyblade and Robinson, 1994), which has elevated Ethiopia since Afar volcanism at ~30 Ma (e.g., Gani et al., 2007).

Despite the presence of the LLVP-related mantle anomaly, the number of distinct plumes present within the rift mantle is uncertain. Ebinger and Sleep (1998) suggest that magmatism in East Africa can be accounted for by the impact of a single channelised plume. However a single mantle plume cannot easily reconcile the geochemistry of plume-influenced basalts sampled from both the Kenyan and Ethiopian rifts, which necessitate the presence of more than one plume-derived mantle source (Rogers et al., 2000; Rogers, 2006; Furman et al., 2006; Nelson et al., 2012). These conflicting ideas may be resolved through two orders of mantle plume; the first order being the deep-set anomaly arising from the African LLVP; the second order being secondary plumes upwelling from the larger-scale primary anomaly at upper mantle-transition zone depths (Pik et al., 2006). Ethiopian and Kenyan Rift noble gas isotopes provide the primary evidence supporting this hypothesis, as they necessitate the interaction of a depleted mantle source with a plume source that is common to the entire EARS, yet feeding different sectors through distinct and discrete subplumes (Halldórsson et al., 2014).

Likewise, whether or not the seismically-identified low-velocity anomaly under Ethiopia can be itself differentiated into separate plumes is a matter of debate. Tomographic models differ in this regard; some models resolve two discrete large-scale plume conduits under Afar and Kenya (Montelli et al., 2006), potentially of differing deep-mantle provenance (Chang and Lee, 2011; Boyce et al., 2021); other models interpret the sub-rift thermal anomaly as an undifferentiated and continuous extension of the African LLVP, noting that multiple plumes may coalesce into one larger feature, both within the mantle and as a consequence of seismic resolution (Hansen et al., 2012). Sub-rift asthenospheric anisotropy, interpreted as lattice-preferred alignment of mantle olivine during lateral mantle flow from the LLVP to the sub-MER low-velocity zone, is mostly in agreement with the latter model (Kendall et al., 2006; Gao et al., 2010).

1.2.4 Depths of melt generation in Ethiopia

Many questions concerning the role of mantle upwellings remain despite the efforts of geophysical studies; is there still a mantle plume actively driving volcanism beneath Afar and the MER, or do geochemical plume signatures arise from remobilisation of material from the 30 Ma plume impact (Gallacher et al., 2016)? How many plumes are responsible for Eocene-Oligocene volcanic activity, and can they be captured by present-day seismic imaging or other methods (Bastow et al., 2008)? Whether the Afar plume and other possible active mantle upwellings exert an influence on present-day rifting and magmatism in the MER and Afar remains uncertain, and the causes for melt production and focusing in this region continues to be a controversial topic. Causes for melting within the MER can be reduced to two primary schools of thought:

- The rifting is passive, and driven solely by extensional deformation of the lithosphere. Resultant magmatism is therefore the result of adiabatic decompression melting of ambient mantle asthenosphere as it passively upwells to the base of the crust with minimal plume influence, as is the case beneath mid-ocean ridges (MORs; e.g., Rychert et al., 2012).

- The rifting is being actively driven by dynamic movements within the underlying mantle. This active upwelling promotes elevated mantle temperatures and decompression melting beneath the MER, permitting melting at depth beneath a thick lithosphere (e.g., Ebinger and Sleep, 1998).

Attempts at differentiating between the two rifting styles in the MER have therefore focussed on identifying the presence/absence of a mechanical boundary layer (mantle lithosphere) beneath the rift, or using geochemical or geophysical means to constrain the depth and degree of melting, and temperature of the sub-rift convecting mantle (asthenosphere).

Evidence for a thermally-driven mantle plume is often implied from elevated mantle temperatures. The most common expression of mantle temperature is potential temperature (T_p), defined by McKenzie and Bickle (1988) as the temperature a solid parcel of mantle would have if it was adiabatically decompressed to the surface of the Earth without melting. Petrological methods of estimating the composition of mantle-derived melts from erupted lava compositions are frequently used to assess T_p. Rooney et al. (2012c) used the PRIMELT-2 software of Herzberg and Asimow (2008) to obtain a mantle T_p anomaly of 140 °C at Djibouti and $\sim$100 °C along the MER, relative to the T_p of ambient sub-ridge mantle (taken as 1350±50 °C; e.g., Herzberg and Asimow, 2015; Matthews et al., 2021). These estimates are determined from lavas erupted within the past 10 Ma; earlier lavas in the region related to major flood basalt eruptions return greater T_p anomalies of up to 170 °C. The magnitude of this thermal anomaly is comparable to those of plume-related settings such as Iceland which have undergone the same methods of study (Herzberg and Gazel, 2009); it therefore seems reasonable to suggest that there is still active mantle upwelling in the present-day MER.

In contrast to petrological methods, S-to-P receiver function imaging of the mantle structure underlying the MER and Afar identifies a strong amplitude change at 75 km beneath the rift flanks attributed to the LAB; this change is absent beneath the MER and Afar Rift; instead a positive amplitude velocity increase is observed (Rychert et al., 2012). By comparing these observations with a synthetic waveform model, Rychert et al. (2012) suggested that this velocity increase could be attributed to the absence of the mantle lithosphere beneath the rifting area, implying that MOR-like decompression melting had initiated without the thermal influence of a plume. This model predicts T_p of 1350–1400 °C, which overlaps with the PRIMELT-2 T_p ranges for the EARS and MORs (Rooney et al., 2012c). This study therefore concludes that there is no geophysical requirement for a mantle plume beneath Afar and the MER, and that volcanism occurs solely though passive adiabatic decompression melting at shallow depths (<80 km). This model of shallow decompression melting is further supported by Hammond et al. (2013) who constrain melting beneath Afar to a maximum depth of $\sim$75 km using travel-time tomography.

Shallow and passive melting is at odds with the results of Ferguson et al. (2013b), who utilise rare-earth element (REE) inversion to constrain depths of melting. Increased medium REE (MREE) and heavy REE (HREE) concentrations require melting within higher pressure garnet-bearing upper mantle as opposed to shallower spinel-bearing mantle (McKenzie and O'Nions, 1991). As garnet preferentially retains HREEs within its crystal lattice, melts generated from deeper garnet-bearing mantle will have an higher MREE/HREE ratio relative to those formed shallower in spinel-bearing mantle. Elevated mantle temperatures and the presence of a thick mechanical boundary layer are therefore necessary to permit this deeper melting, which occurs at depths greater than 80 km (McKenzie and O'Nions, 1991). Ferguson et al. (2013b) argue that this ∼80 km thick sub-rift lithosphere can be maintained through conductive heat loss during slow rifting, and estimate a Afar Rift T_p of 1450 °C, a temperature anomaly of ∼100 °C.

These conflicting results are somewhat reconciled by the use of both petrological and seismological constraints on a geodynamic model (Armitage et al., 2015). The REE compositions still necessitate deep melting and an elevated T_p of 1450 °C; however melt production likely continues to shallower depths beneath a thinner sub-rift lithosphere, rather than beneath one which is still thick (Ferguson et al., 2013b). The positive amplitude increase observed by Rychert et al. (2012) is poorly matched by this model; the velocity increase could be attributed to a gradual increase of melt in the mantle, which can trigger the appearance of discrete discontinuities in receiver function analyses (e.g., as observed at Hawaii; Rychert et al., 2013). Supporting this modelling is a more recent S-to-P receiver function study, which finds less evidence for the 75 km velocity increase observed by Rychert et al. (2012); instead a gradual velocity increase from 40 to 60 km depth is suggested, with a further increase only at 90 km depth (Lavayssière et al., 2018). Lavayssière et al. (2018) suggest that the discrepancy between these two studies is a consequence of their higher frequency waveform dataset, which removes low amplitude phases from the study (such as the 75 km velocity discontinuity of Rychert et al. (2012)). The velocity increase with depth beneath the MER is therefore likely to be gradual, with the lithosphere-asthenosphere boundary (LAB) obscured by melt pockets beneath the rift.

Rayleigh wave tomography illustrates that the low-velocity zone beneath the Ethiopian rift and Afar only extends to ∼150 km depth (Gallacher et al., 2016), contrary to body-wave topographic results highlighting a whole mantle plume (e.g., Bastow et al., 2008). Gallacher et al. (2016) therefore suggest that active upwelling beneath the MER is driven by the buoyancy of retained melt present within solid mantle matrix as opposed to an active plume conduit; however the melt fraction required for this buoyancy-driven melting would have to be similar to the melt fraction at MORs (e.g., McKenzie and O'Nions, 1991). Two problems would then result from this conclusion: the mechanism proposed for buoyancy-driven melting would likely generate a matrix permeability permitting the rapid release and escape of melt, and the melt fraction required (∼20%) would be in excess of melt fractions determined from major element and REE inversion (∼5–10%; Ferguson et al., 2013b; Armitage et al., 2015).

The evidence presented above therefore suggests that a thermo-mechanical boundary layer between the crust and the melting mantle persists beneath the MER and Afar, and that the full transition to oceanic-spreading centre has not been completed. Developing new models to illustrate the evolution from plume-driven broad and deep melting to shallow melting and MOR-like corner flow in magmatic segments are therefore necessary for further understanding of MER melt generation processes.

1.3 Main Ethiopian Rift volcanology: a petrological overview

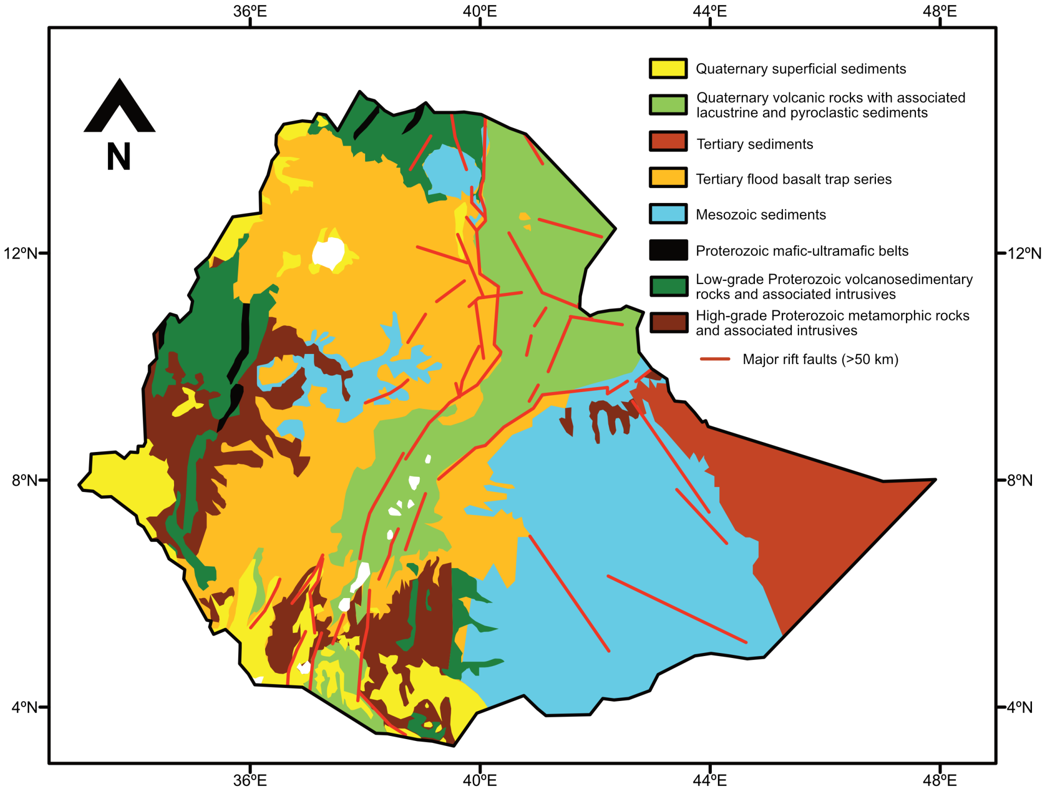

Figure 1.6: Simplified geological map of Ethiopia showing major lithological units and faults. Redrawn after Tefera et al. (1996).

Magmatic development in the MER can be described in terms of three major magmatic phases (e.g., Corti, 2009; Mazzarini et al., 2016); eruption of flood basalts and plateau formation (45–10 Ma); border volcanism during early rift development (11–4 Ma); intra-rift volcanism (∼4 Ma to present day).

Volcanic activity in Ethiopia commenced at 45 Ma in the Turkana depression to the south, which remains sporadically active to the present day (George et al., 1998); these early long-lived volcanic eruptions were bimodal, producing widespread basaltic lava flows and rhyolites. Volcanism peaked at ∼30 Ma with the eruption of flood basalts in Northern Ethiopia and Yemen (Figure 1.6; Rooney, 2017, and references therein). Following this major eruption, shield volcanoes developed along the surface of the volcanic plateau until 10 Ma, erupting transitional and alkaline basalts and trachytes (Piccirillo et al., 1979; Furman et al., 2006).

Initial rifting within the MER itself from ∼11 to ∼7 Ma produced silicic volcanoes along the border faults marking the edges of the rift (Wolfenden et al., 2004). Such volcanoes form the YTVL, the east-west alignment on the western shoulder of the MER (Abebe et al., 1998; Corti, 2009) believed to be an off-suture former extension of NMER rifting (Keranen and Klemperer, 2008).

Volcanism migrated into the rift centre from ∼4 to 1 Ma with basaltic activity along the rift magmatic segments (Abebe et al., 2007; Corti, 2009). During this period, pyroclastic deposits from silicic centres blanketed the rift floor (Chernet et al., 1998; Corti, 2009). Further development of silicic centres from ∼650 ka are dominated by caldera formation events and associated pyroclastic activity from the major silicic centres that lie along the rift axis (e.g., Siegburg et al., 2018), positionally dictated by the position of reactivated pre-rift fractures and areas of underlying lithospheric weakness (Acocella et al., 2003; Lahitte et al., 2003; Korme et al., 2004; Abebe et al., 2007). Several periods of enhanced silicic volcanic activity are recorded between 320 and 170 ka; the factors triggering this ‘flare-up’ period, recorded through radiometric dating of ignimbrites, are still uncertain (Mohr et al., 1980; Hutchison et al., 2016b). Despite the prominence of these major silicic eruptions, basaltic activity in the rift has dominated from ∼2 Ma, forming spatter cones, scoria cones, maars, and rift fissures (e.g., Chernet et al., 1998; Rooney et al., 2011).

At the present day, the floor of the MER is marked by major silicic calderas, related pyroclastic deposits, and basaltic scoria cone fields and fissure eruptions which themselves are interlain with fluvio-lacustrine sedimentary deposits related to subsidence (Figure 1.6). InSAR and GPS observations at several rift volcanoes suggest that magmatism and deformation beneath volcanic centres is still ongoing (Biggs et al., 2011; Lloyd et al., 2018).

The last volcanoes to erupt in the MER were Fantale, Kone and Tullu Moje, all in the 19th century/earliest 20th century (Wadge et al., 2016), which consisted of volumetrically-significant silicic lavas and volcaniclastic deposits, and less voluminous basaltic activity (Peccerillo et al., 2003). The most recent Ethiopian volcanism is in Afar along the Afar Rift sector of the Red Sea Rift (Ferguson et al., 2010).

Past studies have systematically analysed the individual major volcanic complexes of the MER, including Aluto (Hutchison et al., 2015, 2016a,b,c; Gleeson et al., 2017), Boset-Bericha (Ronga et al., 2010; Siegburg et al., 2018), Gedemsa (Peccerillo et al., 2003; Giordano et al., 2014), Fantale (Giordano et al., 2014; Iddon et al., 2019), Kone (Iddon et al., 2019), Tullu Moye (Tadesse et al., 2022), and Boku (Boccaletti et al., 1999; Tadesse et al., 2019). Other studies have considered overarching geochemical trends in basaltic material throughout the entire EARS or MER (Rogers, 2006; Furman et al., 2006; Furman, 2007; Rooney et al., 2007; Ayalew et al., 2016; Nicotra et al., 2021), or between the basalts of the WFB and SDFZ (e.g., Rooney, 2010; Rooney et al., 2011; Nicotra et al., 2021). This section will briefly summarise the major petrological observations observed at and around MER volcanoes.

1.3.1 Main Ethiopian Rift geochemistry: rhyolites

Quaternary volcanism in and around MER central volcanoes is characterised by strongly bimodal mafic and felsic activity (Figure 1.7). Rhyolites are typically associated with the central volcano itself, while basalts are typically erupted with fissure eruptions and scoria cones to its flanks (Ebinger and Casey, 2001), with little material sampling the intermediate compositions between the basaltic and rhyolitic endmembers (Peccerillo et al., 2003, 2007; Abebe et al., 2007, Figure 1.7). Suggestions for this regional-scale compositional gap (the ‘Daly Gap’, after Daly, 1925) often relate bimodal activity at these centres either to fractional crystallisation of mantle-derived basalts to generate rhyolites (e.g., Peccerillo et al., 2007), melting of basaltic lower crust followed by fractional crystallisation (e.g., Trua et al., 1999), or the generation of silicic melts by crustal anatexis of old continental crust and basalt (e.g., Black et al., 1997).

Fractional crystallisation of basalts in shallow crust (<200 MPa) by as much as 90% without much crustal contamination at major silicic centres is supported by trace element investigations (Peccerillo et al., 2003; Giordano et al., 2014; Hutchison et al., 2016c) and statistical and thermodynamic modelling (Rooney et al., 2012b; Gleeson et al., 2017).

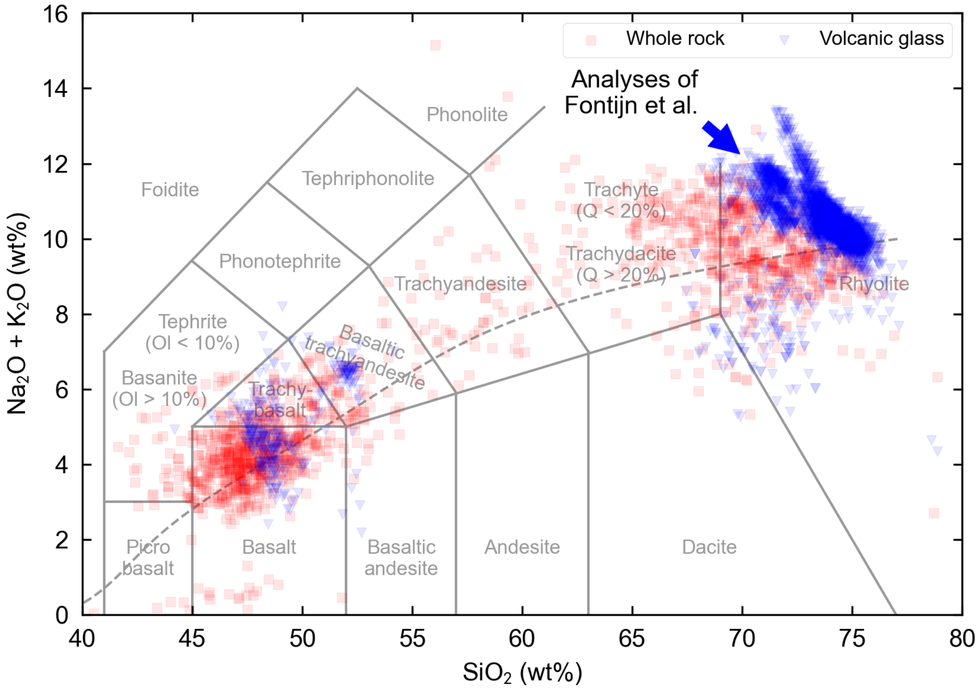

Figure 1.7: Total alkali-silica (TAS) plot (Le Bas et al., 1986) of all erupted products from the MER (tholeiitic-alkaline divide of Irvine and Baragar, 1971). The geochemical data set for the MER is compiled using the GEOROC database for the MER, selecting whole-rocks and volcanic glasses (`http://georoc.mpch-mainz.gwdg.de/georoc/`). The high number of analyses from Fontijn et al. (2018), which form a noticeable trend in the rhyolite data, is highlighted. The vast majority of samples plot within the basaltic and rhyolitic fields, with comparatively fewer intermediate samples, a phenomenon termed the 'Daly Gap'.

This pressure of fractionation correlates with the position of strong gravity anomalies in the shallow crust (e.g., Cornwell et al., 2006), suggesting that shallow magma storage systems are likely common along the MER, and fed by intrusion (Gleeson et al., 2017). Trace element concentrations remain constant throughout the basalt-rhyolite suite, and are distinct from the trace element composition of Precambrian crust (Iddon et al., 2019); Sr, Nd, and O isotope systematics also differentiate erupted lavas from continental crust compositions (Hutchison et al., 2018). It is therefore unlikely that a Daly Gap can arise solely from crustal contamination or anatexis.

Density stratification has also been suggested as a supporting mechanism by which a Daly Gap could arise. Low-density silicic magmas occupying the shallower levels of magma reservoirs restrict the eruption of higher density intermediate and mafic melts (Peccerillo et al., 2003). In addition, the development of mush during intermediate/mafic fractionation increases the viscosity of lower layers, further inhibiting their eruption (Gleeson et al., 2017). Fractionation models of magmatic evolution at Aluto also demonstrate that magma SiO_2 increases rapidly over a short crystallisation interval across a correspondingly short temperature interval, causing the system to 'skip over' intermediate compositions (Gleeson et al., 2017). Similar models for rhyolites of Kone and Fantale confirm that Daly Gaps may arise at other magmatic centres in a similar manner (Iddon et al., 2019). Understanding how basaltic magmas are generated and emplaced in the rift crust will provide new constraints on such models describing melt evolution from basalt to rhyolite, and provide more knowledge on how MER volcanoes operate.

1.3.2 Main Ethiopian Rift geochemistry: basalts

Rift basalts form scoria cones and associated lava flows along the lengths of the WFB and SDFZ (Abebe et al., 2007; Rooney et al., 2011; Nicotra et al., 2021). A product of magma-assisted rifting, the cones and associated basaltic flows arise from dyke-induced faulting linked to the intersection of faults with caldera complexes and fracture networks, and form linear chains along the SDFZ and WFB magmatic segments (Peccerillo et al., 2003; Korme et al., 2004; Kurz et al., 2007; Mazzarini et al., 2013a; Hunt et al., 2019). In literature, these scoria cones are also termed basaltic vents, or monogenetic volcanic fields (e.g., Mazzarini et al., 2016).

MER basalts are predominantly alkaline to transitional (e.g., Rooney et al., 2007, 2012b), and are geochemically distinct to other basalts erupted along the EARS (Furman, 2007). Relative to the other sectors of the EARS, Ethiopian Rift basaltic materials are high K/Th and have lower incompatible element concentrations, indicative of greater melt fractions than Turkana, the Eastern Rift, or the magma-poor Western Rift (Furman, 2007). Similarly, Pb-isotope systematics separate MER basalts from other East African basalts (Furman, 2007).

Major element geochemistry of MER basalts is consistent with the melting of fertile spinel peridotite at lithospheric pressures, with minor contributions from a garnet-bearing source suggested from trace elements (George and Rogers, 2002; Furman, 2007; Ayalew et al., 2016). High Na_2O relative to K_2O in MER basalts suggests that amphibole contributes to the final melt (Furman, 2007; Ayalew et al., 2016). Amphibole is unstable at asthenospheric temperatures and pressures; signatures of amphibole melting therefore suggest that the sub-continental lithospheric mantle is metasomatised. Indeed, metasomatism of the lithosphere is also evident from enrichment of rift basalts in incompatible trace elements (e.g., Rooney et al., 2005; Ayalew et al., 2016), the geochemistry of plateau shield volcanoes (e.g., Rooney et al., 2017), and mantle xenoliths (e.g., Trestrail et al., 2017). Melting of this metasomatised lithospheric mantle may contribute to the final basalt (Ayalew et al., 2016), either via in-situ melting of lithospheric mantle (e.g., Rooney et al., 2017) or the melting of gravitationally destabilised lithosphere at asthenospheric pressures (Furman et al., 2016). The signature of amphibole melting in the MER and Afar is less prevalent than other localities along the EARS such as Kenya or the Turkana Depression (Furman, 2007), perhaps echoing the tectonic maturity of these sectors relative to those in the south.

Mantle-derived basalts can be differentiated by their radiogenic isotope compositions, which can reflect mantle source composition (e.g., Hofmann et al., 1986; Zindler and Hart, 1986; Stracke et al., 2005). Sr-Nd-Pb isotope systematics suggest mantle contributions from a MORB-source-like depleted asthenospheric mantle source (depleted mantle, DM), a metasomatised Pan-African lithospheric source (taken as high-μ by Ayalew et al., 2016, HIMU) and an enriched mantle source endmember which is isotopically distinct from the HIMU Pan-African lithosphere (enriched mantle, EM; Trua et al., 1999; Rooney et al., 2012a; Ayalew et al., 2016). MER isotope compositions overlap with those of Afar basalts, it is believed that this enriched source component is representative of the Afar mantle plume (Furman, 2007; Rooney et al., 2012a; Ayalew et al., 2016). This Afar plume contribution recognised in rift basalts increases from the south to the north of the MER, suggesting that the asthenospheric and lithospheric mantle components mixed to form a hybrid mantle composition prior to further mixing with the enriched Afar plume source on the lithospheric base (Rooney et al., 2012a). This increasing plume source influence is also captured by La/Yb ratios, which decrease from south-east to the north-west. An along-strike increase in melt fraction or enriched mantle source composition which can generate the observed La/Yb variations can both result from corresponding changes in mantle compositional heterogeneity (Ayalew et al., 2016). An enriched component may also contribute melting mantle pyroxenite, which has been proposed to justify extensive melting in the absence of a significant (>200 °C) thermal anomaly (Rooney et al., 2012c).

Basalts within the MER have not been significantly contaminated by continental crust. MER lavas have similar Ce/Pb (20–34) to OIB and MORB (Ce/Pb=25±5; Hofmann et al., 1986), in contrast to the low Ce/Pb of continental crust (Ce/Pb=3.3–3.9; Rooney et al., 2007; Ayalew et al., 2016). Likewise, ^{87}Sr/^{86}Sr and ^{143}Nd/^{144}Nd does not correlate with MgO; crustal assimilation and magmatic fractionation are therefore disconnected (Ayalew et al., 2016). Trace element compositions of MER basalts are therefore solely a consequence of melting mantle lithologies, and are unlikely to have interacted with continental crust. In contrast to rift basalts, 30 Ma flood basalts are extensively contaminated (e.g., Pik et al., 1999), perhaps owing either to present-day rift crust comprising more basalt than at 30 Ma or to the crustal residence time of rift melts relative to flood basalts (Rooney et al., 2007). While geophysical imaging of substantial crustal intrusion offers support to the former hypothesis (e.g., Keranen et al., 2004; Whaler and Hautot, 2006), the crustal residence times of basalts in the MER have yet to be quantified.

Comparative geochemical studies of basalts from the SDFZ and the WFB have revealed several trends differentiating the two rift segment chains. The major and trace element geochemistry of SDFZ basalts suggests that, after olivine, clinopyroxene has been preferentially fractionated over plagioclase at lower crustal pressures ($<$0.6 MPa; $\sim$20 km) (Rooney et al., 2007; Rooney, 2010), which is supported by clinopyroxene barometry (Rooney et al., 2005). Individual pressure estimates of clinopyroxene crystals give a large range of pressures up to 0.9 MPa ($\sim$30 km depth), indicative of a complex magmatic system comprising reservoirs throughout the crust (Rooney et al., 2005). In contrast, clinopyroxene barometry reveals that WFB magmas fractionate extensively in the upper-mid crust (Rooney et al., 2007). The Sr and V chemistry of basalts, which are more compatible in plagioclase and clinopyroxene respectively, can also be used to assess crystallisation sequences. With decreasing MgO, V decreases within WFB basalts and Sr decreases within SDFZ basalts; plagioclase and clinopyroxene are therefore the first preferentially crystallised phases in the WFB and SDFZ respectively, illustrating their different fractionation depths (Rooney et al., 2014). These conclusions are additionally supported by spatial analysis of scoria cones. Cone clustering in the WFB is more intense than in the SDFZ, and cluster analysis of these vents infer maximum depths of magmatic reservoirs at $\sim$16 km for the WFB and $\sim$30 km for the SDFZ; SDFZ magmas originate from deeper in the Earth's crust than the WFB (Mazzarini et al., 2013b).

Further differences between the two magmatic lineations arise from Tb/Yb, a measure of mantle source mineralogy. The SDFZ typically has higher Tb/Yb than the WFB, suggesting that there is more garnet lherzolite in the SDFZ melting mantle source. Garnet is a mineral only stable in mantle rocks at depth (e.g., Nickel, 1986); the lithosphere of the SDFZ is hence believed to be thicker than that of the WFB (Rooney, 2010; Rooney et al., 2011). Despite this observation, both the SDFZ and the WFB show a wide range of Tb/Yb, and it is likely that both spinel and garnet lherzolite sources contribute to final erupted melts at both settings (Rooney, 2010; Rooney et al., 2011).

No studies have been performed on basaltic geochemical variability along or across a MER magmatic segment; however heterogeneity in basalt geochemistry is evident on the length scales of neighbouring scoria cones (Rooney et al., 2011). Studies performed on the Dabbahu-Manda Hararo (DMH) Rift Zone in Afar illustrate a difference in geochemistry between axial melts and those lavas erupted off-axis (Ferguson et al., 2013a,b); a similar difference may therefore be apparent in MER segments.

1.3.3 Rift carbon emissions

Recent reviews of carbon contributions from volcanoes and tectonic settings have emphasised the importance of rift-related carbon release to the deep carbon cycle. Over geological time, volcanic emissions from continental rifts may contribute a similar amount of carbon to the atmosphere as other tectonic settings, such as the mid-ocean ridge system and island arcs (Dasgupta and Hirschmann, 2010; Kelemen and Manning, 2015; Wong et al., 2019). Continental rift length has been previously linked to variations in atmospheric CO_2, which is a direct control on global climate (Brune et al., 2017). An understanding of carbon release from continental rifts is therefore important to understand the means by which tectonic change can affect the surface conditions of the Earth.

Melt generation beneath the sub-continental lithospheric mantle during rifting liberates carbon previously stored within the sub-continental lithosphere and continental crust, transporting it to the surface where it is degassed to the atmosphere in addition to asthenosphere-derived magmatic carbon (Foley and Fischer, 2017; Muirhead et al., 2020). The presence of metasomatic carbon-bearing phases within the sub-continental lithospheric mantle is known from xenoliths (e.g., Casagli et al., 2017; Trestrail et al., 2017) and implied from melting models (e.g., McKenzie, 1989; Foley and Fischer, 2017) and the petrology of erupted rift lavas (Furman et al., 2016; Rooney et al., 2017). Decarbonation of crustal limestones and carbonates by magmatic heat or reaction with silica can also generate significant amounts of CO_2 (e.g., Sano and Marty, 1995; Mason et al., 2017).

Past studies of volatile degassing in continental rifts have primarily focussed on the diffuse degassing of volatiles through the Earth's crust (Brune et al., 2017, and references therein). The low solubility of CO_2 in magmas encourages extensive degassing at great depths within the Earth (e.g., Dixon, 1997). This passive degassing of CO_2 is poorly constrained, as it percolates out over a wider area than active emissions; nevertheless these diffuse emissions are an important component in Earth's deep carbon budget (e.g., Burton et al., 2013; Werner et al., 2019). The volume of CO_2 released diffusively at tectonic or volcanic settings can be estimated using measurements of CO_2 fluxes in groundwater, volcanic plumes, and soils. Soil surveys within the EARS have provided constraints to diffuse CO_2 degassing within the Magadi-Natron basin at the Kenya-Tanzania border and the MER (Lee et al., 2016; Hunt et al., 2017; Muirhead et al., 2020). Diffuse carbon degassing is not constant throughout the rift, but is correlated with the position of fault zones and volcanic structures (Hutchison et al., 2015; Lee et al., 2016; Robertson et al., 2016; Muirhead et al., 2016; Hunt et al., 2017), and increases as the rift spatially transitions from cratonic to thinned lithosphere, possibly linked to the advection of carbon-rich cratonic root material towards thinned lithosphere as rifting develops (Muirhead et al., 2020). Carbon isotope compositions and concentrations of CO_2 outgassing at Lake Tanganyika and the Kenyan Rift suggest that mantle-derived carbon dominates contributions to the observed CO_2 in the earliest stages of continental rifting rather than from organic carbon (Botz and Stoffers, 1993; Lee et al., 2016; Robertson et al., 2016), although individual samples may include a significant crustal limestone-derived (Lee et al., 2016) or organic component (Hunt et al., 2017). Rift fault systems may therefore provide a network for magmatic carbon to percolate to the surface (Faulkner et al., 2010, and references therein).

As established in Section 1.2.2, continental rifts are significantly spatially variable over the course of their development; this spatial variability may be reflected by variable diffuse CO_2 fluxes along the length of a rift. The many influences on continental rift development produce a significant range of continental rift basin areal CO_2 fluxes worldwide (Brune et al., 2017, and references therein). From measurement of diffuse degassing at various sites along the MER, Hunt et al. (2017) suggest a CO_2 flux of 0.52 to 4.36 Mt yr^{-1} for the MER, and, extrapolating from this MER value, 3.9 to 32.7 Mt yr^{-1} for the Eastern Rift of the EARS (Hunt et al., 2017). This estimate is significantly smaller than the CO_2 flux estimate for the Eastern Rift extrapolated from the Kenyan Rift (38–104 Mt yr^{-1}; Lee et al., 2016). There is also significant heterogeneity in CO_2 fluxes within individual rift sectors, as carbon fluxes vary both along and across rift strike depending on available channels for volatile release, such as faults (e.g., Lee et al., 2016; Robertson et al., 2016;

Hunt et al., 2017). Deep carbon contributions may therefore vary substantially within different sectors of the EARS.

While diffuse degassing has been quantified in the MER, active degassing (i.e., degassing from active volcanoes) has not. The study of volatiles in melt inclusions within crystal phases, particularly within early crystallising olivine, can provide a carbon flux in magmatic settings (e.g., Wallace et al., 2015). Such studies have been performed previously for other volcanic settings to obtain CO_2 concentrations in primitive basalts and estimates of storage pressure from volatile saturation modelling (e.g., Wallace, 2005; Blundy et al., 2010; Hartley et al., 2014). The only work on melt inclusions performed on MER materials thus far is that of Iddon and Edmonds (2020). Iddon and Edmonds utilise volatile and trace element compositions of melt inclusions from MER basaltic and rhyolitic products to gauge the distribution of magmas within the MER crust. Olivine-hosted basaltic melt inclusions from the central volcanoes Kone and Aluto and the Butajira volcanic field are included in their study. CO_2 contents range from <500 ppm to over 3000 ppm. However, this study does not consider the loss of melt inclusion CO_2 to shrinkage bubbles, choosing instead to select only melt inclusions without visible shrinkage bubbles whenever possible (Iddon and Edmonds, 2020); these CO_2 concentration estimates must therefore be regarded as minima.

1.4 Thesis aims and outline

The primary aim of this thesis is to provide stronger constraints on basaltic processes in the MER through a detailed petrological and geochemical study. Using these methods, I aim to unravel new information about the magmatic behaviour and character of late-stage continental rifting. This thesis is divided into three investigations, starting in the sub-MER mantle and concluding at the rift surface. The first study, divided into two chapters, is an investigation into the thermal and compositional properties of the Ethiopian mantle using a combined petrological thermometry and inversion modelling approach. The second study resolves the storage pressures of sub-rift melts in the Ethiopian crust through detailed compositional analysis of olivine-hosted melt inclusions. The final study resolves the timescales of melt disequilibrium in the crust immediately prior to basaltic melt eruption through olivine Fe-Mg interdiffusion chronometry.

The thesis is organised into the following chapters:

- **Chapter 2** summarises the fieldwork and sample preparation undergone, and provides a thorough description of the utilised instrumentation and analytical techniques to generate the data in the thesis.

- **Chapter 3** begins our petrological journey into rift magmatism through a discussion of melt generation processes in the sub-rift mantle. I use new independent estimates of olivine crystallisation temperature at the MER and Afar, determined via olivine-spinel Al-exchange thermometry, to determine the temperatures at which primitive mantle-derived melts arrive at the rifting crust.

- **Chapter 4** follows on directly from Chapter 3, and uses these estimates of basalt liquidus temperatures, in conjunction with pythonic mantle modelling methods, to explore melting conditions in the Ethiopian Rift and Afar Rift systems.

- **Chapter 5** rejoins our mantle-derived melts in the crust, where they are stalled and stored prior to eruption. Through the geochemical analysis of olivine-hosted melt inclusions I apply volatile saturation barometry (CO_2-H_2O) to estimate melt storage pressures in the MER crust.

- **Chapter 6** concludes our ascent through the crust by resolving the timescales of processes resulting in final eruptive ascent. The application of olivine diffusion chronometry to MER samples is used to determine the timescales of crustal olivine disequilibrium, driven by dyke intrusion, immediately prior to eruption.

- **Chapter 7** summarises this thesis, and places my findings into wider context, highlighting potential paths for research to follow in the future.

Chapter 2

Analytical methods

This chapter describes the procedures undergone during collection, preparation, and analysis of the samples in this study. In addition, instrument calibration, analytical setups, and data processing are detailed in full. Additional methods not covered within this chapter are described in detail within the relevant subsequent chapters.

2.1 Fieldwork campaign

Samples for this study were collected in Ethiopia during the period 12th to 22nd January 2019. The objective of fieldwork was to sample a wide range of glassy and crystalline eruption products from Quaternary basaltic scoria cones in the MER, with emphasis of capturing along-rift-scale variations in conditions of magma generation and transport. Sampling was performed with the field assistance of David Ferguson, Yared Sinetebeb, and Yafet Gebrewold Birhane, with additional technical assistance provided by Amdemichael Zafu Tadesse and Gezahegn Yirgu.

Sample localities within the Main Ethiopian Rift (MER) are shown in Figures 2.1, 2.3, and 2.5. Most scoria and lava samples were collected by hand from surface exposures, although collection methods were dependent on the condition of the outcrop. A significant number of the cones in the sampling regions were covered in grassy vegetation; large volcanic ejecta pieces from these cones were sampled provided that their cores remained black and glassy. A number of cones in the Ethiopian Rift have been extensively quarried for scoria, which is locally used as road-building material; these quarries permit easy accessibility to the cone interior where fresh material can be collected. Furthermore, these quarries allow for sampling along the stratigraphy of the cone, and hence the potential for geochemical variability over the course of a cone-forming event to be identified (see Figures 2.2B and C, 2.4B and C, 2.6). A 3 mm soil sieve was used to separate small grains from the larger ejecta pieces to identify mineral phases and glassy scoria pieces in these quarries. Large ejecta pieces collected were typically 2–3 cm in diameter with a glassy interior of at most 80 % vesicularity of mm-scale spherical vesicles. Several scoria localities host ejecta weathered to a red-brown colour; the interiors of larger bomb pieces however tend to remain glassy, and any phenocryst phases show little outward evidence for alteration. Minerals of 3 mm size or smaller comprise a large part of the separated small fraction.

Extensively sampled localities within the MER were avoided (e.g., Rooney et al., 2005; Furman, 2007; Iddon et al., 2019; Iddon and Edmonds, 2020). Instead, sampling was focussed on the lesser-sampled scoria cone fields to the north of Abaya Lake, the south-east of Ziway Lake, and the cones to the south-east of the city of Adama, termed the Boku Volcanic Complex (Tadesse et al., 2019). The 121 samples collected from 82 localities in these three regions are primarily basaltic scoriae and lava; other rocks collected include ignimbrites, rhyolites, ash, and obsidians. Basaltic lavas were sampled by hand, typically from hammering of outcrops, and were mostly unaltered. A variety of lavas from fault/fissure eruptions were sampled; pieces were typically up to 10 cm in width. Care was taken to avoid sampling alteration by trapped volatile phases in vesicles. Other materials were sampled to expand the University of Leeds' in-house collection of Ethiopian material, including Hobicha rhyolite (KW-MER19-07), crystalline obsidian from Salewa Dore dome (KW-MER19-44), and ash-bearing lacustrine deposits near Aluto (KW-MER19-68). Such samples, detailed in Appendix A.1, may provide a basis for future investigations, but do not play a significant role in this study.

It should be noted that sampling campaigns in the MER and Ethiopia in general are often subject to local politics and accessibility, as such every effort was made to ensure that all the material collected from these rift sectors was representative of the sample sets.

2.1.1 North Abaya Lake

The region north of Abaya Lake is topographically dominated by the Hobicha rhyolitic centre, whose caldera takes the form of a flattened horseshoe of diameter ∼10 km curving westward (Figure 2.1). Rhyolitic lavas and pyroclastic deposits are well exposed along the two halves of the caldera walls, with one rhyolite flow from the inner caldera wall providing a K-Ar age of 1.57 Ma (see Chernet, 2011). The maximum extents of rhyolitic volcanism

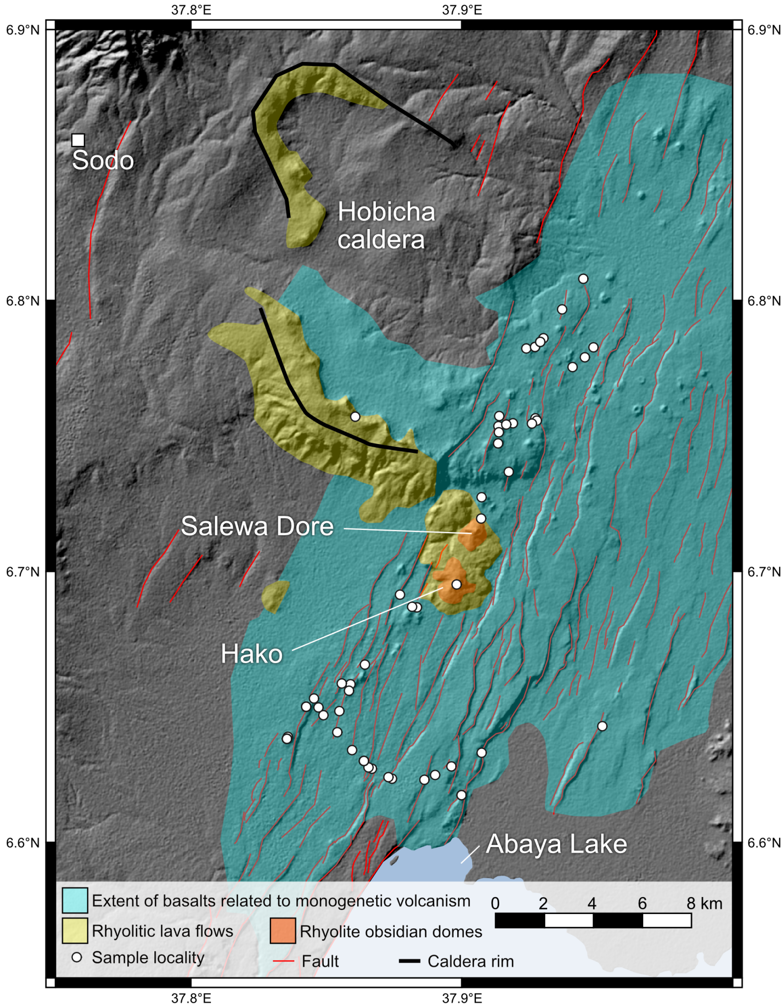

Figure 2.1: Simplified geological map of the North Abaya Lake region showing distribution of volcanic deposits and major stuctural features, redrawn after Chernet (2011), Corti et al. (2013b), and Di Rienzo (2019). The location of the geological map is outlined in Figure 1.2.

lie to the west and north-west of Hobicha, away from the study area; the full extent of rhyolitic exposure has therefore not been included in Figure 2.1. Two exceptions to this generalisation are the twin obsidian domes of Salewa Dore and Hako, which are located along the southern flank of the Hobicha caldera and bound by two major graben-forming faults. Their material remains fresh and glassy, with alteration localised only to fumeroles; it is therefore thought that these two domes represent the youngest rhyolitic activity in the region (Chernet, 2011; Corti et al., 2013b).

NNE-trending faults and basaltic scoria cones dominate the region to the east of Hobicha caldera (Figure 2.1). These basaltic features are Pleistocene-Holocene in age, and are associated with the similarly trending structural features of the rift volcano-tectonic segments. Scoria cones are present throughout the fault structures (Figures 2.2A-D), neither preferring a position on the tip nor centre of each fault, in contrast to similar volcanism observed in the Red Sea Rift (Corti et al., 2013b). Chernet (2011) identifies two distinct

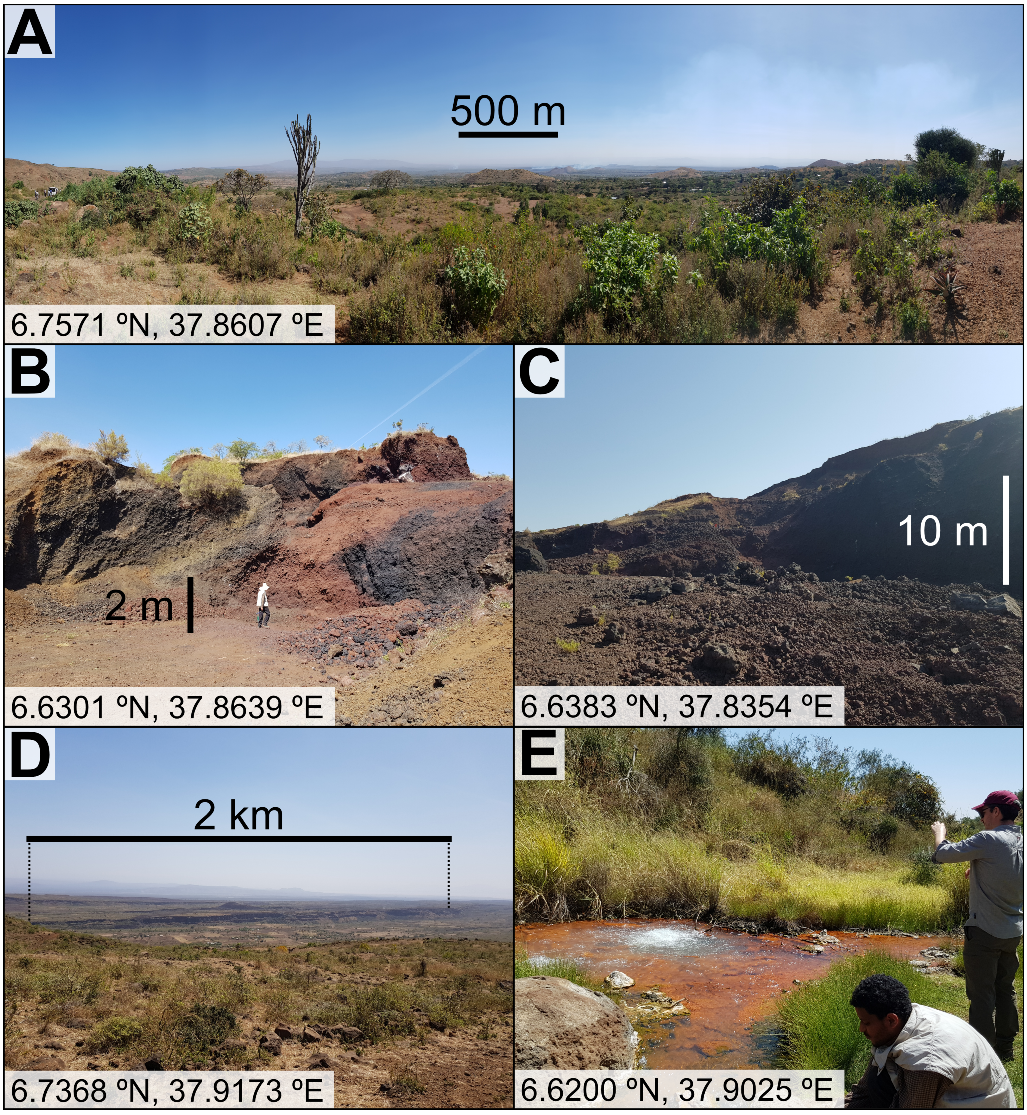

Figure 2.2: Field photographs from the North Abaya Lake region. A is a panoramic photograph of the Abaya Lake cone field from the south-eastern edge of Hobicha caldera, facing east; B and C show two examples of quarried scoria cones sampled; D is a photograph highlighting significant intra-rift rift-parallel faults and associated cones taken from Hobicha caldera facing south; E is a photograph of hot springs found within the field area.

basaltic groups on the basis of the preservation of both their volcanic structures (e.g., condition of cones and flows) and the nature of the faults cutting these units. The older unit is exposed over the majority of the fault and cone system, whereas the overlying younger basalts are exposed adjacent to Hobicha and to the immediate north-east of the two obsidian domes. It should be noted that no geochronology has been performed to differentiate these two mapped units; hence in Figure 2.1 they are shown as undifferentiated. Pre-rift basalts are exposed to the east and west of Abaya Lake, and outcrops are likely covered by the lake; no pre-rift basalts are thought to be present in the study area.

The most recent geological deposits are lacustrine sediments and alluvium linked to the fluctuation of the water level of Abaya Lake (Corti et al., 2013b). Basaltic eruptions are evident as hyaloclastite in layers in some sections of lake sediment, suggesting that lake sediment deposition and basaltic activity were often contemporaneous (Torre et al., 2007; Chernet, 2011).

Sampling in this region has been minimal, with the only geological map and regional geology of the region being drawn from Chernet (2011). In the Abaya Lake region, Rooney (2010) sampled basalts predominantly to the west of the lake for major and trace element study, with no samples collected from inside the study area. The faults in the region were analysed extensively by Corti et al. (2013b), who concluded through radiometric carbon dating that faults remained active during the Holocene, as late as 10,900 years before the present. Of more interest perhaps is the noticeable geothermal activity evident near the lake, which has attracted a number of studies. Hydrothermal manifestations are evident in the field area (Figure 2.2E), and have been previously mapped in detail by Chernet (2011). Hydrothermal activity is thought to be linked to the presence of a rhyolitic magma reservoir beneath the region at shallow depths (Chernet, 2011); this is supported by isotopic signatures (δ^{13}C, ^{3}He/^{4}He) indicating that volatiles from these sites are predominantly mantle-derived (Minissale et al., 2017).

Samples from Abaya Lake were collected with additional field assistance and guidance from Snorri Gudbrandsson and Dario Di Rienzo of *Reykjavik Geothermal* and the University of Iceland respectively, who were in the field to study the geochemistry of local groundwater. In addition, the Abaya sample set was shared with Dario Di Rienzo for the completion of his master's work, during which he performed a series of electron probe and inductively coupled plasma-optical emission spectroscopy (ICP-OES) analyses on whole rocks and minerals (Di Rienzo, 2019). Scoriae were collected predominantly from quarried

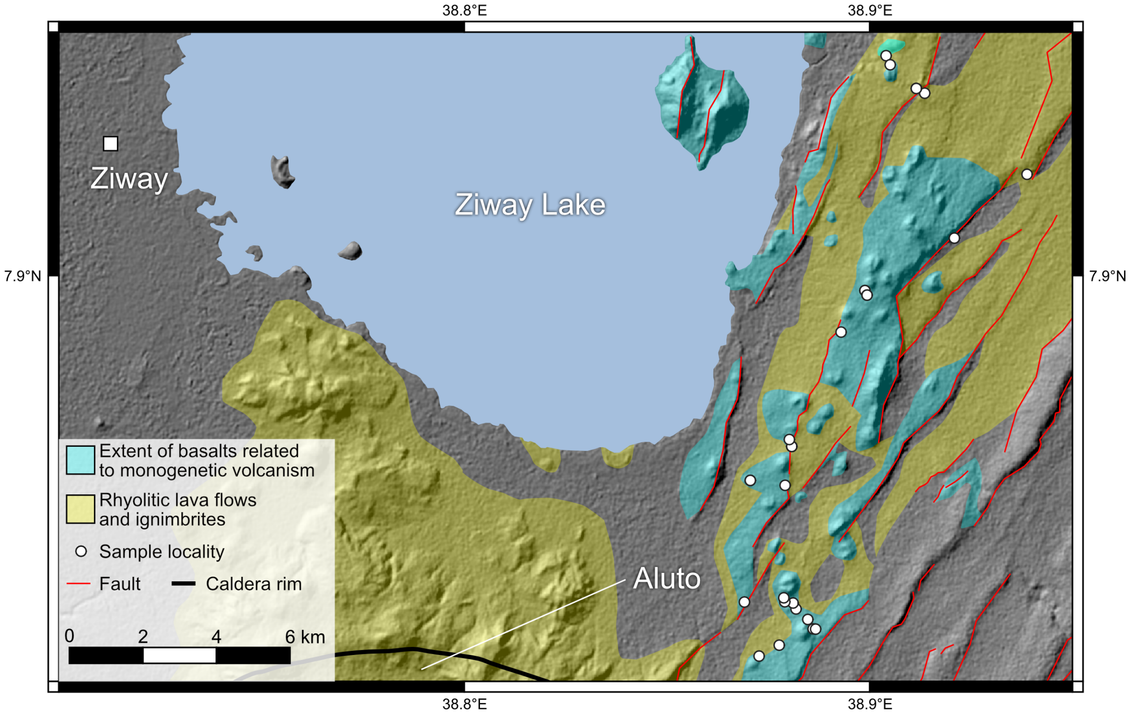

Figure 2.3: Simplified geological map of the South East Ziway Lake region showing distribution of volcanic deposits and major stuctural features, redrawn after Trua et al. (1999), Boccaletti et al. (1999), and Hutchison et al. (2016b). Uncoloured regions of the map can be attributed to lacustrine/alluvial sedimentary deposits near the lake, and unwelded ignimbrites from other silicic centres to the east of the cone field. The location of the geological map is outlined in Figure 1.2.

scoria cones, while basalts were often collected on roadsides adjacent to major faults. In the field, basalts were either aphyric, or bore distinct phenocrysts of plagioclase. Other samples collected included ignimbrites near Abaya Lake, and rhyolitic material from Hobicha, Salewa Dore, and Hako. Preliminary observations of samples from Abaya Lake, confirmed by Di Rienzo (2019), determined that olivine was absent as a phenocryst phase in this region. As a result, these samples play no part in the following chapters, but are nonetheless mentioned in this thesis for context, e.g., in the event of further study.

2.1.2 South East Ziway Lake

The Ziway Lake monogenetic field is located along the south-eastern shore of the eponymous lake. The features of the WFB are distinct on digital elevation models (Figure 2.3); the NNE-trending faults of the Wonji Fault Belt (WFB) and associated scoria cones are clear, as are the rhyolite flows of the nearby Aluto silicic centre. The majority of research previously performed in and around Ziway Lake has focussed on Aluto itself, the major

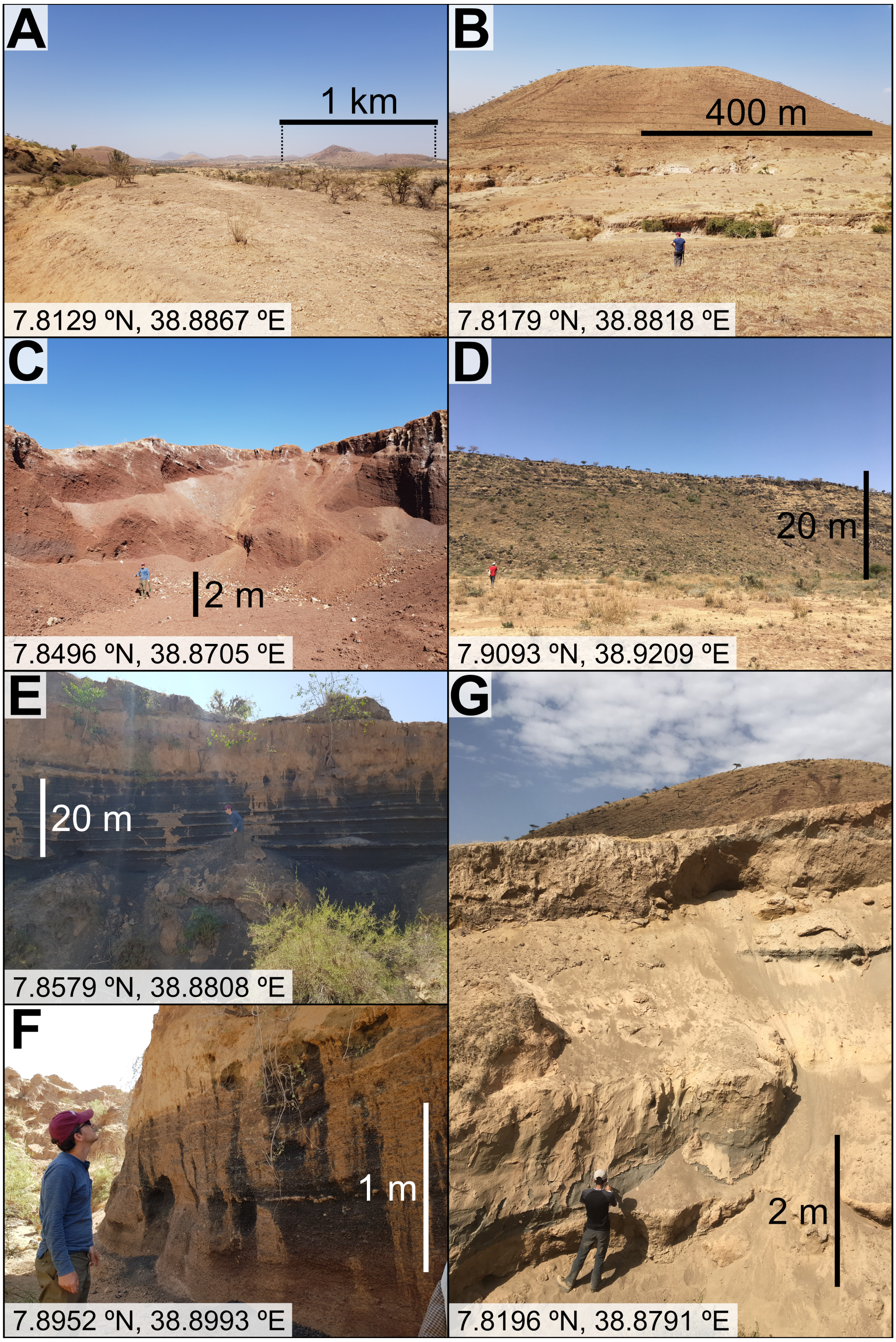

Figure 2.4: Field photographs from the South East Ziway Lake region. A is a photograph of the Ziway Lake cone field taken from within the field, facing east; B and C show two examples of scoria cones sampled; D is a photograph of a normal fault with significant throw and associated basaltic lava flow; E and F show scoria deposits regularly interbedded with lacustrine deposits; G shows the sampling of ashfall deposits linked with the eruptions of the nearby Aluto centre.

silicic centre located to the south of the lake (e.g., Hutchison et al., 2015, 2016a,b,c; Gleeson et al., 2017; Fontijn et al., 2018), with little work performed on the adjacent Ziway cone field. The last campaigns within the cone field were for basalt major elements and trace element analysis, with additional work to determine mineral major elements and whole-rock isotopes (Trua et al., 1999; Boccaletti et al., 1999; Fontijn et al., 2018).

Broad-scale geological maps are provided by Trua et al. (1999) and Boccaletti et al. (1999). The rocks in the study region can be broadly subdivided into two major units: rhyolites and pyroclastic deposits associated with the eruptions of the Aluto centre (termed the Aluto-Berecha Unit by Boccaletti et al. (1999)), and basaltic material forming fissure flows and scoria cones (termed the Galo-Salen Unit by Boccaletti et al. (1999)). These rocks can be considered coeval, owing to their similar K-Ar radiometric ages (0.83 Ma and younger) and intertwined stratigraphy (WoldeGabriel et al., 1990). Field observations, supported by the observations of Boccaletti et al. (1999), suggest multiple phases of basaltic activity which can be differentiated according to their crystal content; the oldest lavas are porphyritic, bearing large crystals of plagioclase, clinopyroxene, and some olivine; more recent material, including the material comprising the scoria cones, are either aphyric or bear large crystals of plagioclase and clinopyroxene only. Only one cone visited within the region bore clearly phyric olivine (locality references KW-MER19-58), which is utilised for the study comprising Chapter 6.

The cones and faults of the Ziway Lake monogenetic field are topographically distinct from the lower relief silicic deposits that fill the regions between them (Figure 2.4A and B). Quarries provide the easiest access to scoria (Figure 2.4C), while lavas are best exposed along the large intra-rift faults in the region (Figure 2.4D). Additionally, ephemeral stream valleys expose underlying interbedded scoria, lacustrine sediments (Figure 2.4E and F), and the thick silicic ashfall deposits blanketing the region (Figure 2.4G).

2.1.3 Boku Volcanic Complex (SE Adama)

The Boku Volcanic Complex (termed BVC or Boku in this thesis) is located to the south-east of the major city of Adama (formerly Nazret), and is the site of a collapsed caldera, termed the Boku Caldera in literature. The rhyolitic remnants of Boku form two halves of a shattered horseshoe curving north-west in the topography of the region (Figure 2.5. To the north-east of the collapsed caldera is the Boset-Bericha Complex; to the south-east the Sodore Volcanic Field; to the south-west the Gedemsa volcano. The caldera itself

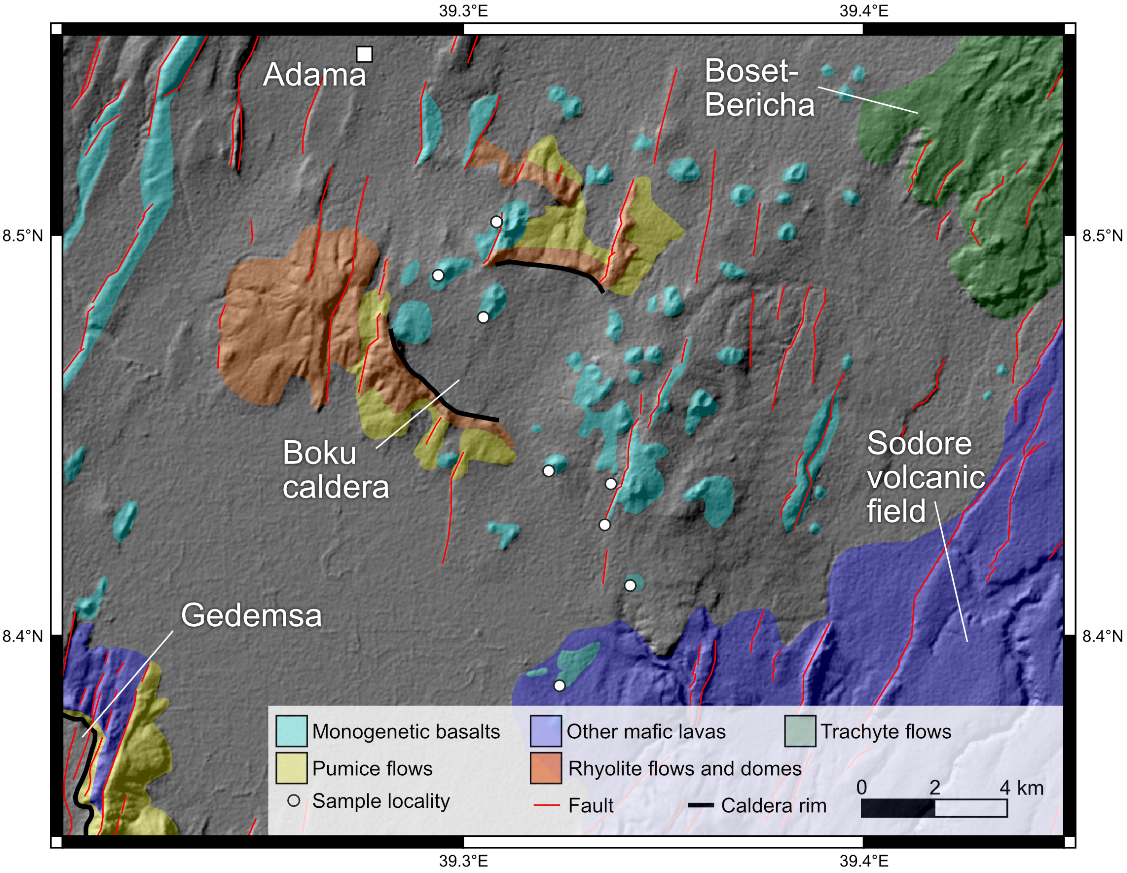

Figure 2.5: Simplified geological map of the Boku Volcanic Complex to the south-east of Adama showing distribution of volcanic deposits and major stuctural features, redrawn after Boccaletti et al. (1999), Hutchison et al. (2016b), Siegburg et al. (2018), and Tadesse et al. (2019). The location of the geological map is outlined in Figure 1.2.

is cut by the faults and cones of the WFB, termed the Melkasa Unit by Boccaletti et al. (1999). These basaltic features represent the most recent volcanic activity in the region, constrained to <200 ka by K-Ar radiometric dating (Morton et al., 1979).

As with the other two study areas, previous work performed on the Boku complex has been limited. The volcanic stratigraphy of the region was established by Boccaletti et al. (1999) following previous radiometric dating studies (e.g., Morton et al., 1979). The most and extensive recent work performed on this area by Tadesse et al. (2019) yielded major and trace element compositions of basalt and rhyolite whole-rock samples. No previous work has focussed solely on mineral phases from these regions, nor mineral-hosted melt inclusions.

A selection of basaltic scoriae and lavas were sampled from several quarried cones in the BVC (Figure 2.6). Scoria deposits bore noticeable pieces of volcanic bomb, which contain sizeable phenocrysts of 3–10 mm in size, primarily of olivine (∼60-70 %), but with smaller fractions of phyric plagioclase and clinopyroxene. Olivine crystals and basalts from this region form the basis of all three research chapters in this thesis.

2.2 Sample preparation

Fractions sieved in the field (Figure 2.7A) were inspected using a binocular microscope and crystals of olivine, feldspar, and clinopyroxene were picked by hand; in addition to crystals, pristine scoria glass fragments were also picked for carrier glass analyses. From the picked crystal fractions, olivine with visible glassy melt inclusions were selected.

Melt inclusions from East Ziway are mostly crystalline, hosting noticeable crystals of plagioclase, pyroxene, and spinels. These inclusions were deemed inappropriate for analysis, as simple glass matrix corrections could not be applied for probe work. Melt inclusions from the Adama region are glassy, and typically host a shrinkage bubble of up to 10% the volume of the melt inclusion. Prior to mounting and polishing, melt inclusions were checked for evidence of cracking and decrepitation (Maclennan, 2017).

Olivine crystals and fragments of glass with no visible matrix crystals were mounted onto 25 mm diameter epoxy resin blocks (Figure 2.7B). On the one occasion where a mount had not set correctly, the poor binding between the sample crystals and resin was remedied through recasting in epoxy resin and careful re-polishing. Once set, each mount was ground with silicon carbide paper to expose the crystal or glass fragment at the surface of the mount. Following exposure, the mount surface was progressively polished from 6 μm to 0.25 μm grade with diamond pastes. For electron backscatter diffraction further polishing of the sample mounts was achieved using Syton silica polishing fluid. The mounts were initially photographed using a binocular microscope camera to identify inclusions, and individual grains assigned labels to facilitate identification during analysis. Further inspection was performed using an optical microscope under transmitted and reflected light, which permitted identification of inclusions of melt and spinel exposed on polished crystal surfaces.

Raman spectroscopy and subsequent SIMS analyses necessitated refinement of the sample preparation process (Chapter 5). Rather than mounting crystals en masse onto an epoxy mount, each individual melt inclusion-hosting crystal was first mounted onto a frosted glass slide with acetone-soluble CrystalBond^{TM} adhesive, and then ground using the thin section grinding machine at the School of Earth and Environment at the Univer-

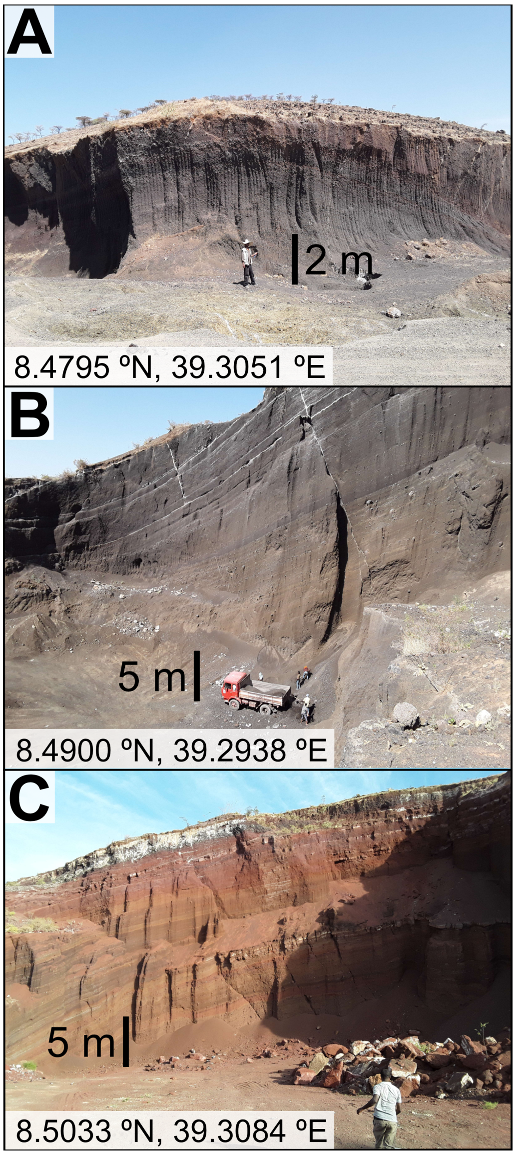

Figure 2.6: Field photographs of quarried scoria cones within the Boku Volcanic Complex.

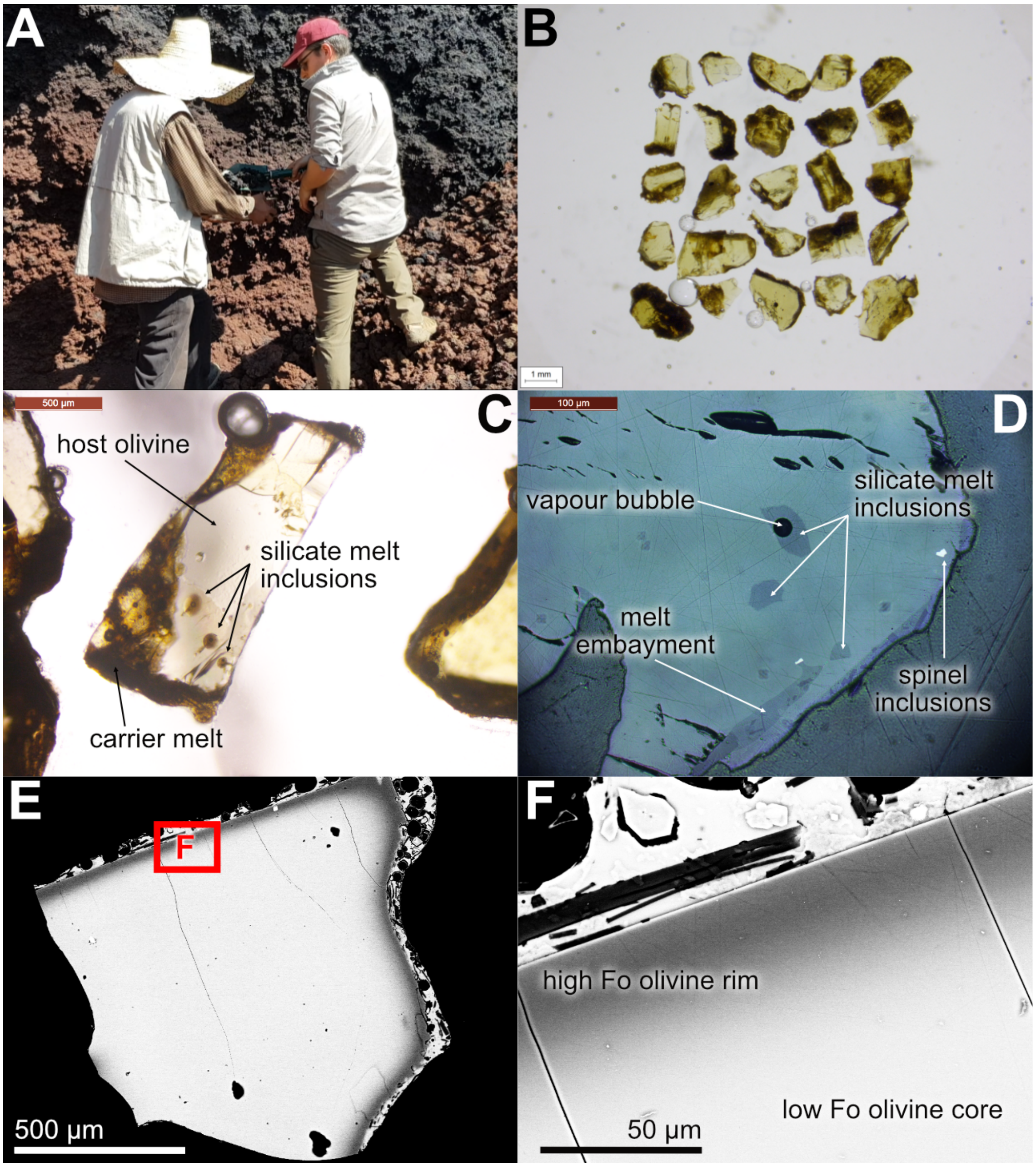

Figure 2.7: Selection of photographs illustrating sample preparation and characterisation. A. Field photograph showing use of soil sieve after extraction of scoria from a quarried cone using a shovel. B. Polished olivine crystals exposed on the surface of an epoxy mount. C. Transmitted light microscope photograph of an olivine crystal hosting multiple melt inclusions. D. Reflected light microscope photograph of an olivine crystal hosting a number of inclusions. E. Backscatter electron image of an olivine crystal demonstrating a bright core and dark rim. F. Detail of the olivine rim in E to show diffusive boundary between rim and core.

sity of Leeds. The coarse grind was then progressively polished through ∼30 seconds of hand-lapping using 9 μm Al_2O_3 powder followed by progressive polishing with 6 μm and 3 μm diamond pastes. This process was repeated twice: once to expose a 'window' into the interior of the crystal to identify and estimate depths of melt inclusions from the polished surface, and a second time to grind and polish down to within the required distance of the melt inclusion. The polished crystals were sonicated for at least 10 minutes prior to Raman analyses.

Subsequent exposure of the melt inclusion for probe work involved further grinding and polishing which was performed through careful 9 μm Al_2O_3 powder hand-lapping and polishing with 15, 9 and 6 μm diamond pastes. Upon exposure of their melt inclusions, the crystals were removed from the glass slide, cleaned with acetone and by sonification. These crystals were then transferred to epoxy mounts, taking care to preserve the polished face flat on the mount surface, where they were prepared and polished to 0.25 μm grade using the procedures described above. Before analysis, the polished mounts were cleaned with acetone and placed in an ultrasonic bath for at least 10 minutes. Each melt inclusion-hosting olivine crystal on these epoxy mounts was extensively characterised under transmitted and reflective light (Figure 2.7C and D). A gold coat was applied to the mount in preparation for ion probe analyses, which was subsequently removed prior to electron probe analyses by polishing with 0.25 μm diamond paste for 2 minutes. All mounts were carbon coated before electron probe and electron microscopy.

Several selected whole-rock samples of lava and scoria of ∼60 g mass were crushed by hand with a pestle and mortar, with care taken to select pieces of rock that had not been extensively weathered. These samples were then powdered using an agate ball mill at the University of Leeds. The mill was used at a low velocity for five minutes, and was cleaned thoroughly using warm water in between uses. The resultant powders are of a grade finer than 150 μm. These powders were subsequently used for XRF and ICP-MS analyses (see Sections 2.7.1 and 2.9.1 for further sample preparation details).

2.3 Precision and accuracy of analyses

Precision and accuracy is assessed for all secondary standards analysed in this thesis. Data precision (P, in %) is determined by:

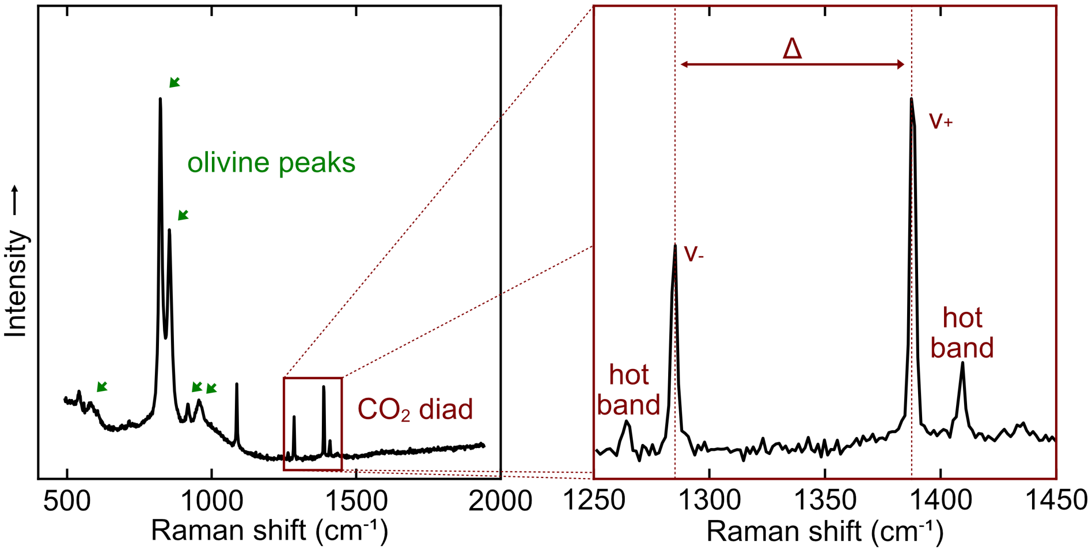

Figure 2.8: Raman spectrum for a melt inclusion vapour bubble in an olivine-hosted melt inclusion. The olivine peaks and CO_2 diad are highlighted. The distance between the ν_- and ν_+ peaks is given by the diad splitting Δ, and is dependent of the density (pressure) of the CO_2 medium. The hot bands flanking the diad result from the thermal energy of the vibrating molecules and take no part in this study.

$$P = 100 \cdot \frac{\sigma}{\bar{x}} \tag{2.1}$$

where σ is the standard deviation of the sample population and $\bar{x}$ is the mean of the sample population.

Data accuracy (A, in %) is determined by:

$$A = 100 \cdot \frac{\bar{x} - x_{ref}}{x_{ref}} \tag{2.2}$$

where x_{ref} is the reference value of the secondary standard used.

2.4 Raman spectroscopy

The formation of a bubble in a melt inclusion arises from the pressure-temperature-composition-volume properties of magmatic systems (e.g., Maclennan, 2017). An entrapped melt inclusion will shrink relative to its host phenocryst owing to their differing thermal expansion properties, developing a vacancy (bubble) into which pressure-soluble volatiles in the melt will exsolve into as the melt contracts and the inclusion pressure falls below that of volatile saturation (Moore et al., 2015). Bubble formation therefore produces two phases into which volatiles such as CO_2 may partition: the silicate melt and the vapour bubble.

Advances in the understanding of the post-entrapment processes of melt inclusions have recently produced a library of literature utilising Raman spectroscopy to determine CO_2 densities in melt inclusion bubbles, often in conjunction with subsequent analysis of the glass by SIMS (see Section 2.5) (e.g., Hartley et al., 2014; Moore et al., 2015; Taracsák et al., 2019). This rise in popularity can be attributed to the relatively rapid time of analysis (∼5 minutes to generate one spectrum), excellent spatial resolution (confocal beam spatial resolutions are typically 1 μm), and the simplicity in analysis. In addition, Raman spectroscopy is a non-destructive method, permitting repeat analyses of samples on multiple Raman machines without degradation.

Raman spectroscopic analysis is employed to determine and observed vibration modes of molecules, and is dependent on the inelastic scattering of photons by molecular vibrations, known as Raman scattering. A monochromatic light source (e.g., a laser) interacting with the sampled medium may be affected by Raman scattering, resulting in the raising or diminishing of the energy of the light, dependent on the frequency of vibration of the molecules constituting the medium. This affected light is subsequently collected and filtered to display a spectrum of the light affected by vibrational modes – the Raman spectrum.

The Raman spectrum of CO_2 contains several well-defined peaks, which persist even at low CO_2 densities. These peaks result from the four vibrational modes of the CO_2 molecule: a symmetric stretching mode ν_1, an anti-symmetric stretching mode ν_3, and two degenerate (same frequency) bending modes (ν_{2a} and ν_{2b}, collectively ν_2). The symmetry and energy of the first excited state of the ν_1 mode (1332.87 cm^{-1}) matches that of the second excited state of ν_2 (1335.14 cm^{-1}), permitting the two states to mix in a process termed Fermi resonance (Fermi, 1931; Gordon and McCubbin, 1966). Fermi resonance has two effects on the CO_2 Raman spectrum. Firstly the comparatively higher energy ν_1 mode shifts to an even higher energy, and the lower energy ν_2 mode correspondingly lowers its own energy. Secondly, the weaker excited ν_2 gains intensity at the cost of ν_1 losing intensity, resulting in the two transitions producing similar intensities. This admixing of the two vibrational states of CO_2 results in two strong peaks in the Raman spectrum at ∼1388 cm^{-1} (termed ν_+) and 1285 cm^{-1} (termed ν_-), which are diagnostic of CO_2 and collectively known as the Fermi diad (Figure 2.8).

It has been commonly accepted that the distance between these two strong CO_2 peaks (termed the diad peak splitting distance, Δ) is dependent on the pressure or density of CO_2 vapour within the medium (Wang and Wright, 1973). This correlation between the peak splitting and density can be empirically parameterised if the density of the CO_2-hosting medium is known; this can be achieved, for example, by controlling the pressure of CO_2 within a high-pressure optical cell (e.g., Lamadrid et al., 2017). However, as a result of differences in Raman instrument hardware and analytical conditions, there exists a significant number of differing and contrasting densimeters in the literature, which yield significant differences in densities for the same diad split (Lamadrid et al., 2017). Therefore, selecting a single densimeter from the literature for a given Raman instrument results in significant uncertainties in determining the absolute density of CO_2 in samples, and hence will affect accurate estimation of magmatic storage depths and carbon fluxes. Densimeter correlations must therefore be calibrated for each Raman instrument under specific analytical conditions prior to analysis of unknowns.

It should also be mentioned that it is possible to detect H_2O using Raman spectroscopy. However, Moore et al. (2015) note that both glass and vapour phases contribute to the H_2O Raman peak at 3500 cm^{-1}. Discerning the presence of H_2O within a bubble from H_2O frozen within glass is therefore not possible.

2.4.1 Instrumentation

Olivine crystals were ground down and polished such that bubble-bearing melt inclusions were within 100 μm of the polished surface; this was to minimise the attenuation of the laser signal by reducing the thickness of the olivine medium. Melt inclusions with multiple bubbles were not analysed owing to the difficulty in resolving the CO_2 density of each individual bubble.

In this study, the densities of CO_2 were measured in melt inclusion shrinkage bubbles at the Department of Earth Sciences, University of Cambridge. CO_2 vapour within melt inclusion bubbles were determined using a confocal Horiba LabRAM 300 Raman spectrometer with a holographic grating of 1800 grooves/mm. A laser beam was provided by a 100 mW Ventus 532.05 nm source, and was focussed on the sample using an Olympus LMPLFLN 50× working distance objective lens. The slit width was set to 100 μm and the confocal aperture to 300 μm. The detector used is a Peltier front-illuminated 1024 × 256 pixel CCD. All analyses were performed at ambient room temperature. Calibration was performed using a Si chip; the instrument was calibrated at the start of every day by assessing the linearity of the spectrum relative to the 0 cm^{-1} peak arising from the laser source and the Si peak at 520.69 cm^{-1}. Instrument drift was monitored through the analysis period using a secondary standard.

Removal of artefacts was accomplished through multiple accumulations (5 × 60 s). Where signal strength of the diad was weak, longer count times were used at the expense of number of accumulations (4 × 90 s). Secondary standards were run with a shorter regime of 4 × 30 second accumulations as their CO_2 diad signals were typically stronger than those of the samples.

2.4.2 Calibration and data processing

Measured spectra were fitted with Gaussian peaks. The spectral region around each peak was visually assessed to allocate points to the peak and to the background. A fourth-order polynomial was then fitted to the allocated background points to determine a background curve for the diad peak region. This background was then subtracted from the raw spectrum data to produce a background-corrected spectrum. Gaussian curves were then fitted to the diad peak iteratively through least-squares minimalisation performed via the *optimize.leastsq* function of the Python library SciPy (Virtanen et al., 2020, Figure 2.9). Peak splitting was determined by calculating the difference between the centres of the two Gaussian peaks, and converted into a CO_2 density using a linear densimeter function calibrated for the instrument by Wieser et al. (2021):

$$\rho_{\mathrm{CO_2}} = 0.3217\Delta - 32.9955 \tag{2.3}$$

This CO_2 density ($\rho_{\mathrm{CO_2}}$) is converted into a CO_2 concentration through mass balance between bubble and melt volumes (Hartley et al., 2014):

$$\text{Vapour bubble CO}_2\text{ (ppm)} = 10^6 \times \frac{\rho_{\mathrm{CO_2}} \times V_{\mathrm{bubble}}}{(V_{\mathrm{inclusion}} - V_{\mathrm{phases}}) \times \rho_{\mathrm{melt}}} \tag{2.4}$$

where ρ_{melt} is the density of the melt, V_{bubble} is the volume of the bubble, $V_{\mathrm{inclusion}}$ is the volume of the melt inclusion, and V_{phases} is the volume of other phases present within the that are volumetrically significant (e.g., spinel crystals, sulfides). The total CO_2 of the inclusion is subsequently determined by combining the bubble CO_2 concentration with the CO_2 concentration of the melt (determined by ion probe).

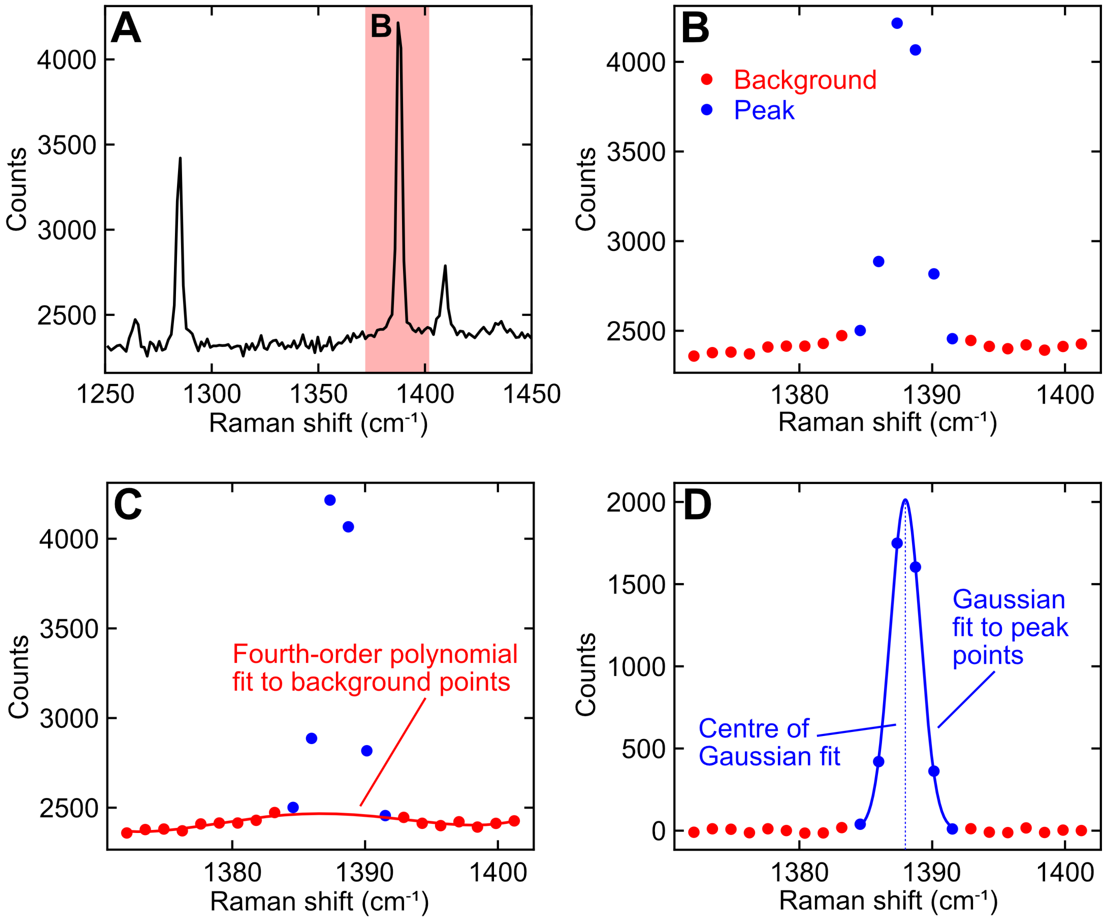

Figure 2.9: Example Raman spectrum illustrating the fitting procedure used to determine diad splitting distance. A. Raman spectrum of the diad region for CO_2. The ν_+ peak is highlighted in red and is used to illustrate the fitting procedure in the other subfigures. B. The spectrum points subdivided into peak and background points. The points are visually differentiated to provide the best peak fit. C. A fourth order polynomial is fit to the background points using a least squares procedure. D. This background polynomial is subtracted from the spectrum points. The resultant background-corrected spectrum peak points are then fit with a Gaussian curve by least squares. The centre of the Gaussian curve is taken as the peak centre.

2.4.3 Data quality

Uncertainty in Raman spectroscopy arises from three principal sources: the uncertainty from estimating the volume of the melt inclusion and the shrinkage bubble, the uncertainty from measurement of diad splitting, and the uncertainty from densimeter calibration.

The former uncertainty is the most dominant. Melt inclusions in this study have a variety of morphologies, ranging from ellipsoidal to near-polygonal and irregular shapes (e.g., Figure 2.7C and D). It is difficult to correctly assess the three-dimensional shape of the inclusion without resorting to a tomographic method. While X-ray tomography has been performed previously on minerals hosting melt inclusions (e.g., Pamukcu et al., 2015), it remains a fairly costly and time-consuming procedure. It is therefore simpler, albeit less accurate, to estimate the area of the visible melt inclusion cross section and link this area to the overall volume of the melt inclusion. High-resolution imagery of melt inclusions and melt inclusion bubbles considered in this study were therefore traced and fitted with a best-fit ellipse using the graphical processing program ImageJ (Schneider et al., 2012) to determine an appropriate estimate for cross-sectional area.

While major and minor axes of ellipses formed from the intersection of a plane (e.g., a polished surface) with an ellipsoidal melt inclusion can be estimated reasonably precisely using this method, linking these two semi-axes to ellipsoidal volume is challenging. Attempts to estimate three-dimensional ellipsoidal volume from a two-dimensional elliptical intersection often rely upon the major and minor semi-axes of the visible ellipse (a and b) to determine the length of a third semi-axis c normal to the plane of intersection. A significant number of studies have assumed that this third semi-axis is equal to the smaller of the two visible semi-axes, such that $a > b = c$ (e.g., Hartley et al., 2014). Other studies have suggested that the arithmetic mean ($c = \frac{1}{2}(a+b)$, e.g., Moore et al., 2015) or the geometric mean ($c = \sqrt{ab}$, e.g., Ni et al., 2017) of the two visible axes is more appropriate. Tucker et al. (2019) explore these three assumptions through a Monte Carlo method, in which randomly sized ellipsoids are generated which are intersected by randomly oriented planes to produce ellipses of intersection, mimicking the polished surfaces of randomly oriented melt inclusions. The volumes of the ellipsoids are then compared to the volumes estimated using the methods listed above. They conclude that the most appropriate volume estimate using a visible elliptical intersection is provided by the arithmetic mean of the two visible semi-axes, however with a 1σ error range of -48% to 37% of the correct value. The assumption that the third semi-axis is equal to the visible minor semi-axis significantly underpredicts the melt inclusion volume, and the geometric mean assumption, while more appropriate than $a > b = c$, shows a greater uncertainty range and mean deviation from the correct value than the arithmetic mean (Tucker et al., 2019).

Uncertainty arising from the measurement of diad splitting in a vapour bubble is dependent on the spectral resolution of the Raman machine used in the analysis. This uncertainty was mitigated through the repeat measurement of bubbles. At least three discrete measurements were performed on each melt inclusion bubble, varying the position and focus of the Raman laser to provide three unique spectra. The standard deviation of the three spectra provides an indicator of the uncertainty of the true diad splitting of the inclusion bubble. Uncertainty from diad splitting was also quantified through repeated measurement of a secondary standard. The secondary standard used in our study is a synthetic quartz fluid inclusion (10 mol FIE) calibrated using a high-pressure optical cell at Virginia Tech Raman, which has been previously used as a standard to calibrate the Department of Earth Sciences Raman at the University of Cambridge (Wieser et al., 2021). 10 mol FIE was analysed at regular intervals throughout the day to check for instrument drift. Figure 2.10 shows repeat measurements of the Cambridge Raman instrument over the course of a day, for five days. Noticeably, mean peak splitting appears to decrease over the course of a day, albeit taking a somewhat random path to achieve this. While non-linearity within the Fermi diad region of the Raman spectrum is typically assessed by neon emission spectrum lines (e.g., Lamadrid et al., 2017), the Cambridge setup cannot assess both the sample and the Ne lamp. The fluid inclusion secondary standard is therefore used as an alternative.

Wieser et al. (2021) report a mean and standard deviation for 10 mol FIE diad splitting of 102.971 cm^{-1} and 0.026 cm^{-1} respectively. These values match my mean and standard deviation for the same standard (102.973 cm^{-1} and 0.024 cm^{-1}), with a percentage difference in the means of 0.02 %. Precision in measuring bubble density was 5.8 %, and the accuracy relative to the mean diad splitting of Wieser et al. (2021) was 0.9 % (Equations 2.1 and 2.2). This accuracy difference is minuscule compared to the other uncertainties in this study, including the uncertainty from repeat measurements of the same sample (∼7 %) and the uncertainty expected from measuring melt inclusion and bubble volumes (see above).

Instrument drift on the five days of analysis was particularly noticeable on the third (12/02/20) and fifth and last (14/02/2020) days, in which there was a noticeable gradual decrease in mean standard diad splitting as the day progressed (Figure 2.10). The nar-

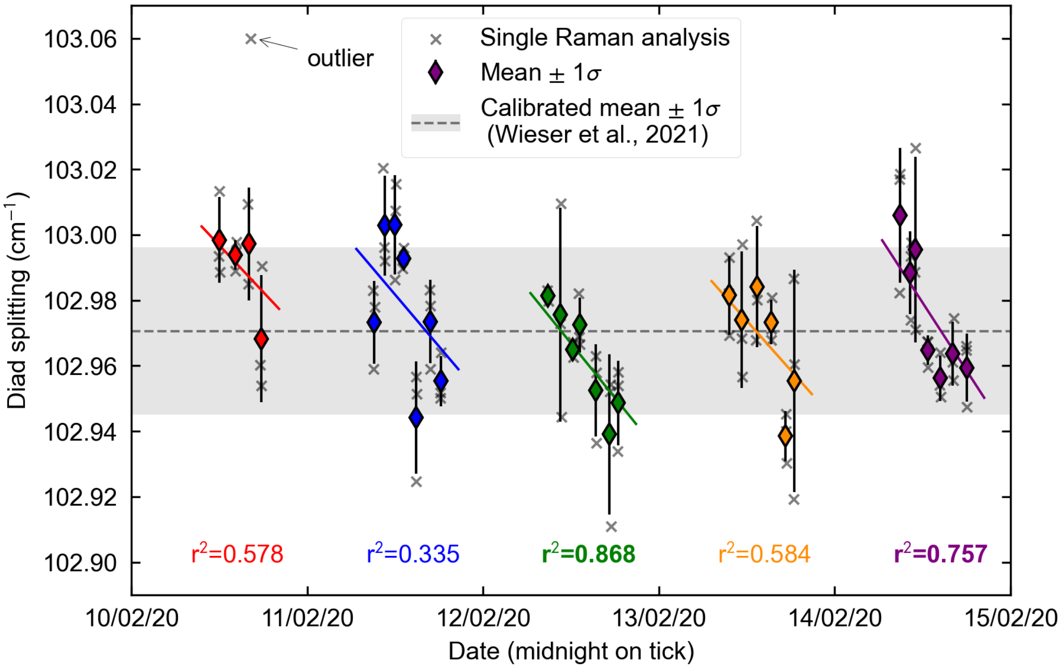

Figure 2.10: Secondary standard 10 mol fluid inclusion E analyses over the five analytical sessions at the University of Cambridge plotted against time of analysis. Single Raman analyses of the standard are shown as crosses; the means of several single measurements taken minutes apart are shown as coloured diamonds with an error bar corresponding to the standard deviation of the repeated analyses. The mean standard measurement of Wieser et al. (2021) is shown as a horizontal dashed line with a shaded region corresponding to a single standard deviation measurement. Mean standard analyses are fit by a linear regression line to gauge instrument drift; corresponding r^2 values are shown beneath each analytical run. The two instrument drift corrections on 12/02/2020 and 14/02/2020 show significant time-dependent instrument drift (shown as bolded r^2 values) and have been corrected in the final dataset. A single outlier on 10/02/2020 is annotated and removed from the final secondary standard datasets.

rowing of the diad split was also noticeable on other days, but the temporal variability was often random and less pronounced as on days 3 and 5. The driving factor behind instrument drift is unclear, but could be related to the cooling of the Raman environment as the day drew to a close. Drift was corrected using a linear regression fit through mean standard Fermi diad splittings for these two days (Figure 2.10). The percentage offset of the standards to the calibrated mean value of Wieser et al. (2021) was calculated as a function of time; this correction was then applied to the analyses performed over the course of the day. The magnitude of the density correction was fairly minor (Figure 2.11); the majority of corrected analyses were within ±5 % of the original measurement, with

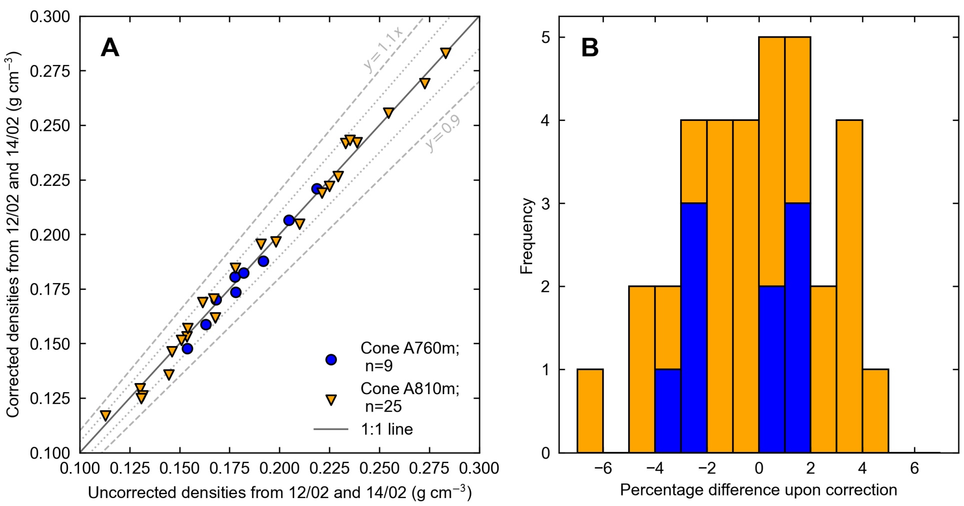

Figure 2.11: Figures illustrating the effect of linear regression corrections for Raman analyses undergone on days 12/02/2022 and 14/02/2022. A. Scatter plot comparing uncorrected calculated densities to corrected densities. B. Histogram of percentage differences upon application of the linear regression correction.

the most substantial deviation of 6 %.

Finally, there is uncertainty in the calibration of the densimeter line. The intrinsic uncertainty of the densimeter is itself dependent on the uncertainty on measuring diad splitting. Through repeated measurements of primary standards Wieser et al. (2021) suggest an 95 % uncertainty interval comprising uncertainties of the gradient (±0.026 g cm^{-3}/cm^{-1}) and the intercept (±2.7 g cm^{-3}) of Equation 2.3. However, this uncertainty is dwarfed when compared to the uncertainty associated with selecting literature calibrations and the aforementioned uncertainty in estimating melt inclusion and bubble volumes.

2.5 Secondary ion mass spectrometry (SIMS)

Secondary ion mass spectrometry (SIMS) is a technique used to analyse the chemical composition of a sample. This analysis involves bombarding a sample surface using a focussed beam of primary ions, such as $^{16}O^{-}$. Bombardment results to the excavation of a 1–2 μm crater on the sample surface, ejecting, or sputtering, charged particles termed secondary ions from the surface. These secondary ions are accelerated by a high primary voltage, and are then collected by an immersion lens and directed into a mass spectrometer. The mass spectrometer differentiates ions by their energy and charge/mass ratio through a combination of electrostatic and magnetic analysers respectively; by using both sets of analysers a high mass resolution is obtained (on the order of ppm-ppb). The differentiated secondary ions are then detected using a Faraday cup or an electron multiplier. The low detection limits owing to this 'double focussing', in conjuction with straightforward sample preparation and good spatial resolution (<25 μm), has promoted SIMS as a principal method of melt inclusion composition analysis. Furthermore, the ability to determine the concentrations from H to U permits the study of light trace elements that cannot be assessed by other techniques, such as water and carbon.

In this study the concentrations of H_2O, CO_2, F and a selection of rare-earth elements were measured in melt inclusions and matrix glasses at the NERC Ion Microprobe Facility at the University of Edinburgh using a Cameca IMS 4f. NERC grant IMF694/1119 was awarded for this study for one week of analysis time. Owing to limited access to the ion microprobe facility during the COVID-19 pandemic, instrument setup, calibration, and data collection were all performed by Dr. Cristina Talavera Rodriguez in May 2021; analytical details provided in the following sections have been forwarded by Dr. Talavera Rodriguez.

2.5.1 Instrumentation

Sample mounts were prepared as described in Section 2.2. Prior to analysis the sample mounts were gold coated to minimise the potential difference between the sample and the extraction lens, and therefore reduce surface charging during the analyses. Charging was also mitigated by using a primary beam of O^- ions, which have the advantage over other beam species (e.g., Cs^+) of preventing charge build-up on insulating sample surfaces. A strong vacuum is necessary during SIMS to minimise the probability of the interception of a secondary ion by a gas molecule during analysis. The storage pressure of the samples in the ion probe was $< 4 \times 10^{-8}$ torr, which was further reduced to $< 5 \times 10^{-9}$ torr during the analytical period. Samples were stored under vacuum for several hours prior to analysis to allow outgassing to occur, limiting instrument backgrounds.

Positive secondary ions were generated using a 13 kV primary beam of $^{16}O^-$ ions. The generated secondary ions were then accelerated to 5 keV, offset by -50 eV for ^{12}C and -75 eV for ^{1}H, ^{19}F and the trace elements to limit transfer of molecular ions into the secondary column. The primary beam used during acquisition ranged between 5–6 nA, with a raster size of 15 μm to emplace single oval spots within the inclusion.

$^{26}Mg^+$, $^{30}Si^+$ $^{40}Ca^{2+}$, $^{85}Rb^+$, $^{88}Sr^+$, $^{89}Y^+$, $^{138}Ba^+$, $^{139}La^+$, and $^{140}Ce^+$ were counted

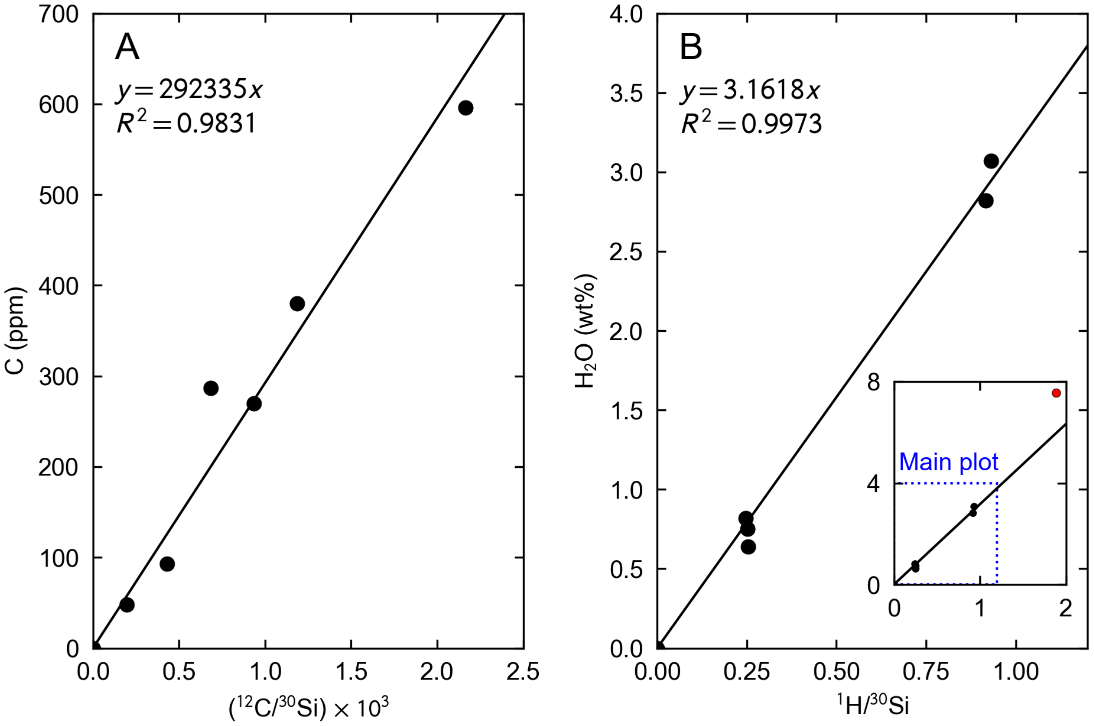

Figure 2.12: Carbon (A) and water (B) calibration curves showing reference C and H_2O concentration against measured $^{12}C/^{30}Si$ and $^{1}H/^{30}Si$ of ion probe standards. The inset figure in B illustrates a standard measurement (M21), shown in red, which was analysed but not used for determining the calibration curve.

for 2 seconds, $^{7}Li^{+}$ was counted for 3 seconds, $^{1}H^{+}$, $^{11}B^{+}$, $^{24}Mg^{2+}$, $^{35}Cl^{+}$, $^{93}Nb^{+}$, $^{141}Pr^{+}$, $^{143}Nd^{+}$, $^{157}Gd^{+}$, $^{159}Tb^{+}$, and $^{161}Dy^{+}$ were counted for 5 seconds, $^{149}Sm^{+}$, $^{171}Yb^{+}$, and $^{175}Lu^{+}$ were counted for 8 seconds, and $^{19}F^{+}$ and $^{12}C^{+}$ were counted for 10 seconds. These counts were normalised to ^{30}Si and converted into concentrations.

2.5.2 Calibration and data processing

The first 7 of 15 total C cycles and the first 10 of 20 total H_2O cycles were discarded to avoid the effects of surface contamination and to allow the C and H_2O signals to stabilise. Relative ion yields of both volatiles correlate with SiO_2 concentration, and plotting $^{1}H/^{30}Si$ or $^{1}2C/^{30}Si$ against H_2O or CO_2 produces a working curve for glasses of variable SiO_2 (Blundy and Cashman, 2008). The calibration lines for C and H_2O were calculated by running seven standards with known volatile concentrations and variable SiO_2 at the start of each session (M40, N72, M36, M21, M5, M10, M47; Shishkina et al., 2010). N72 basaltic glass is an international standard with negligible C and H_2O concentration (Shishkina et al., 2010). This standard was therefore used for background correction during the plotting of the calibration line; N72 was analysed for C and H_2O, and the recorded count rates for these elements were subtracted from the raw data. Calibration curves are shown in Figure 2.12. For F and trace elements, the data reduction software JCION5 was used, with the GSD standard used to calculate relative ion yields for the trace elements based on Si. Calibration was performed in this session using MPI-DING glasses (GSD-1, NIST610, KL2-G, ML3B; Jochum et al., 2006).

Raw data from SIMS is provided in terms of counts per second. Conversion of counts per second into concentration requires referencing of the secondary ion counts to those of a secondary ion species whose concentration is known (Blundy and Cashman, 2008). After correcting the raw data for background counts, the data were normalised to ^{30}Si. Calculation of concentrations from count rates is dependent on using well-calibrated standards to bracket the range of unknown compositions. The standards used for C and H_2O are silicate glass standards of Shishkina et al. (2010), and the standards for F and trace elements are a selection of international reference glasses.

Precisions of 18 % and 30 % were achieved for C and H_2O respectively, and accuracies of better than 35 % were achieved for both volatile elements (Equations 2.1 and 2.2). Concentrations of F were based on analyses of the KL2-G standard, and those of traces were done with respect to the GSD-1 standard. Depending on the secondary standard assessed, the majority of trace element precisions range from <5 to 15 %, with trace element accuracy typically <5 %. F returns a precision of <1 % in KL2-G. However, the majority of my unknown samples exceed the F concentration of the standards. Given the close correlation between assessing F through SIMS and assessing F via methods that use different standards (e.g., EPMA; Taracsák et al., 2019), I believe that despite being outside the standard range the F returned by SIMS is accurate within uncertainty for the F within the sample.

2.6 Electron probe microanalysis (EPMA)

Electron probe microanalysis (EPMA) is a widely used analytical technique used to non-destructively determine the chemical composition of a sample by bombarding it with an electron beam. This bombardment scatters electrons from the inner orbitals of target atoms, generating orbital vacancies; transfer of electrons into these vacancies releases energy in the form of X-ray photons in a process known as X-ray fluorescence (XRF). The X-ray lines generated are unique to every element (as every element has a unique electron structure), and intensities of each line are a function of their concentration within the sample.

These characteristic X-ray wavelengths are counted by either energy dispersive (ED) or wavelength dispersive (WD) spectroscopy. ED spectroscopy uses a semiconductor detector to collect X-rays of all wavelengths produced from the sample. In contrast, WD spectroscopy utilises crystal lattice diffraction to focus on specific X-ray wavelengths generated from the sample, which are then directed towards detectors. To cover the range of wavelengths generated from a sample of heterogeneous chemical composition, multiple crystals of different interplanar lattice spacings are necessary for WD spectroscopy. Despite this additional caveat, and the longer counting times needed relative to ED spectroscopy, WD spectroscopy offers higher X-ray peak resolution and a better signal-to-noise ratio ideal for geochemical analysis.

EPMA is primarily used for major element analyses of minerals and glasses, although some minor elements and the volatile elements F, Cl and S can also be measured (Kent, 2008). The 1–2 μm electron beam used for analyses permits excellent spatial resolution. In this study major elements and select trace elements of basaltic glasses and olivine are analysed by WD EPMA, as they appear in higher concentrations and are hence less subject to the uncertainties that may arise from background corrections when at low concentrations.

2.6.1 Instrumentation

Major and minor elements were analysed in matrix glasses, melt inclusions, and host olivine crystals by EPMA. Analyses were performed using the JEOL JXA8230 at Leeds Electron Microscopy and Spectroscopy Centre (LEMAS), University of Leeds. Samples were fully carbon coated prior to analysis to promote conductivity. They were then placed into the instrument chamber under vacuum conditions. WD analyses were performed using five spectrometers with TAP, TAPH, LIFH, PETJ, and LIFL crystals. Redistribution of Na and K is known to occur in basaltic glasses as a result of charge building in the beam interaction volume (e.g., Kent, 2008). To minimise the effects of Na and K redistribution the beam current was lowered for measurements of these two cations in basaltic glass.

X-ray intensities are determined by counting output pulses over a given period of time during WD analysis. These count rates are converted into concentrations through application of linear background corrections and matrix (ZAF) corrections against input standard compositions; this is all achieved through the ProbeForEPMA software of the instrument (Donovan, 2021). Peaking of the instrument using these standards was also performed prior to each run to maximise output X-ray intensities. Final oxide concentrations are provided as weight percent upon calculation of oxide concentrations through stoichiometry.

A preliminary qualitative mapping stage was undertaken for olivine-spinel aluminium-exchange thermometry. Olivine crystals are known to host zones of differing major and trace element composition, which arise from several processes. To ensure that quantitative points selected were representative of the olivine composition used for the thermometer, the region around and including the spinel inclusion were qualitatively mapped out for Al, Mg, P, Ni, and Ca. These regions, comprising several 7 x 7 μm sized pixels, were analysed for 0.5 seconds per pixel, with a 200 nA beam with 15 kV acceleration voltage. X-ray counts were collected for each pixel and used as a proxy for qualitative concentration of a particular element. Quantitative points were then selected by considering the zoning within each olivine-spinel region.

2.6.2 Data quality

Data reduction, necessary to convert raw X-ray data into geochemical quantities, was performed for both glass and olivine using ProbeForEPMA software (Donovan, 2021). Single point detection limits are based on the counts of the unknown sample, the counts of the standard, and the magnitude of any matrix corrections applied. Average detection limits for each element are presented in Tables 2.1–2.5. Any values below detection were rejected from the dataset. Analyses with totals less than 98 wt% or greater than 102 wt% were also rejected for olivine.

Secondary standards were measured periodically over the course of a run to determine accuracy, precision, and oxide totals. Instrument drift was also corrected for using secondary standard measurements by determining the percentage offset of the secondary standard value from a known standard value over time and applying the same correction to the analysed unknowns. Secondary standards for glass were KL2-B and ML3B-G (Jochum et al., 2006); for olivine USNM 2566 and NMNH 111312-44 (*Smithsonian Microbeam Standards Datasheets* 2019); for spinel NMNH 117075 (*Smithsonian Microbeam Standards Datasheets* 2019). Major elements (>0.4 wt%) analysed by EPMA in olivine, spinel and glass have precisions typically $\leq$6 % and accuracy $\leq$3 % (Equations 2.1 and

Table 2.1: EPMA conditions for glass measurements. All analyses were run with a 5 μm beam at 15 kV acceleration voltage, at 6 nA beam current for Na and K, and 15 nA beam current for the rest.

Element	Peak (s)	Crystal	Detection limit (ppm)	Standard
Si	20	TAP	173	Anorthoclase USNM 133868
Mg	20	TAP	154	Olivine USNM 2566
Fe	20	LIFL	416	Glass USNM 111240/52
K	15	PETH	277	Obsidian USNM 72854
Al	20	TAP	227	Anorthoclase USNM 133868
Ca	20	PETH	111	Wollastonite
Na	25	TAP	658	Jadeite
Mn	20	LIFL	412	Rhodonite
Ti	20	PETH	178	Rutile
P	20	PETH	228	Apatite

Table 2.2: EPMA conditions for olivine measurements for olivine-spinel thermometry. All analyses were run with a 1 μm beam at 15 kV acceleration voltage and 100 nA beam current.

Element	Peak (s)	Crystal	Detection limit (ppm)	Standard
Si	20	TAP	87	Olivine USNM 2566
Mg	40	LIFH	76	Olivine USNM 2566
Fe	30	TAPH	160	Haematite
Mn	60	LIFH	56	Rhodonite
Al	140	TAP	18	Almandine
Ca	100	PETJ	34	Diopside
Cr	30	LIFL	96	Cr_2O_3
Ni	60	LIFL	104	Ni metal
Ti	100	LIFH	38	Rutile
P	80	PETJ	42	Apatite

Table 2.3: EPMA conditions for spinel measurements for olivine-spinel thermometry. All analyses were run with a 1 μm beam at 15 kV acceleration voltage and 40 nA beam current.

Element	Peak (s)	Crystal	Detection limit (ppm)	Standard
Si	20	TAP	81	Diopside
Mg	10	LIFH	149	Diopside
Fe	30	TAPH	151	Haematite
Mn	60	LIFH	96	Rhodonite
Al	60	TAP	45	Almandine
Ca	60	PETJ	71	Diopside
Cr	30	LIFL	171	Cr_2O_3
Ni	60	LIFL	177	Ni metal
Ti	60	LIFH	78	Rutile
P	80	PETJ	68	Apatite

Table 2.4: EPMA conditions for olivine measurements for melt inclusion post-entrapment crystallisation corrections. All analyses were run with a 1 μm beam at 20 kV acceleration voltage and 40 nA beam current.

Element	Peak (s)	Crystal	Detection limit (ppm)	Standard
Si	30	TAP	81	Almandine
Mg	30	LIFH	149	Olivine USNM 2566
Fe	30	TAPH	151	Almandine
Mn	30	LIFH	96	Rhodonite
Al	60	TAP	45	Almandine
Ca	60	PETJ	71	Wollastonite
Cr	30	LIFL	171	Cr_2O_3
Ni	30	LIFL	177	Ni metal
Ti	30	LIFH	78	Rutile

Table 2.5: EPMA conditions for olivine measurements for olivine diffusion chronometry. All analyses were run with a 1 μm beam at 20 kV acceleration voltage and 40 nA beam current.

Element	Peak (s)	Crystal	Detection limit (ppm)	Standard
Si	30	TAP	53	Almandine
Mg	30	TAP	62	MgO
Fe	30	LIFH	82	Almandine
Mn	30	LIFH	63	Rhodonite
Al	30	TAP	65	Almandine
Ca	70	PETJ	47	Wollastonite
Cr	30	LIFL	100	Cr_2O_3
Ni	30	LIFH	97	Ni metal
Ti	30	LIFL	160	Rutile

2.2). In olivine, precision for Al was assessed at 11 % with lower on-peak count times of 60 seconds, and 8 % with 140 seconds; precisions and accuracies for MnO and P_2O_5 in basaltic glass standards were assessed to be 20 % and 5 %, and 14 % and 12 % respectively.

2.7 X-ray fluorescence (XRF)

X-ray fluorescence (XRF) is a natural phenomenon utilised for chemical analyses. The principles of the XRF method are similar to those of EPMA, albeit the sample is bombarded with high energy X-rays rather than an electron beam. Bombarding a sample with high energy X-rays excites electrons within its atomic structure. Relaxation of these electrons results in the release of secondary, lower-energy X-rays characteristic of the element in question, termed fluorescent radiation. The intensity of these fluorescent X-rays is representative of the concentration of their corresponding elements. These X-rays can be separated by the use of a WD spectrometer (see Section 2.6). XRF spectroscopy utilises the XRF effect to determine the major and trace element geochemistry of rock samples. The major benefits of XRF spectrometry in comparison to EPMA are the relatively rapid and cheap analyses, albeit at the cost of lower spatial resolution. In addition, elements with atomic number <11 cannot be accurately determined.

2.7.1 XRF sample preparation and instrumentation

Samples were powdered as described in Section 2.2. Owing to the COVID-19 pandemic, the final stages of XRF sample preparation and the analyses themselves were performed by Lesley Neve at the University of Leeds. Prior to analyses all samples were dried at 105 °C to remove any remaining moisture. After drying, loss on ignition (LOI) was assessed. 1–2 g of the sample were loaded into a porcelain crucible of known mass and weighed. The crucible was then left in a furnace for at least one hour (typically overnight) at 1025 °C. After removal, the sample was allowed to cool until returned to room temperature in a desiccator to negate absorption of air moisture before being weighed again. LOI was then calculated using the following expression:

$$\%LOI = \frac{m_{\text{sample}} - m_{\text{residue}}}{m_{\text{sample}}} \cdot 100 \tag{2.5}$$

where m is the mass of the sample or residue. It is worth noting that the escape of volatiles during LOI will generally increase the mass among all other oxides as their

Oxide	Detection limit (wt%)	Calibration Range (wt%)
SiO_2	0.01	0–100
TiO_2	0.01	0–3.7
Al_2O_3	0.01	0–60
Fe_2O_3	0.01	0–100
MnO	0.01	0–20
MgO	0.03	0–40
CaO	0.01	0–70
Na_2O	0.03	0–10
K_2O	0.01	0–15
P_2O_5	0.01	0–8
Cr_2O_3	0.01	0–20

Table 2.6: Major element calibration details for the Rigaku XRF.

relative proportions in the residue compared to the original powdered sample increases. Furthermore, the oxidation of FeO to Fe_2O_3 will raise the mass of Fe_2O_3 in comparison to the masses of the other oxides.

To produce a fused bead free of mineral structure, a flux was added to the dried sample powder. 0.4 g of the sample was mixed in a 1:10 ratio with 4 g of flux comprising 66 % lithium tetraborate and 34 % lithium metaborate (masses ±0.0002 g), and supplemented with 3 drops of lithium iodide to limit the viscosity of the melt. The sample-flux powder mixtures, loaded into platinum +5 % gold alloy crucibles, were placed into a furnace at 1150 °C for 20 minutes to completely melt and fuse, and then cast into a bead within a platinum mould. Care was taken to avoid scratching the inner parts of the platinum alloy crucible and risk sample contamination, and to ensure that the sample was dissolving completely in the flux without bubble formation. The bead was then allowed to cool to room temperature, and placed into warm 25 % HCl to clean. Spectroscopy was performed using the Rigaku ZSX Primus WDXRF at the University of Leeds.

2.7.2 Data quality

The standards USGS BCR-1 and STSD-4 were run at the start of every XRF session, and were additionally run every 10 samples. Repeat measurement of these standards yielded a precision of 1% for all elements and accuracy of $\leq$4 % for most elements (Equations 2.1 and 2.2). Accuracies of 6 %, 8 % and 5 % were obtained for Al_2O_3, MnO, and P_2O_5 respectively in BCR-1, and 7 % for TiO_2 in STSD-4. All samples yielded totals within the range 97.95–100 wt%.

2.8 Scanning electron microscopy (SEM)

Scanning electron microscopy (SEM) is an imaging method which utilises a focussed beam of electrons to scan the surface of a sample. These electrons interact with the atoms in the sample, providing information about composition and crystal orientation. This section outlines the SEM techniques that used in this thesis.

2.8.1 Backscatter electron imaging

Backscattered electrons are the product of the elastic scattering of primary (beam-sourced) electrons when they encounter an atom. Some electrons, when pulled towards the positively charged nucleus of an atom, will circle around the nucleus and re-emerge out of the sample surface. Upon contact with a backscatter electron detector in the path of an electron a signal is produced which can subsequently be used to produce an observable image. Larger atomic nuclei in the sample surface will deflect more incident electrons than smaller nuclei. The brightness of the backscatter electron image greyscale will depend on the atomic mass of the sample material. Because the forsterite (Fe-Mg) composition of olivine is linearly proportional to the brightness of olivine in a backscatter electron image, high magnification and high contrast imagery of olivine using SEM can be used to quantify profiles of olivine composition, which is used for the diffusion studies undertaken in Chapter 6 (Figure 2.7E and F). Backscatter electron imaging for this Chapter was performed using the Cameca FEI Quanta 650 SEM at LEMAS, University of Leeds, using a 20 kV beam.

2.8.2 Electron backscatter diffraction

Electron backscatter diffraction (EBSD) is an SEM technique used to study crystalline materials, more specifically the structure and crystal orientation of the material.

EBSD is dependent on the diffraction of electrons about a crystal lattice. Bragg diffraction occurs when radiation with a wavelength comparable to atomic spacings in a crystal lattice is scattered regularly by the atoms comprising that lattice; in the case of particles such as electrons, the wavelength can be determined through de Broglie relations. In the crystal lattice, lattice planes are separated by the interplanar distance d; as scattering is regular, if the scattered waves constructively interfere, the path difference between the waves will be given by $2d\sin\theta$, where θ is the glancing angle measured from the incident surface. The effect of interference intensifies because of the cumulative effect of reflection in successive crystallographic planes of the lattice, culminating in Bragg's law for a crystalline sample, which describes the condition at which constructive interference is strongest:

$$2d\sin\theta = n\lambda \tag{2.6}$$

where n is a positive integer and λ is the wavelength of the incident radiation.

A diffraction pattern is obtained by measuring the intensity of scattered waves as a function of scattering angle. Very strong intensities (Bragg peaks) are obtained in the diffraction pattern at the points where the scattering angles satisfy the Bragg condition. In EBSD, an electron beam generated by the SEM is directed onto a steeply tilted ($\sim$70 $\circ$), flat and polished sample. With a stationary beam, the EBSD pattern projects spherically from the point where the beam is incident on the sample. A phosphorus screen in the specimen chamber permits the imaging of the diffraction pattern by converting electrons to light; coupling to a lens in the diffraction camera permits the image formed on the phosphorus screen to be focussed onto a charge-coupled device (CCD) camera.

Inside the SEM, electrons backscattering from the sample may exit near the Bragg angle and diffract to form Kikuchi bands, patterns of electron scattering corresponding to each of the diffracting crystal lattice planes, as they are paths where electrons backscatter with little energy loss. Each band in the diffraction pattern is correlated to the Miller indices of the diffracting plane which forms it. If the geometry of the crystal is well described, then the bands in the diffraction pattern can be linked to the orientation of the crystal.

Diffraction pattern bands are detected by EBSD software using a Hough transform, a feature extraction process by which every band in the diffraction pattern is linked to a pixel in Hough space. Converting the strongest bands in the diffraction pattern into bright peaks aids computational identification. Upon indexing, the band locations can then be linked to the underlying crystal orientation as angles between lattice planes. Observed Kikuchi bands are unique to the orientation of the sample crystal and the wavelength of the incident electron beam, and can therefore be compared with look-up tables of crystal data to index the crystal of interest. The orientation of each sampled point can hence be matched to a reference crystal orientation.

EBSD analyses were preformed using the Cameca FEI Quanta 650 at LEMAS, University of Leeds, using a 20 kV 6 μm beam on Aperture 3. Data reduction was performed using Aztec Crystal software to obtain olivine crystal orientation data. A region of around 1000–10000 pixels of size 5–15 μm was mapped within each crystal. Data reduction to determine mean crystal orientation was performed with Python 3 code. Further method details are provided in Chapter 6.

2.9 Inductively coupled plasma mass spectrometry (ICP-MS)

An inductively coupled plasma is a gas that has been ionised into cations and free electrons through energy generated through electromagnetic conduction, atomising most molecules present in the sample. Inductively-coupled plasma mass spectrometry (ICP-MS) is a form of mass spectrometry which utilises this plasma-generating process to generate constituent ions of a sample. These ions are subsequently fed through a mass spectrometer to determine mass-to-charge ratios of ions within the sample and therefore the sample's chemical composition. In this study, solution ICP-MS is utilised to determine bulk rock trace elements of 10 whole-rock samples from the Boku Volcanic Complex.

2.9.1 Solution ICP-MS sample preparation and instrumentation

Prior to analysis, samples were digested in strong acids. Powdered basalt and scoria samples and their containing vials were weighed prior to sample digestion for ICP-MS. Powders were subsequently digested in 1 ml of ultra-pure (UpA) HNO_3 and 4 ml of UpA HF for three days, followed by 2.66 ml of reverse aqua regia (3 parts UpA HNO_3 to 1 part HCl) and 1 ml UpA HCl for another three days each, with at least 20 minutes time in an ultrasonic bath in each acid solution. In between each digestion step the samples were dried of the previous acid(s). Extensive care was taken to avoid contamination during digestion. After the final HCl digestion stage the powders were dried and dissolved in 3 ml of UpA HNO_3, which was then divided into two 1.5 ml aliquots, of which one was used for ICP-MS. These 1.5 ml aliquots of whole-rock solutions digested in HNO_3 were diluted in 48.5 ml 18.2 mΩ deionised water to achieve a solution of 3 % HNO_3.

Instrumentation and analyses were performed by Dr. Samantha Hammond using the Agilent 8800 QQQ at the Open University. The ICP-MS was run in one of three collision cell modes to remove interferences:

- No gas mode is used for measuring ions when no interferences resulting from the constituents of the sample plasma gas were expected (e.g., ^{7}Li, ^{45}Sc, ^{47}Ti).
- Collisional (He) mode is used for measuring ions when interferences were expected that could be removed through kinetic energy discrimination (e.g., ^{52}Cr, ^{55}Mn, ^{59}Co).

Analyte cations and oxide or polyatomic interferences travel through the collision cell where they collide with He atoms. In doing so, both analytes and interferences lose some kinetic energy. Larger ions, such as the oxides and polyatomics, lose a lot more kinetic energy as a result of a higher number of collisions owing to their greater cross-sectional area. A voltage barrier at the cell exit then filters out the lower energy ions and removes interferences at the expense of a lower analytical sensitivity, as some of the higher energy targeted analyte will also be captured by the filter.

- Reactive (O_2) mode is used for measuring ions when interferences result from overlapping of isotopes with the same charge/mass ratio, or if interferences cannot be removed by kinetic energy discrimination, e.g., if the interference signal is large compared to the signal of the target analyte, especially if analyte sensitivity is significantly affected by kinetic energy discrimination (e.g., the rare-earth elements). The introduction of O_2 gas to the collision cell is used to remove known, reactive interferences from each analyte, and to also generate ionic oxides of each analyte such that higher background interferences at lower charge/mass ratio can be avoided. Using this mode, rare-earth elements were mass shifted and measured as their corresponding oxides.

Samples were run with an internal standard bled in (Be, Rh, In, Tm, and Bi), which was used to monitor and correct for plasma fractionation and instrument drift during the course of the analyses. Reference material BHVO-2, sample A79 (triplicate sample 1) and an in-house 2 % HNO_3 solution were used as monitors to track and correct for further instrument drift. Monitors were run every five unknowns. If further drift correction was necessary, it was performed based on the behaviour of sample A79 (triplicate sample 1).

2.9.2 Data quality

Calibration standards were run at the start of the analytical period, followed by the samples. Precision and accuracy were achieved through analysis of a triplicate sample (A79) and the measurement of reference standards BHVO-2, JP-1, and WS-E. Corrections to account for differences in the concentration of the sample dissolved in 3 % HNO_3 were calculated as the product of the proportional differences of dissolved sample mass from 50 mg and the mass of the dissolved solution from 50 g.

Detection limits were at most 0.012 μg/g. The precision recorded by the triplicate sample was typically <4 % for most elements, with only Ti (7 %), Ta (15 %), and Tl (8 %) recording a greater spread in concentrations (Equation 2.1). Accuracy recorded by the BHVO-2 standard was <5 % for most elements (see Table 2.7), and for the WSE standard was <10 % (Equation 2.2). Accuracies are significantly more variable in the JP-1 standard owing to overall lower concentrations of trace elements in JP-1 relative to the other reference materials. As there are multiple compositional values of JP-1 recorded in the literature with no one preferred value, I use the mean of JP-1 trace element concentrations listed on GeoREM as a reference value.

Two blank samples (solutions with no dissolved material) additionally underwent the sample preparation process and subsequent analyses to evaluate possible contamination related to sample processing. The majority of elements determined through ICP-MS return concentrations of less than 0.20 μg/g, demonstrating that possible contamination in my samples is minimal. Differences in TiO_2, MnO and Cr_2O_3 concentrations, which are oxides determined through both ICP-MS and XRF, can be attributed to the precision of the respective instruments used to measure these oxides and the effect of performing LOI on XRF-determined oxide concentrations.

2.10 Modelling of post-entrapment processes

Olivine-hosted melt inclusions are subject to compositional changes that occur after they are entrapped. These processes must be accounted and corrected for if the original composition of the melt inclusion is to be determined. One visible change that may occur is the sequestering of volatiles into a shrinkage bubble during cooling (see Section 2.4). Less visibly noticeable is a change in the major element composition of the melt inclusion as a result of post-entrapment crystallisation of olivine on the walls of the inclusion, which is an inevitable consequence of cooling the inclusion-host system (Kent, 2008). The composition of this crystallising rim is governed by the distribution coefficient of Fe and Mg between olivine and liquid, K_D, where:

$$K_D = \frac{(X_{\mathrm{Fe}^{2+}}/X_{\mathrm{Mg}})^{\mathrm{olivine}}}{(X_{\mathrm{Fe}^{2+}}/X_{\mathrm{Mg}})^{\mathrm{liquid}}} = 0.30 \pm 0.03 \tag{2.7}$$

and X_{Mg} refers to the molar fraction of Mg, and likewise $X_{\mathrm{Fe}^{2+}}$ for that of Fe^{2+}. K_D is mostly independent of pressure, temperature, bulk composition, and oxygen fugacity, and has a constant value of 0.30±0.03 which is robust over the conditions of crystallisation

Table 2.7: Estimates of accuracy and precision of trace elements analysed by solution ICP-MS in whole rock standard BHVO-2, based on five monitoring analyses. Precision and accuracy are calculated according to Equations 2.1 and 2.2. Reference values for BHVO-2 are obtained from Eggins et al. (1997). RSD is the analytical relative standard deviation.

Isotope	Reference (μg/g)	Mean (μg/g)	RSD (%)	1σ (μg/g)	Precision (%)	Accuracy (%)
^{7}Li	4.90	5.18	1.16	0.09	1.71	5.65
^{45}Sc	31.80	34.62	0.84	0.61	1.77	8.85
^{47}Ti	16610.00	17597.05	0.94	198.76	1.13	5.94
^{51}V	321.00	341.99	1.00	3.88	1.13	6.54
^{52}Cr	289.00	304.13	1.10	7.46	2.45	5.23
^{55}Mn	1290.00	1412.02	1.12	30.40	2.15	9.46
^{59}Co	45.00	48.28	1.56	0.89	1.85	7.30
^{60}Ni	120.00	126.37	0.92	2.65	2.10	5.31
^{63}Cu	136.00	139.94	1.28	2.08	1.49	2.90
^{66}Zn	105.00	105.85	1.26	1.89	1.78	0.81
^{71}Ga	21.00	21.78	1.24	0.42	1.92	3.73
^{85}Rb	9.50	10.12	1.58	0.08	0.77	6.49
^{88}Sr	390.00	419.98	1.26	3.83	0.91	7.69
^{89}Y	28.00	29.63	1.42	0.47	1.58	5.82
^{90}Zr	180.00	189.52	0.88	1.30	0.69	5.29
^{93}Nb	19.50	20.60	1.10	0.16	0.77	5.63
^{95}Mo	4.07	3.90	0.92	0.02	0.53	4.24
^{118}Sn	2.30	2.15	1.46	0.02	0.73	6.64
^{121}Sb	0.10	0.10	3.74	0.00	2.84	0.97
^{133}Cs	0.10	0.10	5.56	0.00	1.98	3.62
^{137}Ba	133.00	130.78	1.12	1.40	1.07	1.67
^{139}La	15.50	16.42	0.88	0.12	0.70	5.96
^{140}Ce	38.00	39.57	0.84	0.28	0.71	4.13
^{141}Pr	5.45	5.58	0.50	0.07	1.34	2.39
^{146}Nd	24.70	26.46	0.84	0.28	1.08	7.11
^{147}Sm	6.17	6.67	0.70	0.07	1.00	8.18
^{153}Eu	2.06	2.10	1.28	0.02	0.97	2.15
^{157}Gd	6.22	6.71	0.88	0.08	1.18	7.85
^{159}Tb	0.95	1.03	0.84	0.01	1.45	8.13
^{163}Dy	5.25	5.64	0.70	0.07	1.20	7.47
^{165}Ho	1.00	1.06	0.86	0.01	0.64	6.06
^{166}Er	2.56	2.72	0.78	0.03	1.16	6.29
^{172}Yb	1.98	2.00	2.60	0.04	2.22	1.19
^{175}Lu	0.28	0.29	1.24	0.00	1.17	4.32
^{178}Hf	4.30	4.63	1.30	0.03	0.60	7.67
^{181}Ta	1.20	1.32	1.70	0.02	1.14	9.73
^{205}Tl	0.02	0.03	6.72	0.00	8.16	10.43
^{208}Pb	1.65	1.62	1.52	0.01	0.40	2.24
^{232}Th	1.22	1.15	1.10	0.03	2.82	5.65
^{238}U	0.41	0.40	1.48	0.01	3.69	3.11

expected for basaltic magmas (Roeder and Emslie, 1970; Putirka, 2005). Post-entrapment crystallisation progressively decreases the proportion of Mg in the melt relative to Fe^{2+}, resulting in the incremental crystallisation of a lower Mg olivine zone around the inclusion. The concentrations of all elements incompatible in olivine are also raised in the melt inclusion itself as post-entrapment crystallisation progresses.

This process is further complicated by diffusive re-equilibration between the host crystal and the inclusion, which is dependent on the different diffusivities of the elements present in both olivine and melt. Diffusional processes will result in the loss or gain of elements in the inclusion, and are expected to be more apparent in small, slowly cooled melt inclusions owing to shorter lengthscales and longer timescales for equilibration. Rapid diffusion of H^+ may occur through olivine, resulting in rapid re-equilibration of the melt inclusion with the carrier liquid, either dehydrating or re-hydrating the inclusion (e.g., Hartley et al., 2015). Another process that must be considered is Fe-Mg interdiffusion between olivine and melt, which is rapid and may result in significant loss of Fe from the melt inclusion. Re-equilibration of an Fe-rich (and Mg-poor) olivine rim with its more Mg-rich core forms a concentration gradient, which forces Fe to diffuse from the melt inclusion to the olivine rim to maintain the olivine-melt equilibrium established between rim and inclusion (Danyushevsky et al., 2000). The Fe recorded within the inclusion therefore falls below the liquid line of descent marked by carrier glasses and whole rocks. This process, commonly termed ‘Fe-loss’, is the largest source of error in post-entrapment crystallisation correction calculations and must be carefully considered in order to provide a strong estimate of the initial composition of the melt inclusion.

Post-entrapment crystallisation corrections can be made through experimental rehomogenisation of the inclusion to the temperature at which the inclusion was trapped; however this method is only applicable if there has been minimal diffusive re-equilibration between the melt inclusion and its host, as Fe-loss and H_2O is irreversible through experimental methods (Danyushevsky et al., 2000; Gaetani and Watson, 2000). Most studies therefore rely upon corrections made through by numerical calculations in which an olivine composition in equilibrium with the trapped melt is iteratively added to the melt composition until the melt is in equilibrium with the composition of the host olivine in concordance with Equation 2.7.

In this study, post-entrapment crystallisation and Fe-loss is corrected using Petrolog3 software (Danyushevsky and Plechov, 2011), which is one of the most commonly used methods to restore initial compositions of melt inclusions (e.g., Rose-Koga et al., 2021). The Petrolog3 algorithm for post-entrapment crystallisation correction simulates the re-homogenisation of the inclusion through the incremental addition of equilibrium olivine to the composition of the host inclusion at a given temperature, pressure, and oxygen fugacity, which corresponds to the olivine saturation surface. Upon achieving equilibrium, the software accounts for Fe-loss by simulating Fe-Mg exchange between olivine and melt, which is dependent on the initial FeO of the melt, termed FeO* in Petrolog3. The FeO of the equilibrium melt is compared to FeO*. If the simulated melt FeO is lower than that of FeO*, the program increases the experimental temperature while maintaining equilibrium between inclusion and host. This process is then reiterated until FeO matches the specified FeO* of the inclusion. This post-entrapment crystallisation process was applied to all melt inclusions considered in this study, and is detailed further in Chapter 5.

Chapter 3

Exploring rift geodynamics in Ethiopia I: olivine-spinel Al-exchange thermometry of Ethiopian Rift basalts

In this chapter and Chapter 4 I aim to develop a new independent estimate of Ethiopian mantle potential temperature and composition. This is achieved through the use of experimentally calibrated thermometry, in this case the olivine-spinel Al-exchange thermometer of Coogan et al. (2014), to obtain the crystallisation temperature of olivine crystals in mantle-derived melts. In the subsequent chapter, I use a Python melting library, which I have co-developed, to invert these crystallisation temperatures alongside other petrological and geophysical constraints to obtain mantle temperature and composition.

This chapter establishes the context behind this study, and the geochemical data used to obtain temperatures of crystallising olivines. The position of these olivine crystals on the liquid line of descent from a primary melt are established, allowing for the estimation of the crystallisation temperatures of the first olivines to form from a mantle-derived melt, i.e., the basalt liquidus.

3.1 Introduction

The influence of mantle dynamics on late-stage continental rifting and the formation of ocean basins is a subject of ongoing research and debate (see Section 1.2.3). The presence of upwelling thermo-chemical plumes beneath magmatically active rifts influences the temperature, composition, and lithology of the sub-rift mantle, governing the conditions of magma generation. As late-stage extension in volcanic rifts is believed to be strongly affected by repeated intrusions of magma that both accommodate extension and alter the thermo-mechanical structure of the crust (e.g., White et al., 2008; Bastow and Keir, 2011), unravelling the role that mantle conditions play in continental rift magmatism is key to understanding the geodynamic context of mature rifts.

Ongoing rift-related volcanism in Ethiopia provides an opportunity to study the intertwining of continental rift processes with mantle plume behaviour. Flood basalts in northern Ethiopia are correlated with the impingement of a mantle plume head at the base of the Ethiopian lithosphere at ∼30 Ma (e.g., Hofmann et al., 1997) and a persistent plume influence to the present day is inferred from both magma chemistry (e.g., Rooney et al., 2012a; Ferguson et al., 2013b) and geophysical observations (e.g., Bastow et al., 2008; French and Romanowicz, 2015). These studies highlight a significant thermal and geochemical deviation of the present-day Ethiopian mantle from the ambient mid-ocean ridge basalt (MORB) mantle source. Thermo-chemical anomalies will affect mantle melting behaviour, enhancing melt production due to elevated mantle temperatures and the presence of more 'fusible' lithologies, i.e., lithologies that will generate more melt per unit of heat expended in the melting process.

One regularly explored avenue of resolving sub-rift mantle characteristics has been to determine mantle potential temperatures (T_p). Thermo-chemical mantle plumes will have elevated T_p relative to 'ambient' MORB-source mantle. Petrological methods estimating Ethiopian mantle temperature strongly suggest an excess T_p of >100 °C above the ambient MORB mantle value of ∼1350 °C (e.g., Rooney et al., 2012c). Basalt major element thermometry returns T_p values of 1400–1490 °C for the Main Ethiopian Rift (MER) and Afar (Rooney et al., 2012c), in close concordance with trace element models for Afar basalts which suggest melting at a similar T_p beneath a relatively thick lithosphere (Ferguson et al., 2013b; Armitage et al., 2015). However, a caveat of using methods based solely on basalt geochemistry is that assumptions must be made about mantle source composition, which will affect the thermodynamic properties of the mantle and hence the composition of generated melts (see appendix of Matthews et al., 2021). Furthermore, geochemical equilibrium between the mantle and observed melts must be established or assumed.

Geophysical approaches have also been used to infer the melting behaviour of the Ethiopian mantle, but cannot straightforwardly resolve the thickness of the lithosphere. For example, S-to-P receiver functions highlight the absence of a seismically distinct lithosphere-asthenosphere boundary (LAB) beneath the MER and Afar rift axes (Rychert et al., 2012; Lavayssière et al., 2018) demonstrating that melt within the lithosphere may obscure a prominent LAB from seismic imaging (Lavayssière et al., 2018). Numerical models that reconcile both magma chemistry and receiver function observations argue for an elevated T_p of 1450 °C beneath a significantly thinned, yet still present (∼50 km thick) lithosphere comprising crust and lithospheric mantle (Armitage et al., 2015). Similar observations from Rayleigh wave tomography agree that sub-rift mantle melting is likely to be relatively deep, and driven by active melt-retention buoyancy (Gallacher et al., 2016).

In addition to raising mantle temperatures, plumes can also affect sub-rift melting processes by altering the lithological composition of the mantle. The extension of sub-rift seismic anomalies to the lower mantle beneath Ethiopia (e.g., Bastow et al., 2008) and highly radiogenic isotopes from MER and Afar basalts (e.g., Rooney et al., 2012a) suggest that the plume is compositionally distinct from ambient mantle. An important feature in this regard is the possible presence of more fusible pyroxenitic domains derived from the recycling of oceanic crust (e.g., Herzberg, 2011; Shorttle et al., 2014) or through the dripping of pyroxenitic material from thermally and gravitationally unstable metasomatised lithosphere (Furman et al., 2016). Indeed the presence of asthenospheric mantle pyroxenites have previously been posited as a possible driver for deep melting beneath Ethiopia in the absence of significantly elevated T_p (Rooney et al., 2012c). Additionally, it is probable that the Ethiopian mantle, like many other plume-affected localities, is partially composed of refractory harzburgitic material, the depleted residue from previous melting (Stracke et al., 2019). The presence of multiple melting and non-melting lithologies in the Ethiopian mantle will dictate the thermal pathway taken during decompression melting, which will likely deviate from that inferred via single-lithology (peridotite) melting models (Phipps Morgan, 2001; Matthews et al., 2021). Furthermore, melting a mixed lithology mantle will produce magmas that differ in major element, trace element, and radiogenic isotopic compositions compared to those derived from a purely peridotite source (Herzberg, 2011;

Shorttle et al., 2014). The recent study of Ethiopian mantle xenoliths has additionally highlighted the presence of highly fusible metasomatic domains in the Ethiopian lithospheric mantle which may also contribute to the chemistry of erupted rift basalts (e.g., Casagli et al., 2017; Rooney et al., 2017). Petrological models linking the observed composition of rift basalts to the composition and thermal state of a multi-lithology mantle source are therefore necessary to explore how multiple melting lithologies in the sub-rift mantle may contribute towards magmatism and rifting in Ethiopia.

In this study, divided between this chapter and the following chapter, I investigate melt generation beneath the MER and Afar via a mantle melting model constrained by olivine crystallisation temperatures and REE concentrations observed in rift zone magmas. My multi-lithology melting approach is based on that of Matthews et al. (2021) who demonstrated that variations in olivine crystallisation temperatures can be related to the temperature and lithological composition of the melting mantle and can therefore be used to estimate mantle T_p independent of magma chemistry. This method provides an alternative and complementary approach to previous studies that investigated mantle temperatures in Ethiopia using peridotite-only melting models (e.g., Rooney et al., 2012c; Ferguson et al., 2013b; Armitage et al., 2015).

This chapter investigates how the temperature of olivine crystallisation can be determined using petrological methods, and how these crystallisation temperatures can then be used to assess the liquidus temperature of mantle-derived basalts. The subsequent chapter describes the mantle melting methodology and inversion techniques employed in this study, and the use of these primary liquidus temperatures as a constraint on determining the temperature and composition of the melting Ethiopian mantle.

3.2 Samples and methods

The MER samples used in this study are basaltic scoriae collected from two monogenetic fields in the rift centre: the East Ziway Lake cone field (Section 2.1.2) and the Boku Volcanic Complex (Section 2.1.3) Phyric olivine crystals were visibly present in one scoria cone locality in East Ziway (Z58a, locality reference KW-MER19-58a), whereas Boku had more extant olivine among its cones. The olivine crystals analysed in this study were separated from olivine-phyric basaltic scoria collected from monogenetic cones in the MER and Afar related to late-stage magmatic-tectonic rift zones (e.g., Rooney et al., 2011). Samples from

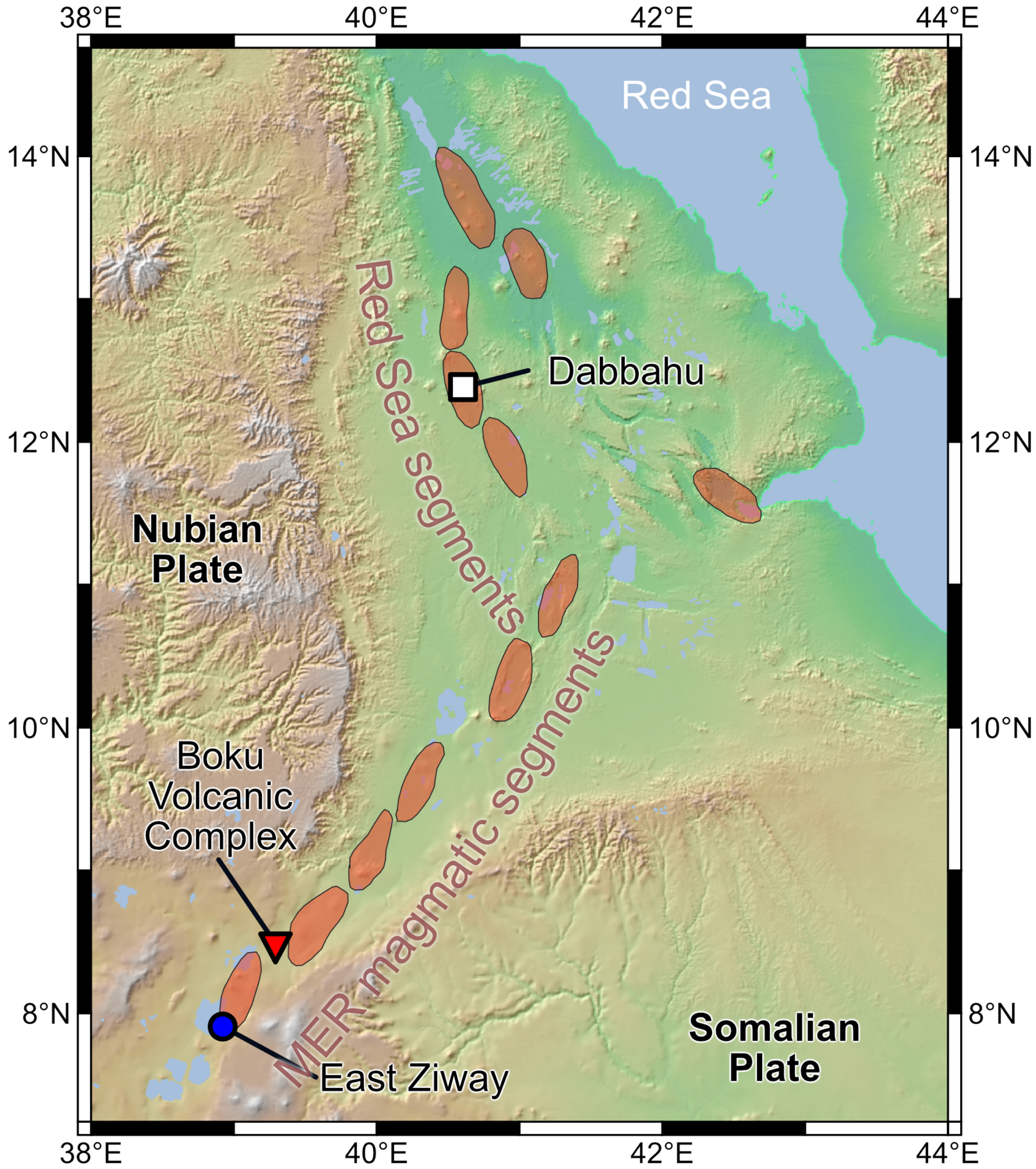

Figure 3.1: Map of the northernmost East African Rift showing the sampled locations in this study, with Main Ethiopian Rift (MER) and Afar Rift magmatic segments highlighted in red (after Hayward and Ebinger, 1996).

the MER were collected from cones Z58a and A81 (locatity reference KW-MER19-81-0m) within the Boku Volcanic Complex (see Figure 1.1). Fresh olivine crystals from scoria cones within these monogenetic fields were picked by hand from disaggregated scoriae, mounted in epoxy resin and polished using silicon carbide papers and diamond suspensions (as described in Section 2.2). The main phenocryst phase within these scoriae is olivine with plagioclase feldspar also present as a smaller fraction (<15 %) phenocryst phase at Boku and a roughly equivalent fraction (∼50 %) at East Ziway. Samples from Afar were collected at the recently active Dabbahu Rift Zone and are predominantly olivine-phyric (e.g., Ferguson et al., 2010, see Figure 1.1). Picked olivines were mounted in epoxy resin and polished for electron probe microanalysis (EPMA).In addition to these samples olivine crystals from the Dabbahu rift system of the Afar sector of the Red Sea Rift were analysed (sampled by Ferguson, 2011). Only crystals hosting fully enclosed spinel inclusions were chosen to avoid selecting spinels that had re-equilibrated with their carrier magma after then were entrapped.

Extension within the MER at Ziway and at Boku is primarily accommodated by a segmented network of dyke-induced faults in the rift centre (e.g., Mazzarini et al., 2013a), along which scoria cones are found (e.g., Rooney et al., 2011). Seismic evidence suggests that the lower crust in this section of the MER has been modified by repeated dyke intrusions (e.g., Maguire et al., 2006; Hammond et al., 2011). At Ziway, scoria cone-forming basalts are dated to 800–300 ka (WoldeGabriel et al., 1990; Trua et al., 1999); at Boku, cones are associated with post-caldera basaltic activity dating to ∼200 ka (Tadesse et al., 2019). In Afar, the tectonic-magmatic segmentation of the rift system is more distinct, and faulting and volcanism are strongly focussed along magmatic rift zones (Hayward and Ebinger, 1996). The crust here is thinner compared to the MER and predominantly igneous in nature (Hammond et al., 2011). At the Dabbahu rift segment, which has been the locus of magmatically driven extension in this section of the rift system since at least ∼200 ka (Ferguson et al., 2013a), the most recent volcanic activity occurred in 2005–2010 and involved a series of intrusive and eruptive events (e.g., Ferguson et al., 2010).

3.2.1 Olivine-spinel Al exchange thermometry

Olivine and spinel are among the first phases to crystallise from mantle-derived melts, and for co-crystallisation to occur they must develop in equilibrium with each other. Equilibrium is suggested by the common occurrence of spinel inclusions within olivine crystals;

these two mineral assemblages therefore record the initial chemical conditions under which mantle-derived magmas begin co-crystallising olivine and spinel. The concentration of Al in olivine is a strong function of temperature, becoming more compatible in olivine with increasing temperature (De Hoog et al., 2010). However unlike the Fe-Mg system used in olivine-liquid thermometers, Al is a slow-diffusing species in olivine, mostly occupying the tetrahedral sites, and is therefore less susceptible to being reset after crystallisation (Spandler and O'Neill, 2010; Zhukova et al., 2017). The olivine-spinel Al-exchange thermometer can hence provide a means of estimating olivine crystallisation temperatures (T_{crys}) for magmas without requiring knowledge of the initial melt composition (Coogan et al., 2014).

An initial study of Al partitioning between olivine and spinel as a function of temperature by Wan et al. (2008) calibrated an experimental thermometer between 1250 and 1450 °C at 100 kPa, which was established to be pressure-independent or near-independent at crustal pressures (Wan et al., 2008). Further experiments performed by Coogan et al. (2014) resulted in an updated parameterisation (Equation 3.1).

$$T(^{\circ}\mathrm{C}) = \frac{10,000}{0.575 + 0.884 + \mathrm{Cr\#} - 0.897\ln(k_d)} - 273.15 \tag{3.1}$$

where the distribution coefficient of Al, k_d, is defined as:

$$k_d = \frac{\mathrm{Al_2O_3}^{\mathrm{olivine}}}{\mathrm{Al_2O_3}^{\mathrm{spinel}}} \tag{3.2}$$

and the chromium number Cr# is defined as:

$$\mathrm{Cr\#} = \left(\frac{\mathrm{Cr}}{\mathrm{Cr} + \mathrm{Al}}\right)^{\mathrm{spinel}} \tag{3.3}$$

Al_2O_3 in Equation 3.2 is given as wt% and Al and Cr in Equation 3.3 are given as molar fractions. In these new experiments Coogan et al. confirm that the effects of silica activity ($a_{\mathrm{SiO_2}}$) and oxygen fugacity ($f\mathrm{O_2}$) are minor and within thermometer uncertainty (<20 °C), and note a moderate correlation between uptake of P and Al in olivine arising as a result of their coupled substitution. The primary control of Al partitioning between olivine and spinel at crustal conditions is therefore temperature, with near-independence from pressure, $a_{\mathrm{SiO_2}}$, and $f\mathrm{O_2}$. The partitioning of P into olivine and Ti into spinel should, however, be taken into consideration, as both processes may influence the partitioning of Al into olivine and spinel respectively, and hence affect the calculated temperature (as noted by Jennings et al., 2019).

These recent developments in constraining the behaviour of Al in olivine has led to the application of the olivine-spinel Al-exchange thermometer to a host of magmatic settings including mid-ocean ridges (Coogan et al., 2014; Matthews et al., 2021), large igneous provinces (LIPs; e.g. Coogan et al., 2014; Heinonen et al., 2015; Xu and Liu, 2016; Jennings et al., 2019), Iceland (Spice et al., 2016; Matthews et al., 2016), and Hawaii (Matthews et al., 2021) but not to continental rift magmas. Primary T_{crys}, liquidus temperatures of the most primitive mantle-derived melts, obtained for non-rift tectonic settings, either directly or through secondary correction of Al-exchange T_{crys} values, show substantial variations between MORB and plume-derived basalts, consistent with elevated mantle T_p at plume settings. However, without further constraints on melting geometry and mantle source composition, differences in T_p cannot be resolved from differences in T_{crys} alone (Matthews et al., 2021). In this study I therefore integrate results from olivine-spinel Al-exchange thermometry with other constraints on magmatic processes in the MER and Afar to constrain likely values for mantle T_p.

3.2.2 Analytical methods

Geochemical data on olivine and spinel were collected by EPMA over three analytical sessions using the JEOL JXA8230 microprobe at the University of Leeds, U.K. Only olivines completely enclosing spinel inclusions were selected.

During the first session, qualitative maps were recorded for the areas surrounding and including the spinel inclusion to assess the presence of zoning in Al, P, Ni, Ca and Mg within both the host olivine and spinel inclusion, following the method and analytical conditions of Matthews et al. (2021) (see Section 2.6.1). These maps illustrate that the majority of crystals do not show any significant variability in Al and P count rates on the scale of the map ($\sim$100 μm; e.g., Figures 3.2 and 3.3), suggesting that Al uptake in olivine resulting from increased P concentrations is minimal (Coogan et al., 2014) and equilibrium Al was not changing during crystallisation. Zoning in Mg, Ni, and Ca is observed and these zones were avoided if possible during subsequent point analyses.

In the following two sessions, quantitative analyses within both phases were performed for Fe, Mg, Si, Mn, Al, Ca, Cr, Ni, Ti, and P using the qualitative maps as guidance; analytical conditions are presented in Tables 2.5 and 2.3 for olivine and spinel respectively. Longer count times were taken for Al in olivine, as it is present in low concentrations (<700 ppm, De Hoog et al., 2010; Coogan et al., 2014). Points within olivine were selected

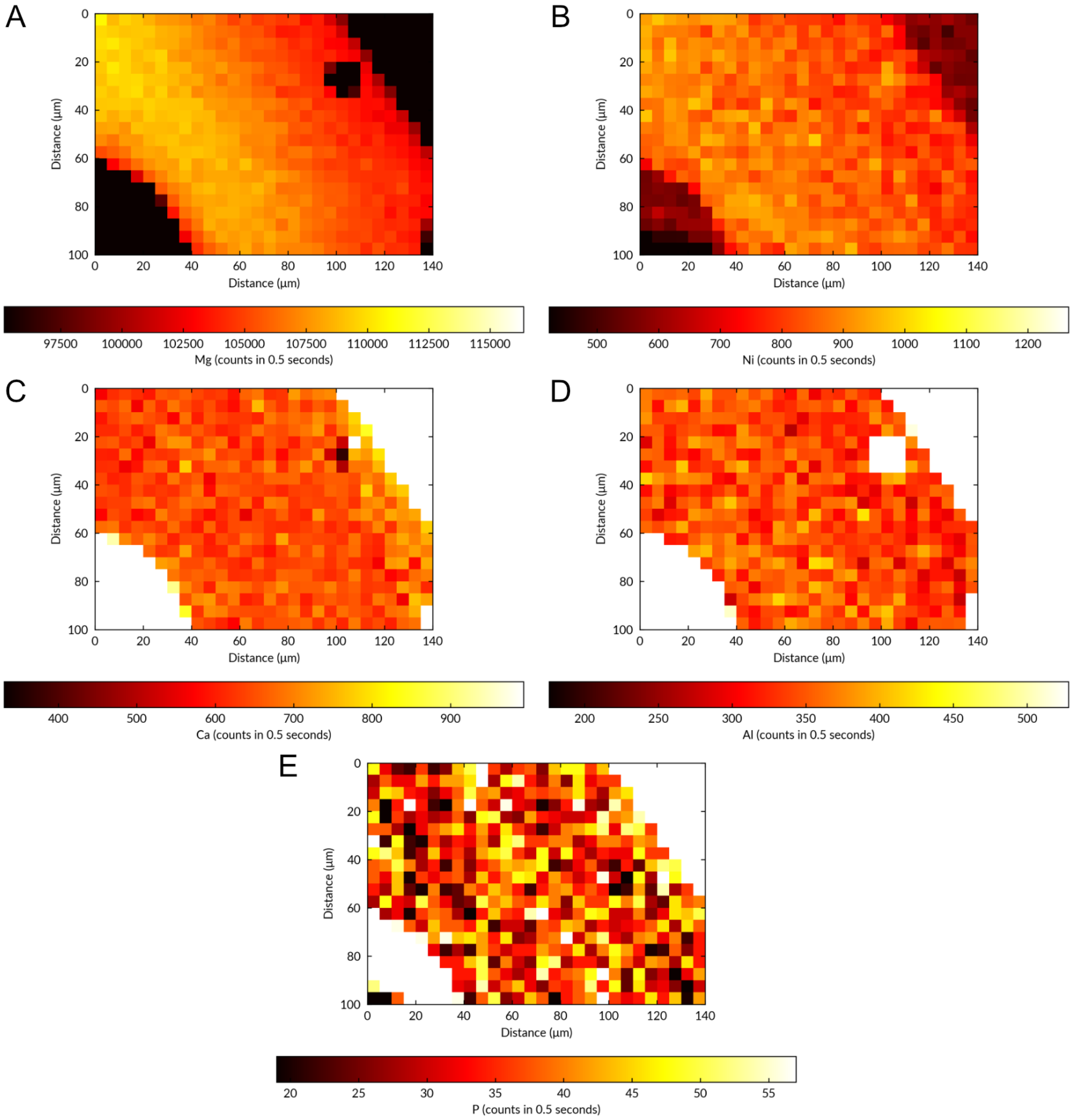

Figure 3.2: X-ray map of olivine-spinel pair AO3_A0 for the following elements: A. Mg, B. Ni, C. Ca, D. Al, E. P. The spinel inclusion is dark in the Mg map and bright in the Al map (subfigures A and D). Colorbar limits are selected to best display variability in elemental concentration, and are not absolute. Note the zoning in Mg and Ni evident in subfigures A and B, which is not accompanied by corresponding changes in Ca, Al, or P (subfigures C-E).

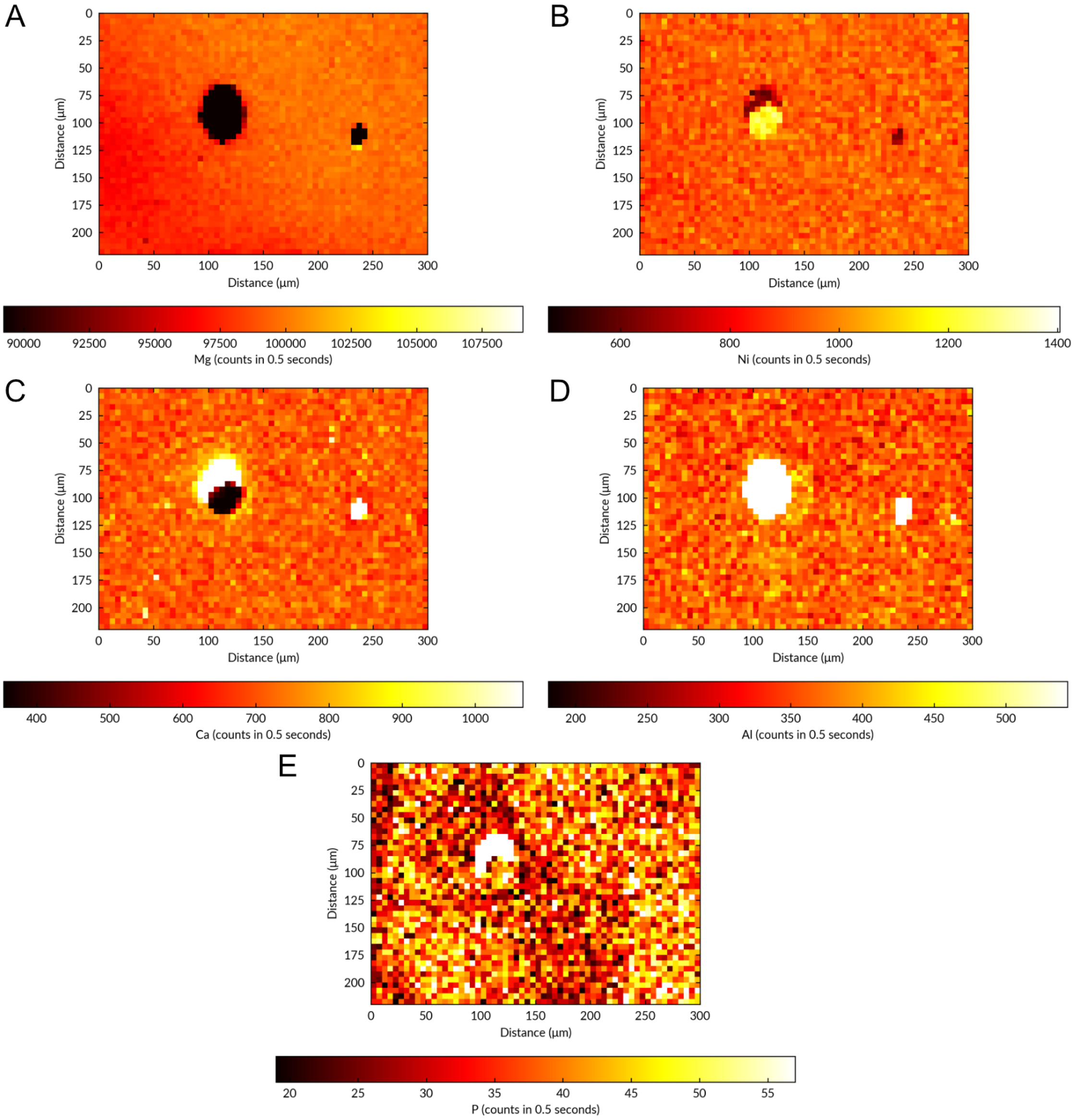

Figure 3.3: X-ray map of olivine-spinel pair DO0_A4a for the following elements: A. Mg, B. Ni, C. Ca, D. Al, E. P. The spinel inclusion is the elliptical inclusion on the right, which is dark in the Mg map and bright in the Al map (subfigures A and D). The feature on the left is a melt inclusion hosting a possible nickel sulphide, which is dark in the Ca map (subfigure C). Colorbar limits are selected to best display variability in elemental concentration, and are not absolute. Note the zoning in P and evident in subfigure E, which is not correlated to Al (subfigure D).

at least 10 μm away from the olivine-spinel boundary to avoid secondary fluorescence of X-rays from spinel into olivine which increases the measured Al_2O_3 in olivine (Jennings et al., 2019). Any points sampling more than one crystal had consistent variations across all major elements and were removed from the dataset. Care was also taken to avoid selecting points across zones of Fe-Mg evident from qualitative maps. Analytical conditions for quantitative point analyses in olivine and spinel are provided in Tables 2.2 and 2.3 respectively. Secondary standard analyses are included in Appendix A.2.

Uncertainties in olivine crystallisation temperature are determined through Monte Carlo propagation (n=10000), which allows the uncertainty of chemical analyses to be propagated assuming Gaussian error distributions with means and standard deviations comprising the values and their respective uncertainties. An inherent experimental uncertainty with a standard deviation of 14 °C is included to account for the combined uncertainty of the thermometer calibration (Matthews et al., 2016).

3.3 Analytical results

3.3.1 Olivine and spinel geochemistry

Mean olivine and spinel compositions determined by repeat analyses are shown in Figure 3.4. The complete dataset is presented within Appendix A.2. The Fe-Mg ratio of olivine crystals is described using forsterite (Fo, in mol%), given by the following expression:

$$\mathrm{Fo} = 100 \cdot \frac{\mathrm{Mg}}{\mathrm{Mg} + \mathrm{Fe}} \tag{3.4}$$

where Mg and Fe are given as molar fractions.

Ziway Lake olivines exhibit lower Fo than both Boku and Dabbahu (Fo_{66-75}); Boku and Dabbahu Rift olivines hosting spinel inclusions are Fo_{76-86}. In particular, the Fo range of Dabbahu Rift olivine (Fo_{76-86}) overlaps considerably with the previous observations of Fo_{76-83} from Dabbahu volcano basalts (Field et al., 2013). There is poor correlation between olivine Fo and Al_2O_3 (r^2=0.27), especially for the Dabbahu dataset (r^2=0.12; Figure 3.4A). High olivine Al_2O_3 concentrations are linked to higher T_{crys} and crystallisation from more primitive melts, therefore in the absence of Fe-Mg re-equilibration higher Fo is expected. The implications of possible Fo-Al_2O_3 decoupling in Section 3.4. Olivine Al_2O_3 does not correlate with P_2O_5 or TiO_2, suggesting that Al_2O_3 uptake is not affected by P-Al or Ti-Al substitution (Coogan et al., 2014; Jennings et al., 2019).

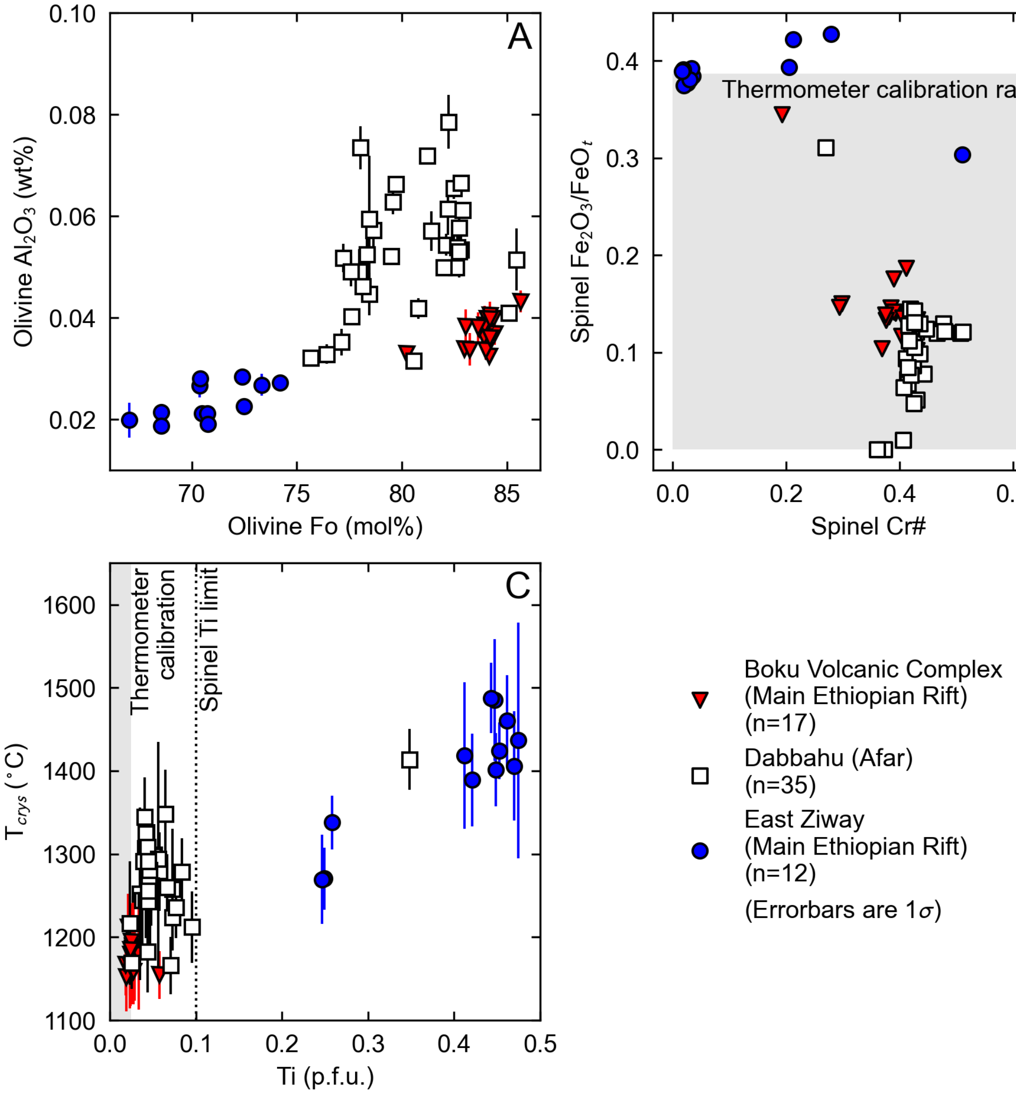

Figure 3.4: Geochemistry of olivine-spinel pairs used for olivine-spinel Al-exchange thermometry. A. Al_2O_3 concentration in olivine as a function of their Fo content for all Ethiopian Rift and Afar samples. Uncertainties of Al_2O_3 are presented as 2σ error bars; uncertainties in Fo are smaller than the marker size. B. Cr_2O_3 concentration in spinel as a function of estimated Fe_2O_3/FeO_t content for all Ethiopian Rift and Afar samples. Fe_2O_3/FeO_t is estimated using the stoichiometric method of Droop (1987). The shaded area shows the calibrated range of the olivine-spinel Al exchange thermometer. C. Olivine crystallisation temperature as a function of Ti (per formula unit in spinel). Temperature uncertainties are presented as 2σ as determined from Monte Carlo error propagation. The shaded area shows the Ti calibration range of the thermometer (Wan et al., 2008; Coogan et al., 2014).

The compositions of inclusions of spinel are shown in Figures 3.4B and C. Fe_2O_3 is estimated from total spinel FeO on a basis of four oxygens and should be considered as approximate (Droop, 1987). All spinel inclusions from Boku and Dabbahu fall within the calibrated Cr# and Fe_2O_3/FeO_t range of the thermometer (Cr# <0.69 and Fe_2O_3/FeO_t <0.4 respectively; Figure 3.4B), however several East Ziway spinels exceed calibrated Fe_2O_3/FeO_t. The spinels in this study are relatively high in Ti and most samples exceed the thermometer calibration range of Ti per formula unit (p.f.u.) (<0.025; Figure 3.4C). While uptake of Ti can affect the activity coefficients of Al and Cr in spinel, biasing temperatures from high Ti spinels (e.g., Jennings et al., 2019), previous Al-exchange studies note that Ti contents <0.32 Ti p.f.u. do not produce anomalous results (Coogan et al., 2014; Heinonen et al., 2015; Jennings et al., 2019). To err on the side of caution, all of the olivine-spinel pairs I consider in this chapter to calculate T_{crys} values have spinel Ti p.f.u. ≤0.1 (Figure 3.4C). This mandated filtering removes all East Ziway analyses and one Dabbahu analysis from the remainder of this work.

3.3.2 Olivine crystallisation temperatures

My T_{crys} results are plotted in Figure 3.5. Boku T_{crys} range from 1152±40 °C to 1212±40 °C with the highest T_{crys} recorded by the most forsteritic olivine (Fo_{86}). Boku T_{crys} and Fo are well-constrained, with most T_{crys} values within mutual uncertainty and the majority of olivine-spinel pairs clustering between Fo_{82-85} and tightly between $Fo_{83.5-84.5}$. Dabbahu Rift olivine-spinel pairs record temperatures from 1166±34 °C to 1344±48°C, however, there is no clear trend between Fo and T_{crys} (Figure 3.5), suggesting that Fo may have become decoupled from Al by diffusive exchange of Mg and Fe with the surrounding magma between crystallisation and eruption.

The mean T_{crys} of Boku olivines (1177±16 °C) is lower than that of Dabbahu (1267±43 °C). This temperature difference could imply that primary magmas at Dabbahu are hotter than Boku, assuming that the olivine captured in my sample sets are the first to crystallise. If Boku and Dabbahu magmas do crystallise at similar temperatures, it is plausible that this difference in mean T_{crys} arises from the under-sampling of crystals that fractionated earlier at Boku compared with Dabbahu.

Figure 3.5 shows the T_{crys} distributions of my Ethiopian samples in comparison with those of MORB, Iceland, Hawaii, and LIPs. Boku T_{crys} are lower than the highest recorded MORB T_{crys} (1289±34 °C; Matthews et al., 2021) and record a lower median T_{crys} than

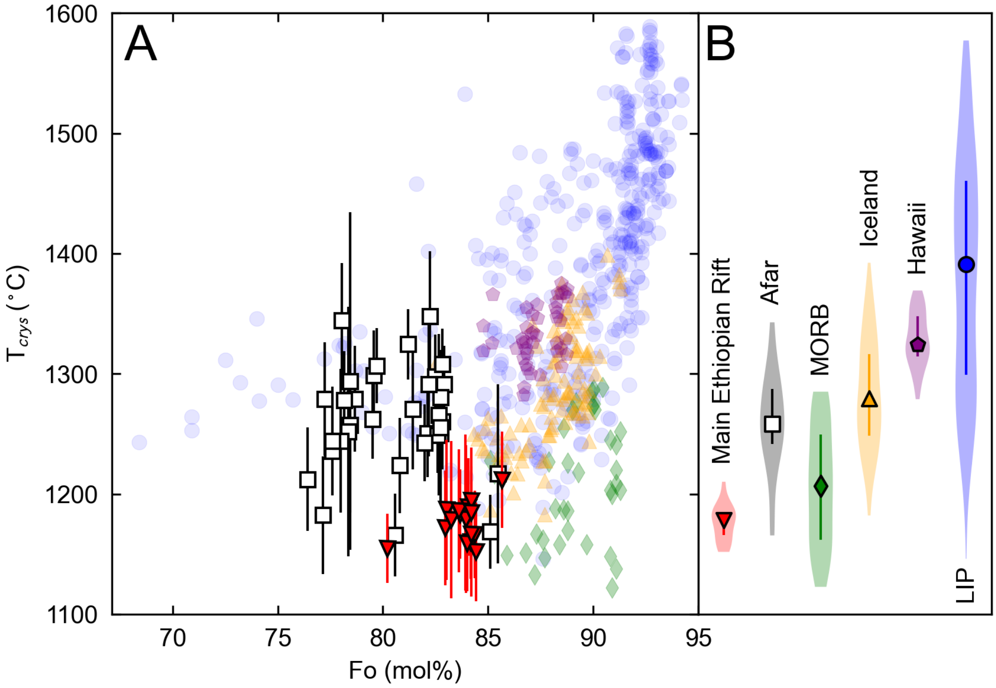

Figure 3.5: Olivine crystallisation temperatures for the Main Ethiopian Rift and Afar presented alongside a global compilation of olivine-spinel Al exchange crystallisation temperatures. The subfigure on the left shows crystallisation temperatures plotted against olivine Fo, and the subfigure on the right shows violin plots of crystallisation temperature. The global compilation data is sourced as follows; MORB (Coogan et al., 2014; Matthews et al., 2021); Iceland (Spice et al., 2016; Matthews et al., 2016); Hawaii (Matthews et al., 2021); LIP (Coogan et al., 2014; Heinonen et al., 2015; Xu and Liu, 2016; Spice et al., 2016; Liu et al., 2017; Trela et al., 2017; Matthews et al., 2016; Jennings et al., 2019).

that of MORB. However, Boku olivines are mostly lower Fo than the MORB olivines for which Al-exchange temperatures have been obtained. The higher temperature Dabbahu distribution overlaps with the MORB distribution as well as the plume-influenced settings of Iceland and Hawaii. Only the highest temperature Dabbahu olivines exceed the highest MORB T_{crys}, and are comparable with the highest T_{crys} recorded from Iceland and Hawaii.

These T_{crys} are the hottest recorded for olivine in continental rift zones. Models for Boku melts using Rhyolite-MELTS (Gualda et al., 2012) suggest that olivine is the first phase to crystallise parental melts at 1141±30 °C, followed by spinel at 1091±40 °C (Tadesse et al., 2019); however the parental melt in this study has likely already substantially cooled and fractionated. Olivine-liquid equilibria of Dabbahu volcano olivine crystals (Roeder, 1974) provides estimates of 1113±53 °C and 1117±53 °C (Field et al., 2013). These T_{crys} are within uncertainty of the lowest T_{crys} recorded for the Dabbahu

Rift by olivine-spinel Al exchange thermometry, however the Dabbahu volcano olivines used are significantly lower forsterite ($Fo_{<65}$) than those of this study and are likely to have crystallised from a more-evolved and cooler melt.

3.4 Estimating primary olivine crystallisation temperature

The olivines used in this study are relatively evolved (lower Fo) compared to most of those which the Al-exchange thermometer has been applied previously (Figure 3.5). They are therefore unlikely to be representative of the first crystals to form from high MgO mantle-derived primary melts, which are typically $Fo_{\sim 91}$ (e.g., Rooney et al., 2005) owing to the equilibrium partitioning of Fe-Mg between melt and olivine (Roeder and Emslie, 1970). Olivine Fo subsequently decreases with progressive crystallisation and cooling as MgO in the magma is expended. Crystallisation temperatures recorded by the highest Fo olivines are therefore expected to be closest to the liquidus temperature of the primary magma. As the melting model predicts olivine T_{crys} at the basalt liquidus, it is necessary to estimate the T_{crys} of the first olivine to crystallise from the primary mantle melt ($T_{crys}^{primary}$). To do so, the Fo-T_{crys} distributions observed in Figure 3.5 must be studied to limit uncertainty in estimating $T_{crys}^{primary}$ from T_{crys}. In other words, are my T_{crys} indicative of initial crystallisation from a primary mantle-derived melt and subsequently subject to subsequent decoupling of Fe-Mg in olivine, or do they record crystallisation after the cooling and fractionation of the initial melt after crustal emplacement?

Olivines of Fo_{91} thought to be in equilibrium with primary mantle-derived melts have not been observed within erupted rift lavas. MER olivines up to Fo_{90} have been recorded (e.g. Peccerillo et al., 2003; Rooney et al., 2005), and the highest Fo Dabbahu Rift olivines of Fo_{86} are recorded within my dataset. $Fo_{\geq 91}$ olivine could crystallise and stall in the sub-rift crust; melt is known to be present in the deepest parts of the MER and Afar crust before transport to shallow reservoirs (Rooney et al., 2007; Ebinger et al., 2008; Rooney, 2010; Field et al., 2012, 2013; Desissa et al., 2013), and it is feasible that extensive olivine fractionation could occur at depth in the crust or lithospheric mantle. If $Fo_{\geq 91}$ olivines are produced but not erupted, then extrapolation to high Fo and correspondingly high T_{crys} will be necessary to determine primary crystallisation. Alternatively, the highest T_{crys} recorded may be similar to the initial T_{crys} if intially high Fo olivines have reequilibrated to lower Fo via Fe-Mg diffusion. Since Al_2O_3 diffuses slower than Fe-Mg in olivine (Spandler and

O'Neill, 2010) this will decouple the Al-in-olivine T_{crys} from Fo (see Hawaii distribution of Matthews et al., 2021).

Low Fo olivines can develop during fractional crystallisation or via diffusive re-equilibration with more evolved melts, for example within an interdiffusing mush pile (Thomson and Maclennan, 2013). Furthermore, pyroxenite-derived melts will crystallise lower Fo olivine than lherzolite-derived melts at the same temperatures, and progressive mixing of pyroxenite-derived melts into lherzolite-derived melts will cause the Fo content of crystallising olivine to decrease faster than in a pure lherzolite melt (Matthews et al., 2021). To estimate $T_{crys}^{primary}$ of the first olivine crystallising from a mantle-derived melt these mechanisms must be considered, and, if necessary, T_{crys} projected back to higher Fo and $T_{crys}^{primary}$.

3.4.1 Petrolog fractionation models

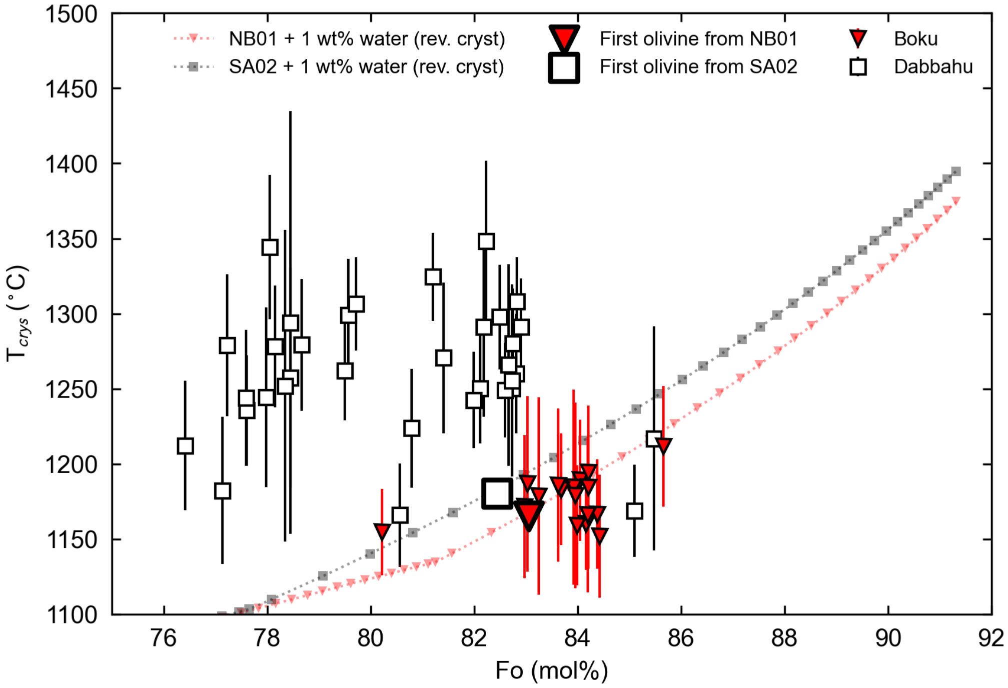

Figure 3.6: Olivine-spinel Al-exchange crystallisation temperatures plotted as a function of olivine Fo, alongside Petrolog3 model fractionation trends for olivine in olivine-fractionation-corrected primitive rift magmas from the Boku Volcanic Complex, Main Ethiopian Rift, and Dabbahu, Afar (see text for details). The first olivine to crystallise from each basalt without correction is shown as a large bold symbol. Markers are at F=0.01 intervals. Uncertainties in T_{crys} are given as 2σ.

I compare the olivine crystallisation trends to model trends calculated using Petrolog3

Table 3.1: Initial compositions of primitive melts used in Petrolog modelling. Oxide compositions are presented as wt%. SA-02 starting melt includes 0.08 wt% Cr_2O_3 (Ferguson, 2011).

Sample	NB-01 (Boku)	SA-02 (Dabbahu)
SiO_2	45.43	47.24
TiO_2	2.19	2.2
Al_2O_3	16.81	14.75
FeO_t	11.46	12.38
MnO	0.19	0.21
MgO	8.81	9.42
CaO	10.52	10.09
Na_2O	2.52	2.41
K_2O	0.46	0.33
P_2O_5	0.33	0.30
Cr_2O_3	0.11	0.08
H_2O	1.00	1.00
Total	99.83	100.33
Reference	Tadesse et al., 2019	Ferguson et al., 2013b

(Danyushevsky and Plechov, 2011). Starting whole-rock compositions are the high MgO basalts NB-01 from Boku (Tadesse et al., 2019) and SA-02 from the Dabbahu Rift (Ferguson et al., 2013b), assuming an initial water content of 1 wt% for both localities typical of rift basalts (Field et al., 2013; Iddon and Edmonds, 2020, see also Chapter 5). Crystallisation occurs at the FMQ oxygen buffer consistent with oxygen fugacity observations at the MER and Afar (e.g. Field et al., 2013; Gleeson et al., 2017; Tadesse et al., 2019). Olivine fractionation is corrected back to Fo_{91} at 8 kbar following the model of Danyushevsky (2001), with both compositions requiring addition of ~25 % olivine. Subsequent fractional crystallisation of olivine, plagioclase feldspar and clinopyroxene is then modelled at 3 kbar using the mineral fractionation models of Danyushevsky (2001) at the FMQ oxygen buffer; 3 kbar pressure is chosen as representative of mid-crustal fractionation (see Chapter 5). These fractionation trends are plotted alongside the olivine-spinel Al-exchange T_{crys} in Figure 3.6, in addition to the first olivine crystallising from the two whole-rock compositions before correction.

Petrolog3 model olivine temperatures encompass the observed range of T_{crys} for Boku and Dabbahu Rift (Figure 3.6). The predicted crystallisation trend for Boku olivine passes through the uncertainty envelope of most Al-exchange T_{crys}. The predicted Dabbahu Rift trend however does not show a similar correlation and the fractionation trend passes through only the lower T_{crys} range of the Fo-clustered olivine distributions. A significant number of olivine-spinel pairs record higher T_{crys} than should be expected for their Fo values. While it is possible to achieve the highest T_{crys} at the Dabbahu Rift with deeper fractionation pressures, Petrolog3 models suggest that these pressures would be significantly in excess of the base of the crust. This is unlikely when considering the distribution of melt under Dabbahu (<35 km depth; Desissa et al., 2013). The fractionation trend does, however, fall close to the most forsteritic (and lower T_{crys}) olivines.

One further consideration must also be the impact of crystallising other minerals along the liquid line of descent, which must be taken into account as phyric plagioclase is present in my samples. The crystallisation of plagioclase and clinopyroxene will level out the liquid line of descent and therefore reduce extrapolated $T_{crys}^{primary}$ by a considerable amount. Parental compositions from the MER and Afar are not known, so it is impossible to determine the degree of fractional crystallisation that has occurred. According to Petrolog models run directly from the two original whole-rock compositions, only olivine crystallises initially; plagioclase enters the liquid line of descent after a further 2–5% olivine crystallisation (Figure 3.6). It is therefore possible, based on these starting compositions and considerations, that all olivines crystallised from predicted precursor melts when only olivine is on the liquidus. However, based on the Fo-T_{crys} distributions, there is a chance that these olivines are not the first to crystallise from a primary mantle melt.

3.4.2 Iterative olivine addition

For sample suites that have no $\mathrm{Fo}_{\geq 91}$ olivine Matthews et al. (2021) use an iterative olivine-addition to obtain likely primary T_{crys} values ($T_{crys}^{primary}$). This is achieved by calculating the Fe^{2+} and Mg of the melt in equilibrium with the crystallised olivine using known olivine-melt partitioning behaviour (Roeder and Emslie, 1970; Putirka, 2008b) and assuming that olivine is one fo the earliest phases to crystallise, and that the proportion of spinel crystallising has negligible effect on melt composition. A small amount of the equilibrium olivine is then returned to the melt, and a new, higher temperature olivine composition is found in equilibrium with the new melt. This iterative process continues until a suitably high Fo and corresponding T_{crys} is recorded. By doing so a liquid line of descent is determined along which observed olivines crystallise. This liquid line of descent can then be used to extrapolate T_{crys} of observed olivines at low Fo back to $T_{crys}^{primary}$ at high Fo that are in equilibrium with mantle-derived melts.

The partition coefficient of a cation i between olivine and melt, $D_i^{\mathrm{ol/liq}}$, is given by the ratio of the concentration of the element between olivine and melt, X_i^{ol} and X_i^{liq} respectively:

$$D_i^{ol/liq} = \frac{X_i^{ol}}{X_i^{liq}} \tag{3.5}$$

where $D_i^{ol/liq}$ is a function of pressure, temperature, and melt composition. Using data from melting experiments, Putirka et al. (2007) calibrated $D_{\mathrm{Mg}}^{ol/liq}$ and $D_{\mathrm{Fe}}^{ol/liq}$ to derive the following equations:

$$\begin{aligned} \ln(D_{\mathrm{Mg}}^{ol/liq}) = & -2.158 + 55.09\frac{P}{T} - 6.213 \times 10^{-2}[\mathrm{H_2O}] \\ & + \frac{4430}{T} + 5.115 \times 10^{-2}[\mathrm{Na_2O + K_2O}] \end{aligned} \tag{3.6}$$

$$\begin{aligned} \ln(D_{\mathrm{Fe}}^{ol/liq}) = & -3.300 + 47.57\frac{P}{T} - 5.192 \times 10^{-2}[\mathrm{H_2O}] \\ & + \frac{3344}{T} + 5.595 \times 10^{-2}[\mathrm{Na_2O + K_2O}] + 1.633 \times 10^{-2}[\mathrm{SiO_2}] \end{aligned} \tag{3.7}$$

where P is pressure in GPa, T is temperature in °C, and oxides in square brackets are given as wt%. Using these equations, the partition coefficients of Fe and Mg between melt and olivine can be calculated for any chosen crystallisation temperature. In the iterations performed in this study, P is assumed to be the pressure at the base of the crust, assuming crustal thicknesses of 28 km and 23 km for the MER and Afar respectively, and a crustal density of 2.8 g cm^{-3}. The value of [$\mathrm{Na_2O+K_2O}$] is assumed to be constant at 5 wt%, and [$\mathrm{SiO_2}$] to be constant at 48 wt%, which are typical for MER basalts. Although those from the MER and Afar will differ from these values, any propagated uncertainty is negligible compared to the uncertainty on the olivine-spinel Al-exchange thermometer.

The cation fractions of Fe and Mg in the parental melt can be calculated using the partition coefficient as described in Equation 3.5. To estimate the olivine composition in equilibrium with a melt composition, the fixed Fe-Mg exchange coefficient (K_D) of Roeder and Emslie (1970) can be utilised (Equation 2.7), which can be rearranged to return $X_{\mathrm{Mg}}^{liq}/X_{\mathrm{Fe}}^{liq}$ as a function of olivine Fo (Equation 3.4):

$$\frac{X_{\mathrm{Mg}}^{liq}}{X_{\mathrm{Fe}}^{liq}} = \frac{K_D \cdot \mathrm{Fo}}{100 - \mathrm{Fo}} \tag{3.8}$$

The rearranged expression for K_D can subsequently be combined with an expression of olivine stoichiometry (Roeder and Emslie, 1970) to estimate the Fe and Mg of a melt in equilibrium with an olivine of known Fo:

$$X_{\mathrm{Mg}}^{liq} D_{\mathrm{Mg}}^{ol/liq} + X_{\mathrm{Fe}}^{liq} D_{\mathrm{Fe}}^{ol/liq} = 0.667 \tag{3.9}$$

By combining these equations the composition of a new melt formed upon addition of a small amount of equilibrium olivine back to the melt can be found:

$$X_i^{liq-new} = \frac{X_i^{ol} \cdot f + X_i^{liq}}{1 + f} \tag{3.10}$$

where i is the partitioning cation between olivine and melt and f is the increment of olivine returned to the melt. By simultaneously solving for these equations I can estimate the temperature at which the new melt composition will saturate in olivine, in other words the T_{crys} of the new olivine. Iteration of this process to Fo$_{91}$, selected for continuity with Matthews et al. (2021), will allow for estimation of $T_{crys}^{primary}$. Selected observed T_{crys} values and their extrapolated $T_{crys}^{primary}$ values are provided in Table 3.2.

In all cases the uncertainty on mean T_{crys} prior to extrapolation is the larger of the standard deviation of T_{crys} values contributing to the mean, or an uncertainty characteristic of the standard deviation of each individual value. Uncertainty in $T_{crys}^{primary}$ is determined by extrapolation of uncertainty of T_{crys} at lower Fo, and uncertainty in estimating $T_{crys}^{primary}$ is propagated by performing separate inversions for each $T_{crys}^{primary}$.

3.4.2.1 Boku

The fractional crystallisation models discussed in the previous section suggest that Boku olivines plausibly lie on liquid line of descent from a primary basalt crystallising only olivine (Figure 3.6). Extrapolation of T_{crys} at low Fo to $T_{crys}^{primary}$ at high Fo is necessary to obtain an estimate for the liquidus temperature of the basalt. To achieve this I use the mean T_{crys} of the Fo$_{83.5-84.5}$ cluster (1175±22 °C) as the starting value and the iterative olivine addition projection of Matthews et al. (2021) described above to extrapolate to $T_{crys}^{primary}$ at Fo$_{91}$ (Figure 3.7A). This yields an estimated $T_{crys}^{primary}$ value for Boku of 1426±26 °C.

3.4.2.2 Dabbahu

As shown in Section 3.4.1, the ancestral melt composition of the Dabbahu Rift olivines remains unclear. The lack of a correlation between Fo and T_{crys} in the Dabbahu Rift dataset implies that these parameters may have become decoupled since initial crystallisation of the olivines. If the olivines are known to fall on a liquid line of descent then the iterative

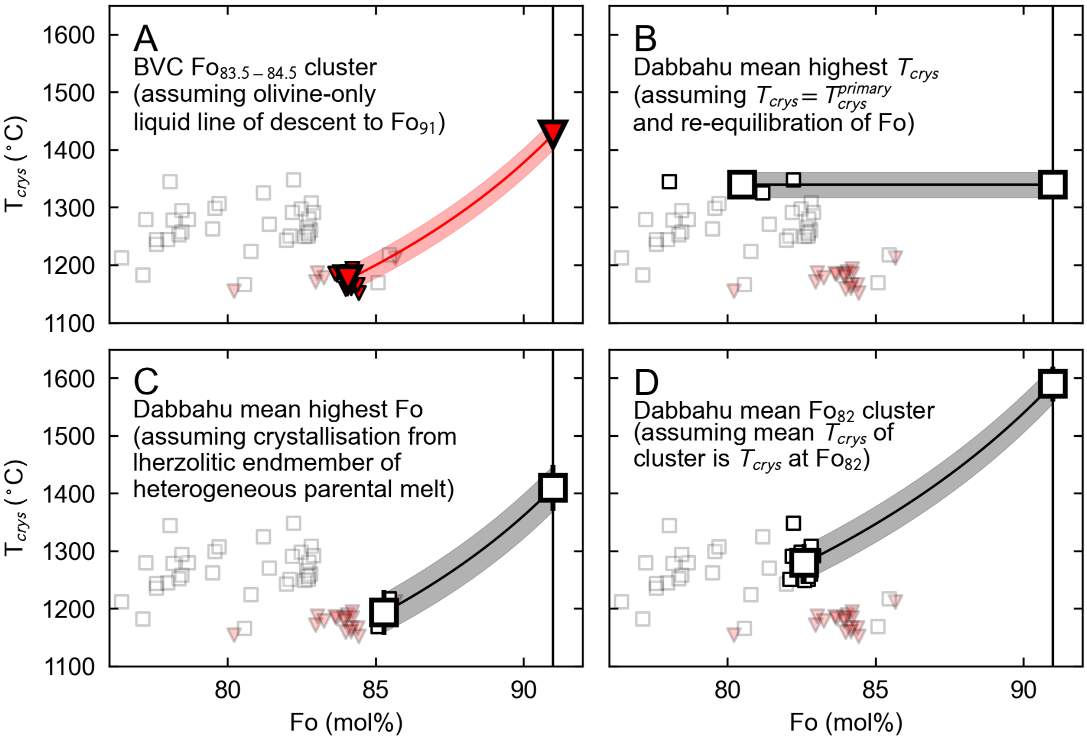

Figure 3.7: Figure illustrating the iterative olivine addition used to determine primary crystallisation temperatures from temperatures obtained from my dataset. The starting temperatures are as follows: A. The mean T_{crys} of the $Fo_{83.5-84.5}$ cluster comprising the highest Fo cluster of points in the Boku dataset, projected to $T_{crys}^{primary}$ at Fo_{91}; B. the mean of the highest Dabbahu T_{crys} values, assumed to be $T_{crys}^{primary}$; C. the mean T_{crys} of the highest Fo olivines in the Dabbahu dataset projected to $T_{crys}^{primary}$; D. the mean T_{crys} of the highest Fo cluster at Fo_{82}, projected to $T_{crys}^{primary}$. The faded triangular and square markers in the plot are the Boku and Afar T_{crys} in the dataset respectively; the small bold markers in the plots are datapoints used to calculate Fo and T_{crys} means, which are subsequently used to project to $T_{crys}^{primary}$ at Fo_{91}. The shaded area represents the propagated uncertainty of the initial crystallisation temperature estimate.

Table 3.2: T_{crys} extrapolations to Fo_{91} applied to observed olivine crystallisation temperatures using the iterative scheme of Matthews et al. (2021), after Putirka (2008b).

Location	Projection method	T_{crys} (°C)	Fo (mol%)	$T_{crys}^{primary}$ (°C)
Boku, MER	-	1175±22	84.07	1426±26
Dabbahu Rift, Afar	Diffusive re-equlibration	1279±30	82.59	1590±33
Dabbahu Rift, Afar	Melt heterogeneity	1217±37	85.47	1409±40

projection can be used to estimate $T_{crys}^{primary}$ from T_{crys} provided that olivine Fo is known. However, if olivines do not lie along a liquid line of descent then other scenarios must be considered in which a single liquid line of descent cannot solely explain the Fo-T_{crys} distribution. I therefore explore three possible scenarios for obtaining a $T_{crys}^{primary}$ value from these data (Figure 3.7B-D).

One possibility is that these olivines has equilibrated their Fo contents with more evolved melts, in which case the highest Dabbahu T_{crys} values (mean of 1339±22 °C) represent those closest to the liquidus temperature of the primary mantle melt crystallising Fo_{91} olivine, i.e., $T_{crys} \approx T_{crys}^{primary}$ (Figure 3.7B). If the crystallisation trend recorded from Petrolog3 is correct then the initial temperature at which olivine begins crystallising (∼1400 °C) is best matched by this highest Dabbahu olivine-spinel Al-exchange T_{crys}. The observed Fo clusters could be derived from the fractionation of mafic olivines and subsequent diffusive re-equilibration to the somewhat common values of the clusters at Fo_{78} and Fo_{82}, which form the two near-vertical arrays in Fo-Tcrys space. If this is the case, then the two high Fo and low T_{crys} olivines are the only crystals with Fo values preserved from the original liquid line of descent (Figure 3.6). If the Petrolog3 fractionation trend is not realistic then additional extrapolation to Fo_{91} and correspondingly higher T_{crys} will be necessary.

Alternatively, melt heterogeneity can also result in non-correlation between Fo and T_{crys} (Matthews et al., 2021). Concurrently mixing melts of differing FeO, for example those derived from lherzolite and pyroxenite, will fractionate olivines with a range of Fo bound by the liquid lines of descent for each melt composition. Pyroxenite-derived melts, which are higher in FeO than lherzolite-derived melts, will crystallise lower Fo olivines relative to lherzolitic melts at the same temperature (Roeder and Emslie, 1970; Jennings et al., 2019). The lowest T_{crys} and highest Fo olivines will therefore lie closest to the low FeO lherzolitic liquid line of descent, as these melts are most likely to have been in equilibrium with Fo_{91} olivine; projection to $T_{crys}^{primary}$ should therefore be performed on these olivines

(Matthews et al., 2021). If heterogeneity from unmixed lherzolite-derived and pyroxenite-derived mantle melts has not been removed by the time melts begin crystallising, then a range of Fo contents would be produced at any given temperature with the highest Fo crystals forming from melts closest to the lherzolitic liquid line of descent (Matthews et al., 2021). Projecting the mean T_{crys} of the two highest Fo olivines (1193±34 °C) back along this liquid line of descent to Fo_{91} gives a $T_{crys}^{primary}$ of 1409±40 °C (Figure 3.7C).

A final possibility is that an initial correlation between Fo and T_{crys}, which existed due to fractional crystallisation, has been distorted by extensive re-equilibration to a common Fo value (Thomson and Maclennan, 2013). Olivines fractionating at different temperatures and compositions can re-equilibrate their Fe-Mg to an average (lower) Fo value in a mush pile (Thomson and Maclennan, 2013), resulting in initially high Fo (and high T_{crys}) olivines losing Fo with time. The mean T_{crys} of this mush pile will fall near the T_{crys} of a crystallising olivine with the same Fo as the common mush pile Fo value, which will lie on the liquid line of descent. Projection from this Fo value and T_{crys} to T_{crys} at Fo_{91} will therefore provide a suitable estimate of $T_{crys}^{primary}$. In this scenario the mean Fo of an equilibrated olivine population (in this case I use the higher Fo_{82} cluster) will still lie along the initial liquid line of descent and projecting back the mean T_{crys} should provide a reasonable estimate of $T_{crys}^{primary}$. Projecting the mean T_{crys} of the Fo_{82} cluster to Fo_{91} gives a $T_{crys}^{primary}$ of 1590±33 °C (Figure 3.7D). These three estimates provide possible T_{crys} values for the Dabbahu magmas between ∼1339–1590 °C.

3.5 Conclusions, part I

Through olivine-spinel Al-exchange thermometry I obtain new petrological olivine crystallisation temperatures for the Boku Volcanic Complex, MER, and the Dabbahu Rift, Afar, with means of 1176±16 °C and 1263±43 °C respectively. Extrapolation of olivine-spinel Al-exchange T_{crys} from low Fo olivines to $T_{crys}^{primary}$ at which olivines in equilibrium with mantle-derived melts are likely to crystallise is accomplished with an iterative olivine addition process to provide estimates of the basalt liquidus at the MER and Afar. Using this process to correct to Fo_{91} olivines I estimate that mantle-derived basalts from Boku begin crystallising within the crust at 1426±26 °C. Several values for $T_{crys}^{primary}$ are obtained for the Dabbahu Rift, ranging from 1339±22 °C to 1590±33 °C depending on the assumptions made during the projection from low Fo to Fo_{91}.

The following chapter illustrates how $T_{crys}^{primary}$, when combined with a model of mantle melting and observed basalt REE concentrations and geophysical observations, can form the basis for inversion of mantle temperature.

Chapter 4

Exploring rift geodynamics in Ethiopia II: modelling the melting Ethiopian mantle

Following on from the work in Chapter 3, in this chapter I describe the mantle melting model and inversion processes that are used to combine petrological and geophysical observations to obtain estimates of mantle temperature.

4.1 Forward modelling: mantle to melt

Predicting observable properties such as olivine T_{crys}, basalt trace element compositions, and melt fractions from mantle T_p necessitates several key assumptions concerning the mechanics of melt segregation, accumulation, and mantle source composition. A model of mantle melting allows these parameters to be determined by predicting thermal pathways from melt generation to crystallisation as a function of mantle T_p and lithological composition.

4.1.1 Multi-lithology melting and the pyMelt library

T_p must exceed $T_{crys}^{primary}$ as heat is expended in the form of latent heat of fusion and adiabatic cooling. The extent of adiabatic cooling is directly affected by the composition of the melting mantle, as non-melting lithologies will act as a thermal buffer and promote melting of fusible lithologies (Phipps Morgan, 2001). The presence of multiple lithologies will also directly affect the thermal pathway undertaken by the melting mantle, as these different lithologies will all bear differing mineral compositions and therefore thermal expansivities. Calculating the thermal pathway travelled by a mantle-derived melt therefore necessitates several key assumptions concerning the mechanics of melt segregation and collection, mantle source composition, and the definition of T_{crys} recorded by thermometry.

A mantle of multiple components in thermal isolation initially follows a solid mantle adiabat dependent on the temperature and composition of the mantle (Phipps Morgan, 2001):

$$\left.\frac{dT}{dP}\right|_S = \frac{\bar{\alpha}}{\bar{\rho}\bar{C_p}}T \tag{4.1}$$

where T is temperature, P is pressure, $\bar{\alpha}$ is the bulk thermal expansivity, $\bar{\rho}$ is the bulk density, and $\bar{C_p}$ is the bulk heat capacity, and S is entropy (McKenzie and Bickle, 1988). This equation holds true after melting so long as the melt remains in thermal isolation. Upon crossing the solidus of one of the components, heat is converted into latent heat of fusion, resulting in decrease to the gradient of the mantle adiabat. The melt productivity of a multi-lithology mantle is calculated by solving the following expression for each lithology (Equation 25 of Phipps Morgan, 2001):

$$\sum_i \phi_i \left[\left(\frac{\partial S_i}{\partial F_i}\right)_{P,T} dF_i + \left(\frac{\partial S_i}{\partial T}\right)_{P,F} dT + \left(\frac{\partial S_i}{\partial P}\right)_{T,F} dP \right] = 0 \tag{4.2}$$

where F is the melt fraction, i is the lithology, and ϕ_i is the fraction of the lithology in the multi-lithology mantle. This results in the following expression for the melt productivity $\frac{dF}{dP}$ of a melting lithology i in a mantle comprising of n components (Equation 29 of Phipps Morgan, 2001):

$$\frac{dF_i}{dP} = -\frac{\frac{\bar{C_p}}{T}\frac{\partial T_i}{\partial P} - \frac{\bar{\alpha}}{\bar{\rho}}\sum_{n\neq i}\left[\phi_n \Delta S_n^m \frac{\frac{\partial T_i}{\partial P} - \frac{\partial T_n}{\partial P}}{\frac{\partial T_n}{\partial F_n}}\right]}{\phi_i \Delta S_i^m + \sum_{n\neq i}\left[\phi_n \Delta S_n^m \frac{\frac{\partial T_i}{\partial F_i}}{\frac{\partial T_n}{\partial F_n}}\right] + \frac{\bar{C_p}}{T}\frac{\partial T_i}{\partial F_i}} \tag{4.3}$$

If the melt productivity of each melting lithology is known, then the temperature gradient within the region where all lithologies are melting is given by:

$$\frac{dT}{dP} = \frac{dT_j^m}{dP} + \frac{dT_j^m}{dF_j}\frac{dF_j}{dP} \tag{4.4}$$

where T_j^m is the temperature of the melting lithology or lithologies, which can be determined using values for one lithology j. As melting progresses with each pressure step the new mantle adiabat is calculated.

The pyMelt Python 3 library is a multi-lithological mantle melting library that I have co-developed with Simon Matthews and Matthew Gleeson (Matthews et al., 2021, 2022, see Declaration for author contributions). This Python library utilises the formulation of Phipps Morgan (2001) to calculate the melting behaviour of a multi-component mantle during adiabatic decompression. pyMelt can determine the melt fraction for any of its parameterised lithologies at a given pressure and temperature, as well as the proportions of the different lithologies that contribute to the final melt. The thermal gradient of a melting multi-lithology mantle is determined through a fourth order Runge Kutta integration over pressure steps of 0.004 GPa starting at the mantle solidus, assuming that melt and residue remain in thermal equilibrium. Melting ceases at the LAB, after which the melts follow a basalt adiabat to crustal pressures where olivine crystallisation begins. The form of the basalt liquidus is linear, and takes the form (Equation 15 of Putirka, 2008a):

$$T_{crys} = T - (P - P_{crys}) \left(\frac{dT}{dP}\right)_{liq} \tag{4.5}$$

where T_{crys} and P_{crys} are the temperature and pressure at which olivine crystallisation occurs, and $(dT/dP)_{liq}$ is the Clapeyron slope of the basalt liquidus. The value of $(dT/dP)_{liq}$ is assumed to be 39.16 K GPa^{-1} (Putirka, 2008b). The use of this function assumes that the melt is not cooled as it passes through the lithosphere, and strictly follows the basalt adiabat, which is appropriate when melt fluxes are high and heat advection dominates over conduction (e.g., Matthews et al., 2016).

The input parameters for this forward model are those that control the thermal pathway of the melting mantle and therefore melt fraction and by extension melt thickness: T_p, mantle composition, lithospheric thickness, and crystallisation pressure. I select a tri-lithology mantle comprising non-melting harzburgite (after Shorttle et al., 2014), a pyroxenite component melting like KG1 (Kogiso et al., 1998), and a lherzolite melting like KLB-1 (Takahashi, 1986). These lithologies in particular are selected for continuity with Matthews et al. (2021). Though this modelling approach necessitates choosing particular lithologies, the inclusion of pyroxenite can equivalently be interpreted as the bulk mantle being made more fusible (e.g., through refertilisation of a lherzolite), and likewise harzburgite interpreted as the bulk mantle becoming more refractory.

4.1.2 pyMelt trace element forward model

To provide additional constraints on melt production, I have updated the pyMelt code to include calculations of the concentrations of incompatible trace elements, such as rare-earth elements (REEs), in the melt. This update predicts the trace element chemistry of a melt produced by melting a mantle comprising multiple lithologies, following the equations of Shaw (1970) and the INVMEL methodology of McKenzie and O'Nions (1991). In this way the chemistry of mantle-derived basalts can be predicted using pyMelt outputs.

The concentration of each trace element within an instantaneous melt c_l and corresponding solid residue c_s are related to each other by the following equations, assuming incremental batch melting (Shaw, 1970):

$$\frac{dc_s}{dX} = \frac{c_s - c_l}{1 - X} \quad \text{and} \quad c_l = \frac{c_s(1 - X)}{\bar{D} - \bar{P}X} \tag{4.6}$$

where X is the total melt fraction, $\bar{D}$ is the bulk distribution coefficient for any given trace element within the solid assemblage, and $\bar{P}$ is the bulk distribution coefficient for the same trace element for the melting assemblage. $\bar{P}$ and $\bar{D}$ are calculated as outlined by McKenzie and O'Nions (1991). As mineral assemblage varies with depth within the Earth, the bulk distribution coefficients $\bar{D}$ and $\bar{P}$ are depth-dependent and not constant across all integration paths. c_l, c_s, $\bar{D}$, and $\bar{P}$ are calculated using the pyMelt pressure and melt fraction outputs for every pressure step. The expressions of Equation 4.6 are numerically integrated using a fourth-order Runge-Kutta scheme from the base of the melting interval ($X = 0$) to the top of the melting interval ($X = X_{total-max}$, where $X_{total-max}$ is the maximum total melt fraction). To avoid Python floating point errors the point solid residue is assumed to be completely depleted when $c_s < 10^{-6}$ ppm. The mean composition of all melt extracted from a single lithology within a given melting column is then determined by:

$$\varphi_{column} = \int_{z_0}^{z_1} \frac{X_{lithology-max} c_l}{1 - X_{total-max}} dz \bigg/ \int_{z_0}^{z_1} \frac{X_{lithology-max}}{1 - X_{total-max}} dz \tag{4.7}$$

where z_0 is the depth at the base of the melting region, z_1 is the depth at the top of the melting region, $X_{lithology-max}$ is the maximum melt fraction of the melting lithology, and $X_{total-max}$ is the maximum total melt fraction of the melting mantle, which is itself a function of T_p, lithospheric thickness, and mantle composition. To obtain the mean composition of the mixed melt extracted from all lithologies the ϕ_{column} of each lithology, weighted by its solid mantle proportion, are summed. When applying this adiabatic decompression melting regime I integrate over the lateral columns comprising the triangular melting region with the following equation, which is valid for any passive melting model (e.g. Plank and Langmuir, 1992; Richardson and McKenzie, 1994; Slater et al., 2001; Maclennan et al., 2001):

$$\varphi_{passive} = \int_{z_0}^{z_1} \varphi_{column}(z_1 - z_0)\frac{dX}{dz}dz \Big/ \int_{z_0}^{z_1} (z_1 - z_0)\frac{dX}{dz}dz \qquad (4.8)$$

Mineral-melt distribution coefficients were collated from the compilations of Gibson and Geist (2010) for olivine, orthopyroxene, clinopyroxene and garnet, and McKenzie and O'Nions (1991) for spinel and plagioclase. While $\bar{D}$ is known to vary for some trace elements in minerals as a function of pressure, temperature and mineral composition (Blundy and Wood, 2003), incorporating all of these effects into pyMelt is beyond the scope of this study. Mantle source mineral proportions are estimated from published KLB-1 and KG1 pseudosections (Jennings and Holland, 2015; Matthews et al., 2021). Proportions are listed for KLB-1 and KG1 in Tables 4.1 and 4.2 respectively; mean mineral proportions in the pressure-temperature intervals listed were selected to avoid high temperatures of melting, and also to avoid subsolidus phase reactions and transitions in the aluminous phase.

I follow McKenzie and O'Nions (1991) in modelling two melting regimes: one in which olivine, orthopyroxene, clinopyroxene and the aluminous phase are all present; and another where only olivine and orthopyroxene are present upon the exhaustion of clinopyroxene and the aluminous phase from the solid mantle residue at a fixed melt fraction X'. The proportion of clinopyroxene and the aluminous phase vary linearly from the initial proportion to zero in the interval $0 < X < X'$, and are equal to zero when $X > X'$; for KLB-1 lherzolite $X' = 0.18$ (e.g. Ball et al., 2021); for KG1 pyroxenite $X' = 0.70$. These values of X' are chosen as they are the approximate sum of clinopyroxene and aluminous phases in KLB-1 and KG1. If melting of these phases dominates the melt generated when $X < X'$, then they will be exhausted when the magnitude of the melt fraction is similar to that of their proportions.

The aluminous mineral phase present in the mantle varies as a function of depth. The garnet-in and spinel-out reactions in lherzolite are modelled as linear functions of pressure and temperature following McKenzie and O'Nions (1991) after high-pressure experiments (Nickel, 1986; Robinson and Wood, 1998):

Table 4.1: Mineral proportions at sub-solidus conditions for KLB-1 lherzolite estimated from published pseudosections at listed temperature and pressure ranges (Jennings and Holland, 2015).

KLB-1	olv	opx	cpx	gnt	spn	plg
$T < 1200°\text{C}$; $P > 6.0$ GPa	0.609	0.125	0.119	0.147	-	-
$T < 1200°\text{C}$; $1.0 < P < 1.5$ GPa	0.597	0.233	0.158	-	0.012	-
$T < 1200°\text{C}$; $P = 0.45$ GPa	0.646	0.208	0.076	-	-	0.070

Table 4.2: Mineral proportions at sub-solidus conditions for KG1 pyroxenite estimated from published pseudosections at listed temperature and pressure ranges (Matthews et al., 2021).

KG1	olv	opx	cpx	gnt	spn	plg
$T < 1160°C; P > 6.0$ GPa	0.181	0.012	0.422	0.385	-	-
$T < 1160°C; 1.2 < P < 1.5$ GPa	0.110	0.178	0.641	-	0.071	-
$T < 1160°C; P = 1.05$ GPa	0.118	0.150	0.655	-	-	0.067

$$T_{sp-out} = 666.7P - 400 \quad \text{and} \quad T_{gt-in} = 666.7P - 533 \tag{4.9}$$

where P is in GPa and T is in °C. Between these two functions, source mineral proportions vary linearly between their proportions in the garnet field and the spinel field. The position of the garnet-spinel transition is thought to be shallower in pyroxenites relative to lherzolites owing to higher Al_2O_3 and lower Mg# in the former which promotes garnet stability (Hirschmann and Stolper, 1996). I model the garnet-spinel transition in pyroxenite to occur linearly between the pressure range 1.5–2.5 GPa (54–90 km), based on the KG1 pyroxenite pseudosection (Matthews et al., 2021).

Several geochemical studies of Ethiopian basalts have provided evidence for the possible introduction of lithospheric melt to mantle-derived melts (e.g., Casagli et al., 2017; Rooney et al., 2017). To model the introduction of a small amount of lithospheric melt I use the geochemical data collected by Casagli et al. (2017) on Ethiopian sub-continental lithospheric mantle xenoliths. I assume the proportion of orthopyroxene is 0.30, the proportion of clinopyroxene is 0.22 (the average clinopyroxene/orthopyroxene ratio recorded by Casagli et al. is 0.73), with the remainder olivine. Clinopyroxene and orthopyroxene compositions are chosen from lherzolite samples FE7 and MM4b respectively. Finally, I assume that olivine does not contribute any trace elements to the final melt owing to their typically low concentrations and partition coefficients (De Hoog et al., 2010; Spandler and O'Neill, 2010).

The batch melting equation is used for the melting of lithospheric domains:

$$C_l = \frac{C_l^0}{(1-F)\cdot \bar{D} + F} \tag{4.10}$$

where C_l is the final melt composition, C_l^0 is the initial melt composition, F is the remaining melt fraction, and $\bar{D}$ is the bulk distribution coefficient.

Subsequent crystallisation of olivine from primary melts is calculated using the distribution coefficients as referenced above. The equation used is the fractional crystallisation equation, which is applied to the results of mantle melting:

$$C_l = C_l^0 \cdot F^{(\bar{D}-1)} \tag{4.11}$$

where all variables and coefficients are as described for Equation 4.10.

4.2 Inverse modelling: melt to mantle

The pyMelt forward model allows estimation of T_{crys}, trace element composition, and melt thickness from a given T_p, mantle composition, lithospheric thickness and crystallisation pressure, assuming that the first olivine crystallises at or near the primary basalt liquidus temperature. Through inversion of this forward model I can use observed T_{crys}, REE distributions, and thickness of igneous crust to reconstruct the thermal pathway undertaken by mantle melts and obtain T_p, mantle lithological composition, and the uncertainty in these parameters while accounting for uncertainty in the observed data.

4.2.1 Bayesian inference, nested sampling, and MultiNest

Inverse modelling is performed using the Python 3 wrapper of MultiNest, a Bayesian inference tool which utilises a Monte Carlo Markov Chain nested sampling algorithm (Buchner et al., 2014; Feroz et al., 2019, and references therein). Statistical inference is a means by which data analysis can be used to determine the properties of an underlying probability distribution. This process can be streamlined with the introduction of Bayes' theorem as more information, also termed evidence, becomes available. The probability for the hypothesis, or model, is updated according to Bayes' theorem for model selection (Feroz et al., 2009):

$$P(\Theta \mid \mathbf{D}, H) = \frac{P(\mathbf{D} \mid \Theta, H) P(\Theta \mid H)}{P(\mathbf{D} \mid H)} \tag{4.12}$$

For mantle melting the hypothesis or model (H) describes the proposed behaviour of the system, in this case the behaviour of the melting mantle which is described by the parameterisations of individual melting lithologies and the formulation of Phipps Morgan (2001) incorporated into pyMelt. This model in turn is described by the parameters (Θ) that control the thermal pathway and melt geochemistry: the potential temperature T_p, the pyroxenite and harzburgite composition of the mantle ϕ_{px} and ϕ_{hz} respectively, the pressures at the base of the lithosphere and crust, controls on mantle buoyancy (i.e., the temperature and composition of ambient mantle), and the REE composition of the mantle. The data ($\mathbf{D}$) are then the observed and measured consequences of mantle melting; olivine crystallisation temperatures, REE distributions, and volumes of melt generated.

In Equation 4.12, $P(\Theta \mid H) \equiv \pi(\Theta)$ is the prior probability of the hypothesis before the data are considered. In other words, they describe the probability distributions of the model parameters before they are compared to the observed data. A uniform prior is a probability function in which all possible values are equally likely; this prior is chosen for unconstrained model parameters whose true value is unknown but whose limits can be estimated, and are hence left open (e.g., T_p). Gaussian priors use a normal probability distribution defined by a mean and standard deviation; this prior is selected for those parameters with independent estimates and uncertainties (e.g., LAB depth). In each case the independent estimate is used as the mean, and any inherent uncertainty is the standard deviation. For mantle source composition, the inherent uncertainty was set to ±10% of the mean.

$P(\Theta \mid \mathbf{D}, H) \equiv \mathcal{P}(\Theta)$ is the posterior distribution, i.e. the probability distribution of the parameters given both the data and the hypothesis. $P(\mathbf{D} \mid \Theta, H) \equiv \mathcal{L}(\Theta)$ is the likelihood, a measure of how well the evidence matches with the given hypothesis, i.e., a measure of the misfit of the model to the data. When MultiNest is used with pyMelt, the likelihood is accessed with the following log-likelihood function $\ln(\mathcal{L})$:

$$\ln(\mathcal{L}) = \sum_{x} \ln(\mathcal{L}_x) \tag{4.13}$$

where for each parameter x for the inversion to match, the contribution to the log-likelihood is:

$$\ln(\mathcal{L}_x) = -\frac{1}{2}\ln(2\pi\sigma_x^2) - \frac{(x_{\text{obs}} - x_{\text{calc}})^2}{2\sigma_x^2} \tag{4.14}$$

where x_{obs} is the observed value from the data, σ_x is the standard deviation of x_{obs}, x_{calc} is the corresponding value of the data predicted from the model.

The final term in Equation 4.12 is the denominator $P(\mathbf{D} \mid H) \equiv \mathcal{Z}(\Theta)$, which is the Bayesian evidence. The Bayesian evidence is required to normalise the posterior distribution over all parameters (Feroz et al., 2009):

$$\mathcal{Z} = \int \mathcal{L}(\Theta)\pi(\Theta)d^N\Theta \tag{4.15}$$

where N is the number of parameters (the dimensionality of the parameter space).

To combine parameter estimation with error propagation, the posterior distributions within the region of maximum likelihood are assessed, i.e., solutions where the model best fits the data. This is achieved through the use of Monte Carlo Markov Chain Bayesian inversion, in which all parameters are simultaneously estimated, and new model solutions are chosen depending on the outcome of the previous solution. MultiNest utilises ellipsoidal nested sampling. A fixed number of parameter vectors, termed livepoints, are sorted by their likelihood. A forward model is run with pyMelt using parameters and corresponding prior distributions contained in the livepoints. The result of each forward model is subsequently compared to observed T_{crys}, La/Yb and Dy/Yb ratios, and igneous crustal thickness by the log-likelihood equation (Equations 4.13 and 4.14) to determine the model likelihood. By running a number of forward models (~20,000–30,000) using this method the parameters contained in the livepoints can be clustered into multi-dimensional ellipses, allowing MultiNest to find and follow local maxima of likelihood in the parameter space. The algorithm continues drawing new livepoints until a solution is found with a greater likelihood than the least likely livepoint, which is then removed (Buchner et al., 2014), permitting MultiNest to seek and home in on the most probable regions in the parameter space. Convergence of the marginal likelihood is attained only when sufficient solutions of highest likelihood are available such that the posterior probability distributions for each parameter can be estimated (~8,000–10,000 forward model solutions to the inverse problem). At this point, the algorithm terminates and the region of maximum likelihood is characterised.

Assessing the posterior distributions can provide key information on the model, parameters, and their underlying uncertainties. Although the inversion will favour solutions falling near the medians of the parameter prior estimates, high-likelihood solutions towards the limits of these ranges are also accepted. If posterior distributions correspond well with the prior distributions, then the posteriors are controlled by the priors and uncertainties in the priors can translate into uncertainties in the posteriors. On the other hand, if the posterior distributions do not agree with my initially set priors then the data itself is the primary control on the posterior distributions.

The Python module used to perform an inversion of my olivine-spinel Al-exchange T_{crys} in addition to other constraints is archived in a Zenodo repository which is linked in Appendix A.2.

4.2.2 Prior distributions for Moho and LAB depth

Before inversion, estimates and uncertainties for lithospheric thickness and crystallisation pressure must be established to use as prior distributions.

As discussed in Section 3.1, the presence or absence of a mantle lithosphere is key to understanding melt generation processes beneath the MER. The depth of the LAB controls where melting ceases, and previous petrological models have argued that significant shallow mantle melting does not occur beneath Ethiopia (Rooney et al., 2011; Ferguson et al., 2013b; Armitage et al., 2015). This is because erupted melts have elevated medium REE to heavy REE ratios (e.g., Dy/Yb), consistent with melt production in the presence of the mineral garnet, which is only stable in lherzolite at depths $\gtrsim$85 km. The retention of this garnet-field melting signature suggests that low pressure melting is likely impeded by the presence of a >50 km thick lithospheric lid (e.g., Armitage et al., 2015). These petrological inferences on melting depths are generally consistent with Rayleigh wave tomography, which highlights a low shear velocity region of melt generation at >75 km (Gallacher et al., 2016). Given these observations LAB depths of 60±20 km for both the MER and Afar would be expected, which are used as prior distributions (Table 4.3).

Crystallisation is likely to commence at the base of the crust where ascending melts initially pool (Rooney et al., 2005; Desissa et al., 2013) before continuing to lower pressures via crustal plumbing systems (<0.5 GPa; Rooney et al., 2005; Field et al., 2013; Iddon and Edmonds, 2020). Although some crystallisation is expected to occur at lithospheric mantle pressures (e.g., Rooney et al., 2005), the base of the crust provides a reasonable estimate for the earliest onset of crystallisation. Ethiopian crustal thickness is well characterised though seismic imaging (e.g., Maguire et al., 2006; Hammond et al., 2011; Lavayssière et al., 2018) and recent MER and Afar crustal thickness estimates of 28±3 km and 23±2 km respectively are used as prior distributions for my inversions (Table 4.3).

4.2.3 Melting geometry constraints and igneous thickness

The geometry of the melting region influences both the composition and total quantity of melts produced during mantle upwelling (e.g., Plank and Langmuir, 1992). Melting of the asthenospheric mantle beneath Ethiopia during rifting may be driven by passive decompression beneath a thinning lithosphere, similar but not identical to a mid-ocean ridge environment. In this geometry, the mantle undergoes corner flow within a triangular melting region much like a mid-ocean ridge, but positioned beneath a thick, non-melting lithosphere. By integrating the melt fraction over this region, I obtain a melt thickness (t_m), which is extracted from the top of the melting region and compared to observed crustal igneous thicknesses. To achieve this, a modified crustal thickness equation of White et al. (1992) is used:

$$t_m = \frac{1}{\rho g} \int_{P_1}^{P_2} \frac{F}{1-F} \, dP \tag{4.16}$$

where P_1 and P_2 are the pressures at which melting begin and cease respectively, F is melt fraction as a function of pressure, ρ is the density of the mantle, and g is gravity. While the triangular geometry that arises from passively driven upwelling probably does not capture the true complexity of sub-rift melting, it provides a means to test how changing mantle temperature and lithospheric thickness affects melt production.

The passive geometry does not include a weighting factor for active upwelling. Active upwelling of the mantle will flux more material through the base of the melting region, promoting garnet-field melting and therefore potentially increasing the concentration of light REEs relative to heavy REEs (e.g. Maclennan et al., 2001). The effects of active upwelling are also tested in my inversions by including an exponentially decaying weighting function $w(P)$ in Equation 4.16 as described in Matthews et al. (2022):

$$t_m = \frac{1}{\rho g} \int_{P_1}^{P_2} (1 + w(P)) \frac{F}{1-F} \, dP \tag{4.17}$$

where:

$$w(P) = \mu \exp\left(\frac{1}{\lambda}\frac{P_{max} - P}{P_{max} - P_{min}}\right) \tag{4.18}$$

and μ is the amplitude of the decay function, λ is the wavelength of the decay function, and P_{max} and P_{min} are the maximum and minimum pressures of the melting column. This function effectively describes a pulse of fluxed material at the base of the melting region, which exponentially decays to the passive case with decreasing pressure.

Owing to the large scale of the seismic velocity anomaly in the sub-rift mantle (Hammond et al., 2013) I believe that modelling melting with an alternative plume conduit geometry is unsuitable for this study. I also require that the melting mantle must be buoyant with respect to ambient mantle otherwise mantle upwelling will not be possible (e.g., Shorttle et al., 2014), which effectively limits the proportion of pyroxenite in the permitted solutions.

Total crustal thickness in the MER and southern Afar appears to be largely maintained until the final stages of continental rifting by magmatic intrusion (Bastow and Keir, 2011). Seismic studies of the rift-axis crust illustrate that the thickness of the upper crust is predominantly affected by rift-related thinning while the lower crust remains thick owing to intrusion (Maguire et al., 2006; Hammond et al., 2011). By comparing pre- and post-rift upper and lower crust at Dabbahu, Armitage et al. (2015) inferred that the Afar crust comprises 11–15 km of magmatic material. Adopting their method, I can estimate the thickness of melt (t_m) in the MER. To do this I use thicknesses of original, unstretched crust inferred from the Ethiopian plateau of 21 km for the upper crust and 23 km for the lower crust (Maguire et al., 2006) and upper and lower crustal thicknesses within the MER near Boku that range from 14–17 and 16–20 km respectively (Maguire et al., 2006). This gives a stretch factor of 1.2–1.5 and suggests that the lower crust comprises $\sim$3–6 km of igneous material. I therefore choose t_m of 4.5±1.5 km and 13±2 km for the MER and Afar respectively (Table 4.3).

4.2.4 Rare-earth element ratio constraints

My inversions can be further constrained by comparing REE concentrations from pyMelt to those observed in the Boku and Dabbahu basalts (Table 4.3). The La/Yb and Dy/Yb ratios of the lavas are matched to those generated by my model. Ratios are used as they are less affected by crystal fractionation and accumulation than absolute

Table 4.3: Table summarising prior distributions and data constraints on my inversions. References as follows: 1. Ferguson et al. (2013b), 2. Armitage et al. (2015), 3. Lavayssière et al. (2018), 4. McDonough and Sun (1995), 5. Workman and Hart (2005), 6. Gale et al. (2013), 7. Tadesse et al. (2019). The composition KG1 refers to 50:50 DMM:average MORB.

Prior distributions	Boku Volcanic Complex	Dabbahu Rift	References
LAB depth (km)	60±20	60±20	1, 2
Moho depth (km)	28±3	23±2	3
Lherzolite	PM±10%	PM±10%	4
Pyroxenite	KG1±10%	KG1±10%	5, 6

Data constraints			
$T_{crys}^{primary}$ (°C)	1426±26	variable (Chapter 3)	This study
t_m (km)	4.5±1.5	13±2	This study; 2
La/Yb	9.70±0.85	2.17±0.07	1, 7
Dy/Yb	7.34±1.93	2.21±0.13	1, 7

concentrations.

REE compositions must be established for the two melting lithologies in my model. The primary prior distributions for the lherzolite REE concentrations are defined as normal distributions centred on the concentrations of La, Dy, and Yb in the primitive mantle (PM; McDonough and Sun, 1995), with a standard deviation of 10% of their concentration as reported. I additionally consider the consequences of using lower concentrations for lherzolite more typical of the depleted mantle (DMM), which are found to yield similar results to PM-composition lherzolite. A 50:50 mixture of DMM (Workman and Hart, 2005) and average MORB (Gale et al., 2013) is used to approximate the REE composition of a KG1-like mixed-lithology pyroxenite. Like the lherzolite I allow KG1-composition pyroxenite to vary according to a normal distribution with a standard deviation of 10% centred on the reported La, Dy, and Yb concentration.

Post-inversion, I also allow for the possible addition of small-fraction melts from destabilisation of metasomatised domains in the Ethiopian lithospheric mantle (e.g., Casagli et al., 2017; Rooney et al., 2017), which can occur as ascending melts interact with the lithosphere (e.g., Rooney et al., 2017) or via lithospheric drip (Furman et al., 2016). I can also modify the absolute concentrations of REEs in the final basalt to account for fractional crystallisation of olivine in the lithosphere. The calculations underlying both processes are described in full in Section 4.1.2.

4.3 Inversion results

My inversion solutions are presented as posterior probability distributions; the complete collection of parameters describing these posterior distributions are presented in Appendix A.2. In the inversion figures displayed in this section, the left subfigures illustrate sections through the crust and uppermost mantle, and the right subfigures present T_p and mantle compositions. REE distributions are also illustrated in these figures (concentrations are shown despite inverting for ratios to illustrate the fitting between modelled and observed basalts). The absolute concentrations of model REE distributions can differ from those observed in the basalts, which can be attributed to differences in true and modelled mantle source compositions, the absence of melts not captured in my inversion model, fractional crystallisation, or a combination of these, which are considered below. Selecting a mantle with lower concentrations of REEs (but the same La/Yb and Dy/Yb ratios) will result in a REE trend that falls beneath those that are modelled.

The REE distributions resulting from my inversions are obtained by running forward models of the posterior distribution medians, which are overlain on top of sampled forward models deemed high-likelihood by the inversion algorithm for comparison. These median distributions do not reflect true solutions generated by the MultiNest inversion or take into account co-variation between different parameters; each solution will have its own combination of parameter values. Forward model REE concentrations do not affect the calculations but are the results of them, and are ultimately controlled by the La/Yb and Dy/Yb constraints in the inversion. Also shown in the inversion figures are the REE composition of the magma following the addition of 5% of a 1% batch lithospheric melt, before and after correction for fractional crystallisation. The addition of lithospheric melt primarily alters the concentrations of lighter REEs and can be evaluated via the effect on the fit to the observed La/Yb. As discussed below, this improves the fit between the observed and modelled magma compositions, however given the uncertainties in, and trade-offs between, the mineralogy and composition of lithospheric mantle, melt fraction, and degree of melt addition, it is not possible using this method to uniquely constrain the extent of lithospheric melting and/or contamination of the mantle-derived magmas.

4.3.1 PM-composition mantle lherzolite

Inversions performed with PM composition lherzolite in a tri-lithology mantle also comprising KG1 composition pyroxenite and non-melting harzburgite are considered in this section.

4.3.1.1 Boku Volcanic Complex

The results of the joint T_{crys}-REE inversion for Boku are shown in Figure 4.1, with $T_{crys}^{primary}$ of 1426±26 °C representing the mean T_{crys} of the $Fo_{83.5-84.5}$ cluster projected to Fo_{91} (Section 3.4.2.1). The inversion returns a median T_p of 1500^{+32}_{-42} °C for a tri-lithology mantle. To match both the t_m constraint and REE concentration ratios the inversion favours a LAB depth of ∼90 km, which falls outside the uncertainty of my prior estimate of 60±20 km, suggesting that the majority of forward models trialled with this range of LAB depth fail to match the observed data. The median mantle resulting from this inversion is mostly PM-composition lherzolite (∼80%), with the remainder predominantly harzburgite. The inversion results share La/Yb and Dy/Yb ratios within uncertainty of observed Boku basalts. The effect of introducing small-fraction lithospheric melts to my inversion result is therefore minor, but does improve the fit to the observed La/Yb. Fractionation of olivine from the primary magma sufficiently concentrates REEs in the residual melt to match observed basalts (Figure 4.1).

4.3.1.2 Dabbahu Rift

Inversion posterior distributions for the Dabbahu Rift (Figure 4.3) are derived from the three possible $T_{crys}^{primary}$ values described in Section 3.4.2.2. All Dabbahu inversions return T_p in excess of MORB (1508^{+37}_{-33} °C; 1565^{+49}_{-45} °C; 1658^{+41}_{-45} °C), in concordance with an elevated Ethiopian mantle T_p. However, the median thickness of the lithosphere in all three models is variable, with the lowest $T_{crys}^{primary}$ reproducible from a lithosphere <50 km thick (Figures 4.3A, C, E). Continued melting to shallower depths in this model (Figures 4.3A and B) is required to produce sufficient volumes of magma to match the t_m constraint for Afar (13±2 km) at lower T_p, whereas the other two models produce these melt volumes with significantly elevated T_p and a comparatively thicker lithosphere (Figures 4.3C-F). These three model inversions illustrate a notable trade-off between T_p and LAB depth. This arises because the La/Yb constraint cannot be matched by the inversion and consequently the light REE portion of the modelled distribution deviates significantly from the observed

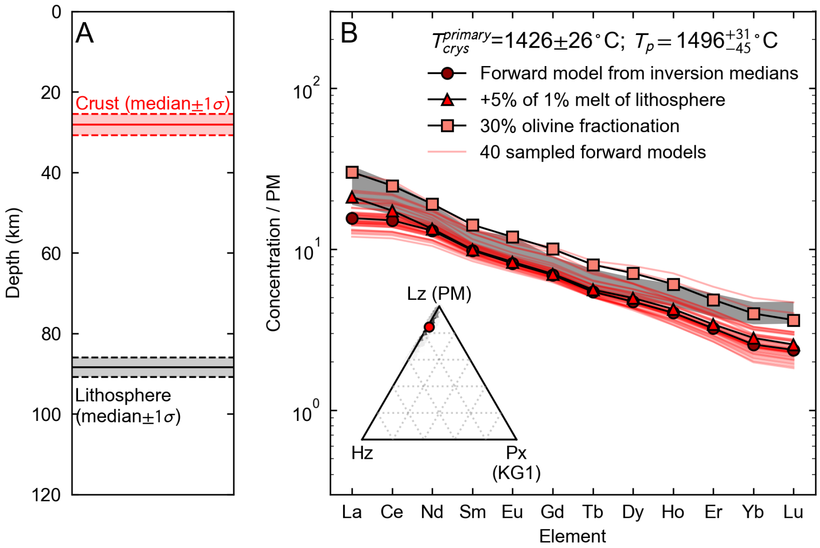

Figure 4.1: Posterior distributions for mantle T_p, composition, crystallisation depth and lithospheric thickness at the Boku Volcanic Complex, Main Ethiopian Rift, using a PM lherzolite. The initial olivine T_{crys} of the posteriors is the mean T_{crys} of $\mathrm{Fo}_{83.5-84.5}$ olivines projected to T_{crys} at Fo_{91}. Subfigure A is a vertical section through the uppermost rift crust and mantle showing the most likely depths of the Moho and the lithosphere-asthenosphere boundary (LAB) as determined from the inversion. The base of the crust and lithosphere are shown as red and black lines with 1σ shaded area respectively. Subfigure B shows the REE distribution of a pyMelt forward model run using the medians of the inversion posterior distributions as starting parameters (circles), i.e. T_p (given in the subfigure legend), mantle harzburgite and pyroxenite, lithospheric thickness, and crystallisation pressure. This median forward model is overlain on 40 sampled high-likelihood forward models. The rare-earth element distribution marked with triangles is the composition of the melt upon addition of 5% small-fraction lithospheric melt, and the squares mark the same distribution upon fractionation of 30% olivine. Literature data showing basalt rare-earth element concentration ranges from Boku are illustrated as the grey area (Tadesse et al., 2019). All distributions are normalised to PM (McDonough and Sun, 1995). The inset ternary plot shows the posterior distributions of acceptable mantle compositions in a space defined by non-melting harzburgite (Hz), PM-composition lherzolite (Lz), and KG1-composition (50:50 DMM:average MORB) pyroxenite (Px). The coloured dot in the inset ternary shows the median mantle composition from which the REE distribution is derived.

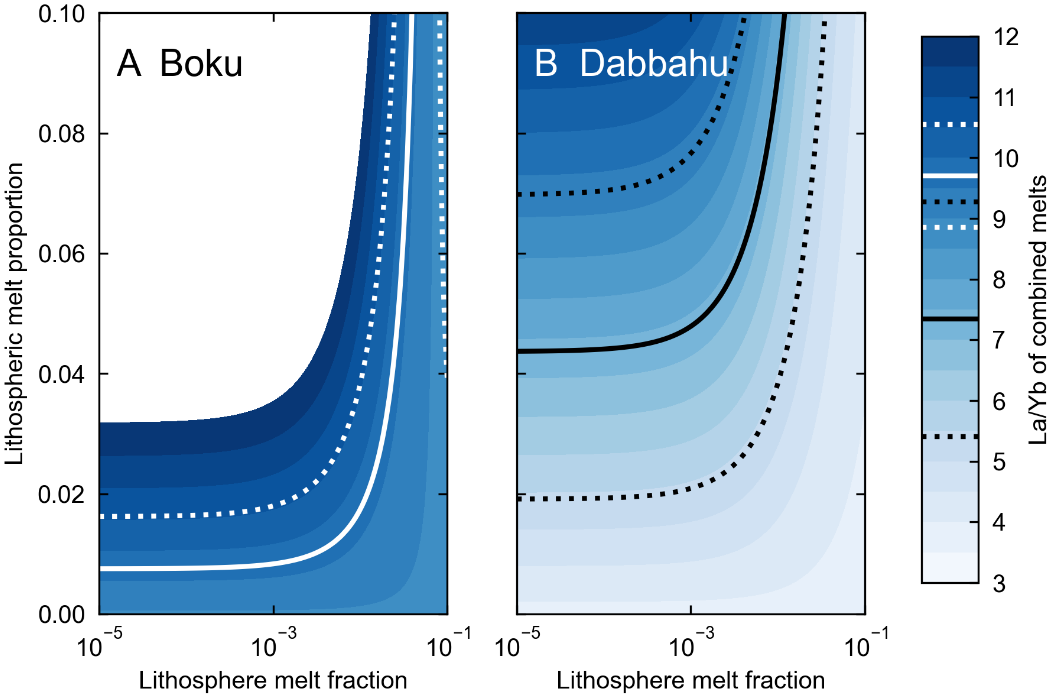

Figure 4.2: Figure illustrating the La/Yb of combined melts with changing lithospheric melt fraction and proportion of lithospheric melts mixed into asthenospheric melts for A. Boku, and B. Dabbahu (model with $T_{crys}^{primary}$ of 1339±22 °C). The mean and ± 1 standard deviation of Boku (Tadesse et al., 2019) and Dabbahu (Ferguson et al., 2013b) basalt La/Yb are shown as the white and black solid and dashed lines respectively.

values (Figures 4.3B, D and F). Extensive melting is required to fit t_m at Afar, however this has the effect of diluting the REEs as melt generation progresses. Dy/Yb is mostly well matched by these inversions, and all three models retain the garnet signature observed in medium-heavy REEs.

The addition of a minor volume of lithospheric melt significantly improves the fit to the La/Yb values. Figure 4.2 demonstrates that a trade-off exists between the degree of lithospheric melting and the amount of lithospheric melt added to asthenospheric melts that can ultimately match observed Dabbahu basalts; this trade-off exists on top of the many trade-offs between lithospheric mantle mineralogy and composition that are difficult to quantify. I therefore select a batch melt fraction of 1%, of which a proportion of 5% is mixed into the asthenospheric melts resulting from my inversions. This value is within the permitted 1σ envelope illustrated for Dabbahu basalts, and falls just outside the same envelope for Boku (Figure 4.2).

The inversion with the highest starting $T_{crys}^{primary}$ of 1590±33 °C returns a T_p which is ∼300 °C hotter than ambient mantle and over 100 °C hotter than the other Dabbahu inversions (Figures 4.3E and F). In contrast to the cooler models, t_m is matched by melting a highly harzburgitic mantle, which promotes substantial melting of the lherzolitic and pyroxenitic components. Of the three inversions, the REE distribution predicted from the medians of this model provides the worst fit to the observed trends (Figure 4.3F). Furthermore, the best-fitting lithospheric thickness is ∼90 km, thicker even than the lithosphere underlying the Ethiopian and Somalian plateaux (Rychert et al., 2012; Lavayssière et al., 2018) which is highly unlikely in this mature rift system. I therefore conclude that this higher $T_{crys}^{primary}$ value is unsuitable for Dabbahu Rift magmas and the results of this inversion are not included in the following discussion.

4.3.2 DMM-composition mantle lherzolite

The chosen lherzolite REE composition in the previous section is the primitive mantle (PM) of McDonough and Sun (1995). In this section I discuss the consequences of using a more depleted mantle lherzolite composition than PM. This depleted composition is the depleted MORB mantle (DMM) of Workman and Hart (2005), which is especially depleted in light REEs relative to PM. I choose to test this composition as radiogenic isotopes of MER and Afar basalts fall between DMM and PM (e.g., Furman, 2007; Ferguson et al., 2013b), although owing to the possible presence of pyroxenite isotope contributions from distinct lithologies cannot be inferred. I can, however, consider the effects of changing the lherzolite composition.

A series of inversions are run in which the DMM composition of lherzolite is permitted to vary according to a normal distribution centred on the DMM values of La, Dy, and Yb, with a standard deviation of 10% of this chosen REE value.

Figure 4.4 illustrates the posterior results of inversions using a DMM composition lherzolite. In all cases the median T_p are similar to those returned from the PM inversions. Lithospheric thicknesses are lower than, but within mutual uncertainty of, those of the PM lherzolite inversions; each inversion requires a greater degree of melting to satisfy both the REE constraints and melt thicknesses. Mantle lithology differs between the DMM and PM models, which also has an effect on the REE distributions and lithospheric thicknesses; a greater amount of REEs must be sourced from the more productive pyroxenite lithology, which in turn affects the contributions from the melting lherzolite and harzburgite. Forward models for the Boku locality return absolute REE concentrations simiar to the observed

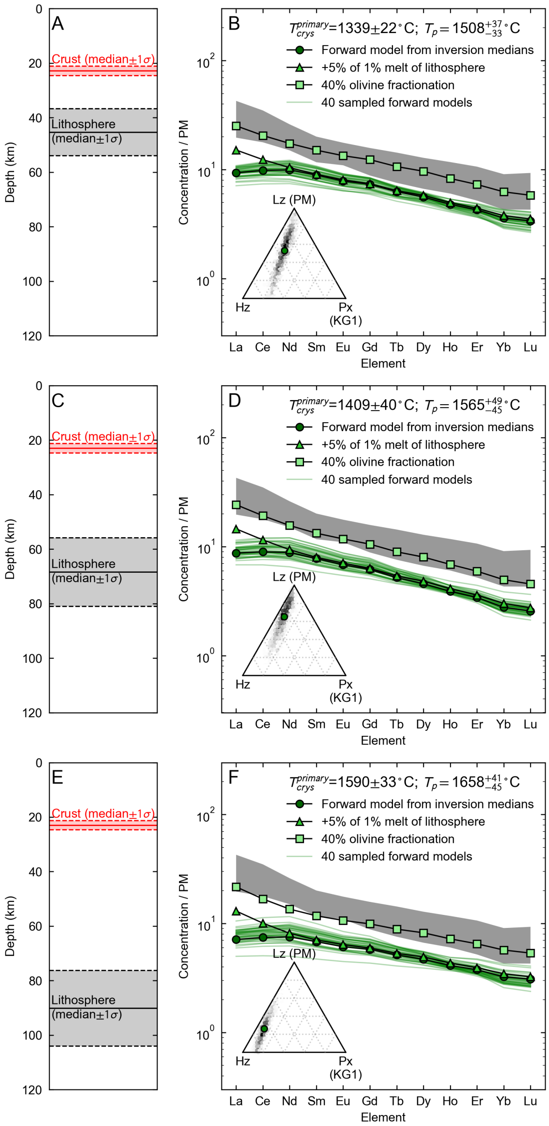

Figure 4.3: Posterior distributions for mantle T_p, composition, crystallisation depth and lithospheric thickness at the Dabbahu Rift, Afar, using a PM lherzolite. Subfigures A and B show the results of inverting from the mean of the highest olivine T_{crys} (1339±22 °C), subfigures C and D the results from projecting the T_{crys} of the highest Fo olivines to $T_{crys}^{primary}$ at Fo_{91} (1409±40 °C), subfigures E and F the results from projecting the mean T_{crys} of the highest Fo cluster (Fo_{82}) to $T_{crys}^{primary}$ at Fo_{91} (1590±33 °C). Figure contents are as described in Figure 4.1. Literature data showing basalt rare-earth element concentrations are illustrated as the grey areas in subfigures B, D and F (Ferguson et al., 2013b).

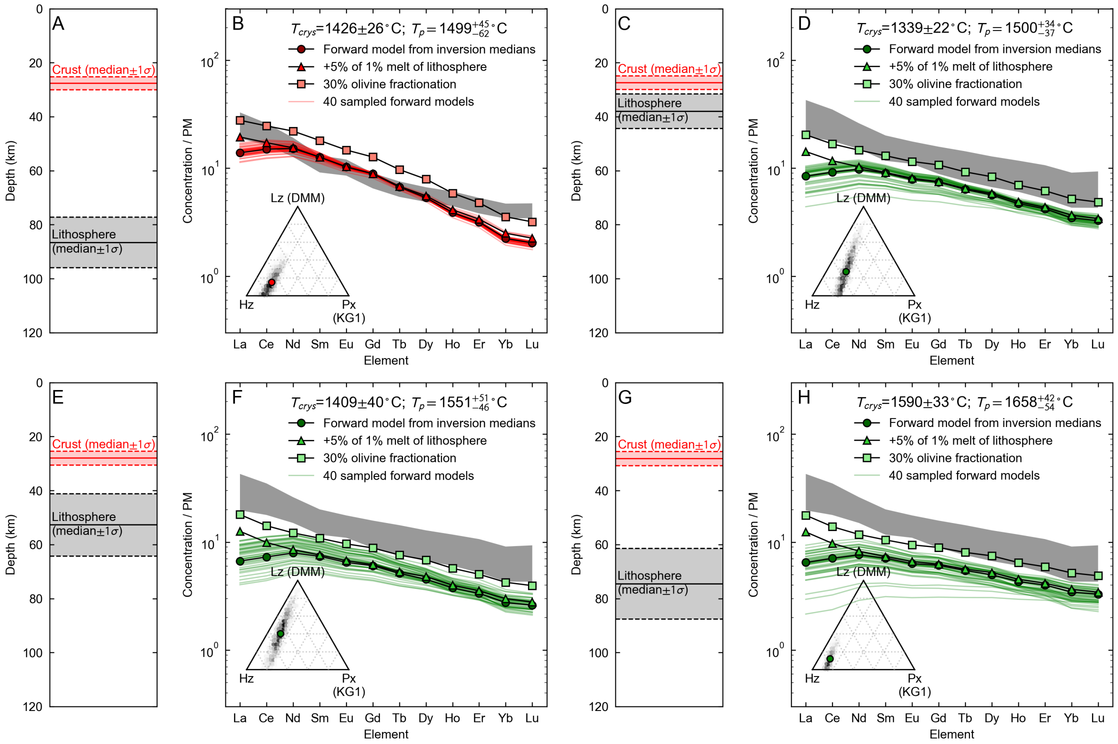

Figure 4.4: Posterior distributions for mantle T_p, composition, crystallisation depth and lithospheric thickness of the Boku Volcanic Complex, MER and Dabbahu Rift, Afar, using a DMM lherzolite mantle. Subfigures A and B show the results of inverting from the projected Boku T_{crys} (1426±26 °C), subfigures C and D the mean of the highest olivine T_{crys} (1339±22 °C), subfigures E and F the results from projecting the T_{crys} of the highest Fo olivines to Fo_{91} (1409±40 °C), subfigures G and H the results from projecting the mean T_{crys} of the highest Fo cluster to Fo_{91} (1590±33 °C). Figure contents are as described in Figure 4.1. Literature data showing basalt rare-earth element concentrations are illustrated as the grey areas in subfigures B, D, F, and H (Ferguson et al., 2013b; Tadesse et al., 2019).

basalts but with a stronger garnet signature, which in this case is inherited by melting of a highly enriched mantle as opposed to the more refractory PM lherzolitic mantle (Figure 4.4B). REEs are instead sourced from fusible pyroxenite. The overarching REE distribution is of the same order of magnitude as the observed data, but has significant differences in the medium and heaviest REEs. In all Afar cases, forward models run with the inversion result medians as parameters return absolute REE concentrations nearly identical to the PM models (Figures 4.4D, F and H). Some median forward models can obtain the observed basalt REE concentrations with fractionation of olivine (e.g., Figure 4.4D). However for most cases the DMM inversion medians cannot sufficiently match the observed absolute basalt trend, even with a realistic degree of olivine fractionation (e.g., Figures 4.4F and H). I therefore believe that PM lherzolite is an adequate composition to use for inversions as

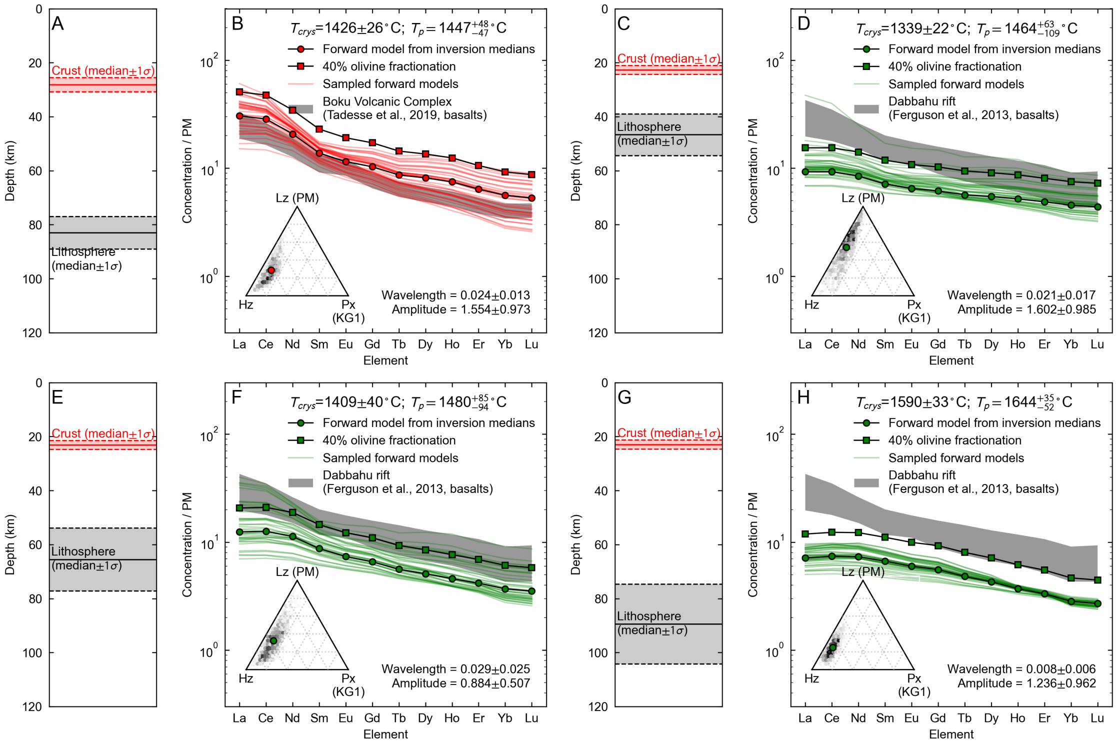

Figure 4.5: Posterior distributions for mantle T_p, composition, crystallisation depth and lithospheric thickness of the Boku Volcanic Complex, MER and Dabbahu Rift, Afar, using an exponentially decaying active upwelling weighting function. Subfigures A and B show the results of inverting from the projected Boku T_{crys} (1426±26 °C), subfigures C and D the mean of the highest olivine T_{crys} (1339±22 °C), subfigures E and F the results from projecting the T_{crys} of the highest Fo olivines to Fo_{91} (1409±40 °C), subfigures G and H the results from projecting the mean T_{crys} of the highest Fo cluster to Fo_{91} (1590±33 °C). Figure contents are as described in Figure 4.1. Literature data showing basalt rare-earth element concentrations are illustrated as the grey areas in subfigures B, D, F, and H (Ferguson et al., 2013b; Tadesse et al., 2019).

PM lherzolite median models can both match REE ratios and fall near the absolute REE concentrations of basalts, although I do acknowledge that a trade-off is possible between mantle depletion in all REEs relative to PM and the degree of fractionation from the resultant primary mantle melt.

4.3.3 Passive vs active upwelling

As discussed in Section 4.2.3, I make use of a deep triangular melting geometry to calculate melt thickness constraints and REE concentrations. While in Sections 4.3.1.1 and 4.3.2 a passive regime is utilised (via Equation 4.16), in this section I perform additional inversions using Equations 4.17 and 4.18, with uniform prior distributions for μ and λ of 0–1 and 0–4 respectively.

Inversions run with the active upwelling weighting function are illustrated in Figure 4.5. The active upwelling Boku inversion (Figures 4.5A and B) return results for lithospheric thickness, T_p and mantle composition almost identical to that of the passive model. The best-fitting wavelength of the decay function is near zero; the model favoured by the inversion is therefore that of the passive inversion. There is greater difference in the active upwelling inversions for Dabbahu (Figures 4.5 C-H), as these inversions favour a greater decay wavelength than that of Boku. While lithospheric thickness remains consistent between the two models, there are differences in mantle lithological composition, which trades off with the two coefficients of the upwelling function. Furthermore, the temperature of the mantle is cooler in all three cases, as the pulse of melting at the base of the melting column can contribute both trace elements and additional melt volumes without an increase in T_p. Despite these differences, the wavelength of exponential decay continues to be very small, suggesting that it only has a minor effect limited to the base of the melting column. Finally, I note that there is a trade-off between the amplitude and wavelength of the decay function, which adds an additional layer of uncertainty when determining the active upwelling behaviour of the mantle. Taking all of these factors into account, I conclude that the passive upwelling models are within mutual uncertainty of these active upwelling models owing to the relatively low weighting factors selected by the inversions. I therefore believe that the passive upwelling models selected in Section 4.3.1.1 are appropriate for discussion without further consideration of active upwelling. Owing to the broad nature of the sub-Afar thermal anomaly (e.g., Bastow et al., 2008; Hammond et al., 2013) relative to narrow anomalies in the mantle underlying Hawaii, the conduit plume geometry of Matthews et al. (2021) is not considered.

4.3.4 Inversions without T_{crys}: are selected $T_{crys}^{primary}$ appropriate?

In this section the starting $T_{crys}^{primary}$ values for the inversion are considered again. While the basalts selected as possible starting materials for both Boku and Dabbahu are only saturated in olivine as predicted by Petrolog (Figure 3.6), and remain saturated only in olivine by the time erupted basalt compositions are achieved, the possibility reamins that the Petrolog input parameters are different to those modelled above. I cannot therefore rule out the possibility that the choices of $T_{crys}^{primary}$ are appropriate.

I consider a top-down approach by running inversions in the absence of the T_{crys} constraint to estimate the range of crystallisation temperatures expected if only the other

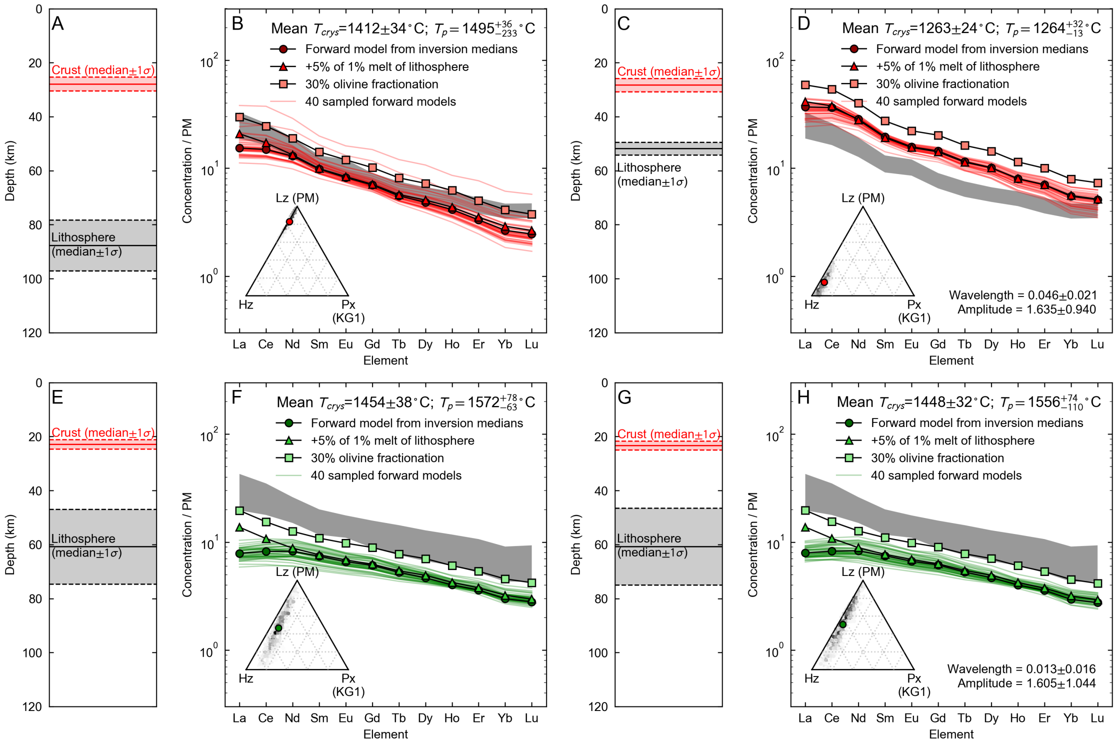

Figure 4.6: Posterior distributions for Main Ethiopian Rift and Afar inversions without a $T_{crys}^{primary}$ constraint. Inversions are passive upwelling (A and B) and active upwelling (C and D) at Boku, and passive upwelling (E and F) and active upwelling (G and H) at Dabbahu. The $T_{crys}^{primary}$ given in each figure is the mean and standard deviation of the $T_{crys}^{primary}$ of the 40 sampled forward models depicted in each subfigure. Figure contents are as described in Figure 4.1

constraints (t_m and REE ratios) are considered. In this way my projected $T_{crys}^{primary}$ can be compared to the maximum $T_{crys}^{primary}$ that inversion forward models may produce. The results of the inversions are shown in Figure 4.6.

Boku inversions without a $T_{crys}^{primary}$ constraint are shown in Figures 4.6A-D. The passive upwelling case is shown in Figures 4.6A and B, and shares a similar lithospheric thickness and mantle potential temperature as Figure 4.1. Mean $T_{crys}^{primary}$ of 40 sampled forward models (1412±34 °C) is similar to the petrologically estimated $T_{crys}^{primary}$ of 1426±26 °C (Section 3.4.2.1), and $T_{crys}^{primary}$ of these models range from 1250 °C to 1433 °C. As the maximum model $T_{crys}^{primary}$ and the mean $T_{crys}^{primary}$ are close in value, the majority of the sampled forward models therefore return $T_{crys}^{primary}$ similar to the extrapolated petrological $T_{crys}^{primary}$, suggesting that it is a suitable value for maximum and possibly true $T_{crys}^{primary}$. The active upwelling model, shown in Figures 4.6C and D, favours a thin lithosphere and a very cool mantle. All melt is produced by a short melting column near the LAB fuelled by a pulse of upwelling at the base of the column, which produces melts that crystallise at similar temperatures to the initially recorded T_{crys} of 1175±22 °C. While an argument could be made for an anomalously low T_p using this figure, this is unlikely to be the case for several reasons: 1. a cool mantle is at odds with observations of slow seismic velocities under the Ethiopian Rift (Bastow et al., 2005), 2. the resultant trace element distributions fall above the observed REE distribution and cannot match erupted lavas through fractionation, and 3. the projected mantle lithological composition is highly harzburgitic. It is therefore unlikely that the $T_{crys}^{primary}$ and active upwelling case shown here are physically correct.

Dabbahu inversions for both passive and active upwelling mantles are presented in Figures 4.6E-H, and agree considerably despite the exponential weighting imposed in the latter case. $T_{crys}^{primary}$ of the 40 sampled passive forward models range from 1392–1546 °C with a mean of 1454±39 °C, and are 1388–1526 °C and 1448±32 °C respectively for the 40 sampled active forward models. These ranges of $T_{crys}^{primary}$ is covered by my three selections for $T_{crys}^{primary}$ in Section 3.4.2.2, with means within uncertainty of $T_{crys}^{primary}$ from projecting from the highest Fo olivines (1409±40 °C). I therefore believe that from these inversions and sampled forward models that my choices in $T_{crys}^{primary}$ are justified as constraints for inversion.

4.4 Discussion

The Ethiopian mantle T_p of 1500–1550 °C suggested from the majority of inversions are in good concordance with previous petrological and geophysical estimates (Rooney et al., 2012c; Ferguson et al., 2013b; Armitage et al., 2015). These inversions, given the constraints placed upon them, can replicate observed T_{crys}, t_m, and medium-heavy REE distributions within this T_p range (Figures 4.1 and 4.3). Mantle T_p also appears to be consistent within uncertainty throughout the overall Ethiopian rifting region, as the calculated T_p for the MER (1496^{+31}_{-45} °C) and Afar (1508^{+37}_{-33} °C and 1565^{+49}_{-45} °C) cannot be differentiated with confidence despite the differences in their model priors. The same conclusion is reached when considering alternative mantle compositions and active mantle upwelling (Figure 4.4 and 4.5). Variability in magma generation between the northern MER and central Afar is therefore likely to be driven solely by the depth of the LAB and minor variations in source lithology.

The light REE data from Dabbahu, and to a lesser extent Boku, can be more closely

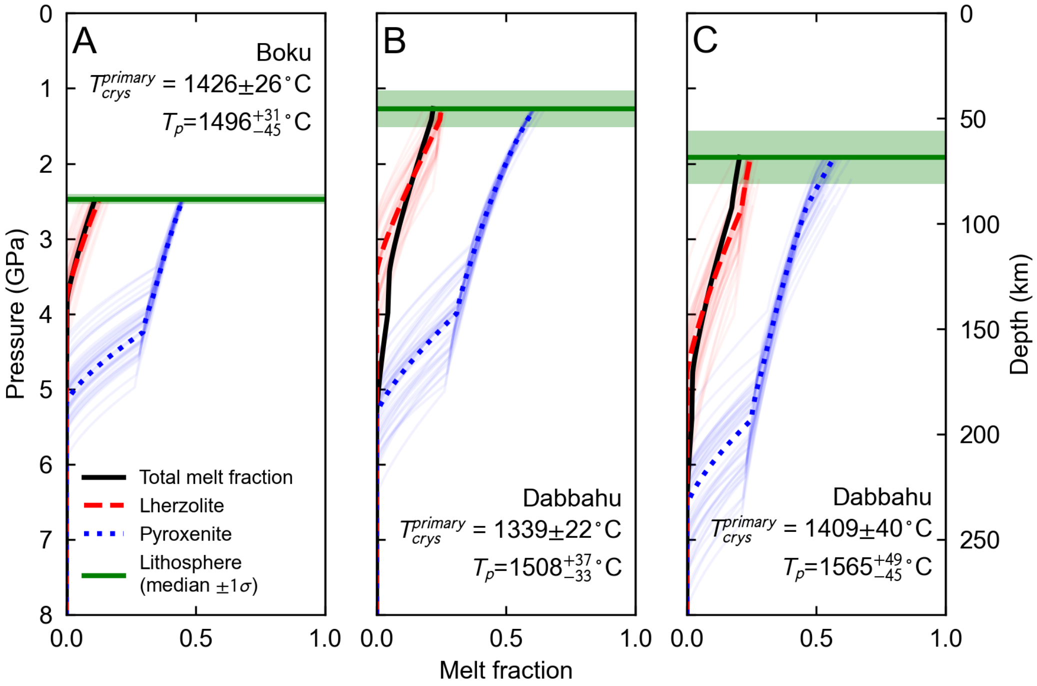

Figure 4.7: Melt fraction as a function of pressure for Boku (A) and Dabbahu Rift (B and C), calculated using PM lherzolite forward models with parameters dictated by inversion posterior distribution medians. The Afar forward models use the inversion results for the primary crystallisation temperature of 1339±22 °C (B) and 1409±40 °C (C). Melt fractions are shown for lherzolite (dashed red line), pyroxenite (dotted blue line), and the total mantle (solid black line). The solid green line and green shaded area show the position of the posterior median lithosphere with 1σ uncertainty. The faded red and blue lines represent the lherzolite and pyroxenite melting curves of 40 sampled forward models respectively.

matched with a minor addition of small-fraction lithospheric melts to the modelled mantle-derived magmas (Figure 4.3 and 4.2). This occurs despite including La/Yb as a constraint, demonstrating that the inversion model parameters cannot combine to closely match all constraints. The involvement of lithospheric materials in the petrogenesis of these magmas is supported by observed deficits in K versus other geochemically similar elements in magmas from the MER (Furman, 2007; Tadesse et al., 2019) and Afar (Ferguson et al., 2013b), which can arise due to interactions with K-bearing phases in metasomatised lithospheric mantle (Class and Goldstein, 1997). A detailed investigation of this process is beyond the scope of this study, but could be investigated in future work.

My models predict that the lithological composition of the mantle under the MER is primarily a mixture of lherzolite and non-melting harzburgite (Figure 4.1B), the precise proportions of which depend on the fusibility and REE composition of the melting lithologies selected for the inversions. A lower harzburgite proportion would be favoured if mantle lherzolite is more depleted in light REEs than PM, as this could allow lower degrees of lherzolite or pyroxenite melting to match observed REE distributions owing to a reduced thermal buffering effect (see Section 4.3.2). Likewise, a high harzburgite proportion could result from compensating for the productivity of the chosen lherzolite and pyroxenite melting models (Matthews et al., 2016). In reality, trace element enrichment does not necessarily correlate with lithology melt productivity, as assumed in this model. In the MER, a more fusible mantle component is considered unnecessary to match REE ratios and t_m (Figure 4.1B), however, such a component is required in Afar, both to introduce trace element enrichment to the melting mantle and to produce a garnet signature at depth. As a further consequence, the permitted compositional range for Afar inversions favour a mantle which is much less refractory than the MER. These mantle composition solutions form linear trends in compositional ternary space (Figure 4.3B and D), which is constrained by t_m. Compositional enrichment in the mantle under Afar compared to the MER could be linked to the positioning of the Afar plume, the centre of which is considered closer to the Dabbahu Rift than Boku based on regional variations in basalt radiogenic isotope ratios (Rooney et al., 2012a).

There is a notable contrast in the predicted thickness of the lithosphere between the two localities. My MER inversion favours a LAB depth of ~90 km (Figure 4.1A), in general agreement with geophysical observations that mantle melting here occurs at depths >75 km (e.g., Gallacher et al., 2016). As the Afar inversions cannot match the La/Yb constraint without the addition of lithospheric melts, a notable trade-off exists between LAB depth and T_p. Afar LAB depths are predicted to be lower than the MER (50–70 km; Figures 4.3A, C, E). For the lowest $T_{crys}^{primary}$ inversion this is notably less than that estimated by Ferguson et al. (2013b) (>80 km), who used a single lithology peridotite melting model to match observed REEs. While both my results and those of Ferguson et al. (2013b) argue for a deep onset of melting beneath Afar due to an elevated mantle T_p, the continuation of melting to shallower depths beneath a thinner lithospheric lid predicted by my model is necessary to generate enough melt to match the central Afar t_m of 13±2 km, which significantly exceeds that of the MER (4.5±1.5 km). This is required even with the inclusion of a more fusible and enriched component in the mantle source, which begins melting deeper than the lherzolitic component (5–6 GPa; Figure 4.7). I note that this maximum pressure of melting is also broadly consistent with Rayleigh-wave tomography (Gallacher et al., 2016). The lherzolite component begins melting at a lower pressure (3–4 GPa; Figure 4.7), by which time nearly half of the available pyroxenite has melted despite the total mantle melt fraction being only ∼3% or less (Figure 4.7). In this way, the constraints on my inversion (T_{crys}, La/Yb, Dy/Yb, and t_m) can be matched by procuring the REE garnet signature at depth through extensive melting of a fusible and enriched lithology in an elevated temperature mantle before dilution of the garnet melting signature, and increasing melt volumes, via shallower melting of less productive lithologies. Further enrichment in light REEs can subsequently be achieved through minor lithospheric melting. <70 km LAB depths are not necessarily unexpected for Afar as geophysical models have returned similar values (Armitage et al., 2015). The difference in lithospheric thickness between the MER and central Afar is consistent with the latter being at a more-evolved stage of rifting. However, as proposed by Bastow and Keir (2011) and Ferguson et al., 2013b, significant lithospheric thinning still appears to be necessary at the Dabbahu Rift before plate rupture and the onset of true oceanic spreading.

Figure 4.8 compares the T_p values from my inversions to T_p from other locations that have been determined using the same approach and melting models (Matthews et al., 2021). The median T_p of the Ethiopian mantle is hotter than the Siqueiros MORB-source mantle (1364±23 °C), and overlaps with the T_p posterior distributions of other plume-influenced settings such as Iceland and Hawaii. The Ethiopian mantle under Afar is also expected to have a greater proportion of a more enriched melting lithological component than the MORB-source mantle, similar perhaps to that of Iceland (Matthews et al., 2016; Matthews et al., 2021). To constrain this further, future work on primitive Ethiopian basalts, melt inclusions, or xenoliths will be necessary to identify compositional variations in parental basalts attributable to a lithologically hetereogenous source mantle (e.g., Shorttle et al., 2014). Likewise, new information on the storage conditions of olivines at the Dabbahu rift will contribute to a better estimate of $T_{crys}^{primary}$, which will enable better constrained estimates of mantle T_p.

4.5 Conclusions, part 2

Previous geophysical observations of the MER and Afar mantle suggest that mantle temperatures are elevated, and melting in the rift occurs at depth. In the previous chapter,

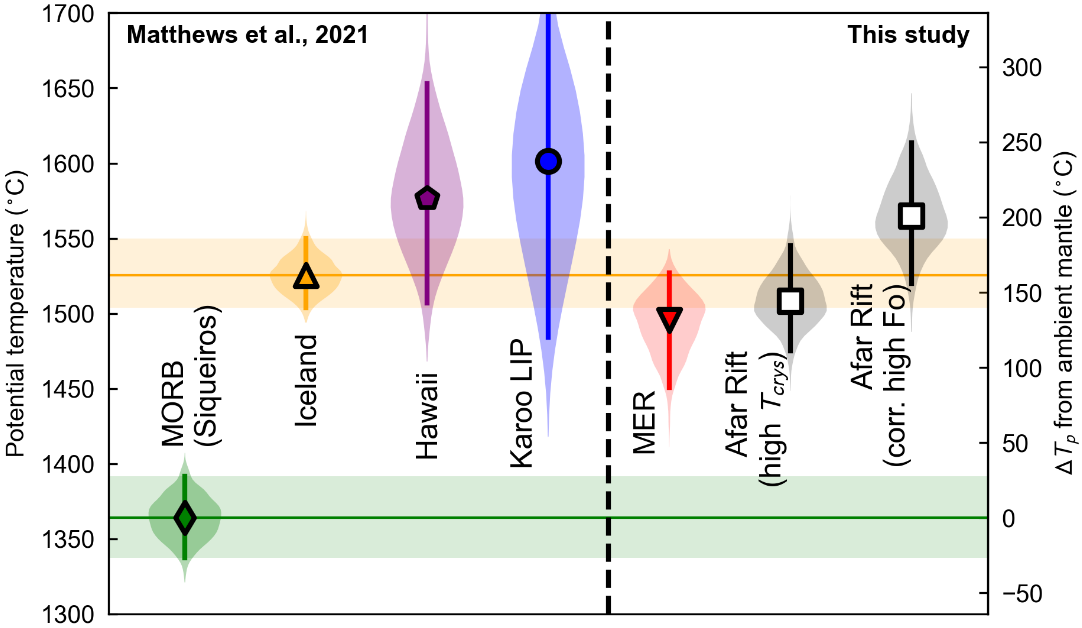

Figure 4.8: Violin plots of potential temperature determined through inversion of pyMelt. All inversion results are obtained using PM lherzolite and a passive triangular model. The Afar temperature distributions are the inversion results for primary crystallisation temperature of 1339±22 °C and 1409±40 °C. Bars within violin plots show 95% confidence interval, and markers display medians. Potential temperature posterior distributions for MORB, Iceland, Hawaii and the Karoo LIP are inversion results from Matthews et al. (2021).

I extrapolated T_{crys} from low Fo olivines, obtained through olivine-spinel Al-exchange thermometry, to $T_{crys}^{primary}$ at which olivines in equilibrium with mantle-derived melts are likely to crystallise. These $T_{crys}^{primary}$, when combined with a model of mantle melting and observed basalt REE concentrations, form the basis for inversion of mantle temperature and lithology. These models reproduce observed crystallisation temperatures and REE concentrations with elevated mantle temperatures that are consistent across Ethiopia (1496^{+31}_{-45} °C at Boku; 1508^{+37}_{-33} °C and 1565^{+49}_{-45} °C at Afar depending on $T_{crys}^{primary}$).

The primary differences between the two rift locations are lithospheric thickness and possibly mantle composition. Lithospheric thickness is estimated to be ~90 km at the MER but ≤70 km at Afar. The primary observed consequence of this lithospheric thinning is the thicknesses of intruded melt present at these two locations, and can be attributed to a more evolved rift system in Afar. Compositionally, the MER mantle is predicted to contain a lower fraction of more enriched lithologies than the Afar mantle (Figures 4.1 and 4.3). Garnet signatures observed in REE distributions from rift basalts from both these localities are expected to be influenced by melting of enriched lithologies at depth, with small-fraction lithospheric melts possibly contributing to light REE concentrations as asthenospheric melts leave the convecting mantle. The presence of more enriched asthenospheric lithological signatures under Dabbahu relative to the MER can possibly be attributed to the positioning of a large-scale plume centred on Afar (Rooney et al., 2012a). This compositional difference also contributes to the differences in melt thickness between the two locations. My results demonstrate that, while elevated relative to mid-ocean ridges, there are no significant mantle temperature variations across the rifting Ethiopian mantle and that variability in rift-related melt generation between the northern MER and in central Afar can be attributed to differences in mantle composition and rift geodynamics.

Chapter 5

Petrological evidence for focussed mid-crustal intrusion in the Main Ethiopian Rift

5.1 Introduction

Evidence from active continental rifts and passive margins suggests that continental break-up often involves intrusion of substantial volumes of magma into the rifting crust (see Section 1.2.2). These magmas can accommodate extension via dyke intrusion and, depending on their distribution in space and time, may alter the thermo-mechanical structure of the crust (e.g., Buck, 2006; Daniels et al., 2014; Lavecchia et al., 2016; Muluneh et al., 2020). Although the syn-rift interplay between magmatism and tectonics is a key ingredient in facilitating continental break-up (e.g., Thybo and Nielsen, 2009; Bastow and Keir, 2011), direct observational constraints on the depths of intruding basaltic magmas in active rifts are lacking. Determining where and how intruded melts accumulate during rift development is crucial for understanding how mantle-derived melts may affect the rheology and density structure of the crust (Buck, 2006; Daniels et al., 2014), altering its response to far-field extensional stresses.

The Main Ethiopian Rift (MER) provides a suitable natural laboratory to examine this interplay between rift geodynamics and magmatic intrusion. As outlined in Section 1.2.1, significant magma intrusion has occurred in the MER lithosphere, focussed under distinct ∼20 km-wide magmatic-tectonic segments (e.g., Bastow et al., 2011, see also Figure 1.4), where as much as half of the crustal volume may comprise new igneous material (Maguire et al., 2006; Daniels et al., 2014). The compositional and thermal effects of magma intrusion may modify the response of the Ethiopian crust to extension, determining where and how strain is localised as rifting proceeds (e.g., Bastow and Keir, 2011; Lavecchia et al., 2016). Furthermore, degassing of these intruded melts during and after emplacement contributes to the significant diffuse CO_2 fluxes measured in the MER (Hunt et al., 2017), which contribute extensively to total volcanic CO_2 outgassing both at the present day (e.g., Lee et al., 2016), and through geological time (Brune et al., 2017; Wong et al., 2019).

In this chapter I aim to resolve the nature of basaltic melt storage in the Main Ethiopian Rift through the study of olivine-hosted silicate melt inclusions. Through careful compositional analysis of these melt inclusions I can use geochemical clues preserved as major element, trace element, and volatile element compositions to understand more about how and where intruded basaltic melts are stored in the rift crust of the northern MER.

5.1.1 Olivine-hosted silicate melt inclusions

Melt inclusions are small droplets of magmatic melt trapped within growing crystals (see Wallace et al., 2021; Rose-Koga et al., 2021, for complete reviews). As they are assumed to sample the magma composition at the time of crystal growth, melt inclusions can provide key geochemical information concerning the spatial, temporal, and compositional evolution of magmas. The preserved major element, trace element, and volatile element concentrations of melt inclusions in crystals are therefore highly sought-after data by geoscientists looking to understand more about the geochemical history and evolution of both mantle-derived melts and melts derived from crustal anatexis.

A key feature of melt inclusions entrapped at depth are their considerable concentration of volatile elements, such as H_2O, CO_2, SO_2, and halides. The solubility of volatiles in a silicate melt is strongly dependent on pressure, major element composition, and melt temperature; CO_2 in particular has a limited solubility in basaltic melts, especially when compared to other volatile species such as H_2O (e.g., Dixon et al., 1995). CO_2 saturates in basaltic melts at crustal depths, resulting in the passive loss of CO_2 from melts in the crust prior to final melt ascent and eruption. These exsolved melts may either degas diffusely if pathways to the Earth's surface are available (e.g., Lee et al., 2016; Tamburello et al., 2018), or form a vapour-rich cap at the top of the magma reservoir if escape is limited (e.g., Iddon and Edmonds, 2020). Erupted lavas are almost completely degassed in volatile elements. The strong dependence of volatile concentration on pressure can therefore be used to assess the saturation pressures of stored crustal melts where crystallisation and co-occurring inclusion entrapment can occur.

Olivine is one of the first phases to crystallise from a mantle-derived melt. Silicate melt inclusions hosted within olivine crystals can therefore provide key information on the magmatic processes occurring within mafic systems which are fed by mantle-derived melts. In particular, geochemical details recorded by primitive or even parental melt compositions may be preserved. As a result, the interrogation of magmatic processes not recorded by erupted lavas can be studied, including the preservation of mantle heterogeneity (e.g., Shorttle et al., 2014), fractionation and mixing trends of evolving basalts (e.g., Sides et al., 2014a), the degassing histories of emplaced melts within the crust (e.g., Hartley et al., 2014; Taracsák et al., 2019), and the influence of melt composition on eruption style (e.g., Sides et al., 2014b). By considering olivine-hosted melt inclusions from the MER, the nature of similar magmatic processes to those listed above can be explored.

5.1.2 Melt inclusion shrinkage bubbles

Further complicating the analysis of melt inclusions is the common presence of the melt inclusion shrinkage bubble. Bubbles form in a melt inclusion when pressure decreases after entrapment (Maclennan, 2017). This can result from several processes (Wallace et al., 2021):

- Melt inclusion post-entrapment crystallisation results in a decrease in the volume of the combined olivine-melt inclusion system. Melt has a lower density than olivine, and during PEC the volume change results in a corresponding pressure change. The resultant vapour phase in the melt inclusion takes the form of a bubble. Saturated volatiles in the melt inclusion will continue sequestering into the bubble as volatile solubility decreases with progressive cooling and decompression (e.g., Danyushevsky et al., 2002). Melt inclusion composition can also change as a result of post-entrapment crystallisation, again resulting in a change in the solubility of CO_2 in the melt phase.

- Cooling of the olivine-melt inclusion system in the absence of post-entrapment crystallisation results in a thermally driven volume decrease; as melt has a greater thermal expansion coefficient, it will contract more than the host olivine, resulting in the formation of a vacancy which takes the form of the bubble. Final cooling of the melt inclusion during the eruption ascent can result in additional bubble expansion.

- Water diffusion in olivine is thought to be rapid, and the diffusive re-equilibration of H^+ from the melt inclusion into the carrier fluid via the host olivine can increase bubble size by changing the internal pressure of the inclusion (Bucholz et al., 2013).

These processes all combine to drive CO_2 from the melt inclusion into the bubble owing to the low solubility of CO_2 in basaltic melts. Determining the volatile saturation pressures of melt inclusions from CO_2-H_2O systematics using the inclusion glass only will therefore provide significantly underestimated results of the overall CO_2 within the inclusion (Aster et al., 2016). To determine the true value of CO_2 concentration originally entrapped within the inclusion, CO_2 in both the glass and the bubble must be accounted for.

A method of determining sequestered CO_2 in melt inclusions must therefore be applied in order to accurately gauge crystallisation pressures. As the melt inclusions in this study consist only of glass and a vapour bubble, I use Raman spectroscopy to obtain an independent measurement of the CO_2 in the bubble (Section 2.4). Raman spectroscopy is often favoured in lieu of melt inclusion rehomogenisation processes as analyses are comparatively rapid and the melt inclusion composition is not modified during analysis; however, carbon-bearing phases formed on bubble-melt interfaces during bubble development, such as carbonate, may themselves sequester CO_2 from the bubble, which cannot themselves be analysed by Raman (Rasmussen et al., 2020; DeVitre et al., 2021a). This will remove observable CO_2 from the bubble-inclusion system, resulting in underestimated CO_2 concentrations. Furthermore, Raman necessitates the requirement for accurate volumetric determinations, which are often difficult in the absence of the appropriate analytical facilities, and costly and time-consuming when such facilities are available (e.g., X-ray tomography, Pamukcu et al., 2015). Raman analyses and data processing must therefore be performed with care in order to appropriately assess uncertainties.

Past applications of Raman spectroscopy to study melt inclusion bubbles have confirmed that bubbles may contain a significant proportion (as much as 90 %) of the CO_2 initially present in the melt (Hartley et al., 2014; Taracsák et al., 2019). However, such studies often apply literature densimeters, which can vary significantly between different parameterisations; this arises as each Raman machine must be individually calibrated for its own densimeter line (Lamadrid et al., 2017). The bubble CO_2 densities predicted by previous studies may therefore deviate substantially from the densities that bubbles may be able to entrap, even in the face of possible inclusion decrepitation (Maclennan, 2017). In summary, in order to gauge the total CO_2 entrapped in a melt inclusion that has a vapour bubble present, the CO_2 of the bubble must be assessed with a calibrated densimeter, and the physical dimensions of the inclusion and bubble characterised.

5.2 Samples and methods

The samples selected for this study are olivine crystals from cones A76 (locality reference KW-MER19-76-0m) and A81 (locality reference KW-MER19-81-0m) in the Boku Volcanic Complex. These olivines are selected as they host glassy melt inclusions, i.e., melt inclusions that have been quenched and have not started to crystallise. While olivine-hosted melt inclusions are also observed in Abaya Lake and Ziway Lake scoriae (see Di Rienzo, 2019, concerning Abaya Lake), unlike those from Boku they are almost completely crystalline, and are therefore not suitable for this study.

Glassy melt inclusions are common within olivine crystals collected from Boku, although small (mostly $\leq 60\mu$m; Figure 2.7). Bubbles are present in the majority of observed melt inclusions, with several melt inclusions often hosting multiple bubbles within one inclusion. Olivine crystals, hosting 77 melt inclusions containing a single bubble only, were mounted onto glass slides using CrystalBond^{TM} and prepared for Raman analyses as described in Section 2.2. Raman spectroscopy was performed under the conditions outlined in Section 2.4. Subsequent preparation to produce epoxy mounts of melt inclusion-bearing olivine crystals were performed as described in Section 2.2.

40 melt inclusions overall, of which 18 were analysed by Raman spectroscopy, were analysed by SIMS (Section 2.5). After SIMS analyses the gold coat was removed by polishing each epoxy block with 0.25 μm grade diamond paste for 2 minutes, and a carbon coat was applied for EPMA, which were performed at LEMAS, University of Leeds (Section 2.6). Analytical conditions for olivine hosts and glass inclusions and carrier liquids are outlined in Tables 2.4 and 2.1 respectively. Two analytical periods for carrier glasses were performed; early analyses were performed as part of the preliminary analysis in May 2019 on a number of different Boku cone carrier liquids (locality references KW-MER19-76, -80, -81, and -82), while later analyses on A76 and A81 carrier liquids were performed during the same analytical period as the melt inclusions (July 2021). Where possible repeat point analyses were performed on single melt inclusions, although this was limited by the size of

the inclusion.

In addition to host olivine, melt inclusion, and carrier glass analyses, whole rock samples from a number of cones within the Boku region were analysed for major elements using XRF (Section 2.7) and trace elements via ICP-MS (Section 2.9). The combined data from these multiple geochemical analyses therefore provides an extensive dataset for MER basaltic materials, which are used in full for this study. Accuracy and precision from secondary standards for all analytical methods used in this study are provided in Appendix A.3.

5.2.1 Post-entrapment crystallisation corrections

After entrapment, melt inclusions will begin crystallising along the walls of the host crystal; this process is termed post-entrapment crystallisation (PEC). In olivine, this process results in the removal of Fe and Mg from the inclusion glass, while simultaneously raising the concentration of elements incompatible in olivine, such as Al, Ca, and the rare-earth elements (REEs). In addition, the diffusion of Fe between the inclusion, olivine host, and to some extent the carrier liquid will result in the loss of Fe from the inclusion. As a result, melt inclusions are typically in disequilibrium with their olivine hosts, and are geochemically more evolved (Wallace et al., 2021). In order to estimate the composition of melt inclusions prior to PEC, corrections must be applied.

Melt inclusion post-entrapment crystallisation and Fe-loss was corrected for using Petrolog3 (Danyushevsky and Plechov, 2011), as described in full detail within Section 2.10. Initial FeO_t was set at 12.69 wt%, which is the mean FeO_t of carrier glasses from Boku as determined by EPMA (see Appendix A.3). The olivine-melt model selected was Danyushevsky (2001), and the FMQ buffer was chosen for the oxidation state (Gleeson et al., 2017). Inclusions were corrected individually via importation of a bulk file containing melt inclusion compositions and host olivine Fo.

5.2.2 Melt fractionation models

Liquid lines of descent for major elements were predicted from primitive basaltic compositions using Rhyolite-MELTS v1.2.0 (Gualda et al., 2012). Models were run at an oxygen fugacity of FMQ, which is characteristic of MER basalts (e.g., Gleeson et al., 2017; Nicotra et al., 2021), starting at 1300 °C and cooling to 1000 °C. Isobaric fractionation at 3 kbar was selected based on the pressures obtained from VESIcal for melt inclusions for which total CO_2 was determined (see results in Section 5.3.2). Model differences arising from varying oxygen fugacity between FMQ-2 and FMQ+1 and pressure between 2–4 kbar were minor, and are therefore not considered further. Trace element partitioning was modelled using the Rayleigh fractionation equation:

$$C_i = C_{0,i} \cdot F^{(\bar{D}_i - 1)} \tag{5.1}$$

Where $C_{0,i}$ is the original concentration of an element i, F is the melt fraction, and $\bar{D}_i$ is the bulk mineral-melt distribution coefficient for that element. Melt fraction and mass proportions of olivine, clinopyroxene and plagioclase feldspar were determined from Rhyolite-MELTS outputs; other mineral fractions were typically <5 wt% and hence were not considered. Mineral-melt distribution coefficients were collated from Neave et al. (2012) and Iddon and Edmonds (2020), and, other than Ba and Sr in plagioclase, were assumed to be constant. Distribution coefficients for Ba and Sr in plagioclase were calculated using the temperature-dependent partitioning of Blundy and Wood (1991):

$$RT\ln(D_{\mathrm{Sr}}) = 26800 - 26700 \cdot X_{\mathrm{An}} \quad \text{and} \quad RTln(D_{\mathrm{Ba}}) = 10200 - 38200 \cdot X_{\mathrm{An}} \tag{5.2}$$

where X_{An} is the molar fraction of anorthite in plagioclase (An=Ca/(Ca+Na+K)), T is temperature, and $R = 8.3145$ J mol^{-1} K^{-1} is the gas constant. X_{An} is determined using the Rhyolite-MELTS output for plagioclase composition.

5.3 Results

5.3.1 CO_2 densities of shrinkage bubbles through Raman spectroscopy

All 77 melt inclusion shrinkage bubbles analysed by Raman spectroscopy returned a Fermi diad diagnostic of the presence of detectable CO_2 vapour (Appendix A.3). Bubble CO_2 densities range from 0.12 to 0.27 g cm^{-3}, with a mean density of 0.19 g cm^{-3} (Figure 5.1), all in excess of the expected detection limit for the Raman machine used (0.02 g cm^{-3}; Wieser et al., 2021). The Raman-analysed vapour bubbles constitute 0.09 to 2.85 vol% of the melt inclusion (Figure 5.2), and are similar in vol% to bubbles from Iceland (Hartley et al., 2014). As shown in Figure 5.1 there are no clear correlations between bubble density and estimated melt inclusion volume (Figure 5.1A), estimated bubble volume (Figure 5.1B), or bubble volume proportion of the melt inclusion (Figure 5.1C). Further-

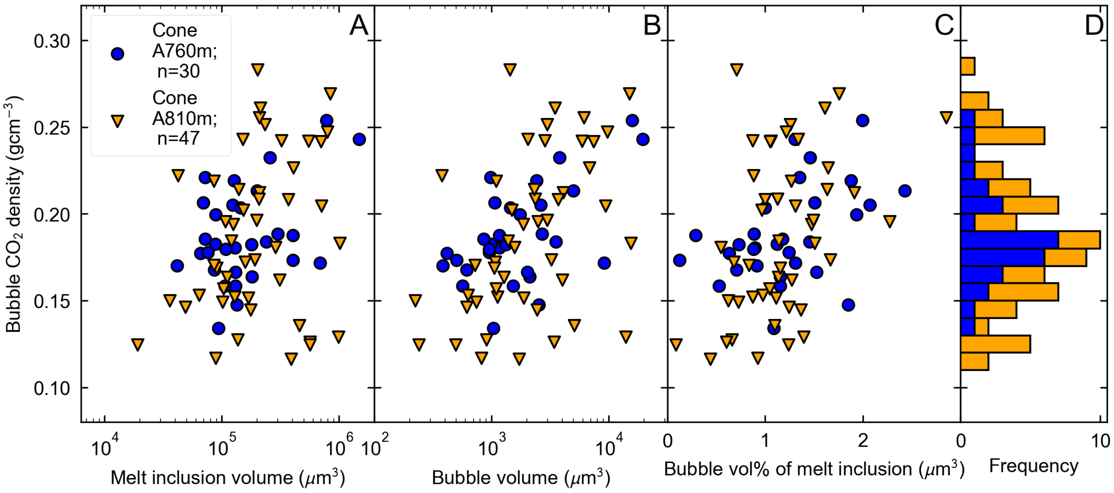

Figure 5.1: Bubble CO_2 density plotted against A. volume of melt inclusions, B. volume of shrinkage bubbles, C. bubble volume percentage of melt inclusions. D. Histogram of bubble CO_2 density.

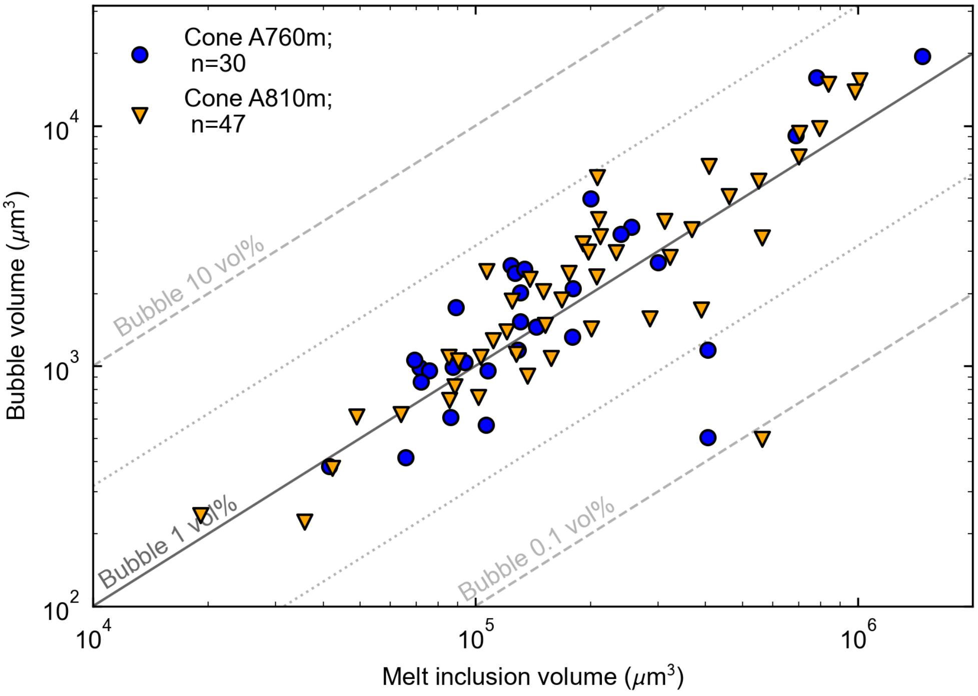

Figure 5.2: Bubble volume plotted against melt inclusion volume.

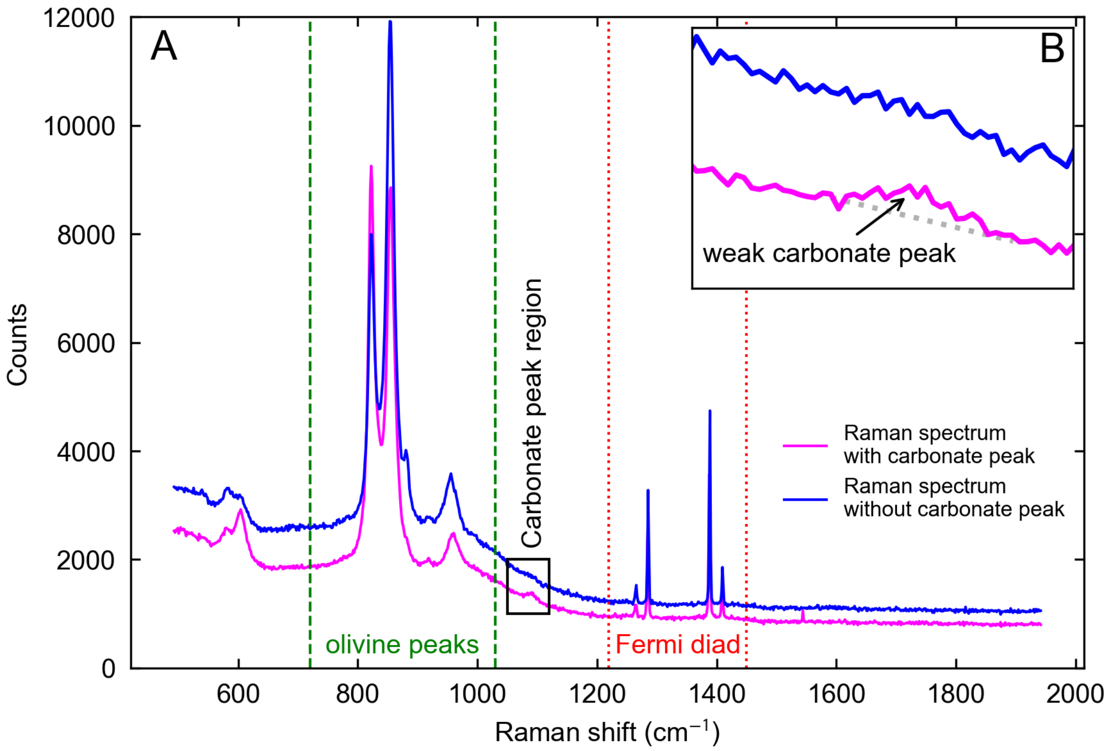

Figure 5.3: A. Raman spectra from this study with and without a carbonate peak at ~1090 cm^{-1}. The region of the olivine peaks and Fermi diad are shown as the dashed and dotted regions respectively. B. Zoom inset on black rectangle in subfigure A.

more, in the samples where SIMS and subsequent EPMA has been performed, there is no correlation between bubble volume proportion and PEC as observed in melt inclusions from Hawaii (Wieser et al., 2021). No difference in bubble densities or melt inclusion and bubble dimensions were observed between the two cones sampled in this study (Figure 5.1D).

~15 % of the shrinkage bubble Raman spectra contain a noticeable carbonate signature (~1090 cm^{-1}; Moore et al., 2015; DeVitre et al., 2021b, Figure 5.3). Only one bubble had a strong Raman carbonate signal, whereas the majority of carbonate signals observed were comparatively weak (as demonstrated in Figure 5.3); the presence of carbonate in MER melt inclusion shrinkage bubbles is therefore believed to be fairly uncommon, and concentrations of carbonate are low when present. Owing to the overlap in CO_2 densities between bubbles that do and do not return a carbonate signature, I believe that the effect of sequestration of CO_2 within carbonate is within uncertainty of the Raman analysis.

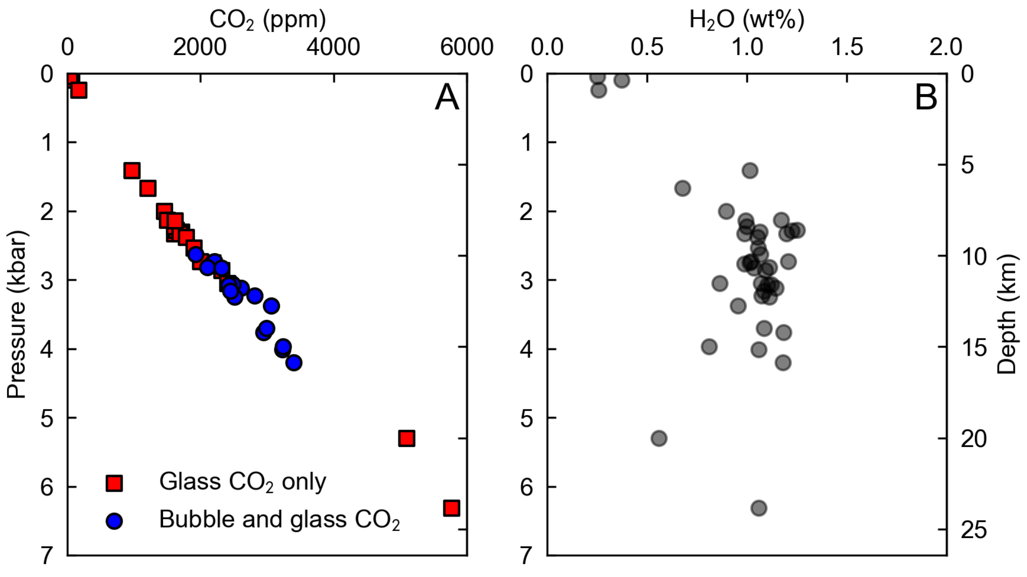

Figure 5.4: A. CO_2 and B. H_2O concentrations of MER melt inclusions plotted against volatile saturation pressures calculated using the MagmaSat volatile solubility model (Ghiorso and Gualda, 2015).

5.3.2 Volatile concentrations and solubility modelling

CO_2 concentrations in melt inclusion glass only as determined by SIMS range from 35–5770 ppm (Appendix A.3). Melt inclusions with CO_2 measurements in both the glass and vapour bubble have total CO_2 contents of 1895–3248 ppm, with 15–46% of the CO_2 residing within the bubble. H_2O concentrations show less variability: discounting the three melt inclusions that have clearly degassed (containing ≤0.4 wt% H_2O), inclusions have a mean H_2O concentration of 1.1±0.2 wt% (Figure 5.4). H_2O does not correlate with Ce, an element of similar mantle-melt compatibility to H_2O, suggesting that the original melt inclusion H_2O has not been altered post entrapment. The average H_2O/Ce of 264±42 for melt inclusions that have not degassed H_2O is in good agreement with mid-ocean ridge H_2O/Ce (245*pm*12, Le Voyer et al., 2017).

Volatile element concentrations, considered alongside the major element composition of melt inclusions, form the basis of volatile saturation barometry. To determine volatile saturation pressures, the open-source Python 3 library VESIcal is used, which is a pythonic wrapper for multiple established CO_2-H_2O solubility models in both basaltic and rhyolitic magmas (Iacovino et al., 2021; Wieser et al., 2022a). VESIcal models were run at a temperature of 1200 °C (Gleeson et al., 2017; Iddon et al., 2019, see also Chapter 3) for

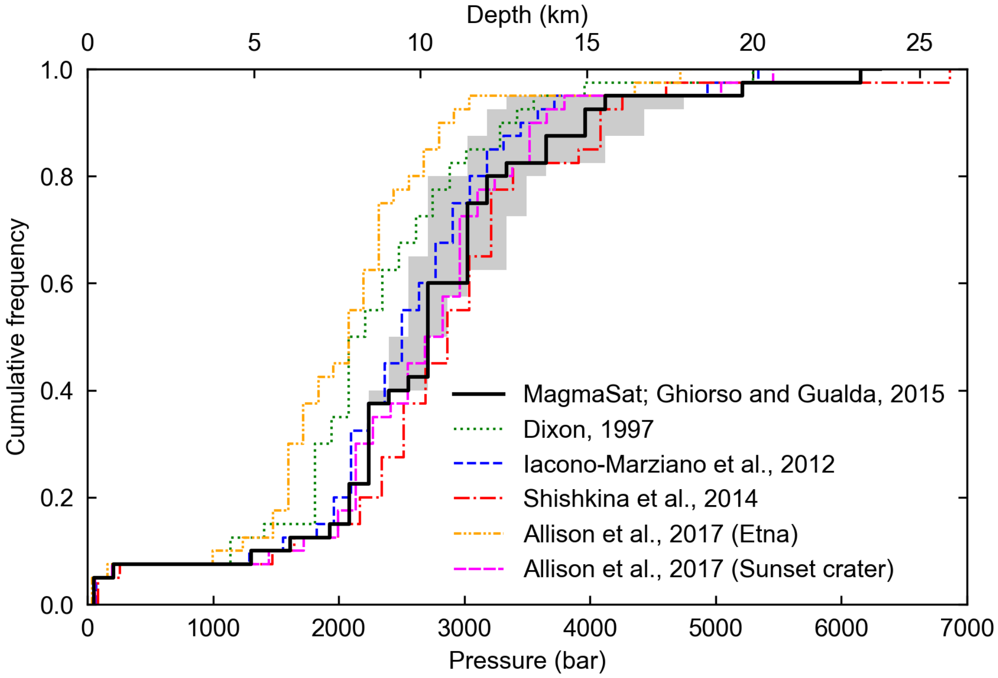

Figure 5.5: Cumulative distribution functions of entrapment pressures from different basalt CO_2-H_2O solubility models. The shaded region shows the error on MagmaSat entrapment pressures resulting from uncertainty in estimating bubble proportions from 2D images (Tucker et al., 2019).

all PEC-corrected melt inclusions in this study. VESIcal was also run for the basaltic melt inclusions in (Iddon and Edmonds, 2020) from MER volcanic centres and off-axis fields, assuming that PEC correction for this dataset was not necessary owing to the low reported PEC (<5 %) – this assumption is necessary in the absence of PEC corrections reported by Iddon and Edmonds. Temperature differences of ±30 °C had a negligible effect on saturation pressure, with the corresponding change in pressure being $\leq$50 bar, or $\sim$0.2 km assuming crustal density of 2.7 g cm^{-3}. Likewise, changing the initial FeO$_t$ by 1.5 wt% during PEC corrections affects MagmaSat pressures by a mean of 8±4 %, which does not significantly influence the results of this study. Uncertainties for volatile saturation pressure in melt inclusions that had been analysed by Raman were determined using minimum and maximum CO_2 expected from 1σ melt inclusion volume uncertainty, which is the most significant uncertainty in my analyses.

I select the thermodynamic MagmaSat volatile saturation model, which accounts for non-ideal mixing in CO_2-H_2O systems (Ghiorso and Gualda, 2015). As shown in Figure 5.4, the primary control on determining saturation pressures for my melt inclusions using MagmaSat is CO_2 concentration; H_2O in my basaltic melt inclusions remains constant at

Table 5.1: Kolmogorov-Smirnov statistics and *p*-values (in brackets) for different solubility models applied to my melt inclusions. Abbreviations are as follows: I.-M.: Iacono-Marziano et al. (2012); Allison-E: Allison et al. (2019) Etna model; Allison-S: Allison et al. (2019) Sunset Crater model.

K-S stat. (*p*)	**MagmaSat**	**Dixon**	**I.-M.**	**Shishkina**	**Allison-E**
Dixon	0.33 (0.03)	-	-	-	-
Iacono-Marziano	0.15 (0.77)	0.25 (0.16)	-	-	-
Shishkina	0.18 (0.58)	0.40 ($3\cdot10^{-3}$)	0.23 (0.27)	-	-
Allison-E	0.40 ($3\cdot10^{-3}$)	0.23 (0.27)	0.38 ($6\cdot10^{-3}$)	0.55 ($7\cdot10^{-6}$)	-
Allison-S	0.08 (1.00)	0.33 (0.03)	0.18 (0.58)	0.15 (0.77)	0.40 ($3\cdot10^{-3}$)

1.1±0.2 wt% up to $\sim$2 kbar, at which point H_2O is lost from the basalt. Other saturation models have been calibrated for the composition and pressure ranges which my basaltic melt inclusion samples occupy, which can be compared to MagmaSat easily using the VESIcal library. Figure 5.5 shows a comparison of MagmaSat to other basalt saturation models which are calibrated for the melt inclusion compositional range of this study (Dixon, 1997, implemented via the simplification VolatileCalc of Newman and Lowenstern, 2002; Shishkina et al., 2010; Iacono-Marziano et al., 2012; Allison et al., 2019). Both the Etna and Sunset Crater models of Allison et al. (2019) are selected in this comparison owing to the broad calibration range of the former and the similarity in composition to my samples of the latter. For the majority of my melt inclusions the difference between a selected model and MagmaSat is typically less than 500 bars ($\sim$2 km; see Figure 5.5). Kolmogotov-Smirnov statistics and *p*-values are presented in Table 5.1.

Entrapment pressures for melt inclusions calculated using MagmaSat and the models of Shishkina et al. (2010), Iacono-Marziano et al. (2012) and the Sunset Crater model of Allison et al. (2019) are statistically indistinguishable using Kolmogotov-Smirnov statistics at $p = 0.05$ (Table 5.1). Owing to the compositional difference between my samples and the Etna basalt, the Allison et al. (2019) Etna model substantially underestimates pressures relative to other models ($p < 0.05$ for all models except for Dixon, 1997; Table 5.1). My samples fall on the North Arch Glasses regression line used to calibrate the ideal mixing model of Dixon (1997) (and by extension the VolatileCalc model implemented in VESIcal Newman and Lowenstern, 2002), and are therefore compositionally suitable for this solubility model. However, it has previously been suggested that this model is appropriate only for low H_2O and CO_2 contents and therefore low pressures (<1000 bar Iacono-Marziano et al., 2012). As the majority of my melt inclusions are likely to be entrapped at mid-crustal depths, the model of Dixon (1997) is unlikely to be suitable for this work. The

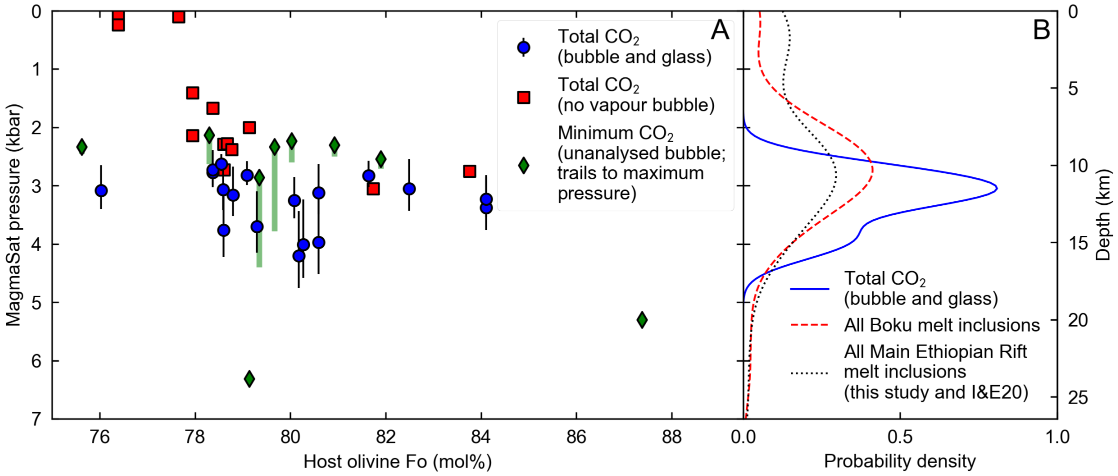

Figure 5.6: A. Volatile CO_2-H_2O saturation pressures of olivine-hosted melt inclusions from the MER, plotted against inclusion olivine host Fo (Equation 3.4). MagmaSat pressure calculations were performed at a temperature of 1200 °C (Gleeson et al., 2017; Iddon et al., 2019, see also Chapter 3). Melt inclusions are categorised on which components are analysed. Physical dimensions of vapour bubbles within inclusions that are analysed only for glass composition can be used to estimate maximum CO_2 if bubble CO_2 density is well characterised (green diamonds); this is performed assuming a density of 0.21 g cm^{-3} (see Section 5.3.3). B. Kernel density probability density curves of melt inclusion sample sets. 'All Boku melt inclusions' includes melt inclusion pressures determined without known total CO_2; 'All Main Ethiopian Rift melt inclusions' includes the reassessed pressures of Iddon and Edmonds (2020) (I&E20) which are determined using the same methods as Boku melt inclusions.

differences between MagmaSat and the other empirical models of volatile saturation are statistically insignificant and my samples are expected to have fractionated within their calibrated temperature and pressure ranges (Figure 5.5). These other models typically fall within the uncertainty envelope of melt inclusion and bubble volumes. I therefore favor the fully thermodynamic parameterisation of MagmaSat over the other empirical models.

Saturation pressures of melt inclusions assessed for total CO_2 contents, calculated using MagmaSat via VESIcal, vary over a relatively narrow pressure range from 2.5–4.5 kbar (Figure 5.6). In the MER these pressures correspond to depths of ~10–15 km (assuming a crustal density of 2.7 g cm^{-3}), among the deepest recorded volatile saturation depths for continental rift magmas. Pressures recorded by melt inclusions without bubbles overlap partially with those that do have analysed bubbles; however, the average CO_2 concentration and therefore pressure of inclusions without a bubble (1832±1338 ppm CO_2; 2.3±1.4 kbar) is typically lower than those with a bubble (2536±398 ppm CO_2; 3.3±0.5 kbar). Two melt inclusions for which only inclusion glass CO_2 is known record higher pressures in excess of

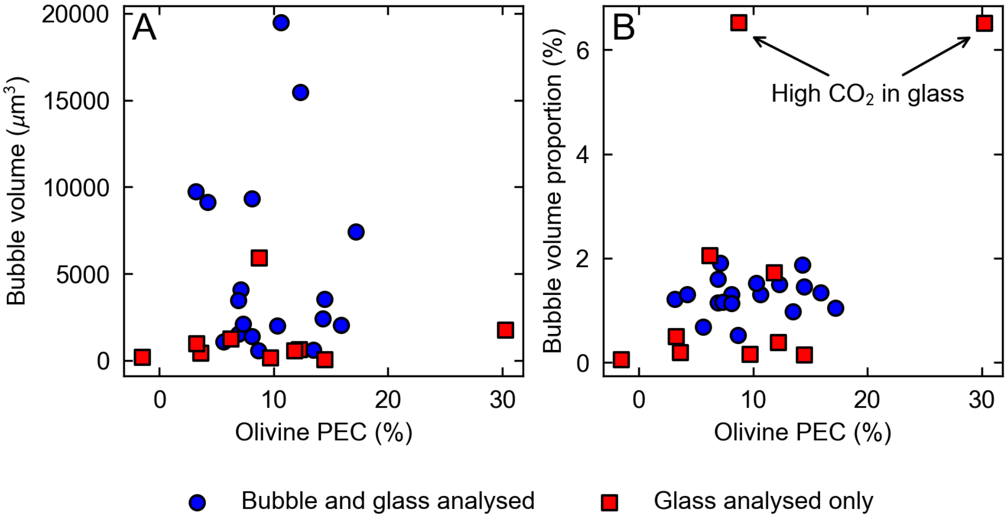

Figure 5.7: Olivine post-entrapment crystallisation of analysed melt inclusions plotted against A. bubble volume, and B. bubble volume as a proportion of the melt inclusion volume.

5 kbar (~20 km). Overall, these barometric results show a relatively limited distribution of magma storage depths with a narrowly focussed zone of intrusion centered at ~12 km depth, coincident with the seismically imaged boundary between the upper and lower crust (Maguire et al., 2006).

5.3.3 Corrections for empty bubbles

Although 77 melt inclusion shrinkage bubbles were analysed by Raman spectroscopy, a significant number could not be analysed by SIMS owing to their small size. The melt inclusions considered in the main text of this study are therefore a mixture of samples that have been analysed by Raman and others which were not, but were selected owing to their size. Several melt inclusions therefore have shrinkage bubbles that were not analysed by Raman prior to SIMS. Where an unanalysed shrinkage bubble is present CO_2 contents are assumed to be minima. However, total CO_2 from these melt inclusions can be estimated using the distribution of densities determined through the Raman spectroscopy of the 76 bubbles in the Raman dataset. By considering this distribution, empty bubble corrections are performed assuming that bubbles have CO_2 densities of 0.21 g cm^{-3}. This density falls near the mean of all melt inclusion vapour bubbles (0.18 g cm^{-3}), and could correspond to the maximum possible CO_2 vapour density below the critical point (DeVitre et al., 2022).

I apply this maximum density with post-rupture measurements of the bubble to estimate total melt inclusion CO_2.

Nine melt inclusions are corrected in this manner. Seven inclusions have maximum pressures within the range 2.5–4.5 kbar (8-18 km), in agreement with melt inclusions which do have analysed vapour bubbles. The remaining two melt inclusions, already recording the highest CO_2 in the dataset from glass analyses only, return maximum possible pressures nearing 10 kbar if bubble CO_2 is estimated, i.e., under the MER crust and within the lithospheric mantle. For these two melt inclusions the bubble constitutes 6.5 vol% of the overall melt inclusion volume and make up more than twice the volume percentage of all other melt inclusion shrinkage bubbles (Figure 5.7). These samples may have significantly degassed, and may have been derived from deepest parts of the sub-rift magmatic system; these inclusions may also have co-entrapped magmatic bubbles and may not be suitable for estimating saturation pressures (e.g., Tucker et al., 2019). Tucker et al. (2019) note that one cannot differentiate between ensnared magmatic vapour bubbles and shrinkage bubbles that form after inclusion formation; in this study I err on the side of caution and do not estimate the pressures of these inclusion while additionally considering their unanalysed bubbles owing to their anomalous size relative to other bubbles.

5.3.4 Melt inclusion glass geochemistry

Melt inclusion major element geochemistry before correction for post-entrapment crystallisation is shown in Figure 5.8 alongside carrier glass analyses. There is significant overlap between melt inclusion major element compositions and those of the carrier glasses; both melt inclusions and carrier glasses from cones A76 and A81 overlap and show no obvious distinction in any geochemical constituent. Melt inclusions are typically higher in Al_2O_3 than the carrier melt, reflecting the fractionation of plagioclase feldspar from the melt which has occurred after inclusion entrapment, and/or post-entrapment crystallisation of the inclusion which removes MgO and FeO from the inclusion major element composition and comparatively raises the concentration of all other major elements. The majority of olivines hosting melt inclusions plot above the equilibrium line of the lower-right subfigure of Figure 5.8 (assuming $K_D = 0.30 \pm 0.03$ Roeder and Emslie, 1970); these inclusions therefore record melt compositions after the removal of olivine via post-entrapment crystallisation.

After post-entrapment crystallisation corrections, the major element composition of

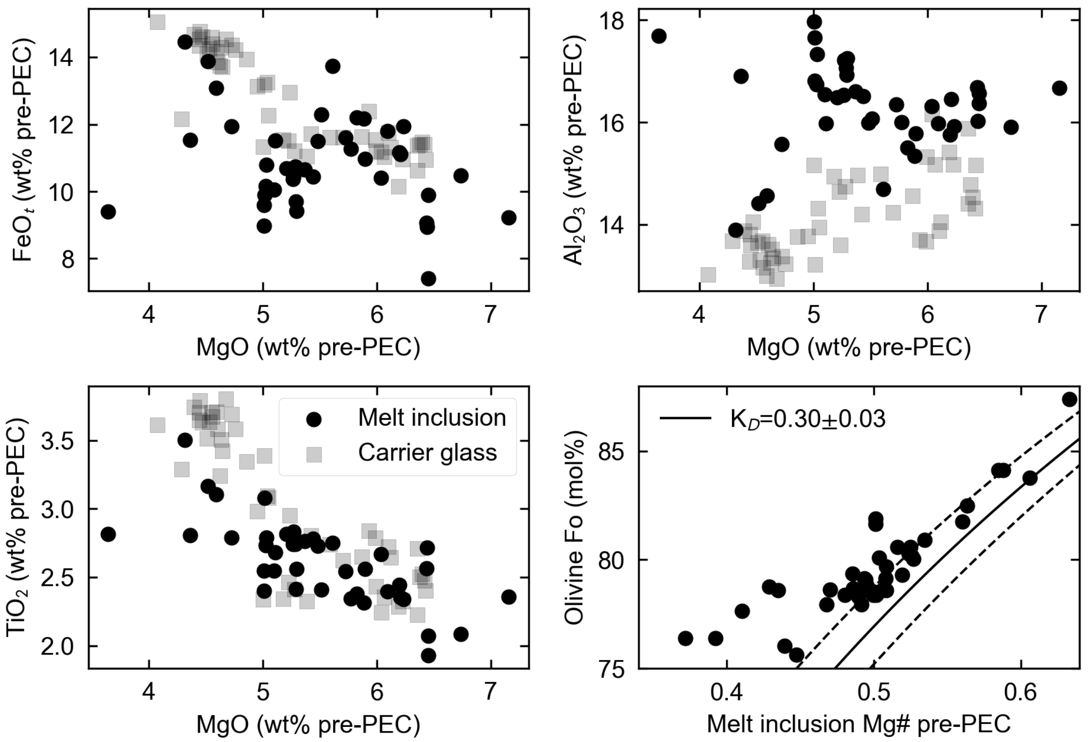

Figure 5.8: Melt inclusion major element geochemistry before post-entrapment crystallisation corrections. Carrier glass compositions are shown as the faded squares. Mg# is calculated as Mg/(Mg+Fe^{2+}), assuming 90 % of Fe is Fe^{2+}. Fo is calculated as shown in Equation 3.4. K_D is chosen as 0.30±0.03 following Equation 2.7 after (Roeder and Emslie, 1970).

intruded melts overlap with whole-rock compositions of erupted lavas (see Appendix A.3; Tadesse et al., 2019; Nicotra et al., 2021). Incompatible trace element concentrations vary considerably in both melt inclusions and lavas, which could result from fractional crystallisation of distinct parental melts and/or mixing between variably fractionated melts with distinct origins (Figure 5.9A, B). Both of these processes can result in a wide spread of melt trace element compositions, as observed in other melt inclusion datasets (e.g., Shorttle et al., 2014; Taracsák et al., 2019). Greater primary compositional variability is preserved in the melt inclusions over the whole rocks, evidenced by variations in trace element ratios that are not significantly affected by fractionation, e.g., La/Yb, Dy/Yb (Figure 5.9C, D). This suggests that the melts entrapped by melt inclusions are of greater compositional variety than erupted lavas.

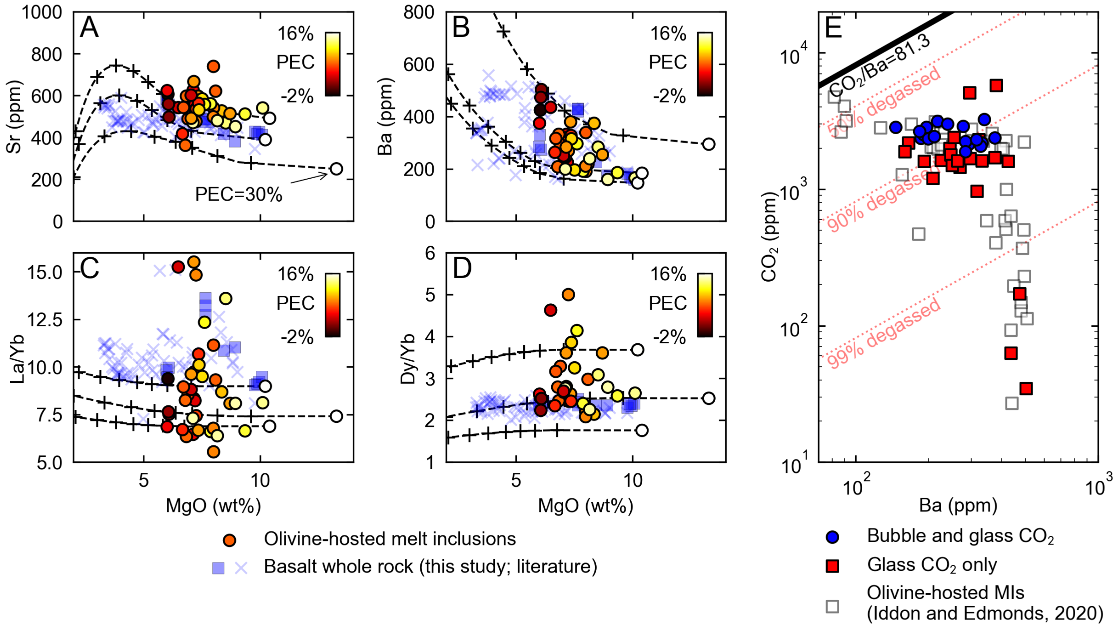

Figure 5.9: A-D. Melt inclusion and whole rock trace element and trace element ratios plotted against MgO (this study; Tadesse et al., 2019; Nicotra et al., 2021). Liquid lines of descent with crosses denoting 10 % fractionation intervals are determined from the three most primitive melt inclusion compositions using Rhyolite-MELTS (Gualda et al., 2012), assuming Rayleigh fractionation with the partition coefficients collated by Iddon and Edmonds (2020). E. Olivine-hosted melt inclusion CO_2 plotted against Ba; primary CO_2/Ba of mid-ocean ridge basalt (Le Voyer et al., 2018). Basaltic olivine-hosted melt inclusions of Iddon and Edmonds (2020) are included as the faded white squares.

5.4 Discussion

5.4.1 Mid-crustal sill complexes in the Main Ethiopian Rift

The heterogeneous trace element compositions recorded by melt inclusions relative to whole-rock basalts suggest that basalts of multiple different compositions are present in the rift crust at the same time (Figure 5.9). Physical interactions between intrusive bodies therefore appears to be limited, which implies that intruded magmas reside in a series of discrete sills emplaced at a common depth. The slightly lower degree of compositional diversity observed in erupted lavas (Figure 5.9C, D), even at higher MgO, suggests that some mixing does occur prior to eruption and that dyke intrusion into the upper crust may involve partially homogenised melts sourced from multiple mid-crustal sills. Erupted melts extend to lower MgO than those in the melt inclusions and pre-eruptive mixing and homogenisation may therefore occur during a final stage of differentiation within upper crustal magma bodies. Mixing in the final moments before eruption may be triggered by downward-propagating seismic activity, which can disturb and mix vertically stacked sills (as observed in Iceland Tarasewicz et al., 2012). Initial compositional variability in magmas may be due to the presence of multiple parental mantle-derived melts within the MER crust, derived from melting multiple source lithologies (e.g., Shorttle and Maclennan, 2011; Shorttle et al., 2014, see also Chapters 3 and 4) and/or unmixed fractional melts of the mantle which can also result in multiple melt compositions from a single melting mantle source (e.g., Gurenko and Chaussidon, 1995).

The presence of melts intruded as mid-crustal sill complexes is strongly supported by geophysical observations of the present-day MER crust. Focusing of ascending basaltic melts at this depth range can, to a first order, be attributed to MER crustal density structure as the mean density of the lower crust exceeds that of the melt inclusions (calculated with DensityX; Iacovino and Till, 2019; cf. Cornwell et al., 2006). Driven by density differences, basaltic melts will rise to mid-crustal depths before they achieve neutral buoyancy and subsequently stall and crystallise. Strong horizontal radial seismic anisotropy observed in the MER at these mid-crustal depths is consistent with the presence of sills (Chambers et al., 2021). Low seismic moment earthquakes in northern MER magmatic segments are distributed within a narrow depth band between 8–16 km and are triggered by movement or emplacement of mid-crustal melts (Keir et al., 2006a; Daly et al., 2008). High-Vp/Vs and high-density bodies are present at these depths under Boku and other segments (Keranen et al., 2004; Cornwell et al., 2006; Daly et al., 2008), as are high-conductivity crustal anomalies (Whaler and Hautot, 2006). Numerical models suggest that the 10–15 km depth range coincides with the weakest part of the Ethiopian crust, which is sandwiched between two strong brittle layers in the upper and mid-lower crust (Muluneh et al., 2020). This weak, ductile mid-crust may therefore be subjected to localised crustal strain accommodation, which facilitates more intrusion and subsequent thermo-mechanical weakening of the rifting crust. The strong brittle crust above this ductile zone prevents further ascent of the buoyant melt, which can only progress to the surface through the breaking of dyke-induced faults (e.g., Rooney et al., 2011).

The lack of evidence for significant melt storage within the upper crust in my dataset contrasts with the depth-distributions for magma storage obtained from suites of melt inclusions collected at large caldera-forming volcanic centers found along the MER (Iddon and Edmonds, 2020). Under these silicic centers, melt storage appears to extend upwards into the upper crust, where evolved magmas are generated via low pressure fractionation

(Iddon and Edmonds, 2020). Notably, the maximum storage depths under MER caldera complexes identified from melt inclusions (Iddon and Edmonds, 2020) and from barometry of xenoliths (Rooney et al., 2005) and clinopyroxenes (Iddon et al., 2019) coincides with the 10–15 km depth range seen in this dataset. This depth range may therefore be the locus of initial basaltic melt emplacement along the MER, with important implications for the strength profile of the crust, such as the creation of a mid-crustal weak layer. With the exception of those below caldera complexes/silicic volcanoes, upper crustal melt bodies (<10 km depth) are likely to be ephemeral, perhaps forming during periodic intrusive-eruptive episodes.

In contrast to the extensive melt inclusion data corresponding to mid-crustal pressures, very few inclusions from my dataset and that of Iddon and Edmonds (2020) record pressures corresponding to the lower crust. Considering the evolved compositions of the olivines in this study (mean Fo_{80}) relative to Fo_{90} olivines in other MER volcanic materials (e.g., Rooney et al., 2005), I posit that an initial stage of fractionation near the Moho prior to ascent to mid-crustal pressures is necessary. This hypothesis is supported by low wavespeeds observed at Moho depths from the presence of melt in the heavily intruded lower crust (Keranen et al., 2009; Chambers et al., 2019), and numerical models suggesting that the lowermost crust is weak, hot and underlies a lower-crustal brittle-ductile transition at 20–25 km (Lavecchia et al., 2016; Muluneh et al., 2020). In addition, radial seismic anisotropy is weaker at lower crustal depths (>16 km), suggesting that the melt storage regimes at these pressures may deviate from the sills inferred in the mid-crust (Chambers et al., 2021). Melts pooling and fractionating at the base of the crust may bypass the ductile lowermost crust entirely if both density differences between melt and crust and lower crustal strain rates are sufficiently high (Muluneh et al., 2021).

5.4.2 CO_2 degassing from intruded melts

Continental rifts, including the MER, are known to be significant sources of passively degassing magmatic CO_2 (Lee et al., 2016; Hunt et al., 2017). By comparing CO_2 concentrations with trace elements with similar behavior during mantle melting (e.g., Ba, Rb), CO_2 degassing from mantle melts can be assessed (e.g., Le Voyer et al., 2018). CO_2/Ba and CO_2/Rb systematics for MER melt inclusions clearly show evidence for degassing, even in inclusions with total CO_2 determinations (Figure 5.9E). Most melts therefore appear to have lost substantial volumes of CO_2 prior to intrusion in the mid-crust and melt inclusion entrapment (Figure 5.9E). While primary magmatic CO_2 contents are not known for MER magmas, the highest observed CO_2/Ba and CO_2/Rb ratios approach those measured in undegassed MORB by Le Voyer et al. (2018) (CO_2/Ba =81.3; CO_2/Rb=991). If this is reflective of primary CO_2/Ba and CO_2/Rb values in MER melts then initial CO_2 contents will be in the range of 1–4 wt%, with ~60–95% of the CO_2 having been exsolved at the mid-crustal pressures of sill emplacement.

CO_2 degassing in the MER, which is likely derived from degassing of magmas intruded into the mid-crust, is focussed along discrete fault zones (Hunt et al., 2017; Jolie et al., 2019). The difference in expected CO_2 concentrations in primary mantle melts and those observed in melt inclusions (mean of 2.0±0.6 wt% with the same CO_2/Ba as MORB) will be representative of the CO_2 degassed during volatile exsolution accompanying the emplacement of melt into the mid-crust. To estimate CO_2 fluxes resulting from the degassing of the intruded melts preserved as inclusions, the quantity of melts supplied to the MER must firstly be assessed. The length of the MER is ~1000 km, and the full spreading rate is ~5.0 mm yr^{-1} (Saria et al., 2014). Assuming a melt density of 2.7 g cm^{-3} (calculated as the mean melt inclusion density in this study using DensityX Iacovino and Till, 2019), and that the CO_2 degassed at mid-crustal pressures is 2.0±0.6 wt% (assuming the same CO_2/Ba as MORB Le Voyer et al., 2018), I can present three possible estimates of intruded melt thickness per unit of rift length:

- The first estimate is reached by assuming that all new rifting crust is igneous; this is a suitable estimate as most present-day extension in the MER is predominantly magma-assisted (e.g., Kendall et al., 2005; Bastow et al., 2010). Using a crustal thickness of 28 km (Lavayssière et al., 2018), melt volume flux is estimated as 0.14 km^3 yr^{-1}, and the corresponding CO_2 flux is 7.6±2.7 Mt CO_2 yr^{-1}.

- Another assumption is that 50% of extension in the MER is accommodated by magmatic intrusion (Daniels et al., 2014). If this is the case, melt volume flux and CO_2 flux are simply half that of the previous case: 0.07 km^3 yr^{-1} and 3.8±1.1 Mt CO_2 yr^{-1} respectively.

- Finally, the proportion of igneous crust in rifting crust can be calculated by comparing crustal thicknesses expected from stretching factors to present-day MER crustal thickness (Armitage et al., 2015). Total crustal thickness in the MER is maintained until the final stages of continental rifting through magmatic intrusion (Bastow and

> Keir, 2011). However, the thickness of the upper crust is maintained by intrusion less-so than the lower crust (e.g, Hammond et al., 2011), and therefore can be used to estimate intruded melt thicknesses when compared to un-rifted crust (Armitage et al., 2015). This has been previously performed in Section 4.2.3 to obtain 3–6 km thickness of igneous crust under Boku. Performing the calculations as above provides melt volume flux estimates of 0.02–0.03 km^3 yr^{-1}, and corresponding CO_2 flux estimates of 0.8±0.2 Mt CO_2 yr^{-1} (assuming 3 km), 1.2±0.4 Mt CO_2 yr^{-1} (assuming 4.5 km), and 1.6±0.5 Mt CO_2 yr^{-1} (assuming 6 km).

These melt volume flux estimates, ranging from 0.02 to 0.14 km^3 yr^{-1}, are very similar to the range estimated by Iddon and Edmonds (2020). Similarly, the corresponding CO_2 flux estimates, which range from 0.8 to 7.6 Mt CO_2 yr^{-1}, are of a related magnitude to total CO_2 emissions of 0.52–4.36 Mt CO_2 yr^{-1} recorded by Hunt et al. (2017). The degassing of mid-crustal sill complexes can supply sufficient CO_2 to match the quantity degassed at geothermal centers in the MER. Furthermore, the restriction of significant degassing to localised regions in the MER (Hunt et al., 2017) may suggest that some regions are subject to active intrusion at the present day whereas other portions are not. Future studies of the Rift should aim to constrain this possible periodicity of melt emplacement, which is further explored in the subsequent chapter.

5.5 Conclusions

This chapter is summarised with Figure 5.10. The evidence from considering the total CO_2 in a melt inclusion suggests that stacked mid-crustal sills in the depth range of 10–15 km are the dominant form of magmatic storage in the MER (Figure 5.10A and B). These sills are known to be horizontally distributed from seismic anisotropy (Chambers et al., 2021), and develop as a consequence of repeated magmatic intrusion into the mid-crust during the progression of late-stage continental rifting. Initially crystallising at or near the Moho, mantle-derived magmas bypass the ductile lowermost crust to arrive at the Ethiopian mid-crust heralded by seismic activity (Figure 5.10C; Muluneh et al., 2020, 2021). These melts are stored as discrete sills in the weak, ductile mid-crust and blocked from further ascent by a strong upper crust (Figure 5.10D). Partial mixing of magmas between sills may occur in the shallow crust prior to eruption, as evidenced by the less variable REE ratio compositions of lavas when compared to melt inclusions (Figure 5.9C).

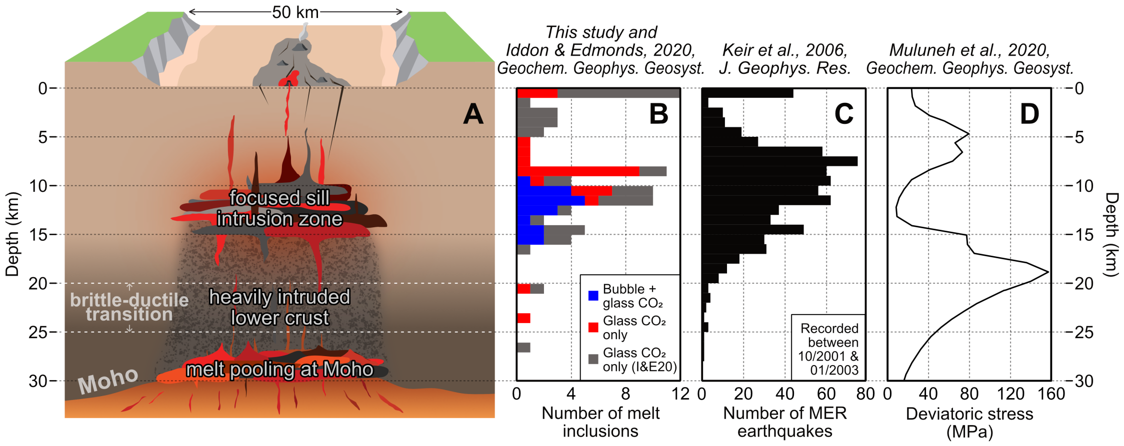

Figure 5.10: A. Summary cartoon illustrating the proposed structure of the MER crust. Horizontal and vertical dimensions not to same scale. B. Histogram of olivine-hosted melt inclusion saturation pressures (this study; Iddon and Edmonds, 2020). C. Histogram of MER earthquakes (Keir et al., 2006a; Daly et al., 2008). D. Numerical model of MER crustal deviatoric stress (Muluneh et al., 2020).

The emplacement of melts into this hot, weak mid-crustal zone has important implications for the distribution of heat during late-stage continental rifting in Ethiopia, and how the Ethiopian crust responds in a thermo-mechanical manner to extensional strain (Daniels et al., 2014). I also establish in this study that the degassing of mantle-derived melts in mid-crustal sill complexes can exsolve enough CO_2 to generate the quantity observed from diffuse passive degassing at the rift surface. This conclusion furthers recent observations that link continental rifts with massive outpourings of CO_2 into the Earth's exogenic systems (Lee and Lackey, 2015; Foley and Fischer, 2017; Brune et al., 2017). The consequences of mid-crustal emplacement of melts must be therefore considered in future models of late-stage continental rifting.

Chapter 6

Timescales of dyke intrusion events in the Main Ethiopian Rift through olivine Fe-Mg interdiffusion chronometry

6.1 Introduction

In active continental rift settings, such as the Main Ethiopian Rift (MER), it has been established that magmatic intrusion into the crust is one of the primary drivers of late-stage continental rifting (see Section 1.2.2). Episodic intrusions of magmas, forming dykes (e.g., Wright et al., 2006) and sills (Chapter 5), will strongly facilitate rifting by thermo-mechanically altering the response of the crust to extensional stresses, hence accommodating extension (Daniels et al., 2014; Lavecchia et al., 2016). Determining the residence times and ascent rates of melts within the crust is therefore key to not only resolving the triggers leading to volcanic rifting events, but also to exploring the longer-term thermal effects of crustal melts on extensional deformation. We also seek to understand whether there are characteristic generic timescales inherent in rifting and dyke intrusion that are common to rifting systems worldwide (e.g., Wright et al., 2012), which may suggest that similar magmatic processes are operating at different rift settings. In the case of the MER, a continental rift with no contemporaneous geophysical observations during a rifting episode, timescales of pre-eruptive magmatic activity may be estimated using petrological observations. Relating these crustal magmatic processes in the MER to seismic observations of active rift systems can provide a more complete understanding of how continental rifts may operate during episodes of intrusive activity, and may lead to better hazard forecasting during future rifting events.

Many active volcanoes at the present day exhibit precursor activity in the hours, days, or weeks preceding an eruption. This activity can take the form of seismicity, surface deformation, and gas release, which offers a convenient way of temporally monitoring the activity of volcanoes undergoing a pre-eruptive phase. However, these data are absent if one is considering volcanic eruptions and processes that occurred in the geological past. In the magmatic segments of the MER, the last volcanic activity involved the eruption of silicic centres in the 18th and 19th century (Wadge et al., 2016), prior to the advent of extensive seismic monitoring in the EARS. In order to determine temporal changes in magmatic behaviour within MER volcanic systems and relate them to modern rifting events which are monitored via ongoing seismicity (e.g., Ebinger et al., 2010; Wright et al., 2012), the petrology of erupted materials must be considered.

Oftentimes pre-eruptive geophysical unrest or gas release may be triggered by a corresponding change in the chemical equilibrium of a magmatic environment. New melt, derived from deeper in the crust or the mantle, will inherently have geochemical properties (e.g., temperature, composition) that are in disequilibrium with new environments during ascent. Disturbing magmatic environments in this manner will therefore result in signatures of chemical disequilibrium and subsequent re-equilibration, such as the compositional zonation of crystals as they attempt to re-equilibrate with their new setting (e.g., Costa et al., 2020). Models describing how re-equilibration can occur in pre-eruptive magmatic settings can be used to obtain timescales between the initial event driving disequilibrium (e.g., the intrusion of new, hot magmas) and the later thermal 'freezing' of the same system, which typically is a product of the eruption itself.

In this study I use Fe-Mg interdiffusion chronometry driven by magmatic disequilibrium to characterise the timescales of olivine storage and magmatic recharge events during late-stage continental breakup in the MER. By doing so I aim to unravel the rate of magmatic recharge events that result in the formation of basaltic scoria cone fields that flank MER central volcanoes, and provide the first petrological estimates of magma storage and transport within a continental rift system.

6.1.1 Diffusion chronometry modelling

Diffusion in minerals can be considered as the movement of ions relative to each other within the crystal lattice (Costa and Morgan, 2010). Diffusion chronometry involves the extraction of timescales from compositional profiles generated through the diffusion process, and is dependent on the rate at which ion exchange reactions occur, upon a change in the system that they are sensitive to (e.g., pressure, temperature, or chemical potential; Dohmen et al., 2017). Diffusion chronometry has several advantages relative to other geochronometry methods (e.g., mineral-reaction chronometry, U-series disequilibria), with the principal advantage of beign able to relate short-period timescales (hours to months) recorded within crystals to specific magmatic processes (Cooper, 2019; Costa et al., 2020; Costa, 2021).

Patterns of chemical zoning with evident diffusion profiles can therefore provide temporal information of magmatic processes occurring immediately prior to eruption that disrupt the chemical equilibrium of crystals. These diffuse chemical profiles can arise from a number of processes, including magma mixing and melt differentiation. If the factors controlling diffusion of particular elements within the crystal are known and well-characterised, the timescale of diffusive re-equilibration can be determined. Diffusion chronometry can therefore provide key information on melt residence times at magmatic temperatures.

The process of diffusion is described and modelled in one dimension using Fick's second law, which predicts how concentration changes with respect to time at any given position along a concentration profile:

$$\frac{\partial C_i(x,t)}{\partial t} = \frac{\partial}{\partial x}\left(D_i \frac{\partial C_i(x,t)}{\partial x}\right) \tag{6.1}$$

where C_i is concentration of element i, t is time, x is distance, and D_i is the diffusion coefficient (also termed diffusivity) of element i with units of $\mathrm{m}^2\ \mathrm{s}^{-1}$. Equation 6.1 assumes that D is independent of position or concentration. To use this equation to determine timescales of magmatic processes, several key points must be considered (Costa and Morgan, 2010):

- The diffusivity D of the diffusing element within the medium of interest must be well understood and parameterised. This is achieved empirically through experimental studies of diffusing elements within the crystal in question (e.g., Dohmen and Chakraborty, 2007; Dohmen et al., 2007).

- Distance profiles of concentration, and therefore the gradients of concentration along the profile, must be well-resolved to apply diffusion chronometry. The precision and spatial resolution of the analytical technique being employed must be able to sufficiently characterise compositional differences across the crystal's diffusion front.
- The assumed shape of the compositional profile at the start of the modelling calculation (termed the initial condition) must be appropriate and supported by analytical observations.
- The boundary between the crystal and the surrounding medium must be well-characterised to model how diffusion in or out of the crystal behaves (termed the boundary conditions).

In crystals, D_i takes the form of an Arrhenian equation, and is dependent on temperature, pressure, oxygen fugacity, crystal composition, and orientation of the crystallographic axes (Dohmen et al., 2017). For example, the interdiffusion of Fe and Mg in olivine along the [001] (c-axis) direction for $fO_2 > 10^{-10}$ Pa is given by the following equation (Dohmen and Chakraborty, 2007; Chakraborty, 2010):

$$D_{\text{olivine}}^{\text{Fe-Mg}} = 10^{-9.21} \cdot \left(\frac{f_{\text{O}_2}}{10^{-7}}\right)^{\frac{1}{6}} \cdot 10^{3\cdot(X_{\text{Fe}}-0.1)} \exp\left(-\frac{201000 + (P - 10^5)\cdot 7 \cdot 10^{-6}}{RT}\right) \tag{6.2}$$

which has been related to the aforementioned factors empirically through experiments (Dohmen et al., 2007; Dohmen and Chakraborty, 2007). In this equation, the compositional term X_{Fe} is the mole fraction of the fayalite (Fe_2SiO_4) component of olivine, and the terms P, T, f_{O_2} and R are the pressure (Pa), temperature (K), oxygen fugacity (Pa) and the universal gas constant (8.3145 J $\text{mol}^{-1}\text{K}^{-1}$) respectively. Diffusion along different crystallographic axes occurs at different rates; the diffusion along the [001] direction in olivine as described above is roughly six times faster than diffusion along the [100] or [010] directions of olivine. The diffusion coefficient for any crystallographic orientation can be derived from the three diffusivities along the three crystallographic axes of olivine using the following relation (Philibert, 1991):

$$D_{\text{trav}}^{\text{Fe-Mg}} = D_{[100]}^{\text{Fe-Mg}}\cos^2(\alpha) + D_{[010]}^{\text{Fe-Mg}}\cos^2(\beta) + D_{[001]}^{\text{Fe-Mg}}\cos^2(\gamma) \tag{6.3}$$

where α, β and γ are angles between the traverse of interest and the *a*-, *b*- and *c*- axes of olivine respectively, and D_i^j denotes the diffusivity of element i with respect to the axis direction or traverse j.

6.1.2 Application of diffusion chronometry to olivine

A crystal in equilibrium with a melt maintains a chemistry that is stable with that of the host magma composition at the given pressure, temperature, and oxygen fugacity. If there is a change in these parameters, the chemistry of the crystal will respond to re-equilibrate to equilibrium conditions. If the crystal remains at these new conditions such that, over time, a particular element can significantly diffuse, then the compositional profile of the element at the crystal boundary will relax; the exterior of the crystal equilibrates instantly with the new environment, and a region of partial equilibration will begin expanding towards the crystal core with time. The smoothed profile will have a shape that is dependent on the diffusivity of the element and the time over which diffusion has been active (Costa and Morgan, 2010).

A commonly used and well-studied mineral that often shows diffusive compositional gradients (noticeably in Fe and Mg, which interdiffuse) is olivine. The composition of olivine is regularly described as the molecular percentage of the forsterite (Mg_2SiO_4) component, Fo, where, for magmatic olivine dominated by Mg and Fe, Fo is calculated as outlined in Equation 3.4, and is intrinsically linked to the Mg# of the olivine's host magma (Equation 6.8). The Fe and Mg of olivine and the melt from whence it crystallises is related by a experimentally determined, near-constant partition coefficient (Equation 2.7; Roeder and Emslie, 1970). Progressive olivine crystallisation preferentially strips the host magma of Mg; over time the magma becomes enriched in Fe. Subsequent crystallising olivine is therefore progressively Mg-poor and Fe-rich (or lower Fo). Olivine introduced into an environment it is not equilibrated with will therefore begin to gain or lose Fe-Mg to reequilibrate with its new magmatic surroundings via a diffusional process. For primary mantle-derived MORB melts, the first crystallising olivine is believed to be $\sim$$Fo_{91}$, a value recorded from the Siquieros transform fault of the East Pacific Rise (Perfit et al., 1996).

An olivine crystal with a composition trending from Mg-rich in the core to Fe-rich in the direction of the rim is described as 'normal-zoned' (corresponding to a rim-ward decrease in Fo). Likewise the term 'reverse-zoned' describes the case where the opposite is true, and the olivine composition becomes progressively more Mg-rich towards the rim (corresponding to a rim-ward increase in Fo; Pankhurst et al., 2018). Normal zoning may arise from the movement of olivine into a more-evolved magmatic environment with a lower Mg# (e.g., during magma ascent; Morgado et al., 2017), whereas reverse zoning may result from more-evolved olivines ending up in contact with less-evolved magmas of higher Mg# (e.g., via mafic magma recharge or the rain of gravitationally unstable olivines; Pankhurst et al., 2018).

Modelling of Fe-Mg interdiffusion in olivine can provide a relative timescale for MER eruption processes, provided that appropriate assumptions are made concerning diffusive behaviour of these ions within the olivine crystal. One-dimensional profiles from rim-to-core are suitable provided that diffusion profiles are short relative to grain size, and that diffusion occurs perpendicular to the grain edges (Costa et al., 2008). Furthermore, one can assume that the crystal is initially compositionally homogeneous before the onset of diffusion (Costa and Chakraborty, 2004; Costa et al., 2008). The magmatic pressures, temperatures, and oxygen fugacities that govern the rate of diffusion within a crystal (Equation 6.2) may be determined using empirical geothermobarometers and oxymeters (e.g., Putirka, 2008b; Coogan et al., 2014) or may be estimated using thermodynamic algorithms such as MELTS (Ghiorso and Sack, 1995; Gualda et al., 2012).

$D^{\text{Fe-Mg}}_{\text{olivine}}$ is dependent on the composition of olivine (Equation 6.2). As a result, analytical solutions to the diffusion equation (Equation 6.1), which typically take the form of an Gaussian error function, are often inappropriate for observed profiles as they rarely employ composition-dependent diffusivities (Costa and Morgan, 2010). The use of finite-difference methods which calculate approximate solutions to the diffusion equation are therefore more frequently used to find numerical solutions to diffusion-related problems (e.g., Costa et al., 2008; Morgan, 2015; Mutch et al., 2021). While numerical solutions often necessitate a significant amount of computing time to calculate, they are versatile and can be adapted to different initial and boundary conditions and diffusivity-dependences (Mutch et al., 2021).

A case of the versatility of numerical solutions is provided by the code AutoDiff, which utilises one-dimensional composition-dependent diffusion model solutions generated by a finite-difference model (e.g., FINDIF, Morgan, 2015, or DBCalc, D. Morgan, unpublished) to compute timescales of diffusion (Couperthwaite et al., 2020). A profile with a greater compositional difference between the core and rim will show greater asymmetry compared to the symmetrical error function sigmoid, owing to the dependence of Fe-Mg diffusivity on olivine composition. Therefore, for a given temperature, oxygen fugacity, crystal anisotropy and compositional contrast, all one-dimensional diffusion profiles will be self-similar in time for any given compositional dependence, i.e., the diffusion profile will have the same geometric features that will be stretched out over space owing to the time over which diffusion has occurred. For example, diffusion for the same compositional contrast after 4 time units will be twice as wide as for 1 time unit, but otherwise the diffusion sigmoids recorded in the concentration profiles will be geometrically identical (Hartley et al., 2016). If the initial conditions and boundary conditions of diffusion are known, then the correct diffusion profile shape can be determined. While finite-difference models can predict the behaviour of a wide variety of boundary conditions, AutoDiff can assume two endmember boundary conditions: an initial boundary condition of a step change in composition or a boundary condition in which the diffusive signal diffuses in from the grain edge through exchange with an infinite external buffer. In a geological context, these scenarios would reflect diffusion between two rapidly developed compositional growth phases within a single crystal that form a step in composition when timescales of growth are very short relative to diffusion, or a carrier melt in disequilibrium with the crystal core from which ions will diffuse in/out (Hartley et al., 2016).

AutoDiff measures the compositional contrast between the 20th and 80th percentiles in the diffusion profile observed in an analysed crystal, and compares the curve with a database of simulated diffusion profiles (Morgan, 2015; Couperthwaite et al., 2020). These model curves all differ in their shape, determined by the degree of compositional dependence, but share the same maximum diffusivity and simulated diffusion time. The appropriate model curve, selected based on the degree of compositional dependence in the natural sample, is then stretched to match the natural data using a scalar value, overlaid at the 50th percentile of the diffusion curve, as a point common to all profiles. This scalar, termed a stretch factor in AutoDiff, is ultimately used to adjust the time of diffusion in the model to determine the final diffusion time recorded by the data. As discussed by Hartley et al. (2016) and Couperthwaite et al. (2020), if, for both sample and model:

$$x \propto \sqrt{Dt} \tag{6.4}$$

and the profile distances can be related by the stretch factor n:

$$x_{\text{sample}} = n x_{\text{model}} \tag{6.5}$$

then the diffusion time recorded by the sample, t_{sample}, can be related to the diffusion time of the model, t_{model}, through substitution of Equation 6.4 into Equation 6.5:

$$t_{\text{sample}} = n^2 \cdot \frac{D_{\text{model}}}{D_{\text{sample}}} \cdot t_{\text{model}} \tag{6.6}$$

To summarise, the methodology underlying the AutoDiff algorithm relates the known time and diffusivity of a modelled curve best matching the compositional contrast observed within the sample to the diffusion time elapsed within the sample. The diffusivity of the sample, D_{sample}, is a function of composition, oxygen fugacity, crystallographic orientation, and temperature, which can all be quantified through geochemical and petrological analysis.

Fe-Mg diffusion chronometry in olivine utilising AutoDiff has been previously used to unravel timescales of mixing and eruption, in particular, for Santorini (Martin et al., 2008), Iceland (Hartley et al., 2016; Pankhurst et al., 2018), Hawaii (Rae et al., 2016; Couperthwaite et al., 2020; Couperthwaite et al., 2022), and the Andes Southern Volcanic Zone (Morgado et al., 2017). Such studies have yielded key information on magma ascent rates and magmatic resident times, often linking such timescales to observed geological events such as seismicity related to crustal magma ascent (Pankhurst et al., 2018). In this study, olivine diffusion chronometry is used to determine timescales of magma replenishment and transport in MER magmatic settings in the build-up to eruption, which can be related to timescales of seismic and magmatic activity during recent dyke intrusion events.

6.2 Analytical methods

The samples used in this study are olivines collected from scoria cones from the Boku Volcanic Complex and East Ziway, two monogenetic cone fields in the MER (see Sections 2.1.2 and 2.1.3 for further locality information). Olivines from disaggregated scoriae are chosen as they are cooled rapidly upon eruption, in contrast to those entrained within lavas which are subject to post-eruptive diffusion of Fe and Mg which is likely to complicate records of pre-eruptive diffusion (Hartley et al., 2016).

In this chapter, olivine composition is described primarily using forsterite (Fo) as defined in Equation 3.4. Fo in its molar fraction form X_{Fo} is also used at points, where:

$$X_{\text{Fo}} = \frac{\text{Mg}}{\text{Mg} + \text{Fe}} = \frac{\text{Fo}}{100} \tag{6.7}$$

where Mg and Fe are given as molar fractions in olivine. The equivalent for silicate melts is the magnesium number Mg#:

$$\mathrm{Mg\#} = \frac{\mathrm{Mg}^{2+}}{\mathrm{Mg}^{2+} + \mathrm{Fe}^{2+}} \tag{6.8}$$

where Mg^{2+} and Fe^{2+} are given as cation fractions in melt; where FeO_t is returned from a glass analysis FeO is assumed to be 90% of the overall melt.

Concentration gradients of Fo are extracted from olivine crystals using a combination of EPMA and backscatter electron (BSE) imaging. Compositional traverses from olivine rims to cores comprising 10–20 points spaced ∼5–15 μm apart were measured in 88 olivine crystals divided between 41 from cone A81 from Boku (locality reference KW-MER19-81-0m) and 47 from cone Z58 within East Ziway (locality reference KW-MER19-58a) on the JEOL JXA8230 EPMA at LEMAS, University of Leeds, with analytical conditions as listed in Table 2.5. The length of the extracted profiles themselves were chosen dependent on the apparent width of diffusion observed through backscatter electron imaging. The starting spot of each traverse was measured ∼5 μm from the edge of the crystal in order to determine the traverse point where the olivine crystal had been entered. Where possible two compositional traverses were taken from different orientations within the same crystal.

High-resolution Fe-Mg diffusion profiles were obtained using backscattered electron (BSE) compositional contrast images, using the FEI Quanta 650 FEGSEM at LEMAS, University of Leeds (Section 2.8.1). Because of the electron backscattering effect (Section 2.8.1), regions of the olivine crystal that are more Fe-rich will appear brighter in greyscale contrast than olivine regions that are more Mg-rich. The pixel-scale resolution of backscatter images (∼0.1 μm) can therefore provide a significant number of datapoints that can be used to characterise the diffusion profile. Greyscale values along traverses were extracted perpendicular to crystal edges (or perpendicular to diffusion fronts if diffusion was not parallel to crystal edges) from BSE images using ImageJ software (Schneider et al., 2012).

BSE traverses were calibrated with EPMA analyses using a minimisation script coded in Python 3. Greyscale and EPMA traverses have similar profile shapes whose values are related by a linear function. The shape of the greyscale profile was manually fitted to the EPMA profile, exploiting this linear proportionality, by minimising the misfit χ^2:

$$\chi^2 = \ln\left(\frac{\sum_{i=1}^{n}\left[|X_{\mathrm{Fo},i} - (\mathrm{g}_i \cdot m + c)|^2\right]}{n}\right) \tag{6.9}$$

where n is the number of probe points present within the greyscale profile, $X_{\mathrm{Fo},i}$ is the electron microprobe compositional value of point i, g_i is the corresponding greyscale value of that point (between 0 and 255), and m and c are the gradient and intercept of the linear function relating the overall greyscale profile to the true compositional X_{Fo} profile.

As probe profiles were collected starting outside the olivine crystal, the greyscale profile distances would be laterally shifted relative to the probe profile. This lateral shift is corrected for in the same Python code by moving the greyscale profile relative to the fixed probe profile. The g_i value best corresponding to $X_{\mathrm{Fo},i}$ was determined, after correcting for traverse shift, through linear interpolation of the nearest greyscale values to the probe point. After manual fits were achieved, the misfit between the greyscale and the probe points (Equation 6.9) was minimised using the *optimize.minimize* function of the Python library SciPy (Virtanen et al., 2020). Even with computational minimisation a manual fitting step is necessary, as *optimize.minimize* cannot find global minima using Equation 6.9. Each profile must also be individually assessed for anomalies in both the greyscale and probe profiles prior to fitting (e.g., cracks, small mineral/melt inclusions). All probe profiles and greyscale profiles were assumed to be parallel (an angled traverse will have the same shape as a parallel one, albeit stretched); minor angles between the probe and greyscale traverses ($\lesssim$10 °) will result in a small trade-off with intercept and gradient which will not significantly affect composition within the diffusing region; major angular differences will result in a very noticeable poor fit between the distances recorded along the BSE and EPMA traverses. Where multiple different fits were possible, the fit with the lowest misfit was chosen, else the diffusion profile was not considered. By using this approach, all greyscale profiles are calibrated such that r^2 between probe data and greyscale data is greater than 0.98.

As diffusion within olivine is strongly anisotropic, the orientation of the crystallographic axes must be determined in addition to the concentration gradients. Crystal orientations were obtained using electron backscatter diffraction (EBSD), performed on the FEI Quanta 650 FEGSEM at LEMAS, University of Leeds. EBSD data was processed with Oxford Instruments Channel 5 software to gather data on crystal orientations. Crystal Euler angles were measured in a region within the core of each olivine crystal as outlined in Section 2.8.2, and characterised using Aztec Crystal software. Pseudosymmetries, arising when multiple orientations could fit the same EBSD data, were removed using Aztec Crystal. Where extreme degrees of pseudosymmetry were present each pseudosymmetry was characterised and assessed separately for diffusion timescales. Anomalous individual pixels within each crystal core region were either removed or retained (and averaged out) owing to the sheer number of matching pixels. If a region of the crystal had a symmetry that did not match the majority of the core it was assumed to be a subgrain and removed from the EBSD map. Null points were either filled via interpolation using Aztec Crystal or removed from the analysed region using Python code.

6.2.1 Uncertainties in diffusion modelling

Diffusion timescales are extracted from compositional profiles in olivine using the edge-buffered AutoDiff model. This boundary condition is described by Couperthwaite et al. (2020) as:

$$\begin{aligned} &t = 0, \quad C = C_0 \quad \text{for all } x \\ &t > 0, \quad C = C_1 \quad \text{for all } x < 0, \text{ and} \quad C_{(x,t)} = f(C, x, D, t) \quad \text{for all } x \geq 0 \end{aligned} \tag{6.10}$$

where C_0 is the initial composition of the olivine crystal, C_1 is the external buffer composition for $t > 0$, D is diffusivity and x is distance, where $x = 0$ is the edge of the crystal. This model assumes that diffusive exchange occurs from the rim to the core of the crystal, with the rim in diffusive communication with the surrounding magma. While some profiles can be fit reasonably well with an initial step condition, edge-buffering is preferred to provide good quality fits and to keep consistency across all profiles.

Uncertainties in obtaining timescale information from diffusion profiles can be mitigated through careful selection of traverse direction. The optimum traverses to select to minimise error are those perpendicular to the crystal face (or diffusional front) which also pass through the centre of the crystal. In general inclined traverses should be avoided, as they will produce a greater apparent diffusional timescale (Costa et al., 2008). Shea et al. (2015) provide more guidance through their modelling of 3D diffusion models of Fe-Mg in olivine:

- Avoid the smallest crystal sections as they are likely to be off-centre, and will not capture the composition of the core. Furthermore, they will be more subject to interaction between multiple diffusion fronts.
- Profiles should be obtained away from crystal corners to avoid interaction between multiple diffusion fronts; for this reason faceted, euhedral crystals are preferred.

- Select olivines with a clear composition plateau in which a compositional rim remains consistent for a distance along the traverse. Dipping plateaus may be indicative of off-centre sections of the crystal.

- Olivine sections not showing symmetry across different faces are likely to be oblique to most faces of the crystal.

Both Costa et al. (2008) and Shea et al., 2015 suggest taking two or more one-dimensional traverses perpendicular to two crystal faces on the same crystal plane where possible, for the dual purpose of verifying observed timescales and ensuring that compositional gradients are diffusion-related and not growth-related. Growth of the crystal in an environment it is in chemical disequilibrium with will also result in growth-driven compositional zones similar to that of diffusion. These guidelines were followed in this study wherever possible and suitable.

A significant uncertainty is associated with the diffusivity D, owing for the need for an accurate understanding of the thermodynamic conditions of storage, which are crucial when determining residence times (Rutherford, 2008). The uncertainties in values for temperature, pressure, and oxygen fugacity during storage must be considered, as diffusion rates vary exponentially with temperature owing to the Arrhenian form of D (see Equation 6.2). Temperature contributes the greatest uncertainty, which can affect the calculated timescale by a factor of 2–4 (Costa et al., 2008). Uncertainties in D additionally arise from uncertainties in activation energy and the pre-exponential factor D_0 (Dohmen et al., 2007; Dohmen and Chakraborty, 2007), which are estimated to contribute as much as 10% uncertainty (Costa et al., 2008).

Individual uncertainties have different effects on D; however, the sum total of these uncertainties are close to log-Gaussian, and can be propagated in log-units before they are returned back to absolute values (Costa and Morgan, 2010). In absolute time, timescale uncertainties are therefore asymmetric. Two approaches commonly taken to propagate uncertainties in diffusion timescales are Monte Carlo error propagation (e.g., Hartley et al., 2016; Pankhurst et al., 2018), or propagation by selecting maximum and minimum D calculated from the maximum and minimum temperature, activation energy, pressure, and pre-exponential factor (Morgado et al., 2017). In this study, uncertainties in temperature, pressure, oxygen fugacity, and backscatter pixel resolution are propagated through Monte Carlo error propagation (n=10,000). Uncertainty from the original calibration of diffusivity (Equation 6.2) is additionally propagated using the experimental data of that study (Dohmen et al., 2007; Dohmen and Chakraborty, 2007).

In this study, sectioning angles are assumed to be perpendicular to crystal faces. While shallow sectioning will result in longer timescales (Costa and Morgan, 2010), several factors may mitigate the overall uncertainty that is generated. The relative size of the crystal is large relative to profile distances, and the magnitude of resultant sectioning uncertainty may be minor relative to uncertainties propagated from the diffusivity, especially given the large population of crystals comprising the dataset of this study (Couperthwaite et al., 2021). Couperthwaite et al. (2021) additionally note that sectioning angles in their study already fall near perpendicular, perhaps owing to a subconscious selection of sectioning angle when mounting olivines.

Finally, Shea et al. (2015) suggest, through random sampling of their model results and using the guidelines listed above, that at least 20 profiles from different olivines within the same sample should be used to obtain diffusion timescales close to the true value. This value is exceeded by the number of profiles collected for this study (n=113).

6.3 Results

6.3.1 Compositions of MER olivines

Olivines from Boku and East Ziway range from 1–4 mm in diameter, and are mostly subhedral with rounded corners (Figure 6.1). Several olivine crystals have irregular and jagged dendritic rims on the scale of 5–10 μm reflective of late-stage growth during rapid cooling (e.g., Welsch et al., 2013). These dendritic rims typically bear small melt embayments of the same lengthscale, and host several small ($\sim$5 μm) inclusions of minerals and melt (Figure 6.1). Normal zoning along this dendritic overgrowth follows the rim of the overgrowth itself, whereas the reverse rims the overgrowth is found on are straight (Figure 6.1C and D); this would suggest that the factors inducing normal zoning within the overgrowth are related to the development of the overgrowth itself, and reverse rim development is separate to overgrowths.

I obtained a total of 113 electron probe profiles from 41 Boku olivines and 47 East Ziway olivines; the analytical data from all profiles are available in Appendix A.4. Of these profiles, 102 from 79 olivines (36 Boku, 43 Ziway) were successfully correlated with their backscatter electron contrast greyscale images.

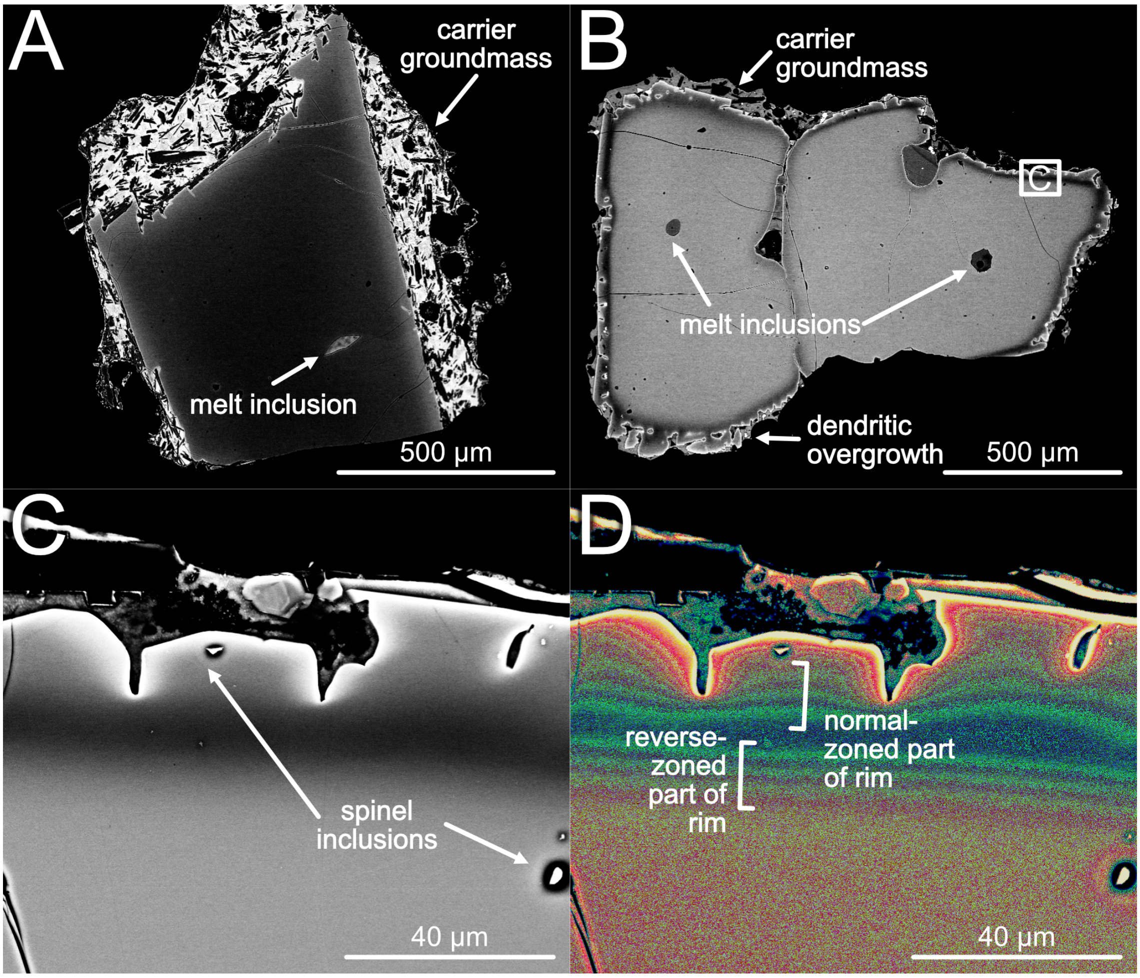

Figure 6.1: Backscatter electron images of compositionally zoned olivine crystals. A. A normal-zoned olivine crystal from the Boku Volcanic Complex (crystal AA-A7). B. A reverse-zoned olivine from the East Ziway cone field (crystal ZA-A6). C. Zoom on crystal in subfigure B detailing zone and dendritic overgrowth in greyscale. Gradients in greyscale, show through false colour (3-3-2 RGB) illustrate geometries of diffusion fronts in subfigure D.

The compositions of these olivines are shown in Figure 6.2. Boku olivine core compositions range from Fo_{69} to Fo_{87}, with a mean of Fo_{81}. Only five crystals have $Fo_{<78}$. These compositions are comparable to other analyses performed on Boku olivines in Chapters 3–5. East Ziway olivines are typically more Fe-rich, recording olivine cores of Fo_{63} to Fo_{88} with a mean value of Fo_{74}, which is again comparable to olivine analyses collected in Chapter 3. The more-evolved composition of East Ziway olivines reflects the higher SiO_2 and lower MgO basalts observed within the Ziway cone field relative to Boku, especially for the cone Z58 from which these olivines are obtained (compare equilibrium fields in Figure 6.2).

Two subsets of olivine crystals can be identified based on their core-to-rim Fe-Mg com-

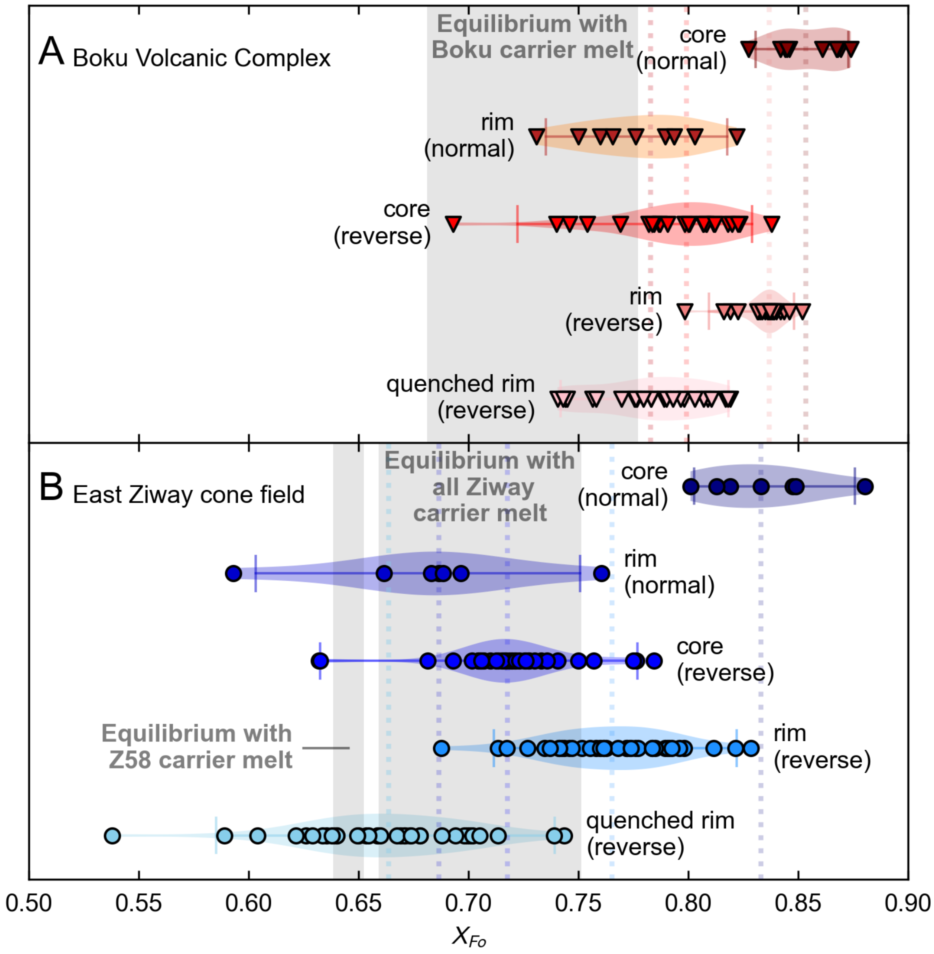

Figure 6.2: Violin plots illustrating core and rim compositions of A. Boku, and B. East Ziway olivines. The descriptor in brackets indicates the overall nature of the profile, with 'normal' and 'reverse' representing a rim-ward decrease and increase in olivine Fo respectively. Quenched reverse-zoned olivine rims are recorded as the composition of the most rim-ward olivine point along a reverse-zoned profile. Dotted vertical lines mark the median of each distribution; not that in subfigure A the medians of normal-zoned olivine rims and quenched reverse-zoned olivine rims overlap. Olivine compositions in equilibrium with carrier melts from each locality are shown as the grey shaded regions, and are calculated from the mean and standard deviation of carrier melt Mg# assuming a K_D of 0.3 (Roeder and Emslie, 1970). Two ranges are shown in subfigure B, as Cone Z58, where the East Ziway olivines were obtained, deviates compositionally from other cones in the region.

positional zoning patterns. The first subset comprises high-Fo core olivines exhibiting a decrease of Fo in a rim-ward direction (‘normal’ zones) – this subset will be termed ‘normal-zoned olivines’ in this chapter (Figure 6.1A). The second subset of olivine crystals, which are more numerous than the first subset, show evidence of compositionally complex ‘reverse’ zoning, i.e., the Fo of the olivine crystal increases from core to rim – these will be termed ‘reverse-zoned olivines’ (Figure 6.1B). These terms used to describe olivines (‘normal-zoned’ and ‘reverse-zoned’) are definitively outlined as the reverse-zoned olivines often have a strong normal component to their overall profile (Figure 6.1D). This normal zone is located on the rim-ward edge of the reverse rim of the crystal, and can additionally be considered for diffusion chronometry. However, as described above, these normal parts of the rims have dendritic features which suggest that they have likely been affected by late-stage growth and subsequent quenching during magma ascent. In such a case, timescales obtained from purely diffusional models such as that employed by AutoDiff must be considered upper limits on timescale, as growth ($x \propto t$) will occur much faster than diffusion ($x \propto \sqrt{t}$) for all but the shortest timescales.

Reverse-zoned olivines dominate both Boku and East Ziway sample sets (Figure 6.2). At both settings, the cores of reverse-zoned olivines are typically lower Fo and less well-constrained than those of normal-zoned olivines. Boku reverse-zoned olivines have cores of Fo_{69-84} compared to normal-zoned olivine cores of Fo_{83-87} (Figure 6.2A); the same is true for Ziway olivines, where normal-zoned cores are Fo_{78-88} in contrast to lower Fo_{63-78} reverse-zoned cores (Figure 6.2B). The outermost normal rims on reverse-zoned olivines are Fo_{74-82} at Boku (mean Fo_{78}), and are as low as Fo_{50} in Ziway reverse-zoned olivines, with a wide range up to Fo_{74} and a mean of Fo_{66} (Figure 6.2).

Normal-zoned olivine cores and reverse-zoned olivine rims from both localities are typically further from equilibrium than the rims of normal-zoned olivines, and the cores and quenched rims of reverse-zoned olivines (Figure 6.2). While these reverse-zoned olivine rims can be attributed to a reduction in the oxygen fugacity of the magmatic system (e.g., as inferred at Stromboli and Hawaii Cortés et al., 2006; Helz et al., 2017), it is more likely that this rim represents rapid growth of high Fo olivine during a pulse of mafic magmatic recharge. Indeed, the higher Fo cores of normal-zoned olivines at both settings (Figure 6.2) implies that they may have accompanied higher Mg# melt into a more evolved environment crystallising comparatively lower Fo olivines. Normal-zoned crystal rims and reverse-zoned cores and quenched rims are more in equilibrium with carrier melts at both

Table 6.1: Basalt compositions used for petrological modelling. Z58 is used for Rhyolite-MELTS modelling of East Ziway melt fractionation for olivine crystallisation temperature (Gualda et al., 2012), and NB-01 (Tadesse et al., 2019) is used for Petrolog3 modelling for olivine growth compositions (Danyushevsky and Plechov, 2011). All concentrations are wt%. Where only one of Fe_2O_3 or FeO is given that value represents total Fe.

Oxide	Z58	NB-01
SiO_2	47.75	45.43
TiO_2	2.171	2.19
Al_2O_3	14.54	16.81
Fe_2O_3	12.16	-
FeO	-	11.46
MnO	0.191	0.19
MgO	7.39	8.81
CaO	9.09	10.52
Na_2O	2.948	2.52
K_2O	1.044	0.46
P_2O_5	0.539	0.33
Cr_2O_3	0.045	-
LOI (1025 °C)	0.14	1.76
Total	98.008	100.48

Boku and East Ziway than the higher Fo normal-zone crystal cores and reverse-zoned rims, assuming an Fe-Mg K_D of 0.3 (Roeder and Emslie, 1970).

It is also worth noting that a significant number of olivine profiles, both normal and reverse-zoned show multiple stages of growth and diffusion near the rim. This complexity takes the form of multiple compositional zones near olivine rims, which cannot all be described in the simple categorisation described in Figure 6.2. Some primarily normal-zoned olivines host a reverse rim (e.g., ZB-B3-SE) or a plateau indicative of late-stage olivine growth (e.g., AA-A5-N), whereas in others the reverse rim of some reverse-zoned olivines is oscillatory (e.g., AA-C3-N). Complete characterisation of such patterns are beyond the scope of this work, but all zones point towards a complex pre-eruptive basaltic system where the olivine struggles to achieve equilibrium with the host melt. For completeness, the collection of diffusion patterns and probe data are provided in Appendix A.4.

6.3.2 Magmatic pressure-temperature constraints

Calculations for Boku olivines were performed at a magmatic temperature of 1180±20 °C and a pressure of 3 kbar reflecting the outcomes of the studies performed in Chapters 3-5. The quartz-fayalite-magnetite (FMQ) oxygen fugacity buffer was chosen based on petrological modelling (Gleeson et al., 2017) and geochemical analyses (Rooney et al., 2007).

Pressure-temperature conditions for Ziway olivines are less evident. Application of the olivine-spinel Al-exchange thermometer on these samples is not possible owing to the high Ti of olivine-hosted spinels (Section 3.3.1). Using the liquid thermometer of Putirka (2008b, Equation 15) via the Python 3 library Thermobar (Wieser et al., 2022b), carrier liquids record temperatures of 1100 °C, assuming 1 wt% H_2O; whole-rock compositions record hotter temperatures of 1150–1230 °C at the same H_2O contents. As temperature is one of the largest contributors to uncertainty in olivine diffusion chronometry (Morgan et al., 2006; Dohmen and Chakraborty, 2007), the Ziway magmatic temperature must be well characterised. However, the Putirka (2008b) thermometer has a substantial standard error of estimate of ±60 °C; other methods of constraining magmatic diffusion temperatures must be explored.

I run a series of Rhyolite-MELTS fractionation models (Gualda et al., 2012) using the whole-rock composition of Z58 scoria as a representative initial melt composition (Table 6.1). By considering the compositions of olivine crystallising from this starting melt, the magmatic conditions where the East Ziway olivine rims are in equilibrium with the melt can be determined. This composition is allowed to fractionate isobarically from 1300 °C to 1000 °C at pressures between 0.001–4.5 kbar in 0.5 kbar intervals and including 0.5–1.5 wt% H_2O in 0.5 wt% intervals. The limits of oxygen fugacity within MER magmatic systems, which range from FMQ-2 to FMQ+1 (Gleeson et al., 2017; Nicotra et al., 2021), are also considered.

The results of MELTS modelling are shown in Figure 6.3. At a fixed oxygen fugacity and variable H_2O contents, olivine reverse zone rims of $Fo_{77\pm3}$ (Figure 6.2) fractionate from melt Z58 at temperatures corresponding to ∼1130 °C with a standard deviation of ∼30 °C (Figure 6.3). Increasing the H_2O content of the melt has a strong effect on the interval of crystallisation for olivine; with increasing H_2O the crystallisation of olivine extends to higher pressures and lower temperatures (Figure 6.3A, C, and D). There is little effect of H_2O or pressure on the composition of crystallising olivine; changing H_2O or pressure affects the crystallisation interval for Ziway olivine rim compositions by ∼10 °C.

Oxygen fugacity has a strong effect on the composition of the crystallising olivine. At lower oxygen fugacities there is more less-oxidised Fe^{2+} in the melt relative to Fe^{3+}; as a result crystallising olivines are more Fe-rich. The interval for crystallising olivine rims therefore occurs at higher temperatures for lower oxygen fugacities (Figure 6.3B). Note also

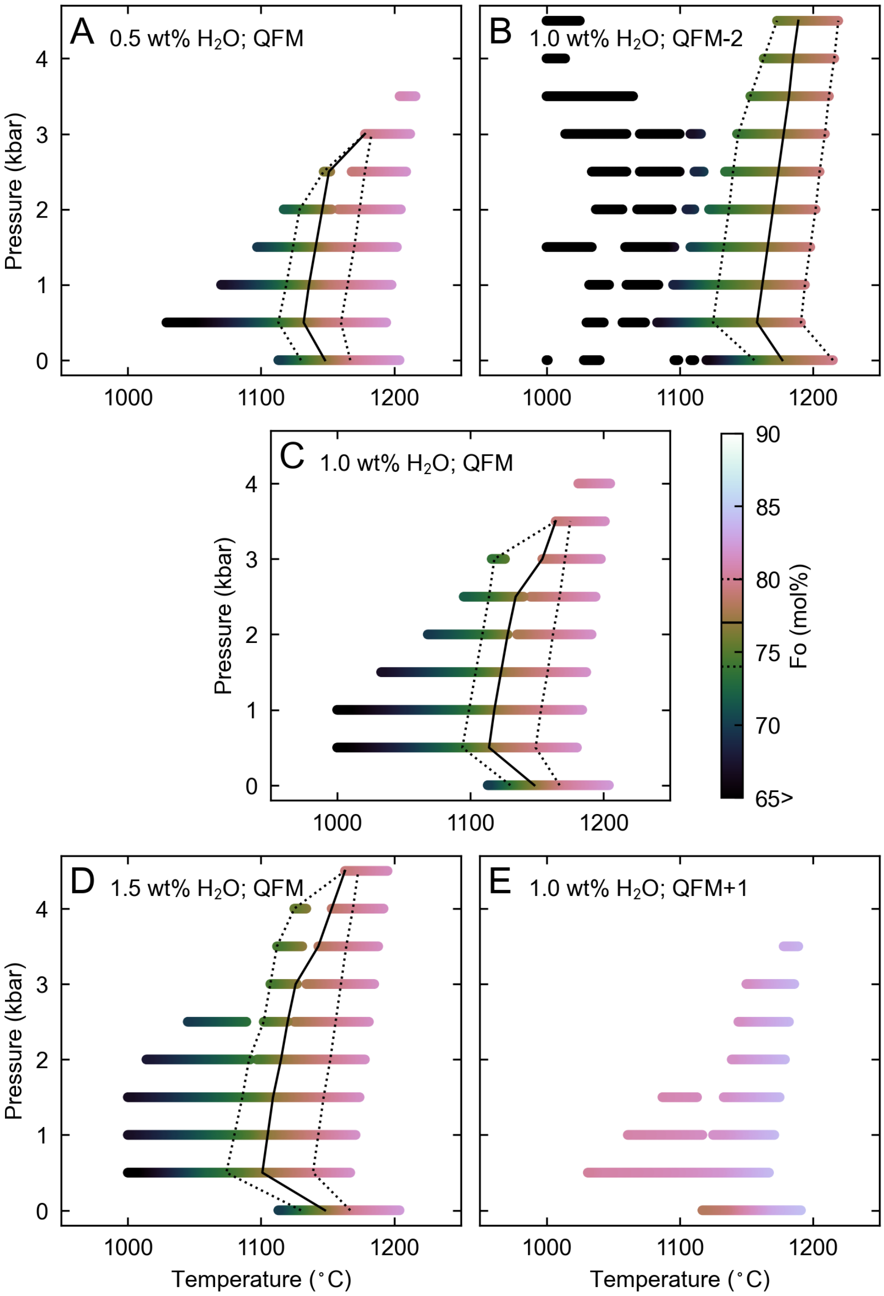

Figure 6.3: Rhyolite-MELTS models run at various starting conditions for composition Z58 from East Ziway (Gualda et al., 2012). Initial melt H_2O contents and oxygen fugacity conditions for each model are provided as annotations within each subfigure. Models are run at pressure intervals of 0.001 kbar up to a maximum pressure of 4.5 kbar (see Chapter 5). The solid black line marks the median rim composition of the reverse-zoned olivines of Fo_{77}, the dotted black lines mark 1σ of ±3 mol% Fo. Note that the model run at FMQ-2 (subfigure B) extends to fayalitic (Fe-rich) components of olivine, and that the model run at FMQ+1 (subfigure E) only achieves $Fo_{<80}$ at the lowest pressures.

that the abundance of Fe^{2+} at FMQ-2 means that Fe-rich olivine continues crystallisation to lower temperatures. Likewise, at higher oxygen fugacities, there is less Fe^{2+} available, and crystallising olivines are Mg-rich to the point where the composition of crystallising rims is not reproducible (Figure 6.3E).

Given these observations, I select a magmatic temperature constraint for East Ziway of 1130±30 °C, corresponding to the temperature range for crystallising olivine rims of $Fo_{77\pm3}$ at 1 wt% H_2O at the FMQ buffer (Figure 6.3C). These conditions best match the H_2O concentrations in rift basalts (Iddon and Edmonds, 2020, Chapter 5) and crystallisation expected at the FMQ buffer (Rooney et al., 2007; Gleeson et al., 2017). Because pressure does not have a strong effect on the crystallising interval or the diffusion timescales relative to temperature or oxygen fugacity (e.g., Morgado et al., 2017), I assume that olivine crystallisation occurs at 3 kbar, reflecting the depth of the melt intrusion zone observed in Chapter 5.

6.3.3 Diffusion timescales

AutoDiff provides Fe-Mg interdiffusion fits to 113 profiles and subprofiles in 59 MER olivines (47 subprofiles in 27 Boku olivines; 66 subprofiles in 32 East Ziway olivines; see Figure 6.4 for examples). These subprofiles are categorised based on their nature as described above (primarily normal-zoned, reverse zone on reverse rim, normal zone on reverse rim), and are all less than 160 μm in length.

Timescales from the three categories are shown in Figure 6.5, including propagated uncertainties from temperature, oxygen fugacity, and greyscale resolution. Propagated uncertainties in individual timescales (1σ) are of the order of 0.25 $\log_{10}$ units for both localities. All other compositional profiles collected from EPMA traverses across olivines were rejected during quality assurance, providing poor fits to AutoDiff either from growth-related zonation or excessive backscatter greyscale noise. Kernel density estimation in log-time is performed using Gaussian approximation (after Silverman, 2018) to determine bandwidth. This method is preferred to using histograms as histogram bin sizes will affect the apparent distribution of times (Rudge, 2008). Other methods more suitable for estimating the bandwidth of multimodal distributions were considered but ultimately were not chosen owing to the scarcity of data in some diffusional subsets (e.g., Sheather and Jones, 1991).

All timescales recorded in this study are less than a year long. The distributions of

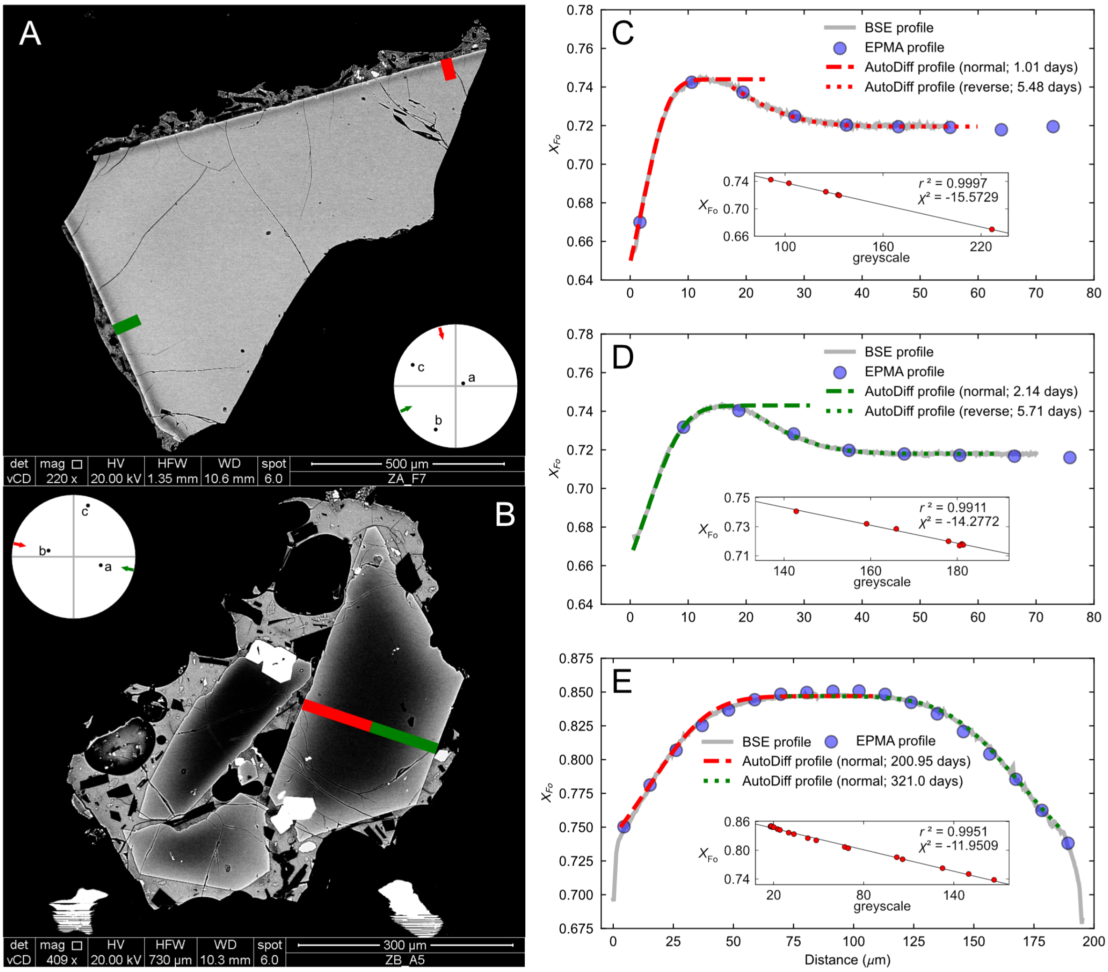

Figure 6.4: Example figure showing application of AutoDiff to representative olivine crystals. Subfigures A and B are respectively backscattered electron images of reverse-zoned and normal-zoned olivine crystals from East Ziway. Profile traverses are shown as the red and green lines. Inset figures show upper hemisphere projections of the orientation of the selected profile traverses (as red and green arrows) relative to the olivine crystallographic axes (a, b and c). Subfigures C and D show two probe and greyscale profiles taken along the rim of the olivine shown in subfigure A; subfigure E shows a single profile taken across the olivine shown in subfigure E. Inset figures depict the calibrations between forsterite content and backscatter electron contrast greyscale, and the r^2 and χ^2 of these fits. Note that the distances of the profiles shown in subfigures C and D differ from that of subfigure E.

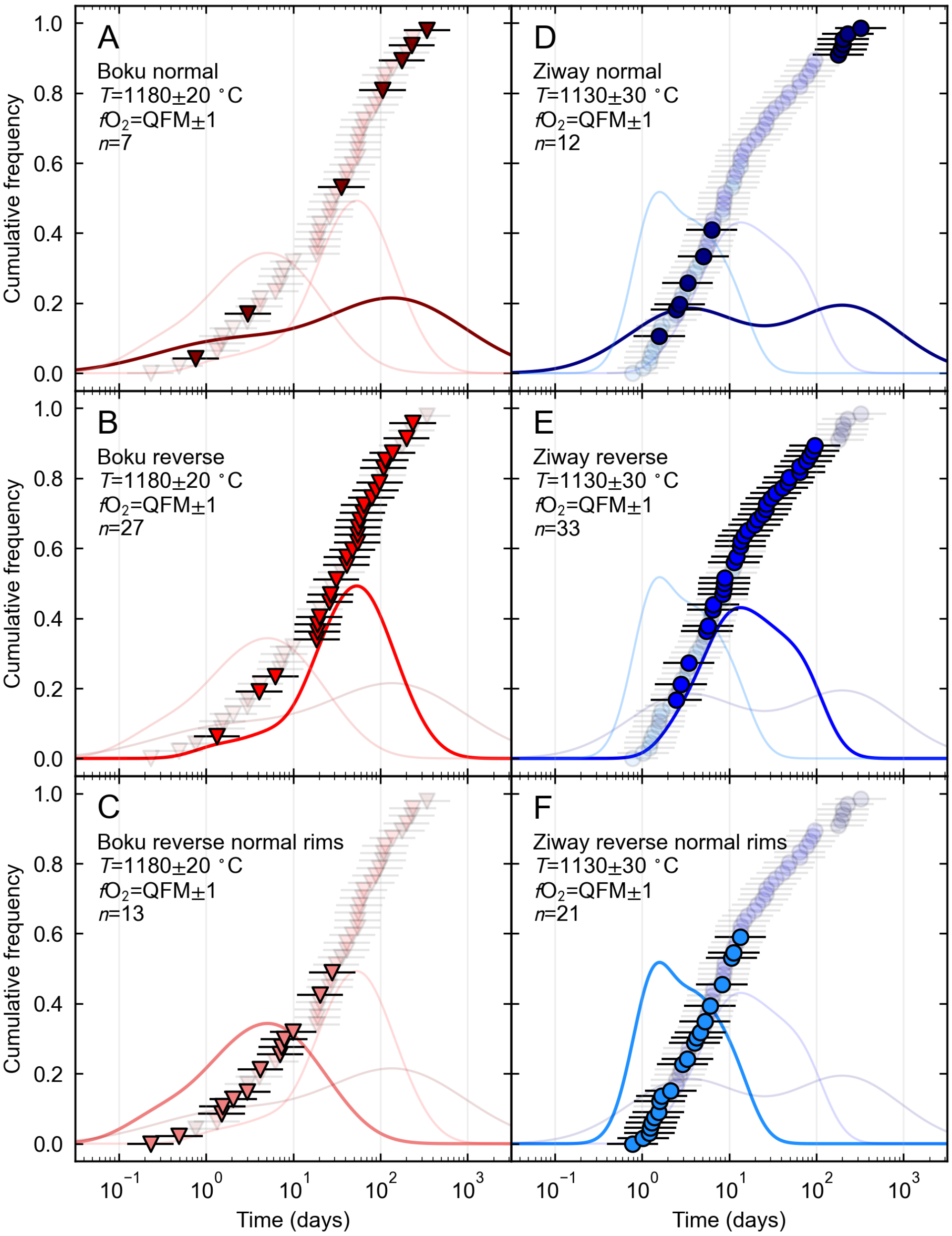

Figure 6.5: Cumulative frequency plots of Boku (A, B and C) and East Ziway (D, E and F) diffusion timescales. Plots are categorised depending on the nature of the subprofile. Uncertainties shown are 1σ. Kernel density plots within each subfigure are shown using Gaussian approximation to determine bandwidth. Relative probability density (the y-dimension of kernel density plots) is consistent across all subfigures.

timescales recorded by both normal-zoned and reverse-zoned olivines, shown in Figure 6.5 are markedly similar between the two localities. No correlation is seen between diffusion timescales and the Fo of crystal cores or rims within each subset. The rarer purely normal-zoned olivines have a near-bimodality to their timescales (Figure 6.5A and D); this is especially evident in the Ziway distribution, where one population records timescales of 1.58–6.24 days and the other 175–321 days (Figure 6.5D). Boku normal-zoned olivines also have a longer timescale population that return 106–343 days of chemical disequilibrium. However, while shorter timescales of 0.75–36 days are recorded by the remainder of the Boku olivines of this normal-zoned subset, the strong bimodality observed in the East Ziway distribution is less evident (Figure 6.5A).

Timescales recorded by reverse-zoned olivines from the normal and reverse part of the high Fo rim overlap for both localities, although the external normal portion of the rims on average record shorter timescales than the reverse portion of the rims (Figure 6.5B, C, E and F). Per individual crystal the diffusional gradient of the normal portion of the reverse rim is typically sharper than that of the reverse portion of the rim, and hence records a shorter timescale of diffusion (e.g., Figure 6.4 A, C and D). These reverse timescales also overlap with the shorter timescale populations of the primarily normal-zoned olivine subset (Figure 6.5A and D). Timescales for the reverse portion of Boku reverse-zoned olivines range from 1.33–236 days, with a log-mean of 39.8 days and 1 log-standard deviation range of 12.5–127 days (Figure 6.5B). This is slightly longer than the timescales recorded from reverse portions of reverse-zoned East Ziway olivines, which range from 2.46–94 days with a log-mean of 17.8 days and 1 log-standard deviation range of 6.30–50.2 days (Figure 6.5E). These reverse-zone timescales from the two localities are within mutual log-standard deviation of each other, although the East Ziway distribution is much broader.

Normal zones on the rim-ward side of reverse-zoned olivines have timescales with log-means and log-standard deviation ranges of 3.57 days and 0.89–14.3 days for Boku and 2.93 days and 1.23–6.96 days for Ziway (Figure 6.5C and F). These normal zones are accompanied by a significant change in composition over the final 5–10 μm towards the rim, and are therefore very likely to have a quenched growth component as mentioned above. If these rims do have a growth component, then the timescales extracted from the normal portion of the reverse rims should be considered upper limits to zone formation. This process is considered and modelled further below (Section 6.3.4).

Crystal	Cooling rate (°C/hr)	Growth rate (m s^{-1})	Cooling range (°C)
AA-D4-N	-0.05	1×10^{-12}	1160–1097
AA-D5-W	-0.1	4×10^{-12}	1160–1064

Table 6.2: Growth rate and cooling rates for dynamic diffusion modelling.

6.3.4 Models considering simultaneous diffusion, growth, and changing boundary conditions

As discussed above, the edge-buffered AutoDiff model presents a convenient 1-D solution to the composition-dependent diffusion equation. However, magmatic systems are seldom as well-behaved as the assumptions made in the diffusion model utilised in AutoDiff. The composition and temperature of the melt will change with time, and olivines will grow while Fe-Mg diffusion is active. The majority of the olivine crystals in this study show evidence that other processes may be active at the same time as diffusion. Dendritic overgrowths present on olivine rims are indicative of possibly concurrent crystal growth, diffusion, and crystallisation. As olivine crystals will form in thermally and compositionally evolving enviornments in the mid-crust, the melt from which olivine crystallises will change composition as diffusion and crystal growth take place, affecting the thermal behaviour of Fe-Mg diffusion and also the composition of crystallising overgrowths in olivine.

To incorporate all of these effects I utilise the methodology employed by Couperthwaite et al. (2021), who consider the concurrent effects of cooling, diffusion, crystal growth, and melt evolution. Simultaneous diffusion and crystal growth modelling is conducted using an iterative 1-D finite difference model coded in Microsoft Excel (Couperthwaite et al., 2021, D. Morgan, unpublished). The initial conditions of the system, including the olivine composition, starting magmatic temperature, oxygen fugacity, melt cooling rate, and crystal growth rate are specified. Diffusional fluxes between cells are calculated per incremental temperature step dictated by the cooling rate, and applied to each finite element. In addition to diffusional fluxes, linear growth, dependent on the equilibrium composition of olivine in the cooling host magma, is calculated for every temperature step. This new growth is applied to the model as a new finite element once the time elapsed is equivalent to the growth step.

The crystallising olivine composition as the melt cools is modelled using Petrolog3 (Danyushevsky and Plechov, 2011). The starting composition of NB-01, a primitive basalt from Boku (Table 6.1; Tadesse et al., 2019), was modelled to crystallise olivine, plagioclase,

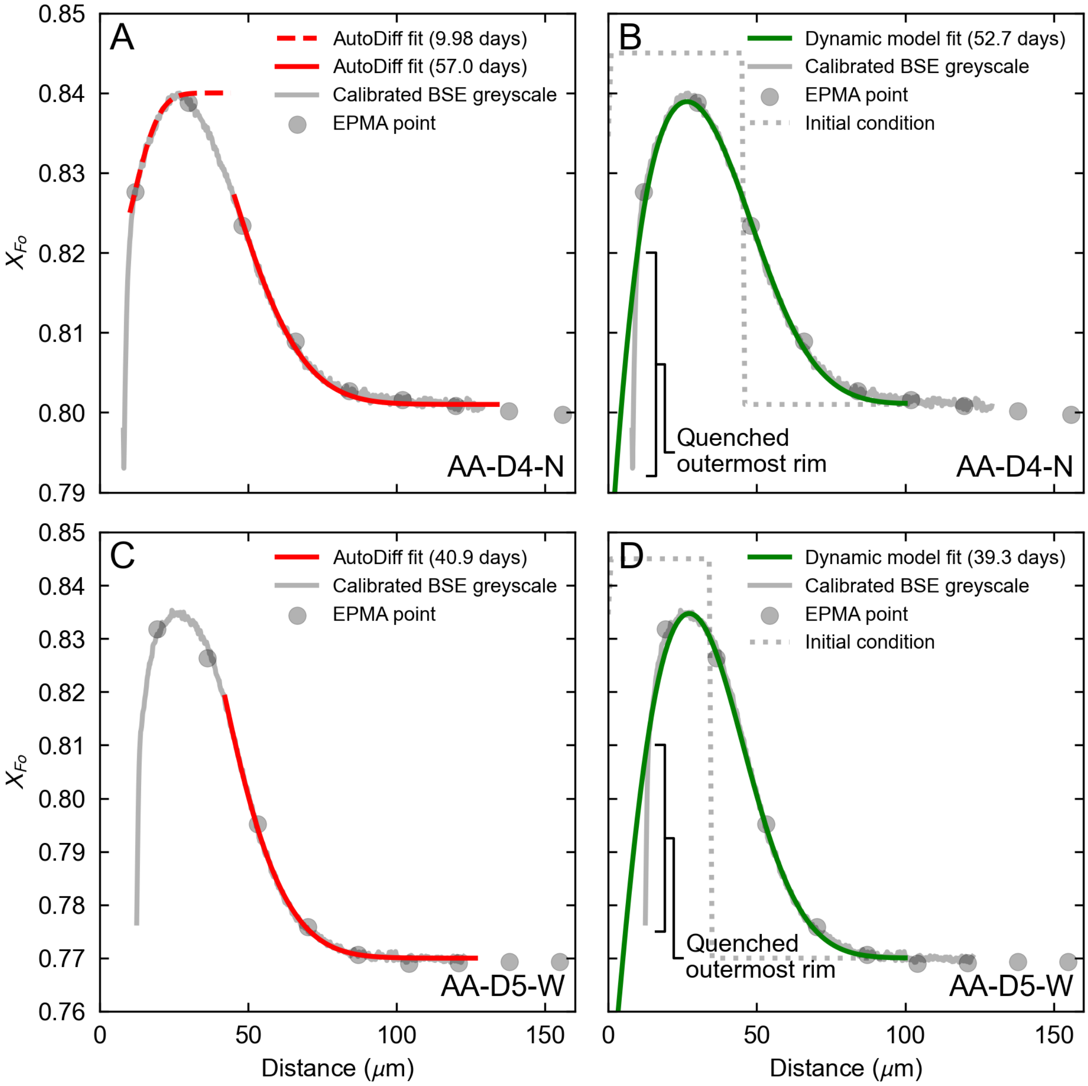

Figure 6.6: Comparison between olivine Fe-Mg diffusion timescales from AutoDiff and a dynamic model. Subfigures A and B show diffusional fits to olivine profile AA-D4-N with AutoDiff and the dynamic diffusion-growth model respectively; subfigures C and D depict the same for olivine profile AA-D5-W.

and clinopyroxene at the FMQ buffer at 3 kbar according to the fractionation models of Danyushevsky (2001). Olivine Fo is then parameterised as a function of melt temperature. As other mineral phases enter the basalt liquidus, the T-Fo curve will form kinks. As a result, for NB01, the parameterisation of olivine composition is divided into temperature intervals:

$$\text{Fo} = \begin{cases} 5.65 \times 10^{-4}T + 0.0249 & \text{if } 1402.7 \leq T < 1433.9 \\ 1.21 \times 10^{-3}T - 0.886 & \text{if } 1336.2 \leq T < 1402.7 \\ 2.17 \times 10^{-3} - 2.16 & \text{if } 1136.5 \leq T < 1336.2 \\ 2.53 \times 10^{-3} - 2.56 & \text{if } 1105.9 \leq T < 1136.5 \end{cases} \tag{6.11}$$

where T is magmatic temperature in K.

Diffusional modelling using this finite difference model was performed at a magmatic pressure of 3 kbar and oxygen fugacity corresponding to the FMQ buffer, as outlined above. Two good quality (low noise) reverse-zoned olivine profiles were selected for these advanced models: AA-D4-N and AA-D5-W, both from Boku. These profiles were iteratively fit by generating databases of olivine compositional profiles, ordered by time intervals, as a function of growth rate and cooling rate using the parameterisation of Equation 6.11. Profiles were assessed by eye to judge the quality of the fit, as computationally assisted fitting is not possible given the various parameters (see below).

Fits using this dynamic model are shown in Figure 6.6. The best fits to these two profiles require both growth and cooling; if only one of these effects is considered then the shape of the profile cannot be completely replicated. Growth is required to match the width of the high Fo olivine reverse rim, and cooling is necessary to achieve the lopsided sigmoidal shape observed in both profiles. Cooling rate is of the order of -0.1 °C hr^{-1}, and the initial growth rate is of the order 1×10^{-12} m s^{-1} (Table 6.2). Compared to cooling and growth rates determined for diffusing olivine in lava flows (e.g., 0.5 °C hr^{-1} and 2×10^{-11} m s^{-1} respectively; Couperthwaite et al., 2021) these rates can be considered slow, suggesting that cooling and growth occurred while still within the crust. That being said, the literature ranges for both olivine growth and cooling rate can be substantial (e.g., Jambon et al., 1992; Hammer, 2006). The values for growth and cooling rates are not independently supported by other observations in MER olivines, and determining the meaning behind these values is beyond the scope of the study outside of application within this model. However, the inclusion of these additional factors demonstrates that a single diffusional timescale, complemented with some degree of olivine growth, can match the observed compositional 'hump' observed in reverse-zoned olivines. The outermost rim of the two olivines considered are poorly fit with the model, which assumes a linear growth rate (Figures 6.6B and D); this discrepancy may arise from a decelerating growth rate or accelerated quenching.

Timescales considering both diffusion and growth can provide very strong fits to both the reverse and normal portions of reverse-zoned olivine profiles. Timescales recorded from these dynamic models are shorter than those yielded from AutoDiff, but within 1 log-sigma uncertainty (Figure 6.6). The primary downside to using this method is that one cannot, as of yet, automate this process using the Microsoft Excel code it is written within. All fits between model and data must be performed by eye, which is oftentimes a time-consuming and frustrating process. The major contributor to this necessity is the trade-off of several parameters in this model, such as the shape and magnitude of the initial condition, growth rate, cooling rate, and the melt evolution parameterisation used. These factors could result in several non-unique fits to the diffusional curve. Finally, in this model a linear growth rate is used, which fails to capture the behaviour of the outermost rims of the profiles (Figures 6.6B and D). More complex growth rate parameterisations are not considered as the bulk of the diffusional profile can be replicated with linear growth, and providing fits to the outermost parts of the profile would take substantial amounts of time for relatively little pay-off, especially given the lack of understanding concerning olivine cooling and growth rates. Full consideration of growth rate, melt cooling rate and diffusion could all be considered through the use of sampling algorithms, such as that described in Chapter 5, which have been used to determine diffusion timescales in Iceland (Mutch et al., 2021). Further investigation, which is beyond the scope of this study, will be necessary to develop a minimisation algorithm for this model which can appropriately determine diffusional timescales while also considering other factors in the magmatic system.

6.4 Discussion

6.4.1 Relating timescales to magmatic processes

Zoning patterns and AutoDiff timescales recorded from both Boku and East Ziway are alike (Figure 6.5), suggesting that similar magmatic processes affect different MER segments. It may therefore also be the case that these processes are common to other

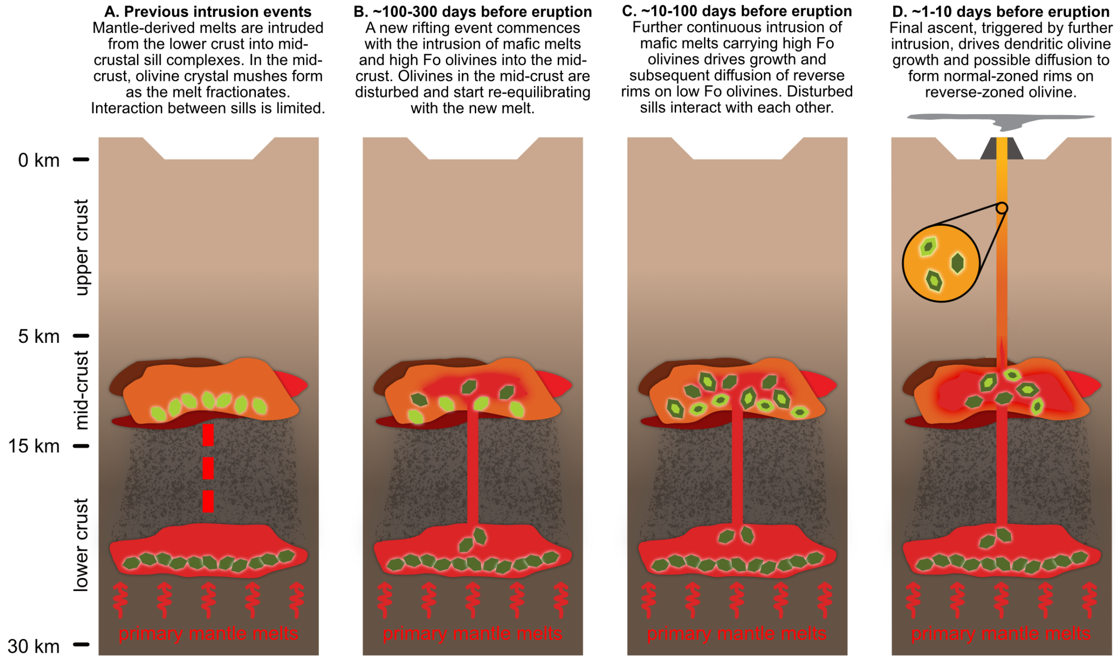

A. Previous intrusion events
Mantle-derived melts are intruded from the lower crust into mid-crustal sill complexes. In the mid-crust, olivine crystal mushes form as the melt fractionates. Interaction between sills is limited.

B. ~100-300 days before eruption
A new rifting event commences with the intrusion of mafic melts and high Fo olivines into the mid-crust. Olivines in the mid-crust are disturbed and start re-equilibrating with the new melt.

C. ~10-100 days before eruption
Further continuous intrusion of mafic melts carrying high Fo olivines drives growth and subsequent diffusion of reverse rims on low Fo olivines. Disturbed sills interact with each other.

D. ~1-10 days before eruption
Final ascent, triggered by further intrusion, drives dendritic olivine growth and possible diffusion to form normal-zoned rims on reverse-zoned olivine.

Figure 6.7: Cartoon illustrating the magmatic processes inferred from olivine Fe-Mg diffusion chronometry. Dark green olivines represent high Fo; light green olivines represent low Fo.

rifting magmatic segments; the implications of this are discussed below (Section 6.4.2). There are broadly three orders of magnitude in the timescales recorded both at Boku and East Ziway, which all correspond to a different subset of zoning pattern. The longest timescales on the order of 100 days are recorded in the MER sample set by high Fo normal-zoned olivines (Figure 6.5A and D). Reverse portions of reverse-zoned olivines differ slightly between Boku and East Ziway, but typically record timescales between 10–100 days; this timescale also coincides with another subset of primarily normal-zoned olivines (Figure 6.5A–D). The normal portion of reverse-zoned olivines, which may be affected by growth, primarily record timescales of less than 10 days (Figure 6.5 E and F).

These processes can be related to possible timescales of dyke intrusion and melt transport during an active episode of rifting in the MER. As reverse-zoned olivine cores are not representative of compositions near equilibrium with mantle-derived melts, it is likely that melt is already present in the mid-crust when the magmatic processes resulting in disequilibrum commence. Evidence of these earlier intrusion events may have completely removed through re-equilibration of the crystal with the host magma in the long periods between discrete magmatic rifting episodes (∼100 years; Ebinger et al., 2013), resulting in the near-homogeneous cores in olivine. This melt will have already fractionated olivine, which may reside in mid-crustal sill complexes as a crystal mush (Figure 6.7A). The longest timescales will coincide with the first emplacement of melt into these MER mid-crustal sill complexes during an intrusion episode (Figure 6.7B). This intruded melt will be more primitive than its surroundings, and will carry high Fo olivines which begin re-equilibrating Fo upon entering the new environment. The source of this melt will either be the lower crust or Moho, or possibly from a deeper reservoir within the mid-crust; as determined in Chapter 5 there is no apparent correlation between olivine Fo and storage pressure.

Intrusion of primitive, high-Mg# melt will trigger the growth of high Fo olivine rims on crystals that have previously formed in the mid-crust (Figure 6.7C). These olivines have cores that are lower Fo than the normal-zoned olivines recording the longest timescales, and are likely to have fractionated to form a crystal mush in mid-crustal sill complexes. Intrusion of deeper mafic melts, and the seismicity that accompanies intrusion, will disturb these systems, potentially causing mush overturn (e.g., Hartley et al., 2016) and gravitational destabilisation of olivines (e.g., Pankhurst et al., 2018). The perturbation of olivines by this influx of mafic melt will result in the growth of high Fo rims; subsequent relaxation of sharp growth boundaries will occur as diffusion commences between rim and core. The broad range of olivine timescales recorded by reverse rims may suggest that mafic influx occurs almost continuously throughout the mid-crustal sill complex, or could represent the perturbation of different sills during a single intrusion episode. Indeed, the wide range of olivine core Fo observed, particularly at East Ziway, may hint at a distributed network of semi-isolated sills that can also generate variable trace element concentrations in melt inclusions (Chapter 5), which each experience their own timeframe for mafic intrusion.

The rim-ward normal zone observed on reverse-zoned olivines, with a maximum timescale of ∼30 days with most timescales between <1–10 days, most likely forms during final magmatic ascent leading up to eruption (Figure 6.7D). The development of this reverse rim appears to be much more constrained at East Ziway compared to Boku, however if this rim does form primarily from growth then it may be the case that timescales of this zoning may be similar, as zoning from growth will form faster than diffusion only. The influence of some growth is also evident from the dendritic growth patterns along the edges of olivine crystals. The timescales recorded from the normal portions of these rims should therefore be considered maxima only.

The compositions of East Ziway olivines are typically more evolved than those at Boku, and have a wider range of compositions (Figure 6.2). While similar processes do occur at these two settings the more-evolved state of East Ziway olivines and carrier melts may suggest that they have had longer to fractionate and cool between eruptive episodes. Intrusive events at East Ziway may therefore occur at a lower rate than Boku, which may be correlated to the position of Boku further north, reflecting how the maturity of the MER, and the EARS as whole, varies along rift. Speculatively, a more mature rift segment may experience rifting episodes at a more rapid rate than one which is less mature.

Timescales from diffusion can be compared to estimates of magma ascent in the MER. Assuming an ascent rate of 0.1 m s^{-1}, the minimum speed necessary for a explosive eruption typical of monogenetic volcanism (Cassidy et al., 2018), and storage depths of 5–15 km in the MER crust (Chapter 5), timescales for magma ascent are calculated to range from 0.58–1.74 days, which falls towards the shorter end of the diffusion timescales recorded for normal portions of reverse-zoned olivines. This calculation suggests either that explosive volcanism in the MER is possible through slower ascent rates, or that the assumed ascent rate of 0.1 m s^{-1} is achieved only during final acceleration in the eruptive conduit with crustal transit occurring at lower speeds. In either case, the timescales recorded in the sample set from these normal rims are likely to be affected by processes other than diffusion. It may also be likely that ascent from the mid-crust is punctuated with several hiatuses. All of these scenarios are possible; at some volcanic settings, magma ascent velocities on the order of 0.01 m s^{-1} can result in scoria cone-forming eruptions (Cassidy et al., 2018), and as discussed above it is likely that the most rim-ward portions of olivine crystals have been affected by late-stage growth which can mimic the sigmoid of a diffusion-only compositional zone (Costa et al., 2020). Hiatuses in magmatic ascent could possibly be tracked by distinct chemical populations of melt inclusions during late-stage olivine overgrowth which will record concurrent volatile degassing and melt evolution; no correlation between major element composition and calculated pressures are observed in my Boku melt inclusions (Chapter 5), and further consideration of ascent pathways is beyond the scope of this study.

6.4.2 Pre-eruptive intrusion in other active rift settings

A parallel can be drawn between diffusion timescales from this study and timescales recorded by seismic and field observations of previous magmatically driven rifting events. This comparison is illustrated in Figure 6.8, which presents the diffusion timescales of this study alongside dyke intrusion intervals collated from the rifting events in Dabbahu, Afar

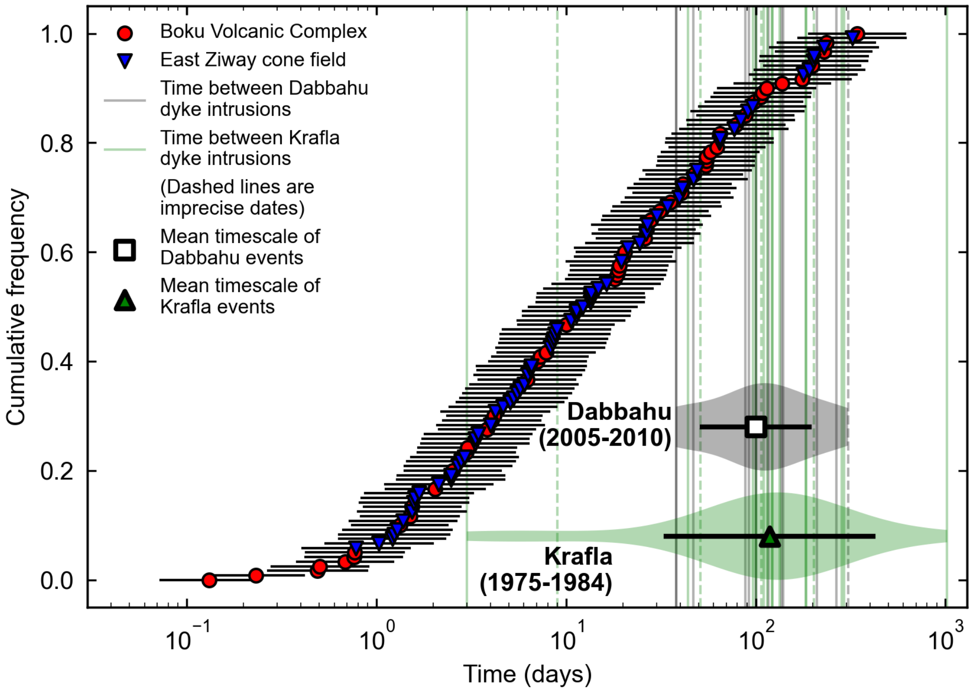

Figure 6.8: Cumulative frequency plot of all timescales collected in this study compared with dyke injection intervals at Dabbahu (2005–2010) and Krafla (1975–1984). Intervals between rifting events are measured from the start of each intrusion event. Dates of intrusions are collated from Grandin et al. (2010, 2011) for Dabbahu and Buck et al. (2006) for Krafla; where dates are given as the month only the start of the month is assumed to calculate time intervals – these timescales are shown as dashed in the figure. Violin plots illustrate the distribution of Dabbahu and Krafla timescale intervals. Bold markers and uncertainty intervals mark the log-mean±one log-standard deviation.

(2005–2010, Ferguson et al., 2010; Ebinger et al., 2010; Grandin et al., 2010, 2011) and Krafla, Iceland (1975–1984, e.g., Buck et al., 2006).

While overall episodes of active rifting can take place over the course of several years (Wright et al., 2012; Ebinger et al., 2013, e.g.,), individual episodes often comprise multiple periods of magmatic intrusion, which have been documented at several subaerial rifts via concurrent seismic activity during intrusion (e.g., Wright et al., 2012). These temporally distinct intrusive periods individually affect different parts of the overall rifting segment, with most melt involved in rifting episodes remaining unerupted (Ferguson et al., 2010). Intervals between seismic events accompanying intrusion events in both Afar and Iceland are on the timescale of several months (e.g., Wright et al., 2012), which matches the longer diffusion timescales recorded by the reverse rims of my reverse-zone olivines and primarily normal-zoned olivines (Figure 6.8). During the episode itself, intrusive activity during the phases of the 2005–2010 Dabbahu rifting episode, involving faulting and magmatic intrusion, is recorded on the scale of hours to days (Ebinger et al., 2010; Ebinger et al., 2013). These short timescales are comparable to the shortest timescales in my sample set, in particular those of the normal portions of reverse rims.

It is therefore likely that the processes recorded by olivine Fe-Mg diffusion are representative of disequilibrium processes which can trigger dyke intrusion events during a rifting episode. Melts, intruded over timescales of several months, will fractionate in the crust until pathways to the surface can be opened. In the meantime, percolating mafic melts can trigger the formation and subsequent diffusion of high Fo reverse rims in olivine. Subsequent intrusion events in the following months can trigger the final eruption of these melts. It should, however, be noted that reverse zoning is neither evident in Dabbahu olivines (Chapter 3), nor in olivine crystals from the Krafla volcanic system (Rooyakkers et al., 2022, although not obtained from the Krafla Fires basalts of 1975–1984). While timescales of intrusion may be of a similar magnitude, magmatic processes governing how diffusional timescales may differ between different settings.

Timescales between rifting cycles in mature magmatic rift segments, inferred from historical records, are believed to be on the scale of ∼100 years (Ebinger et al., 2013). Given that the timescales from olivine diffusion chronometry are all less than a year, it is highly unlikely that processes occurring between dyke intrusions are recorded.

6.5 Conclusions

Dyke intrusion is a fundamental magmatic process in continental rifts that facilitates plate break-up. Using Fe-Mg diffusion chronometry on MER olivine crystals I have determined the timescales of crystal storage and transport prior to scoria cone-forming eruptions. Samples, collected from the Boku Volcanic Complex and East Ziway cone fields, reveal that MER olivines can be broadly divided into two compositional subsets – those with primarily normal zoning, and those with a strong reverse rim. Normal-zoned olivines commonly have higher Fo cores than reverse-zoned olivines, and record timescales of 100 days or longer. The reverse portion of reverse-zoned olivines typically records timescales of 10–100 days, with a normal-zoned quench growth component recording ∼10 days or less. The high Fo normal-zoned population of olivines at both of these settings are indicative of the transfer of more primitive melts into the mid crust, which simultaneously triggers reverse zone growth and subsequent diffusion in lower Fo olivines already present in the mid-crust. Dendritic overgrowth, and the normal zones that form as a result, develops only during magma ascent immediately prior to eruption. The broad range of diffusion timescales suggests that olivines may originate from a number of sills in the mid-crust, which are cross-cut by intruding dykes during an active rifting episode. Constraints on timescales for pre-eruptive mafic intrusion are consistent with timescales of dyke intrusion observed at active rift settings, such as Afar and Iceland.

Chapter 7

Conclusions and further work

The motivation of this project was to explore the processes of melt generation, transport, and storage driving magmatic intrusion in the Main Ethiopian Rift (MER). It has been established through extensive geophysical study that intrusion of basaltic melts into the crust are a primary driver of extension during late-stage continental rifting. A better understanding of basaltic activity in the Main Ethiopian Rift through the avenues of petrology and geochemistry allows for a more complete and robust picture of rift-related magmatism, a principal driver of incipient oceanic spreading. While previous geochemical studies have explored the evolution of basalts to rhyolites under central volcanoes (e.g., Gleeson et al., 2017; Fontijn et al., 2018; Hutchison et al., 2018), this study has primarily focussed on basaltic scoria from flank zones of these centres. By considering these basalts, which have avoided the fractionation and evolution under central volcanoes, the conditions of the melting mantle and deepest crustal storage can be assessed.

7.1 Project summary

This project consists of three major studies, each contributing to illustrating an overarching journey following the ascent of basalts through the Earth's mantle and crust before the eruption of rift lavas.

7.1.1 Rift geodynamics of the Ethiopian mantle

The first study, comprising Chapters 3 and 4, determined the temperature at which rift magmas begin to crystallise using a petrological geothermometer, the olivine-spinel Al-exchange thermometer (Coogan et al., 2014). This thermometer is selected as olivine is one of the first phases to crystallise from a mantle-derived melt. Erupted MER basalts crystallise olivine of Fo_{86} and lower at mean temperatures of 1177±16 °C, which is cooler than the maximum crystallisation temperature at the Dabbahu Rift in Afar of 1344°C, and cooler than the highest temperatures recorded for MORB olivine crystallisation (∼1270–1280 °C). By back-projecting along expected liquid lines of descent to high Fo in equilibrium with primary mantle-derived melts I determined primary olivine crystallisation temperatures for the MER and Afar.

Using these temperatures in conjunction with erupted basalt rare-earth element compositions and geophysical observations, I co-developed a mantle melting model (pyMelt) that could be used to relate the thermal and lithological conditions of the mantle to melt thicknesses and olivine crystallisation temperature. Through a combined integration of melt fraction with mantle composition I expanded pyMelt to support calculations for partitioning of trace elements of mantle lithologies.

By inverting this upgraded pyMelt model, I obtain posterior probability distributions for the most likely mantle conditions that can reproduce observations of rift geophysics and lava geochemistry. From these results I conclude that the temperature of the Ethiopian mantle is elevated by ∼100 °C relative to ambient mid-ocean ridge mantle. This gives a potential temperature of the Ethiopian mantle of ∼1500 °C, which is consistent across both Ethiopia and Afar and in agreement with previous estimates of elevated Ethiopian mantle temperature (Rooney et al., 2012c; Ferguson et al., 2013b; Armitage et al., 2015).

Furthermore, I establish that the primary difference between the MER and Afar Rift is lithospheric thickness, which varies between ∼90 km under the MER to ≤70 km at Afar. This difference in lithospheric thickness, which is inferred from my model reproducing the amount of melt present in the MER and Afar crust, can be attributed to a more evolved rift system in Afar. There may also be compositional differences between the MER and Afar mantle, which is possibly related to the centring of a mantle plume under Afar (Rooney et al., 2012a). While signatures of deep melting in the garnet-stable field of the mantle are present at both the MER and Afar, the necessity of matching the volumes of melt at Afar necessitate the presence of more fusible melting mantle lithologies. While my inversions for Afar struggle to match light rare-earth elements, small-fraction melts, possibly derived from the thermal destabilisation of the lithosphere, can contribute sufficient light rare-earths to asthenospheric melts as they leave the convecting mantle. My results therefore demonstrate that principal variations between MER and Afar magmatism can be attributed to lithospheric thickness, with consistent mantle temperatures across Ethiopia at ∼1500 °C.

This study is the first to explore melt generation processes under the MER and Afar Rift using a petrological method. By applying this approach I provide a new independent estimate of mantle potential temperature, which considers not only a wide variety of geophysical and geochemical constraints but additionally their uncertainties, which are propagated into the final estimates of mantle temperature and composition. The implication of possible compositional differences in the mantles under the MER and Afar, and the potential for contribution from small-fraction lithospheric melts, paves paths for geochemical research that may be explored in the future.

7.1.2 Focussed magmatic intrusion into the Ethiopian crust

The second study, outlined in Chapter 5, concerned the major element, trace element, and volatile composition of olivine-hosted basaltic melt inclusions from a monogenetic cone field in the Main Ethiopian Rift. Melt inclusions, small parcels of early, are primitive melts that are entrapped within growing crystals at depth within the rift crust. Melt inclusions are undegassed compared to erupted lavas, and therefore contain elevated concentrations of volatile elements such as CO_2 and H_2O. Understanding the empirical relationship between melt pressure, temperature, and composition can permit us to determine the pressures at which natural basaltic melts saturate in volatiles, i.e., the pressure conditions at which melts are stored in the crust.

Using volatile solubility models, pressures are determined for the Ethiopian rift to yield a focussed zone of intrusion at 2.5–4.5 kbar depth, or 10–15 km. Furthermore, the trace element variability of these melt inclusions is diverse. As their compositional ranges cannot be replicated by fractionation of a single parental melt, melt inclusions therefore record evidence of parental melt heterogeneity that is preserved through storage in discrete environments. Combining observations from volatile saturation models and these melt inclusion compositions, the igneous structure of the crust is implied to comprise mid-crustal focussed sill complexes, which coincide with geophysical crustal anomalies (e.g., Whaler and Hautot, 2006; Cornwell et al., 2006) and a numerically modelled crustal ductile zone (Muluneh et al., 2020). Observations of CO_2 degassing at the rift surface from soil surveys (Hunt et al., 2017) can be matched by the passive degassing of melts intruded into this zone as determined from melt inclusion CO_2 systematics with incompatible trace elements of similar mantle-melt compatibility, such as Ba and Rb.

The results of this study have important implications for the distribution of heat and magmas in the Ethiopian crust during rifting. Melt, present at mid-crustal pressures, will thermo-mechanically weaken this part of the rifting crust preferentially relative to the upper and lower crust. Exploring how this crustal ductile weak zone behaves in response to extensional stresses relative to more brittle portions of the crust may be a topic for future numerical models of rift deformation. A more widespread study of melt inclusions which do account for the CO_2 entrapped within the inclusion bubble will further resolve the position of sill complexes in the rifting crust, and confirm the ubiquity of mid-crustal sill complexes in the MER. Finally, future geophysical studies may aim to complement my findings by resolving the position of sill complexes within MER magmatic segments through higher resolution methods (if possible).

7.1.3 Olivine diffusion chronometry

The final study, discussed in Chapter 6, ascertains the timescales of dyke intrusion into mid-crustal sill networks during rifting episodes. In order to determine this I use olivine Fe-Mg diffusion chronometry, which utilises the diffusion of the olivine Fe-Mg solid solution within a crystal in thermal or chemical disequilibrium to obtain timescales of said disequilibrium.

Olivine crystals from the Boku and East Ziway cone fields of the MER show significant evidence for pre-eruptive disequilibrium. The foremost of this evidence is the presence of compositional zoning, which takes the form of both low Fo rims around high Fo cores, and high Fo reverse rims around lower Fo olivine cores; this reverse-zoning is prevalent in crystals from both localities, suggesting that similar pre-eruptive processes occur at MER magmatic segments. I convert compositional profiles into timescales of diffusion using the AutoDiff algorithm, which correlates observed profiles to model profiles generated using finite-difference software. Diffusion timescales from olivines that are primarily normal-zoned are near bimodal, with one well-defined peak at $\sim$100 days. The other normal-zoned timescales overlap with reverse-zone timescales, which mostly range from 10–100 days. Normal-zoned olivines therefore record the earliest intrusion in the sill system, which triggers the growth of reverse zones in olivines already present in the mid-crust. Normal-zoned diffusion of reverse rims recording $<$10 days, likely coincident with late-stage growth, occurs only during ascent immediately prior to eruption.

My results indicate that petrological constraints on the timescales of magmatic processes occurring melt intrusion and transport in rift settings can provide an alternate dimension to understanding pre-eruptive magmatic processes which is observed primarily through seismic observations. Timescales of intrusion during rifting episodes in Iceland and Afar suggest that dykes intrude with a periodicity of several months (Wright et al., 2012). This timescale correlates to the maximum olivine Fe-Mg diffusion timescales recorded for both MER localities in this study. The coinciding of these timescales may suggest that similar magmatic processes that drive eruption of monogenetic cones in these rift settings may be operating at the present day in actively rifting regions of the Earth. The observations from olivine crystals collected from the MER may therefore provide insights into the magmatic systems operating under rift segments.

7.2 Suggestions for further work

The studies that contribute to this thesis facilitate several possible further research projects, which are summarised below.

7.2.1 Exploring Ethiopian mantle lithological and compositional heterogeneity

Chapters 3, 4 and 5 highlight the implications of a lithologically heterogeneous mantle on erupted lavas and melt inclusions. Mantle compositional heterogeneity can not only directly affect the major element, trace element, volatile element, and isotope composition of products of melting (e.g., Stracke et al., 2005; Shorttle and Maclennan, 2011; Shorttle et al., 2014; Stracke et al., 2019), but can also affect the thermal pathway undertaken by the mantle as it decompresses and melts (Matthews et al., 2021). Such mantle heterogeneity can arise from the presence of a mantle plume (e.g., Herzberg, 2011), such as that under Afar which has induced isotopic heterogeneities (Rooney et al., 2012a).

Future work can aim to provide further constraints on the character of lithological variability in the Ethiopian mantle. Work performed in Iceland has aimed to unravel the nature of multiple lithologies in the mantle by estimating melt contributions from mantle pyroxenites, primarily through observations of major and trace elements made in the most primitive basalt compositions (Shorttle and Maclennan, 2011; Shorttle et al., 2014). Difficulty in pursuing such ambitions may be restricted by a limited number of Ethiopian basalt samples that are considered primitive (MgO>9.5 wt%; Shorttle and Maclennan, 2011); consulting the GEOROC database of Ethiopian basalts, only 21 of 424 (5%) basaltic-basaltic andesite samples (SiO_2 <57 wt%) with characterised major element concentrations and Nb/Zr (a measure of mantle source heterogeneity) have MgO greater than the 9.5 wt% threshold. Similar observations may arise by performing a wider scale study of Ethiopian melt inclusions, complementing the results recorded in Chapter 5; data must therefore be harvested from primitive melt inclusions such as those considered in this study in order to gauge major and trace element diversity.

New approaches can provide high resolution isotope data from melt inclusions. One potential strand of this research was to analyse digested olivine-hosted melt inclusions using thermal ionisation mass spectrometry (TIMS). A recent development in mass spectrometry has been the production of $10^{13}\Omega$ resistors (Koornneef et al., 2014), which generate a 100× greater output voltage compared to lower resistance $10^{-11}\Omega$ amplifiers that are commonly used to analyse bulk rock. As an increase in resistance generates a corresponding square-root-increase in noise, an overall 10-fold improvement of signal-to-noise ratio is achieved (Koornneef et al., 2014). A benefit of this advancement in the field of igneous petrology is the high-precision resolution of isotope ratios (e.g., $^{87}Sr/^{86}Sr$, $^{143}Nd/^{144}Nd$) in very low mass samples (as low as 10s pg) by TIMS (Koornneef et al., 2014; Koornneef et al., 2015).

A key result of Chapter 5 is that melts arriving in the mid-crustal weak zone of the MER are compositionally diverse. This diversity may be the consequence of possible lithological and compositional mantle heterogeneity (as discussed in Chapters 3 and 4), or may arise from unmixed fractional mantle melts which are also compositional variable (Gurenko and Chaussidon, 1995). An isotopic study of primitive (high MgO) MER melt inclusions can resolve the mantle source endmembers of Ethiopian basalts, and separate influences from the depleted MORB mantle and the Afar plume that can so far only be determined from whole-rock basalts (Rooney et al., 2012a).

7.2.2 Application of experimental rehomogenisation to Ethiopian melt inclusions

The research undertaken in Chapter 5 has been coincident with significant advancements in the methodology used to quantify melt inclusion volatiles. In addition to the developments in Raman spectroscopy methodology discussed in Chapter 5 (e.g., Lamadrid et al., 2017; DeVitre et al., 2021b, 2022), comparisons with melt inclusions analysed by

SIMS after high-pressure rehomogenisation could prove useful in resolving the total CO_2 within an inclusion. Pressurising an inclusion at high temperature will re-dissolve the bubble into the basaltic melt; quenching this rehomogenised system will entrap all CO_2 in the bubble within the frozen glass (Rasmussen et al., 2020). In this way, the uncertainties involved with Raman spectroscopy can be avoided as only SIMS will be necessary to determine inclusion CO_2. Furthermore, this technique is possible on melt inclusions that have been slowly cooled and are subsequently crystalline (e.g., Mironov et al., 2015). The caveats of rehomogenisation include experimentally induced post-entrapment crystallisation or dissolution of the host crystal, which will affect the composition of the original melt inclusion, and the possible diffusion of other volatiles into and out of the host. One such example is H_2O diffusion, which can be rapid (Bucholz et al., 2013). H_2O loss can, however, be countered through hydration of the matrix surrounding the crystal-inclusion system (Mironov et al., 2015; Rasmussen et al., 2020).

During the course of this project, a subset of 10–20 olivine crystals hosting melt inclusions from Boku and East Ziway were sent to Lamont-Doherty Earth Observatory, Columbia University for a collaborative project with Anna Barth, Daniel Rasmussen, and Terry Plank. The aim of this collaboration was to compare the CO_2 concentrations obtained from Raman spectroscopy and SIMS with concentrations of melt inclusions that had been rehomogenised under pressure. A number of these crystals had had their bubbles analysed by Raman spectroscopy; others were from the Ziway Lake region and hence had crystalline melt inclusions. Unfortunately, this project was shelved owing to the COVID-19 pandemic. A future research path may revive this project to assess possible differences between CO_2 assessed via Raman spectroscopy and those from rehomogenisation, a concept which while previously explored by Rasmussen et al. (2020) could be further tested. Another potential line of study could assess whether the focussed sill intrusion zone described in Chapter 5, obtained from observations of total melt inclusion CO_2, is common to other MER magmatic segments. This could be accomplished through the rehomogenisation of crystalline olivine and plagioclase-hosted melt inclusions from Abaya Lake and East Ziway scoriae, which could not be assessed by Raman and SIMS unlike glassy Boku inclusions. Observations of total CO_2 from other rift segments would support the findings of Chapter 5 and provide more evidence for a common depth of rift sill development as suggested from seismic anisotropy (Chambers et al., 2021).

Chapter 8

References

Abebe, B., Acocella, V., Korme, T., and Ayalew, D. (2007). Quaternary faulting and volcanism in the Main Ethiopian Rift. *Journal of African Earth Sciences*. The East African Rift System: Dynamics, Evolution and Environment 48 (2):115–124.

Abebe, T., Mazzarini, F., Innocenti, F., and Manetti, P. (1998). The Yerer-Tullu Wellel volcanotectonic lineament: a transtensional structure in central Ethiopia and the associated magmatic activity. *Journal of African Earth Sciences*. Aspects of Tensional Magmatism 26 (1):135–150.

Acocella, V, Korme, T, Salvini, F, and Funiciello, R (2003). Elliptic calderas in the Ethiopian Rift: control of pre-existing structures. *Journal of Volcanology and Geothermal Research* 119 (1):189–203.

Acton, G. D., Stein, S., and Engeln, J. F. (1991). Block rotation and continental extension in Afar: A comparison to oceanic microplate systems. *Tectonics* 10 (3):501–526.

Adams, A., Nyblade, A., and Weeraratne, D. (2012). Upper mantle shear wave velocity structure beneath the East African plateau: evidence for a deep, plateauwide low velocity anomaly. *Geophysical Journal International* 189 (1):123–142.

Agostini, A., Bonini, M., Corti, G., Sani, F., and Mazzarini, F. (2011). Fault architecture in the Main Ethiopian Rift and comparison with experimental models: Implications for rift evolution and Nubia–Somalia kinematics. *Earth and Planetary Science Letters* 301 (3):479–492.

Allison, C. M., Roggensack, K., and Clarke, A. B. (2019). H_2O–CO_2 solubility in alkali-rich mafic magmas: new experiments at mid-crustal pressures. *Contributions to Mineralogy and Petrology* 174 (7):58.

Armitage, J. J., Ferguson, D. J., Goes, S., Hammond, J. O. S., Calais, E., Rychert, C. A., and Harmon, N. (2015). Upper mantle temperature and the onset of extension and break-up in Afar, Africa. *Earth and Planetary Science Letters* 418:78–90.

Aspinall, W., Auker, M., Hincks, T., Mahony, S., Nadim, F., Pooley, J., Sparks, R. S. J., and Syre, E. (2011). Volcano hazard and exposure in GFDRR priority countries and risk mitigation measures. Tech. rep. 0100806-00-1-R, p. 309.

Aster, E. M., Wallace, P. J., Moore, L. R., Watkins, J., Gazel, E., and Bodnar, R. J. (2016). Reconstructing CO_2 concentrations in basaltic melt inclusions using Raman analysis of vapor bubbles. *Journal of Volcanology and Geothermal Research* 323:148–162.

Ayalew, D., Jung, S., Romer, R. L., Kersten, F., Pfänder, J. A., and Garbe-Schönberg, D. (2016). Petrogenesis and origin of modern Ethiopian rift basalts: Constraints from isotope and trace element geochemistry. *Lithos* 258-259:1–14.

Ayele, A., Stuart, G., and Kendall, J.-M. (2004). Insights into rifting from shear wave splitting and receiver functions: an example from Ethiopia. *Geophysical Journal International* 157 (1):354–362.

Ball, P. W., White, N. J., Maclennan, J., and Stephenson, S. N. (2021). Global influence of mantle temperature and plate thickness on intraplate volcanism. *Nature Communications* 12 (1):2045.

Bastow, I. D., Pilidou, S., Kendall, J.-M., and Stuart, G. W. (2010). Melt-induced seismic anisotropy and magma assisted rifting in Ethiopia: Evidence from surface waves. *Geochemistry, Geophysics, Geosystems* 11 (6).

Bastow, I. D. and Keir, D. (2011). The protracted development of the continent–ocean transition in Afar. *Nature Geoscience* 4 (4):248–250.

Bastow, I. D., Keir, D., and Daly, E. (2011). The Ethiopia Afar Geoscientific Lithospheric Experiment (EAGLE): Probing the transition from continental rifting to incipient seafloor spreading. In: *Geological Society of America Special Papers*. Vol. 478. Geological Society of America, pp. 51–76.

Bastow, I. D., Nyblade, A. A., Stuart, G. W., Rooney, T. O., and Benoit, M. H. (2008). Upper mantle seismic structure beneath the Ethiopian hot spot: Rifting at the edge of the African low-velocity anomaly. *Geochemistry, Geophysics, Geosystems* 9 (12).

Bastow, I. D., Stuart, G. W., Kendall, J.-M., and Ebinger, C. J. (2005). Upper-mantle seismic structure in a region of incipient continental breakup: northern Ethiopian rift. *Geophysical Journal International* 162 (2):479–493.

Bendick, R., McClusky, S., Bilham, R., Asfaw, L., and Klemperer, S. (2006). Distributed Nubia—Somalia relative motion and dike intrusion in the Main Ethiopian Rift. *Geophysical Journal International* 165 (1):303–310.

Benoit, M. H., Nyblade, A. A., Owens, T. J., and Stuart, G. (2006a). Mantle transition zone structure and upper mantle S velocity variations beneath Ethiopia: Evidence for a broad, deep-seated thermal anomaly. *Geochemistry, Geophysics, Geosystems* 7 (11).

Benoit, M. H., Nyblade, A. A., and VanDecar, J. C. (2006b). Upper mantle P-wave speed variations beneath Ethiopia and the origin of the Afar hotspot. *Geology* 34 (5):329–332.

Berhe, S. M., Desta, B., Nicoletti, M., and Teferra, M. (1987). Geology, geochronology and geodynamic implications of the Cenozoic magmatic province in W and SE Ethiopia. *Journal of the Geological Society* 144 (2):213–226.

Biggs, J., Bastow, I. D., Keir, D., and Lewi, E. (2011). Pulses of deformation reveal frequently recurring shallow magmatic activity beneath the Main Ethiopian Rift. *Geochemistry, Geophysics, Geosystems* 12 (9).

Bilham, R., Bendick, R., Larson, K., Mohr, P., Braun, J., Tesfaye, S., and Asfaw, L. (1999). Secular and tidal strain across the Main Ethiopian Rift. *Geophysical Research Letters* 26 (18):2789–2792.

Black, S., MacDonald, R., and Kelly, M. R. (1997). Crustal Origin for Peralkaline Rhyolites from Kenya: Evidence from U-Series Disequilibria and Th-Isotopes. *Journal of Petrology* 38 (2):277–297.

Blundy, J. and Cashman, K. (2008). Petrologic reconstruction of magmatic system variables and processes. *Reviews in Mineralogy and Geochemistry* 69 (1):179–239.

Blundy, J. and Wood, B. (2003). Partitioning of trace elements between crystals and melts. *Earth and Planetary Science Letters* 210 (3–4):383–397.

Blundy, J. D. and Wood, B. J. (1991). Crystal-chemical controls on the partitioning of Sr and Ba between plagioclase feldspar, silicate melts, and hydrothermal solutions. *Geochimica et Cosmochimica Acta* 55 (1):193–209.

Blundy, J., Cashman, K. V., Rust, A., and Witham, F. (2010). A case for CO_2-rich arc magmas. *Earth and Planetary Science Letters* 290 (3):289–301.

Boccaletti, M., Mazzuoli, R., Bonini, M., Trua, T., and Abebe, B. (1999). Plio-Quaternary volcanotectonic activity in the northern sector of the Main Ethiopian Rift: relationships with oblique rifting. *Journal of African Earth Sciences* 29 (4):679–698.

Bonini, M., Corti, G., Innocenti, F., Manetti, P., Mazzarini, F., Abebe, T., and Pecskay, Z. (2005). Evolution of the Main Ethiopian Rift in the frame of Afar and Kenya rifts propagation. *Tectonics* 24 (1).

Botz, R. W. and Stoffers, P. (1993). Light hydrocarbon gases in Lake Tanganyika hydrothermal fluids (East-Central Africa). *Chemical Geology* 104 (1):217–224.

Boyce, A., Bastow, I. D., Cottaar, S., Kounoudis, R., Courbeville, J. G. D., Caunt, E., and Desai, S. (2021). AFRP20: New P-Wavespeed Model for the African Mantle Reveals Two Whole-Mantle Plumes Below East Africa and Neoproterozoic Modification of the Tanzania Craton. *Geochemistry, Geophysics, Geosystems* 22 (3):e2020GC009302.

Brune, S., Williams, S. E., and Müller, R. D. (2017). Potential links between continental rifting, CO_2 degassing and climate change through time. *Nature Geoscience* 10 (12):941–946.

Buchner, J., Georgakakis, A., Nandra, K., Hsu, L., Rangel, C., Brightman, M., Merloni, A., Salvato, M., Donley, J., and Kocevski, D. (2014). X-ray spectral modelling of the AGN obscuring region in the CDFS: Bayesian model selection and catalogue. *Astronomy & Astrophysics* 564:A125.

Bucholz, C. E., Gaetani, G. A., Behn, M. D., and Shimizu, N. (2013). Post-entrapment modification of volatiles and oxygen fugacity in olivine-hosted melt inclusions. *Earth and Planetary Science Letters* 374:145–155.

Buck, W. R. (2006). The role of magma in the development of the Afro-Arabian Rift System. In: *The Afar Volcanic Province within the East African Rift System.* Ed. by G. Yirgu, C. Ebinger, and P. K. H. Maguire. Vol. 259. Geological Society, London, Special Publications, pp. 43–54.

Buck, W. R., Einarsson, P., and Brandsdóttir, B. (2006). Tectonic stress and magma chamber size as controls on dike propagation: Constraints from the 1975–1984 Krafla rifting episode. *Journal of Geophysical Research: Solid Earth* 111 (B12).

Burton, M. R., Sawyer, G. M., and Granieri, D. (2013). Deep Carbon Emissions from Volcanoes. *Reviews in Mineralogy and Geochemistry* 75 (1):323–354.

Calais, E., Ebinger, C., Hartnady, C., and Nocquet, J. (2006). Kinematics of the East African Rift from GPS and earthquake slip vector data. In: *The Afar Volcanic Province within the East African Rift System.* Ed. by G. Yirgu, C. Ebinger, and P. K. H. Maguire. Vol. 259. Geological Society, London, Special Publications, pp. 9–22.

Casagli, A., Frezzotti, M. L., Peccerillo, A., Tiepolo, M., and De Astis, G. (2017). (Garnet)-spinel peridotite xenoliths from Mega (Ethiopia): Evidence for rejuvenation and dynamic thinning of the lithosphere beneath the southern Main Ethiopian Rift. *Chemical Geology*. The role of intraplate magmas and their inclusions in Earth's mantle evolution 455:231–248.

Casey, M., Ebinger, C., Keir, D., Gloaguen, R., and Mohamed, F. (2006). Strain accommodation in transitional rifts: extension by magma intrusion and faulting in Ethiopian rift magmatic segments. In: *The Afar Volcanic Province within the East African Rift System*. Ed. by G. Yirgu, C. J. Ebinger, and P. K. H. Maguire. Vol. 259. Geological Society, London, Special Publications, pp. 143–163.

Cassidy, M., Manga, M., Cashman, K., and Bachmann, O. (2018). Controls on explosive-effusive volcanic eruption styles. *Nature Communications* 9 (1):2839.

Chakraborty, S. (2010). Diffusion Coefficients in Olivine, Wadsleyite and Ringwoodite. *Reviews in Mineralogy and Geochemistry* 72 (1):603–639.

Chambers, E. L., Harmon, N., Keir, D., and Rychert, C. A. (2019). Using Ambient Noise to Image the Northern East African Rift. *Geochemistry, Geophysics, Geosystems* 20 (4):2091–2109.

Chambers, E. L., Harmon, N., Rychert, C. A., and Keir, D. (2021). Variations in melt emplacement beneath the northern East African Rift from radial anisotropy. *Earth and Planetary Science Letters* 573:117150.

Chang, S.-J. and Lee, S. Van der (2011). Mantle plumes and associated flow beneath Arabia and East Africa. *Earth and Planetary Science Letters* 302 (3):448–454.

Chernet, T. (2011). Geology and hydrothermal resources in the northern Lake Abaya area (Ethiopia). *Journal of African Earth Sciences* 61 (2):129–141.

Chernet, T., Hart, W. K., Aronson, J. L., and Walter, R. C. (1998). New age constraints on the timing of volcanism and tectonism in the northern Main Ethiopian Rift–southern Afar transition zone (Ethiopia). *Journal of Volcanology and Geothermal Research* 80 (3):267–280.

Chorowicz, J. (2005). The East African rift system. *Journal of African Earth Sciences*. Phanerozoic Evolution of Africa 43 (1):379–410.

Class, C. and Goldstein, S. L. (1997). Plume-lithosphere interactions in the ocean basins: constraints from the source mineralogy. *Earth and Planetary Science Letters* 150 (3-4):245–260.

Coogan, L. A., Saunders, A. D., and Wilson, R. N. (2014). Aluminum-in-olivine thermometry of primitive basalts: Evidence of an anomalously hot mantle source for large igneous provinces. *Chemical Geology* 368:1–10.

Cooper, K. M. (2019). Time scales and temperatures of crystal storage in magma reservoirs: implications for magma reservoir dynamics. *Philosophical transactions. Series A, Mathematical, physical, and engineering sciences* 377 (2139):20180009.

Copley, A. and Woodcock, N. (2016). Estimates of fault strength from the Variscan foreland of the northern UK. *Earth and Planetary Science Letters* 451:108–113.

Cornwell, D. G., Mackenzie, G. D., England, R. W., Maguire, P. K. H., Asfaw, L. M., and Oluma, B. (2006). Northern Main Ethiopian Rift crustal structure from new high-precision gravity data. In: *The Afar Volcanic Province within the East African Rift System*. Vol. 259. Geological Society, London, Special Publications, pp. 307–321.

Corti, G. (2008). Control of rift obliquity on the evolution and segmentation of the main Ethiopian rift. *Nature Geoscience* 1 (4):258–262.

Corti, G. (2009). Continental rift evolution: From rift initiation to incipient break-up in the Main Ethiopian Rift, East Africa. *Earth-Science Reviews* 96 (1):1–53.

Corti, G., Cioni, R., Franceschini, Z., Sani, F., Scaillet, S., Molin, P., Isola, I., Mazzarini, F., Brune, S., Keir, D., Erbello, A., Muluneh, A., Illsley-Kemp, F., and Glerum, A. (2019). Aborted propagation of the Ethiopian rift caused by linkage with the Kenyan rift. *Nature Communications* 10 (1):1309.

Corti, G., Molin, P., Sembroni, A., Bastow, I. D., and Keir, D. (2018a). Control of Pre-rift Lithospheric Structure on the Architecture and Evolution of Continental Rifts: Insights From the Main Ethiopian Rift, East Africa. *Tectonics* 37 (2):477–496.

Corti, G., Philippon, M., Sani, F., Keir, D., and Kidane, T. (2013a). Re-orientation of the extension direction and pure extensional faulting at oblique rift margins: comparison between the Main Ethiopian Rift and laboratory experiments. *Terra Nova* 25 (5):396–404.

Corti, G., Sani, F., Agostini, S., Philippon, M., Sokoutis, D., and Willingshofer, E. (2018b). Off-axis volcano-tectonic activity during continental rifting: Insights from the transversal Goba-Bonga lineament, Main Ethiopian Rift (East Africa). *Tectonophysics* 728-729:75–91.

Corti, G., Sani, F., Philippon, M., Sokoutis, D., Willingshofer, E., and Molin, P. (2013b). Quaternary volcano-tectonic activity in the Soddo region, western margin of the Southern Main Ethiopian Rift. *Tectonics* 32 (4):861–879.

Cortés, J. A., Wilson, M., Condliffe, E., and Francalanci, L. (2006). The Occurrence of Forsterite and Highly Oxidizing Conditions in Basaltic Lavas from Stromboli Volcano, Italy. *Journal of Petrology* 47 (7):1345–1373.

Costa, F., Dohmen, R., and Chakraborty, S. (2008). Time Scales of Magmatic Processes from Modeling the Zoning Patterns of Crystals. *Reviews in Mineralogy and Geochemistry* 69 (1):545–594.

Costa, F., Shea, T., and Ubide, T. (2020). Diffusion chronometry and the timescales of magmatic processes. *Nature Reviews Earth & Environment* 1 (4):201–214.

Costa, F. (2021). Clocks in Magmatic Rocks. *Annual Review of Earth and Planetary Sciences* 49 (1):231–252.

Costa, F. and Chakraborty, S. (2004). Decadal time gaps between mafic intrusion and silicic eruption obtained from chemical zoning patterns in olivine. *Earth and Planetary Science Letters* 227 (3):517–530.

Costa, F. and Morgan, D. (2010). Time Constraints from Chemical Equilibration in Magmatic Crystals. In: *Timescales of magmatic processes: from core to atmosphere*, pp. 125–159.

Couperthwaite, F. K., Morgan, D. J., Harvey, J., and Kahl, M. (2022). Pre-eruptive timescales from the historical Hapaimamo eruption at Mauna Loa, Hawai‘i. *Journal of Volcanology and Geothermal Research*:107690.

Couperthwaite, F. K., Thordarson, T, Morgan, D. J., Harvey, J, and Wilson, M (2020). Diffusion Timescales of Magmatic Processes in the Moinui Lava Eruption at Mauna Loa, Hawai‘i, as Inferred from Bimodal Olivine Populations. *Journal of Petrology* 61 (egaa058).

Couperthwaite, F. K., Morgan, D. J., Pankhurst, M. J., Lee, P. D., and Day, J. M. (2021). Reducing epistemic and model uncertainty in ionic inter-diffusion chronology: A 3D observation and dynamic modeling approach using olivine from Piton de la Fournaise, La Réunion. *American Mineralogist* 106 (3):481–494.

Daly, E., Keir, D., Ebinger, C. J., Stuart, G. W., Bastow, I. D., and Ayele, A. (2008). Crustal tomographic imaging of a transitional continental rift: The Ethiopian rift. *Geophysical Journal International* 172 (3):1033–1048.

Daly, R. A. (1925). The Geology of Ascension Island. *Proceedings of the American Academy of Arts and Sciences* 60 (1):3–80.

Daniels, K. A., Bastow, I. D., Keir, D., Sparks, R. S. J., and Menand, T. (2014). Thermal models of dyke intrusion during development of continent–ocean transition. *Earth and Planetary Science Letters* 385:145–153.

Danyushevsky, L. V., Della-Pasqua, F. N., and Sokolov, S. (2000). Re-equilibration of melt inclusions trapped by magnesian olivine phenocrysts from subduction-related magmas: petrological implications. *Contributions to Mineralogy and Petrology* 138 (1):68–83.

Danyushevsky, L. V. (2001). The effect of small amounts of H_2O on crystallisation of mid-ocean ridge and backarc basin magmas. *Journal of Volcanology and Geothermal Research* 110 (3):265–280.

Danyushevsky, L. V., McNeill, A. W., and Sobolev, A. V. (2002). Experimental and petrological studies of melt inclusions in phenocrysts from mantle-derived magmas: an overview of techniques, advantages and complications. *Chemical Geology.* Melt Inclusions at the Millennium: Toward a Deeper Understanding of Magmatic Processes 183 (1):5–24.

Danyushevsky, L. V. and Plechov, P. (2011). Petrolog3: Integrated software for modeling crystallization processes. *Geochemistry, Geophysics, Geosystems* 12 (7):Q07021.

Dasgupta, R. and Hirschmann, M. M. (2010). The deep carbon cycle and melting in Earth's interior. *Earth and Planetary Science Letters* 298 (1):1–13.

De Hoog, J. C. M., Gall, L., and Cornell, D. H. (2010). Trace-element geochemistry of mantle olivine and application to mantle petrogenesis and geothermobarometry. *Chemical Geology* 270 (1–4):196–215.

DeMets, C. and Merkouriev, S. (2016). High-resolution estimates of Nubia–Somalia plate motion since 20 Ma from reconstructions of the Southwest Indian Ridge, Red Sea and Gulf of Aden. *Geophysical Journal International* 207 (1):317–332.

DeVitre, C. L., Allison, C. M., and Gazel, E. (2021a). A high-precision CO_2 densimeter for Raman spectroscopy using a Fluid Density Calibration Apparatus. *Chemical Geology* 584:120522.

DeVitre, C. L., Barth, A., Gazel, E., Plank, T. A., and Ramalho, R. (2021b). Solving the Carbonate Problem in Melt Inclusion Bubbles. In: *AGU Fall Meeting Abstracts.*

DeVitre, C. L., Dayton, K., Gazel, E., Barth, A., Plank, T. A., Pamukcu, A., Gaetani, G., and Monteleone, B. (2022). Accounting for Multi-Phase Carbon in Melt Inclusion Bubbles. In: *Goldschmidt Conference Abstracts.*

Desissa, M., Johnson, N. E., Whaler, K. A., Hautot, S., Fisseha, S., and Dawes, G. J. K. (2013). A mantle magma reservoir beneath an incipient mid-ocean ridge in Afar, Ethiopia. *Nature Geoscience* 6 (10):861–865.

Di Rienzo, D. I. (2019). A petrological and geochemical study of a bimodal magmatic sequence from the Abaya volcanic area, Southern Main Ethiopian Rift. MA thesis. University of Iceland.

Dixon, J. E. (1997). Degassing of alkalic basalts. *American Mineralogist* 82 (3-4):368–378.

Dixon, J. E., Stolper, E. M., and Holloway, J. R. (1995). An Experimental Study of Water and Carbon Dioxide Solubilities in Mid-Ocean Ridge Basaltic Liquids. Part I: Calibration and Solubility Models. *Journal of Petrology* 36 (6):1607–1631.

Dohmen, R., Becker, H.-W., and Chakraborty, S. (2007). Fe–Mg diffusion in olivine I: experimental determination between 700 and 1,200°C as a function of composition, crystal orientation and oxygen fugacity. *Physics and Chemistry of Minerals* 34 (6):389–407.

Dohmen, R. and Chakraborty, S. (2007). Fe–Mg diffusion in olivine II: point defect chemistry, change of diffusion mechanisms and a model for calculation of diffusion coefficients in natural olivine. *Physics and Chemistry of Minerals* 34 (6):409–430.

Dohmen, R., Faak, K., and Blundy, J. D. (2017). Chronometry and Speedometry of Magmatic Processes using Chemical Diffusion in Olivine, Plagioclase and Pyroxenes. *Reviews in Mineralogy and Geochemistry* 83 (1):535–575.

Donovan, J. J. (2021). Probe for EPMA v. 13.0.5 User's Guide and Reference (Xtreme Edition). Ed. by D. Kremser, J. Fournelle, and K. Goemann.

Droop, G. T. R. (1987). A General Equation for Estimating Fe^{3+} Concentrations in Ferromagnesian Silicates and Oxides from Microprobe Analyses, Using Stoichiometric Criteria. *Mineralogical Magazine* 51 (361):431–435.

Eagles, G., Gloaguen, R., and Ebinger, C. (2002). Kinematics of the Danakil microplate. *Earth and Planetary Science Letters* 203 (2):607–620.

Ebinger, C. J. and Casey, M. (2001). Continental breakup in magmatic provinces: An Ethiopian example. *Geology* 29 (6):527–530.

Ebinger, C. J., Jackson, J. A., Foster, A. N., Hayward, N. J., McKenzie, D., Kusznir, N., Louden, K. E., Watts, A. B., Menzies, M., and Roberts, A. (1999). Extensional Basin Geometry and the Elastic Lithosphere [and Discussion]. *Philosophical Transactions: Mathematical, Physical and Engineering Sciences* 357 (1753):741–765.

Ebinger, C. J., Keir, D., Ayele, A., Calais, E., Wright, T. J., Belachew, M., Hammond, J. O. S., Campbell, E., and Buck, W. R. (2008). Capturing magma intrusion and faulting processes during continental rupture: Seismicity of the Dabbahu (Afar) rift. *Geophysical Journal International* 174 (3):1138–1152.

Ebinger, C. J., Keir, D., Bastow, I. D., Whaler, K., Hammond, J. O. S., Ayele, A., Miller, M. S., Tiberi, C., and Hautot, S. (2017). Crustal Structure of Active Deformation Zones in Africa: Implications for Global Crustal Processes. *Tectonics* 36 (12):3298–3332.

Ebinger, C. J. and Sleep, N. H. (1998). Cenozoic magmatism throughout east Africa resulting from impact of a single plume. *Nature* 395 (6704):788–791.

Ebinger, C. J., Yemane, T., Harding, D. J., Tesfaye, S., Kelley, S., and Rex, D. C. (2000). Rift deflection, migration, and propagation: Linkage of the Ethiopian and Eastern rifts, Africa. *GSA Bulletin* 112 (2):163–176.

Ebinger, C. J., Yemane, T., Woldegabriel, G., Aronson, J. L., and Walter, R. C. (1993). Late Eocene–Recent volcanism and faulting in the southern main Ethiopian rift. *Journal of the Geological Society* 150 (1):99–108.

Ebinger, C. J., Wijk, J. van, and Keir, D. (2013). The time scales of continental rifting: Implications for global processes. In: *Geological Society of America Special Papers*. Vol. 500. Geological Society of America, pp. 371–396.

Ebinger, C. (2005). Continental break-up: The East African perspective. *Astronomy & Geophysics* 46 (2):2.16–2.21.

Ebinger, C., Ayele, A., Keir, D., Rowland, J., Yirgu, G., Wright, T., Belachew, M., and Hamling, I. (2010). Length and Timescales of Rift Faulting and Magma Intrusion: The Afar Rifting Cycle from 2005 to Present. *Annual Review of Earth and Planetary Sciences* 38 (1):439–466.

Eggins, S. M., Woodhead, J. D., Kinsley, L. P. J., Mortimer, G. E., Sylvester, P., McCulloch, M. T., Hergt, J. M., and Handler, M. R. (1997). A simple method for the precise determination of {$\geq$} 40 trace elements in geological samples by ICPMS using enriched isotope internal standardisation. *Chemical Geology* 134 (4):311–326.

Faulkner, D. R., Jackson, C. A. L., Lunn, R. J., Schlische, R. W., Shipton, Z. K., Wibberley, C. A. J., and Withjack, M. O. (2010). A review of recent developments concerning the structure, mechanics and fluid flow properties of fault zones. *Journal of Structural Geology*. Fault Zones 32 (11):1557–1575.

Ferguson, D. J. (2011). Volcanic and magmatic processes at a young spreading centre in Afar, Ethiopia. PhD thesis. University of Oxford.

Ferguson, D. J., Barnie, T. D., Pyle, D. M., Oppenheimer, C., Yirgu, G., Lewi, E., Kidane, T., Carn, S., and Hamling, I. (2010). Recent rift-related volcanism in Afar, Ethiopia. *Earth and Planetary Science Letters* 292 (3):409–418.

Ferguson, D. J., Calvert, A. T., Pyle, D. M., Blundy, J. D., Yirgu, G., and Wright, T. J. (2013a). Constraining timescales of focused magmatic accretion and extension in the Afar crust using lava geochronology. *Nature Communications* 4:1416.

Ferguson, D. J., Maclennan, J., Bastow, I. D., Pyle, D. M., Jones, S. M., Keir, D., Blundy, J. D., Plank, T., and Yirgu, G. (2013b). Melting during late-stage rifting in Afar is hot and deep. *Nature* 499 (7456):70–73.

Fermi, E. (1931). Über den Ramaneffekt des Kohlendioxyds. *Zeitschrift für Physik* 71 (3):250–259.

Feroz, F., Hobson, M. P., and Bridges, M. (2009). MultiNest: an efficient and robust Bayesian inference tool for cosmology and particle physics. *Monthly Notices of the Royal Astronomical Society* 398 (4):1601–1614.

Feroz, F., Hobson, M. P., Cameron, E., and Pettitt, A. N. (2019). Importance Nested Sampling and the MultiNest Algorithm. *The Open Journal of Astrophysics* 2 (1):10.21105/astro.1306.2144.

Field, L., Blundy, J., Brooker, R. A., Wright, T., and Yirgu, G. (2012). Magma storage conditions beneath Dabbahu Volcano (Ethiopia) constrained by petrology, seismicity and satellite geodesy. *Bulletin of Volcanology* 74 (5):981–1004.

Field, L., Blundy, J., Calvert, A., and Yirgu, G. (2013). Magmatic history of Dabbahu, a composite volcano in the Afar Rift, Ethiopia. *Geological Society of America Bulletin* 125 (1-2):128–147.

Foley, S. F. and Fischer, T. P. (2017). An essential role for continental rifts and lithosphere in the deep carbon cycle. *Nature Geoscience* 10 (12):897–902.

Fontijn, K., McNamara, K., Zafu Tadesse, A., Pyle, D. M., Dessalegn, F., Hutchison, W., Mather, T. A., and Yirgu, G. (2018). Contrasting styles of post-caldera volcanism along the Main Ethiopian Rift: Implications for contemporary volcanic hazards. *Journal of Volcanology and Geothermal Research* 356:90–113.

Franceschini, Z., Cioni, R., Scaillet, S., Corti, G., Sani, F., Isola, I., Mazzarini, F., Duval, F., Erbello, A., Muluneh, A., and Brune, S. (2020). Recent volcano-tectonic activity of the Ririba rift and the evolution of rifting in South Ethiopia. *Journal of Volcanology and Geothermal Research*:106989.

French, S. W. and Romanowicz, B. (2015). Broad plumes rooted at the base of the Earth's mantle beneath major hotspots. *Nature* 525 (7567):95–99.

Furman, T., Bryce, J., Rooney, T., Hanan, B., Yirgu, G., and Ayalew, D. (2006). Heads and tails: 30 million years of the Afar plume. In: *The Afar Volcanic Province within the East African Rift System*. Ed. by G. Yirgu, C. J. Ebinger, and P. K. H. Maguire. Vol. 259. Geological Society, London, Special Publications, pp. 95–119.

Furman, T. (2007). Geochemistry of East African Rift basalts: An overview. *Journal of African Earth Sciences*. The East African Rift System: Dynamics, Evolution and Environment 48 (2):147–160.

Furman, T., Nelson, W. R., and Elkins-Tanton, L. T. (2016). Evolution of the East African rift: Drip magmatism, lithospheric thinning and mafic volcanism. *Geochimica et Cosmochimica Acta*. Magmas and their sources: A special issue honoring Frederick A. Frey 185:418–434.

Gaetani, G. A. and Watson, E. B. (2000). Open system behavior of olivine-hosted melt inclusions. *Earth and Planetary Science Letters* 183 (1):27–41.

Gale, A., Dalton, C. A., Langmuir, C. H., Su, Y., and Schilling, J.-G. (2013). The mean composition of ocean ridge basalts. *Geochemistry, Geophysics, Geosystems* 14 (3):489–518.

Gallacher, R. J., Keir, D., Harmon, N., Stuart, G., Leroy, S., Hammond, J. O. S., Kendall, J.-M., Ayele, A., Goitom, B., Ogubazghi, G., and Ahmed, A. (2016). The initiation of segmented buoyancy-driven melting during continental breakup. *Nature Communications* 7:13110.

Gani, N. D., Gani, M. R., and Abdelsalam, M. G. (2007). Blue Nile incision on the Ethiopian Plateau: Pulsed plateau growth, Pliocene uplift, and hominin evolution. *GSA Today* 17 (9):4.

Gao, S. S., Liu, K. H., and Abdelsalam, M. G. (2010). Seismic anisotropy beneath the Afar Depression and adjacent areas: Implications for mantle flow. *Journal of Geophysical Research: Solid Earth* 115 (B12).

Garnero, E. J., McNamara, A. K., and Shim, S.-H. (2016). Continent-sized anomalous zones with low seismic velocity at the base of Earth's mantle. *Nature Geoscience* 9 (7):481–489.

Gashawbeza, E. M., Klemperer, S. L., Nyblade, A. A., Walker, K. T., and Keranen, K. M. (2004). Shear-wave splitting in Ethiopia: Precambrian mantle anisotropy locally modified by Neogene rifting. *Geophysical Research Letters* 31 (18).

George, R. and Rogers, N. (2002). Plume dynamics beneath the African plate inferred from the geochemistry of the Tertiary basalts of southern Ethiopia. *Contributions to Mineralogy and Petrology* 144 (3):286–304.

George, R., Rogers, N., and Kelley, S. (1998). Earliest magmatism in Ethiopia: Evidence for two mantle plumes in one flood basalt province. *Geology* 26 (10):923–926.

Ghiorso, M. S. and Gualda, G. A. R. (2015). An H_2O–CO_2 mixed fluid saturation model compatible with rhyolite-MELTS. *Contributions to Mineralogy and Petrology* 169 (6):53.

Ghiorso, M. S. and Sack, R. O. (1995). Chemical mass transfer in magmatic processes IV. A revised and internally consistent thermodynamic model for the interpolation and extrapolation of liquid-solid equilibria in magmatic systems at elevated temperatures and pressures. *Contributions to Mineralogy and Petrology* 119 (2):197–212.

Gibson, S. A. and Geist, D. (2010). Geochemical and geophysical estimates of lithospheric thickness variation beneath Galápagos. *Earth and Planetary Science Letters* 300 (3):275–286.

Giordano, F., D'Antonio, M., Civetta, L., Tonarini, S., Orsi, G., Ayalew, D., Yirgu, G., Dell'Erba, F., Di Vito, M. A., and Isaia, R. (2014). Genesis and evolution of mafic and felsic magmas at Quaternary volcanoes within the Main Ethiopian Rift: Insights from Gedemsa and Fanta 'Ale complexes. *Lithos*. Within plate continental magmatism and its mantle sources 188:130–144.

Gleeson, M. L. M., Stock, M. J., Pyle, D. M., Mather, T. A., Hutchison, W., Yirgu, G., and Wade, J. (2017). Constraining magma storage conditions at a restless volcano in the Main Ethiopian Rift using phase equilibria models. *Journal of Volcanology and Geothermal Research* 337:44–61.

Gordon, H. R. and McCubbin, T. K. (1966). The 2.8-Micron Bands of CO. *Journal of Molecular Spectroscopy* 19:137–154.

Grandin, R., Jacques, E., Nercessian, A., Ayele, A., Doubre, C., Socquet, A., Keir, D., Kassim, M., Lemarchand, A., and King, G. C. P. (2011). Seismicity during lateral dike propagation: Insights from new data in the recent Manda Hararo–Dabbahu rifting episode (Afar, Ethiopia). *Geochemistry, Geophysics, Geosystems* 12 (4).

Grandin, R., Socquet, A., Jacques, E., Mazzoni, N., Chabalier, J.-B. de, and King, G. C. P. (2010). Sequence of rifting in Afar, Manda-Hararo rift, Ethiopia, 2005–2009: Time-space evolution and interactions between dikes from interferometric synthetic aperture radar and static stress change modeling. *Journal of Geophysical Research: Solid Earth* 115 (B10).

Gualda, G. A. R., Ghiorso, M. S., Lemons, R. V., and Carley, T. L. (2012). Rhyolite-MELTS: a Modified Calibration of MELTS Optimized for Silica-rich, Fluid-bearing Magmatic Systems. *Journal of Petrology* 53 (5):875–890.

Gurenko, A. A. and Chaussidon, M. (1995). Enriched and depleted primitive melts included in olivine from Icelandic tholeiites: origin by continuous melting of a single mantle column. *Geochimica et Cosmochimica Acta* 59 (14):2905–2917.

Halldórsson, S. A., Hilton, D. R., Scarsi, P., Abebe, T., and Hopp, J. (2014). A common mantle plume source beneath the entire East African Rift System revealed by coupled helium-neon systematics. *Geophysical Research Letters* 41 (7):2304–2311.

Hammer, J. E. (2006). Influence of fO2 and cooling rate on the kinetics and energetics of Fe-rich basalt crystallization. *Earth and Planetary Science Letters* 248 (3):618–637.

Hammond, J. O. S., Kendall, J.-M., Stuart, G. W., Keir, D., Ebinger, C., Ayele, A., and Belachew, M. (2011). The nature of the crust beneath the Afar triple junction: Evidence from receiver functions. *Geochemistry, Geophysics, Geosystems* 12 (12).

Hammond, J. O. S., Kendall, J.-M., Stuart, G., Ebinger, C., Bastow, I., Keir, D., Ayele, A., Belachew, M., Goitom, B., Ogubazghi, G., and Wright, T. (2013). Mantle upwelling and initiation of rift segmentation beneath the Afar Depression. *Geology* 41 (6):635–638.

Hansen, S. E., Nyblade, A. A., and Benoit, M. H. (2012). Mantle structure beneath Africa and Arabia from adaptively parameterized P-wave tomography: Implications for the origin of Cenozoic Afro-Arabian tectonism. *Earth and Planetary Science Letters* 319-320:23–34.

Hartley, M. E., Maclennan, J., Edmonds, M., and Thordarson, T. (2014). Reconstructing the deep CO_2 degassing behaviour of large basaltic fissure eruptions. *Earth and Planetary Science Letters* 393:120–131.

Hartley, M. E., Morgan, D. J., Maclennan, J., Edmonds, M., and Thordarson, T. (2016). Tracking timescales of short-term precursors to large basaltic fissure eruptions through Fe–Mg diffusion in olivine. *Earth and Planetary Science Letters* 439:58–70.

Hartley, M. E., Neave, D. A., Maclennan, J., Edmonds, M., and Thordarson, T. (2015). Diffusive over-hydration of olivine-hosted melt inclusions. *Earth and Planetary Science Letters* 425:168–178.

Hayward, N. J. and Ebinger, C. J. (1996). Variations in the along-axis segmentation of the Afar Rift system. *Tectonics* 15 (2):244–257.

Heinonen, J. S., Jennings, E. S., and Riley, T. R. (2015). Crystallisation temperatures of the most Mg-rich magmas of the Karoo LIP on the basis of Al-in-olivine thermometry. *Chemical Geology* 411 (Supplement C):26–35.

Helz, R. T., Cottrell, E., Brounce, M. N., and Kelley, K. A. (2017). Olivine-melt relationships and syneruptive redox variations in the 1959 eruption of Kīlauea Volcano as revealed by XANES. *Journal of Volcanology and Geothermal Research* 333-334:1–14.

Hendrie, D. B., Kusznir, N. J., Morley, C. K., and Ebinger, C. J. (1994). Cenozoic extension in northern Kenya: a quantitative model of rift basin development in the Turkana region. *Tectonophysics*. Crustal and upper mantle structure of the Kenya Rift 236 (1):409–438.

Herzberg, C. and Asimow, P. D. (2008). Petrology of some oceanic island basalts: PRIMELT2.XLS software for primary magma calculation. *Geochemistry, Geophysics, Geosystems* 9 (9).

Herzberg, C. (2011). Identification of Source Lithology in the Hawaiian and Canary Islands: Implications for Origins. *Journal of Petrology* 52 (1):113–146.

Herzberg, C. and Asimow, P. D. (2015). PRIMELT3 MEGA.XLSM software for primary magma calculation: Peridotite primary magma MgO contents from the liquidus to the solidus. *Geochemistry, Geophysics, Geosystems* 16 (2):563–578.

Herzberg, C. and Gazel, E. (2009). Petrological evidence for secular cooling in mantle plumes. *Nature* 458 (7238):619–622.

Hirschmann, M. M. and Stolper, E. M. (1996). A possible role for garnet pyroxenite in the origin of the "garnet signature" in MORB. *Contributions to Mineralogy and Petrology* 124 (2):185–208.

Hofmann, A. W., Jochum, K. P., Seufert, M., and White, W. M. (1986). Nb and Pb in oceanic basalts: new constraints on mantle evolution. *Earth and Planetary Science Letters* 79 (1):33–45.

Hofmann, C., Courtillot, V., Féraud, G., Rochette, P., Yirgu, G., Ketefo, E., and Pik, R. (1997). Timing of the Ethiopian flood basalt event and implications for plume birth and global change. *Nature* 389 (6653):838–841.

Hofstetter, R. and Beyth, M. (2003). The Afar Depression: interpretation of the 1960-2000 earthquakes. *Geophysical Journal International* 155 (2):715–732.

Hunt, J. A., Pyle, D. M., and Mather, T. A. (2019). The Geomorphology, Structure, and Lava Flow Dynamics of Peralkaline Rift Volcanoes From High-Resolution Digital Elevation Models. *Geochemistry, Geophysics, Geosystems* 20 (3):1508–1538.

Hunt, J. A., Zafu, A., Mather, T. A., Pyle, D. M., and Barry, P. H. (2017). Spatially Variable CO_2 Degassing in the Main Ethiopian Rift: Implications for Magma Storage, Volatile Transport, and Rift-Related Emissions. *Geochemistry, Geophysics, Geosystems* 18 (10):3714–3737.

Hutchison, W., Biggs, J., Mather, T. A., Pyle, D. M., Lewi, E., Yirgu, G., Caliro, S., Chiodini, G., Clor, L. E., and Fischer, T. P. (2016a). Causes of unrest at silicic calderas in the East African Rift: New constraints from InSAR and soil-gas chemistry at Aluto volcano, Ethiopia. *Geochemistry, Geophysics, Geosystems* 17 (8):3008–3030.

Hutchison, W., Fusillo, R., Pyle, D. M., Mather, T. A., Blundy, J. D., Biggs, J., Yirgu, G., Cohen, B. E., Brooker, R. A., Barfod, D. N., and Calvert, A. T. (2016b). A pulse of mid-Pleistocene rift volcanism in Ethiopia at the dawn of modern humans. *Nature Communications* 7:13192.

Hutchison, W., Mather, T. A., Pyle, D. M., Biggs, J., and Yirgu, G. (2015). Structural controls on fluid pathways in an active rift system: A case study of the Aluto volcanic complex. *Geosphere* 11 (3):542–562.

Hutchison, W., Mather, T. A., Pyle, D. M., Boyce, A. J., Gleeson, M. L. M., Yirgu, G., Blundy, J. D., Ferguson, D. J., Vye-Brown, C., Millar, I. L., Sims, K. W. W., and Finch, A. A. (2018). The evolution of magma during continental rifting: New constraints from the isotopic and trace element signatures of silicic magmas from Ethiopian volcanoes. *Earth and Planetary Science Letters* 489:203–218.

Hutchison, W., Pyle, D. M., Mather, T. A., Yirgu, G., Biggs, J., Cohen, B. E., Barfod, D. N., and Lewi, E. (2016c). The eruptive history and magmatic evolution of Aluto volcano: new insights into silicic peralkaline volcanism in the Ethiopian rift. *Journal of Volcanology and Geothermal Research* 328:9–33.

Hübert, J., Whaler, K., and Fisseha, S. (2018). The Electrical Structure of the Central Main Ethiopian Rift as Imaged by Magnetotellurics: Implications for Magma Storage and Pathways. *Journal of Geophysical Research: Solid Earth* 123 (7):6019–6032.

Iacono-Marziano, G., Morizet, Y., Le Trong, E., and Gaillard, F. (2012). New experimental data and semi-empirical parameterization of H_2O–CO_2 solubility in mafic melts. *Geochimica et Cosmochimica Acta* 97:1–23.

Iacovino, K., Matthews, S., Wieser, P. E., Moore, G. M., and Bégué, F. (2021). VESIcal Part I: An Open-Source Thermodynamic Model Engine for Mixed Volatile (H_2O-CO_2) Solubility in Silicate Melts. *Earth and Space Science* 8 (11):e2020EA001584.

Iacovino, K. and Till, C. B. (2019). DensityX: A program for calculating the densities of magmatic liquids up to 1,627 °C and 30 kbar. *Volcanica* 2 (1):1–10.

Iddon, F. and Edmonds, M. (2020). Volatile-Rich Magmas Distributed Through the Upper Crust in the Main Ethiopian Rift. *Geochemistry, Geophysics, Geosystems* 21 (6):e2019–GC008904.

Iddon, F., Jackson, C., Hutchison, W., Fontijn, K., Pyle, D. M., Mather, T. A., Yirgu, G., and Edmonds, M. (2019). Mixing and Crystal Scavenging in the Main Ethiopian Rift Revealed by Trace Element Systematics in Feldspars and Glasses. *Geochemistry, Geophysics, Geosystems* 20 (1):230–259.

Irvine, T. N. and Baragar, W. R. A. (1971). A Guide to the Chemical Classification of the Common Volcanic Rocks. *Canadian Journal of Earth Sciences* 8 (5):523–548.

Jambon, A., Lussiez, P., Clocchiatti, R., Weisz, J., and Hernandez, J. (1992). Olivine growth rates in a tholeiitic basalt: An experimental study of melt inclusions in plagioclase. *Chemical Geology* 96 (3):277–287.

Jennings, E. S., Gibson, S. A., and Maclennan, J. (2019). Hot primary melts and mantle source for the Paraná-Etendeka flood basalt province: New constraints from Al-in-olivine thermometry. *Chemical Geology* 529:119287.

Jennings, E. S. and Holland, T. J. B. (2015). A Simple Thermodynamic Model for Melting of Peridotite in the System NCFMASOCr. *Journal of Petrology* 56 (5):869–892.

Jochum, K. P., Stoll, B., Herwig, K., Willbold, M., Hofmann, A. W., Amini, M., Aarburg, S., Abouchami, W., Hellebrand, E., Mocek, B., Raczek, I., Stracke, A., Alard, O., Bouman, C., Becker, S., Dücking, M., Brätz, H., Klemd, R., Bruin, D. d., Canil, D., Cornell, D., Hoog, C.-J. d., Dalpé, C., Danyushevsky, L., Eisenhauer, A., Gao, Y., Snow, J. E., Groschopf, N., Günther, D., Latkoczy, C., Guillong, M., Hauri, E. H., Höfer, H. E., Lahaye, Y., Horz, K., Jacob, D. E., Kasemann, S. A., Kent, A. J. R., Ludwig, T., Zack, T., Mason, P. R. D., Meixner, A., Rosner, M., Misawa, K., Nash, B. P., Pfänder, J., Premo, W. R., Sun, W. D., Tiepolo, M., Vannucci, R., Vennemann, T., Wayne, D., and Woodhead, J. D. (2006). MPI-DING reference glasses for in situ microanalysis: New reference values for element concentrations and isotope ratios. *Geochemistry, Geophysics, Geosystems* 7 (2).

Jolie, E., Hutchison, W., Driba, D., Jentsch, A., and Gizaw, B. (2019). Pinpointing Deep Geothermal Upflow in Zones of Complex Tectono-Volcanic Degassing: New Insights from Aluto Volcano, Main Ethiopian Rift. *Geochemistry, Geophysics, Geosystems* 20 (8):4146–4161.

Keir, D. (2014). Magmatism and deformation during continental breakup. *Astronomy & Geophysics* 55 (5):5.18–5.22.

Keir, D., Bastow, I. D., Corti, G., Mazzarini, F., and Rooney, T. O. (2015). The origin of along-rift variations in faulting and magmatism in the Ethiopian Rift. *Tectonics* 34 (3):464–477.

Keir, D., Ebinger, C. J., Stuart, G. W., Daly, E., and Ayele, A. (2006a). Strain accommodation by magmatism and faulting as rifting proceeds to breakup: Seismicity of the northern Ethiopian rift. *Journal of Geophysical Research: Solid Earth* 111 (B5).

Keir, D., Hamling, I. J., Ayele, A., Calais, E., Ebinger, C., Wright, T. J., Jacques, E., Mohamed, K., Hammond, J. O. S., Belachew, M., Baker, E., Rowland, J. V., Lewi, E., and Bennati, L. (2009). Evidence for focused magmatic accretion at segment centers from lateral dike injections captured beneath the Red Sea rift in Afar. *Geology* 37 (1):59–62.

Keir, D., Kendall, J.-M., Ebinger, C. J., and Stuart, G. W. (2005). Variations in late syn-rift melt alignment inferred from shear-wave splitting in crustal earthquakes beneath the Ethiopian rift. *Geophysical Research Letters* 32 (23).

Keir, D., Stuart, G. W., Jackson, A., and Ayele, A. (2006b). Local Earthquake Magnitude Scale and Seismicity Rate for the Ethiopian Rift. *Bulletin of the Seismological Society of America* 96 (6):2221–2230.

Kelemen, P. B. and Manning, C. E. (2015). Reevaluating carbon fluxes in subduction zones, what goes down, mostly comes up. *Proceedings of the National Academy of Sciences* 112 (30):E3997–E4006.

Kendall, J.-M., Pilidou, S., Keir, D., Bastow, I., Stuart, G., and Ayele, A. (2006). Mantle upwellings, melt migration and the rifting of Africa: insights from seismic anisotropy. In: *The Afar Volcanic Province within the East African Rift System*. Ed. by G. Yirgu, C. J. Ebinger, and P. K. H. Maguire. Vol. 259. Geological Society, London, Special Publications, pp. 55–72.

Kendall, J.-M., Stuart, G. W., Ebinger, C. J., Bastow, I. D., and Keir, D. (2005). Magma-assisted rifting in Ethiopia. *Nature* 433 (7022):146–148.

Kendall, J.-M. and Lithgow-Bertelloni, C. (2016). Why is Africa rifting? In: *Magmatic Rifting and Active Volcanism*. Ed. by T. J. Wright, A. Ayele, D. J. Ferguson, T. Kidane, and C. Vye-Brown. Vol. 420. Geological Society, London, Special Publications, pp. 11–30.

Kent, A. J. (2008). Melt Inclusions in Basaltic and Related Volcanic Rocks. *Reviews in Mineralogy and Geochemistry* 69 (1):273–331.

Keranen, K. M. and Klemperer, S. L. (2008). Discontinuous and diachronous evolution of the Main Ethiopian Rift: Implications for development of continental rifts. *Earth and Planetary Science Letters* 265 (1):96–111.

Keranen, K. M., Klemperer, S. L., Gloaguen, R., and EAGLE Working Group (2004). Three-dimensional seismic imaging of a protoridge axis in the Main Ethiopian rift. *Geology* 32 (11):949.

Keranen, K. M., Klemperer, S. L., Julia, J., Lawrence, J. F., and Nyblade, A. A. (2009). Low lower crustal velocity across Ethiopia: Is the Main Ethiopian Rift a narrow rift in a hot craton? *Geochemistry, Geophysics, Geosystems* 10 (5).

Kim, S., Nyblade, A. A., Rhie, J., Baag, C.-E., and Kang, T.-S. (2012). Crustal S-wave velocity structure of the Main Ethiopian Rift from ambient noise tomography. *Geophysical Journal International* 191 (2):865–878.

Knappe, E., Bendick, R., Ebinger, C., Birhanu, Y., Lewi, E., Floyd, M., King, R., Kianji, G., Mariita, N., Temtime, T., Waktola, B., Deresse, B., Musila, M., Kanoti, J., and Perry,

M. (2020). Accommodation of East African Rifting Across the Turkana Depression. *Journal of Geophysical Research: Solid Earth* 125 (2):e2019JB018469.

Kogan, L., Fisseha, S., Bendick, R., Reilinger, R., McClusky, S., King, R., and Solomon, T. (2012). Lithospheric strength and strain localization in continental extension from observations of the East African Rift. *Journal of Geophysical Research: Solid Earth* 117 (B3).

Kogiso, T., Hirose, K., and Takahashi, E. (1998). Melting experiments on homogeneous mixtures of peridotite and basalt: application to the genesis of ocean island basalts. *Earth and Planetary Science Letters* 162 (1):45–61.

Koornneef, J., Bouman, C., Schwieters, J., and Davies, G. (2014). Measurement of small ion beams by thermal ionisation mass spectrometry using new 10^{13}Ohm resistors. *Analytica Chimica Acta* 819:49–55.

Koornneef, J. M., Nikogosian, I., Bergen, M. J. van, Smeets, R., Bouman, C., and Davies, G. R. (2015). TIMS analysis of Sr and Nd isotopes in melt inclusions from Italian potassium-rich lavas using prototype 10^{13} {Ω} amplifiers. *Chemical Geology* 397:14–23.

Korme, T., Acocella, V., and Abebe, B. (2004). The Role of Pre-existing Structures in the Origin, Propagation and Architecture of Faults in the Main Ethiopian Rift. *Gondwana Research* 7 (2):467–479.

Kurz, T., Gloaguen, R., Ebinger, C., Casey, M., and Abebe, B. (2007). Deformation distribution and type in the Main Ethiopian Rift (MER): A remote sensing study. *Journal of African Earth Sciences*. The East African Rift System: Dynamics, Evolution and Environment 48 (2):100–114.

Lahitte, P., Gillot, P.-Y., and Courtillot, V. (2003). Silicic central volcanoes as precursors to rift propagation: the Afar case. *Earth and Planetary Science Letters* 207 (1):103–116.

Lamadrid, H., Moore, L., Moncada, D., Rimstidt, J., Burruss, R., and Bodnar, R. (2017). Reassessment of the Raman CO_2 densimeter. *Chemical Geology* 450:210–222.

Lavayssière, A., Rychert, C., Harmon, N., Keir, D., Hammond, J. O. S., Kendall, J.-M., Doubre, C., and Leroy, S. (2018). Imaging Lithospheric Discontinuities Beneath the Northern East African Rift Using S-to-P Receiver Functions. *Geochemistry, Geophysics, Geosystems*.

Lavecchia, A., Beekman, F., Clark, S. R., and Cloetingh, S. A. P. L. (2016). Thermo-rheological aspects of crustal evolution during continental breakup and melt intrusion: The Main Ethiopian Rift, East Africa. *Tectonophysics* 686:51–62.

Le Bas, M. J., Le Maitre, R. W., Streckeisen, A., and Zanettin, B. (1986). A Chemical Classification of Volcanic Rocks Based on the Total Alkali-Silica Diagram. *Journal of Petrology* 27 (3):745–750.

Le Voyer, M., Hauri, E. H., Cottrell, E., Kelley, K. A., Salters, V. J. M., Langmuir, C. H., Hilton, D. R., Barry, P. H., and Füri, E. (2018). Carbon fluxes and primary magma CO_2 contents along the global mid-ocean ridge system. *Geochemistry, Geophysics, Geosystems* 20 (3):1387–1424.

Le Voyer, M., Kelley, K. A., Cottrell, E., and Hauri, E. H. (2017). Heterogeneity in mantle carbon content from CO_2-undersaturated basalts. *Nature Communications* 8:14062.

Lee, C.-T. A. and Lackey, J. S. (2015). Global Continental Arc Flare-ups and Their Relation to Long-Term Greenhouse Conditions. *Elements* 11 (2):125–130.

Lee, H., Muirhead, J. D., Fischer, T. P., Ebinger, C. J., Kattenhorn, S. A., Sharp, Z. D., and Kianji, G. (2016). Massive and prolonged deep carbon emissions associated with continental rifting. *Nature Geoscience* 9 (2):145–149.

Liu, J., Xia, Q. K., Kuritani, T., Hanski, E., and Yu, H. R. (2017). Mantle hydration and the role of water in the generation of large igneous provinces. *Nature Communications* 8 (1):1824.

Lloyd, R., Biggs, J., Birhanu, Y., Wilks, M., Gottsmann, J., Kendall, J.-M., Ayele, A., Lewi, E., and Eysteinsson, H. (2018). Sustained Uplift at a Continental Rift Caldera. *Journal of Geophysical Research: Solid Earth* 123 (6):5209–5226.

Maclennan, J., McKenzie, D., and Gronvöld, K. (2001). Plume-driven upwelling under central Iceland. *Earth and Planetary Science Letters* 194 (1–2):67–82.

Maclennan, J. (2017). Bubble formation and decrepitation control the CO_2 content of olivine-hosted melt inclusions. *Geochemistry, Geophysics, Geosystems* 18 (2):597–616.

Magee, C., Muirhead, J. D., Karvelas, A., Holford, S. P., Jackson, C. A., Bastow, I. D., Schofield, N., Stevenson, C. T., McLean, C., McCarthy, W., and Shtukert, O. (2016). Lateral magma flow in mafic sill complexes. *Geosphere* 12 (3):809–841.

Maguire, P., Keller, G., Klemperer, S., Mackenzie, G., Keranen, K., Harder, S., O'Reilly, B., Thybo, H., Asfaw, L., Khan, M., and Amha, M. (2006). Crustal structure of the northern Main Ethiopian Rift from the EAGLE controlled-source survey; a snapshot of incipient lithospheric break-up. In: *The Afar Volcanic Province within the East African Rift System*. Vol. 259. Geological Society, London, Special Publications, pp. 269–292.

Martin, V. M., Morgan, D. J., Jerram, D. A., Caddick, M. J., Prior, D. J., and Davidson, J. P. (2008). Bang! Month-Scale Eruption Triggering at Santorini Volcano. *Science* 321 (5893):1178–1178.

Marty, B., Pik, R., and Yirgu, G. (1996). Helium isotopic variations in Ethiopian plume lavas: nature of magmatic sources and limit on lower mantle contribution. *Earth and Planetary Science Letters* 144 (1):223–237.

Mason, E., Edmonds, M., and Turchyn, A. V. (2017). Remobilization of crustal carbon may dominate volcanic arc emissions. *Science* 357 (6348):290–294.

Matthews, S., Shorttle, O., and Maclennan, J. (2016). The temperature of the Icelandic mantle from olivine-spinel aluminum exchange thermometry. *Geochemistry, Geophysics, Geosystems* 17 (11):4725–4752.

Matthews, S., Wong, K., and Gleeson, M. (2022). pyMelt: An extensible Python engine for mantle melting calculations. *Volcanica* 5 (2):469–475.

Matthews, S., Wong, K., Shorttle, O., Edmonds, M., and Maclennan, J. (2021). Do olivine crystallization temperatures faithfully record mantle temperature variability? *Geochemistry, Geophysics, Geosystems.*

Mazzarini, F., Corvec, N. L., Isola, I., and Favalli, M. (2016). Volcanic field elongation, vent distribution, and tectonic evolution of a continental rift: The Main Ethiopian Rift example. *Geosphere* 12 (3):706–720.

Mazzarini, F., Keir, D., and Isola, I. (2013a). Spatial relationship between earthquakes and volcanic vents in the central-northern Main Ethiopian Rift. *Journal of Volcanology and Geothermal Research* 262:123–133.

Mazzarini, F., Rooney, T. O., and Isola, I. (2013b). The intimate relationship between strain and magmatism: A numerical treatment of clustered monogenetic fields in the Main Ethiopian Rift. *Tectonics* 32 (1):49–64.

McDonough, W. F. and Sun, S.-s. (1995). The composition of the Earth. *Chemical Geology* 120:223–253.

McKenzie, D. and Bickle, M. J. (1988). The Volume and Composition of Melt Generated by Extension of the Lithosphere. *Journal of Petrology* 29 (3):625–679.

McKenzie, D. (1978). Some remarks on the development of sedimentary basins. *Earth and Planetary Science Letters* 40 (1):25–32.

McKenzie, D. (1989). Some remarks on the movement of small melt fractions in the mantle. *Earth and Planetary Science Letters* 95 (1):53–72.

McKenzie, D. and O'Nions, R. K. (1991). Partial Melt Distributions from Inversion of Rare Earth Element Concentrations. *Journal of Petrology* 32 (5):1021–1091.

Mickus, K., Tadesse, K., Keller, G. R., and Oluma, B. (2007). Gravity analysis of the main Ethiopian rift. *Journal of African Earth Sciences*. The East African Rift System: Dynamics, Evolution and Environment 48 (2):59–69.

Minissale, A., Corti, G., Tassi, F., Darrah, T. H., Vaselli, O., Montanari, D., Montegrossi, G., Yirgu, G., Selmo, E., and Teclu, A. (2017). Geothermal potential and origin of natural thermal fluids in the northern Lake Abaya area, Main Ethiopian Rift, East Africa. *Journal of Volcanology and Geothermal Research* 336:1–18.

Mironov, N., Portnyagin, M., Botcharnikov, R., Gurenko, A., Hoernle, K., and Holtz, F. (2015). Quantification of the CO_2 budget and H_2O–CO_2 systematics in subduction-zone magmas through the experimental hydration of melt inclusions in olivine at high H_2O pressure. *Earth and Planetary Science Letters* 425:1–11.

Mohr, P. A. (1967). Major Volcano–Tectonic Lineament in the Ethiopian Rift System. *Nature* 213 (5077):664–665.

Mohr, P., Mitchell, J. G., and Raynolds, R. G. H. (1980). Quaternary volcanism and faulting at O'A Caldera, Central Ethiopian Rift. *Bulletin Volcanologique* 43 (1):173–189.

Mohr, P. (1983). Ethiopian flood basalt province. *Nature* 303 (5918):577–584.

Montelli, R., Nolet, G., Dahlen, F. A., and Masters, G. (2006). A catalogue of deep mantle plumes: New results from finite-frequency tomography. *Geochemistry, Geophysics, Geosystems* 7 (11).

Montelli, R., Nolet, G., Dahlen, F. A., Masters, G., Engdahl, E. R., and Hung, S.-H. (2004). Finite-Frequency Tomography Reveals a Variety of Plumes in the Mantle. *Science* 303 (5656):338–343.

Moore, L. R., Gazel, E., Tuohy, R., Lloyd, A. S., Esposito, R., Steele-MacInnis, M., Hauri, E. H., Wallace, P. J., Plank, T., and Bodnar, R. J. (2015). Bubbles matter: An assessment of the contribution of vapor bubbles to melt inclusion volatile budgets. *American Mineralogist* 100 (4):806–823.

Morgado, E., Parada, M. A., Morgan, D. J., Gutiérrez, F., Castruccio, A., and Contreras, C. (2017). Transient shallow reservoirs beneath small eruptive centres: Constraints from Mg-Fe interdiffusion in olivine. *Journal of Volcanology and Geothermal Research* 347:327–336.

Morgan, D. J. (2015). FINDIF and AutoDiff: 2-D and 1-D Diffusion Processing From BSE Images With Uncertainty Constraint. In: *AGU Fall Meeting Abstracts*. Vol. 31. AGU, V31B–3031.

Morgan, D., Blake, S., Rogers, N., De Vivo, B., Rolandi, G., and Davidson, J. (2006). Magma chamber recharge at Vesuvius in the century prior to the eruption of A.D. 79. *Geology* 34 (10):845.

Morgan, W. J. (1972). Deep mantle convection plumes and plate motions. *AAPG Bulletin* 56 (2):203–213.

Morton, W. H., Rex, D. C., Mitchell, J. G., and Mohr, P. (1979). Riftward younging of volcanic units in the Addis Ababa region, Ethiopian rift valley. *Nature* 280 (5720):284–288.

Muirhead, J. D., Kattenhorn, S. A., Lee, H., Mana, S., Turrin, B. D., Fischer, T. P., Kianji, G., Dindi, E., and Stamps, D. S. (2016). Evolution of upper crustal faulting assisted by magmatic volatile release during early-stage continental rift development in the East African Rift. *Geosphere* 12 (6):1670–1700.

Muirhead, J. D., Fischer, T. P., Oliva, S. J., Laizer, A., Wijk, J. van, Currie, C. A., Lee, H., Judd, E. J., Kazimoto, E., Sano, Y., Takahata, N., Tiberi, C., Foley, S. F., Dufek, J., Reiss, M. C., and Ebinger, C. J. (2020). Displaced cratonic mantle concentrates deep carbon during continental rifting. *Nature* 582 (7810):67–72.

Muirhead, J. D., Wright, L. J. M., and Scholz, C. A. (2019). Rift evolution in regions of low magma input in East Africa. *Earth and Planetary Science Letters* 506:332–346.

Muluneh, A. A., Brune, S., Illsley-Kemp, F., Corti, G., Keir, D., Glerum, A., Kidane, T., and Mori, J. (2020). Mechanism for Deep Crustal Seismicity: Insight From Modeling of Deformation Processes at the Main Ethiopian Rift. *Geochemistry, Geophysics, Geosystems* 21 (7):e2020GC008935.

Muluneh, A. A., Keir, D., and Corti, G. (2021). Thermo-Rheological Properties of the Ethiopian Lithosphere and Evidence for Transient Fluid Induced Lower Crustal Seismicity Beneath the Ethiopian Rift. *Frontiers in Earth Science* 9.

Mutch, E. J. F., Maclennan, J., Shorttle, O., Rudge, J. F., and Neave, D. A. (2021). DFENS: Diffusion Chronometry Using Finite Elements and Nested Sampling. *Geochemistry, Geophysics, Geosystems* 22 (4):e2020GC009303.

Neave, D. A., Fabbro, G., Herd, R. A., Petrone, C. M., and Edmonds, M. (2012). Melting, Differentiation and Degassing at the Pantelleria Volcano, Italy. *Journal of Petrology* 53 (3):637–663.

Nelson, W. R., Furman, T., Keken, P. E. van, Shirey, S. B., and Hanan, B. B. (2012). Os-Hf isotopic insight into mantle plume dynamics beneath the East African Rift System. *Chemical Geology* 320-321:66–79.

Newman, S. and Lowenstern, J. B. (2002). VolatileCalc: a silicate melt–H_2O–CO_2 solution model written in Visual Basic for excel. *Computers & Geosciences* 28 (5):597–604.

Ni, P., Zhang, Y., and Guan, Y. (2017). Volatile loss during homogenization of lunar melt inclusions. *Earth and Planetary Science Letters* 478:214–224.

Nickel, K. G. (1986). Phase equilibria in the system SiO_2–MgO–Al_2O_3–CaO–Cr_2O_3 (SMACCR) and their bearing on spinel/garnet lherzolite relationships. *Neues Jahrbuch fur Mineralogie, Abhandlungen* 155 (3):259–287.

Nicotra, E., Viccaro, M., Donato, P., Acocella, V., and De Rosa, R. (2021). Catching the Main Ethiopian Rift evolving towards plate divergence. *Scientific Reports* 11 (1):21821.

Nyblade, A. A. (2011). The upper-mantle low-velocity anomaly beneath Ethiopia, Kenya, and Tanzania: Constraints on the origin of the African superswell in eastern Africa and plate versus plume models of mantle dynamics. In: *Geological Society of America Special Papers*. Vol. 478. Geological Society of America, pp. 37–50.

Nyblade, A. A., Knox, R. P., and Gurrola, H. (2000). Mantle transition zone thickness beneath Afar: implications for the origin of the Afar hotspot. *Geophysical Journal International* 142 (2):615–619.

Nyblade, A. A. and Robinson, S. W. (1994). The African Superswell. *Geophysical Research Letters* 21 (9):765–768.

Pamukcu, A. S., Gualda, G. A., Bégué, F., and Gravley, D. M. (2015). Melt inclusion shapes: Timekeepers of short-lived giant magma bodies. *Geology* 43 (11):947–950.

Pankhurst, M. J., Morgan, D. J., Thordarson, T., and Loughlin, S. C. (2018). Magmatic crystal records in time, space, and process, causatively linked with volcanic unrest. *Earth and Planetary Science Letters* 493:231–241.

Peccerillo, A., Barberio, M. R., Yirgu, G., Ayalew, D., Barbieri, M., and Wu, T. W. (2003). Relationships between Mafic and Peralkaline Silicic Magmatism in Continental Rift Settings: a Petrological, Geochemical and Isotopic Study of the Gedemsa Volcano, Central Ethiopian Rift. *Journal of Petrology* 44 (11):2003–2032.

Peccerillo, A., Donati, C., Santo, A. P., Orlando, A., Yirgu, G., and Ayalew, D. (2007). Petrogenesis of silicic peralkaline rocks in the Ethiopian rift: Geochemical evidence and volcanological implications. *Journal of African Earth Sciences*. The East African Rift System: Dynamics, Evolution and Environment 48 (2):161–173.

Perfit, M. R., Fornari, D. J., Ridley, W. I., Kirk, P. D., Casey, J., Kastens, K. A., Reynolds, J. R., Edwards, M., Desonie, D., Shuster, R., and Paradis, S. (1996). Recent volcanism in the Siqueiros transform fault: picritic basalts and implications for MORB magma genesis. *Earth and Planetary Science Letters* 141 (1):91–108.

Philibert, J.-M. (1991). Atom movements - Diffusion and mass transport in solids. EDP Sciences.

Phipps Morgan, J. (2001). Thermodynamics of pressure release melting of a veined plum pudding mantle. *Geochemistry, Geophysics, Geosystems* 2 (4):1001.

Piccirillo, E. M., Justin-Visentin, E., Zanettin, B., Joron, J. L., and Treuil, a. M. (1979). Geodynamic evolution from plateau to rift: major and trace element geochemistry of the central eastern Ethiopian Plateau volcanics. *N. Jb. Geol. Paläont. Abh* 158 (2):139–179.

Pik, R., Marty, B., and Hilton, D. R. (2006). How many mantle plumes in Africa? The geochemical point of view. *Chemical Geology*. Special Issue in Honour of R.K. O'Nions 226 (3):100–114.

Pik, R., Deniel, C., Coulon, C., Yirgu, G., and Marty, B. (1999). Isotopic and trace element signatures of Ethiopian flood basalts: evidence for plume–lithosphere interactions. *Geochimica et Cosmochimica Acta* 63 (15):2263–2279.

Pizzi, A., Coltorti, M., Abebe, B., Disperati, L., Sacchi, G., and Salvini, R. (2006). The Wonji fault belt (Main Ethiopian Rift): structural and geomorphological constraints and GPS monitoring. In: *The Afar Volcanic Province within the East African Rift System*. Ed. by G. Yirgu, C. J. Ebinger, and P. K. H. Maguire. Vol. 259. Geological Society, London, Special Publications, pp. 191–207.

Plank, T. and Langmuir, C. H. (1992). Effects of the melting regime on the composition of the oceanic crust. *Journal of Geophysical Research: Solid Earth* 97 (B13):19749–19770.

Putirka, K. D. (2005). Mantle potential temperatures at Hawaii, Iceland, and the mid-ocean ridge system, as inferred from olivine phenocrysts: Evidence for thermally driven mantle plumes. *Geochemistry, Geophysics, Geosystems* 6 (5):Q05L08.

Putirka, K. D. (2008a). Excess temperatures at ocean islands: Implications for mantle layering and convection. *Geology* 36 (4):283–286.

Putirka, K. D. (2008b). Thermometers and Barometers for Volcanic Systems. *Reviews in Mineralogy and Geochemistry* 69 (1):61–120.

Putirka, K. D., Perfit, M., Ryerson, F. J., and Jackson, M. G. (2007). Ambient and excess mantle temperatures, olivine thermometry, and active vs. passive upwelling. *Chemical Geology*. The Great Plume Debate: Testing the Plume Theory 241 (3):177–206.

Rae, A. S. P., Edmonds, M., Maclennan, J., Morgan, D., Houghton, B., Hartley, M. E., and Sides, I. (2016). Time scales of magma transport and mixing at Kīlauea Volcano, Hawai'i. *Geology* 44 (6):463–466.

Rasmussen, D. J., Plank, T. A., Wallace, P. J., Newcombe, M. E., and Lowenstern, J. B. (2020). Vapor-bubble growth in olivine-hosted melt inclusions. *American Mineralogist* 105 (12):1898–1919.

Richardson, C. and McKenzie, D. (1994). Radioactive disequilibria from 2D models of melt generation by plumes and ridges. *Earth and Planetary Science Letters* 128 (3):425–437.

Ritsema, J., Heijst, H. J. v., and Woodhouse, J. H. (1999). Complex Shear Wave Velocity Structure Imaged Beneath Africa and Iceland. *Science* 286 (5446):1925–1928.

Robertson, E., Biggs, J., Edmonds, M., Clor, L., Fischer, T. P., Vye-Brown, C., Kianji, G., Koros, W., and Kandie, R. (2016). Diffuse degassing at Longonot volcano, Kenya: Implications for CO_2 flux in continental rifts. *Journal of Volcanology and Geothermal Research* 327:208–222.

Robinson, J. A. C. and Wood, B. J. (1998). The depth of the spinel to garnet transition at the peridotite solidus. *Earth and Planetary Science Letters* 164 (1):277–284.

Roeder, P. L. (1974). Activity of iron and olivine solubility in basaltic liquids. *Earth and Planetary Science Letters* 23 (3):397–410.

Roeder, P. L. and Emslie, R. F. (1970). Olivine-liquid equilibrium. *Contributions to Mineralogy and Petrology* 29 (4):275–289.

Rogers, N. (2006). Basaltic magmatism and the geodynamics of the East African Rift System. In: *The Afar Volcanic Province within the East African Rift System*. Ed. by G. Yirgu, C. J. Ebinger, and P. K. H. Maguire. Vol. 259. Geological Society, London, Special Publications, pp. 77–93.

Rogers, N., Macdonald, R., Fitton, J. G., George, R., Smith, M., and Barreiro, B. (2000). Two mantle plumes beneath the East African rift system: Sr, Nd and Pb isotope evidence from Kenya Rift basalts. *Earth and Planetary Science Letters* 176 (3):387–400.

Ronga, F., Lustrino, M., Marzoli, A., and Melluso, L. (2010). Petrogenesis of a basalt-comendite-pantellerite rock suite: the Boseti Volcanic Complex (Main Ethiopian Rift). *Mineralogy and Petrology* 98 (1-4):227–243.

Rooney, T. O. (2010). Geochemical evidence of lithospheric thinning in the southern Main Ethiopian Rift. *Lithos* 117 (1-4):33–48.

Rooney, T. O. (2017). The Cenozoic magmatism of East-Africa: Part I – Flood basalts and pulsed magmatism. *Lithos* 286-287:264–301.

Rooney, T. O., Bastow, I. D., and Keir, D. (2011). Insights into extensional processes during magma assisted rifting: Evidence from aligned scoria cones. *Journal of Volcanology and Geothermal Research*. From maars to scoria cones: the enigma of monogenetic volcanic fields 201 (1):83–96.

Rooney, T. O., Bastow, I. D., Keir, D., Mazzarini, F., Movsesian, E., Grosfils, E. B., Zimbelman, J. R., Ramsey, M. S., Ayalew, D., and Yirgu, G. (2014). The protracted development of focused magmatic intrusion during continental rifting. *Tectonics* 33 (6):875–897.

Rooney, T. O., Furman, T., Bastow, I., Ayalew, D., and Yirgu, G. (2007). Lithospheric modification during crustal extension in the Main Ethiopian Rift. *Journal of Geophysical Research: Solid Earth* 112 (B10).

Rooney, T. O., Furman, T., Yirgu, G., and Ayalew, D. (2005). Structure of the Ethiopian lithosphere: Xenolith evidence in the Main Ethiopian Rift. *Geochimica et Cosmochimica Acta* 69 (15):3889–3910.

Rooney, T. O., Hanan, B. B., Graham, D. W., Furman, T., Blichert-Toft, J., and Schilling, J.-G. (2012a). Upper Mantle Pollution during Afar Plume–Continental Rift Interaction. *Journal of Petrology* 53 (2):365–389.

Rooney, T. O., Hart, W. K., Hall, C. M., Ayalew, D., Ghiorso, M. S., Hidalgo, P., and Yirgu, G. (2012b). Peralkaline magma evolution and the tephra record in the Ethiopian Rift. *Contributions to Mineralogy and Petrology* 164 (3):407–426.

Rooney, T. O., Herzberg, C., and Bastow, I. D. (2012c). Elevated mantle temperature beneath East Africa. *Geology* 40 (1):27–30.

Rooney, T. O., Nelson, W. R., Ayalew, D., Hanan, B., Yirgu, G., and Kappelman, J. (2017). Melting the lithosphere: Metasomes as a source for mantle-derived magmas. *Earth and Planetary Science Letters* 461:105–118.

Rooyakkers, S. M., Stix, J., Berlo, K., Morgavi, D., Petrelli, M., Rusiecka, M. K., Barker, S. J., Charlier, B. L. A., Neave, D. A., Vetere, F. P., and Perugini, D. (2022). Rifting and recharge as triggers of the mixed basalt–rhyolite Halarauður ignimbrite eruption (Krafla, Iceland). *Contributions to Mineralogy and Petrology* 177 (3):32.

Rose-Koga, E. F., Bouvier, A. S., Gaetani, G. A., Wallace, P. J., Allison, C. M., Andrys, J. A., Torre, C. A. Angeles de la, Barth, A., Bodnar, R. J., Bracco Gartner, A. J. J., Butters, D., Castillejo, A., Chilson-Parks, B., Choudhary, B. R., Cluzel, N., Cole, M., Cottrell, E., Daly, A., Danyushevsky, L. V., DeVitre, C. L., Drignon, M. J., France, L., Gaborieau, M., Garcia, M. O., Gatti, E., Genske, F. S., Hartley, M. E., Hughes, E. C., Iveson, A. A., Johnson, E. R., Jones, M., Kagoshima, T., Katzir, Y., Kawaguchi, M., Kawamoto, T., Kelley, K. A., Koornneef, J. M., Kurz, M. D., Laubier, M., Layne, G. D., Lerner, A., Lin, K. Y., Liu, P. P., Lorenzo-Merino, A., Luciani, N., Magalhães, N., Marschall, H. R., Michael, P. J., Monteleone, B. D., Moore, L. R., Moussallam, Y., Muth, M., Myers, M. L., Narváez, D. F., Navon, O., Newcombe, M. E., Nichols, A. R. L., Nielsen, R. L., Pamukcu, A., Plank, T., Rasmussen, D. J., Roberge, J., Schiavi, F., Schwartz, D., Shimizu, K., Shimizu, K., Shimizu, N., Thomas, J. B., Thompson, G. T., Tucker, J. M., Ustunisik, G., Waelkens, C., Zhang, Y., and Zhou, T. (2021). Silicate melt inclusions in the new millennium: A review of recommended practices for preparation, analysis, and data presentation. *Chemical Geology* 570:120145.

Rudge, J. F. (2008). Finding peaks in geochemical distributions: A re-examination of the helium-continental crust correlation. *Earth and Planetary Science Letters* 274 (1):179–188.

Rutherford, M. J. (2008). Magma Ascent Rates. *Reviews in Mineralogy and Geochemistry* 69 (1):241–271.

Rychert, C. A., Hammond, J. O. S., Harmon, N., Michael Kendall, J., Keir, D., Ebinger, C., Bastow, I. D., Ayele, A., Belachew, M., and Stuart, G. (2012). Volcanism in the Afar Rift sustained by decompression melting with minimal plume influence. *Nature Geoscience* 5 (6):406–409.

Rychert, C. A., Laske, G., Harmon, N., and Shearer, P. M. (2013). Seismic imaging of melt in a displaced Hawaiian plume. *Nature Geoscience* 6 (8):657.

Sano, Y. and Marty, B. (1995). Origin of carbon in fumarolic gas from island arcs. *Chemical Geology* 119 (1):265–274.

Saria, E., Calais, E., Stamps, D. S., Delvaux, D., and Hartnady, C. J. H. (2014). Present-day kinematics of the East African Rift. *Journal of Geophysical Research: Solid Earth* 119 (4):3584–3600.

Schneider, C. A., Rasband, W. S., and Eliceiri, K. W. (2012). NIH Image to ImageJ: 25 years of image analysis. *Nature Methods* 9 (7):671–675.

Shaw, D. M. (1970). Trace element fractionation during anatexis. *Geochimica et Cosmochimica Acta* 34 (2):237–243.

Shea, T., Costa, F., Krimer, D., and Hammer, J. E. (2015). Accuracy of timescales retrieved from diffusion modeling in olivine: A 3D perspective. *American Mineralogist* 100 (10):2026–2042.

Sheather, S. J. and Jones, M. C. (1991). A Reliable Data-Based Bandwidth Selection Method for Kernel Density Estimation. *Journal of the Royal Statistical Society. Series B (Methodological)* 53 (3):683–690.

Shishkina, T., Botcharnikov, R., Holtz, F., Almeev, R., and Portnyagin, M. (2010). Solubility of H_2O- and CO_2-bearing fluids in tholeiitic basalts at pressures up to 500MPa. *Chemical Geology* 277 (1-2):115–125.

Shorttle, O. and Maclennan, J. (2011). Compositional trends of Icelandic basalts: Implications for short–length scale lithological heterogeneity in mantle plumes. *Geochemistry, Geophysics, Geosystems* 12 (11):Q11008.

Shorttle, O., Maclennan, J., and Lambart, S. (2014). Quantifying lithological variability in the mantle. *Earth and Planetary Science Letters* 395:24–40.

Sides, I. R., Edmonds, M., Maclennan, J., Houghton, B. F., Swanson, D. A., and Steele-MacInnis, M. J. (2014a). Magma mixing and high fountaining during the 1959 Kīlauea Iki eruption, Hawai'i. *Earth and Planetary Science Letters* 400:102–112.

Sides, I. R., Edmonds, M., Maclennan, J., Swanson, D. A., and Houghton, B. F. (2014b). Eruption style at Kilauea Volcano in Hawai'i linked to primary melt composition. *Nature Geoscience* 7 (6):464–469.

Siegburg, M., Bull, J. M., Nixon, C. W., Keir, D., Gernon, T. M., Corti, G., Abebe, B., Sanderson, D. J., and Ayele, A. (2020). Quantitative Constraints on Faulting and Fault Slip Rates in the Northern Main Ethiopian Rift. *Tectonics* 39 (8):e2019TC006046.

Siegburg, M., Gernon, T. M., Bull, J. M., Keir, D., Barfod, D. N., Taylor, R. N., Abebe, B., and Ayele, A. (2018). Geological evolution of the Boset-Bericha Volcanic Complex, Main Ethiopian Rift: ^{40}Ar/^{39}Ar evidence for episodic Pleistocene to Holocene volcanism. *Journal of Volcanology and Geothermal Research* 351:115–133.

Silverman, B. W. (2018). Density estimation for statistics and data analysis. Routledge.

Simmons, N. A., Forte, A. M., and Grand, S. P. (2007). Thermochemical structure and dynamics of the African superplume. *Geophysical Research Letters* 34 (2).

Slater, L., McKenzie, D., Gronvold, K., and Shimizu, N. (2001). Melt Generation and Movement beneath Theistareykir, NE Iceland. *Journal of Petrology* 42 (2):321–354.

Smithsonian Microbeam Standards Datasheets (2019). Tech. rep. National Museum of Natural History, p. 63.

Spandler, C. and O'Neill, H. S. C. (2010). Diffusion and partition coefficients of minor and trace elements in San Carlos olivine at 1,300°C with some geochemical implications. *Contributions to Mineralogy and Petrology* 159 (6):791–818.

Spice, H. E., Fitton, J. G., and Kirstein, L. A. (2016). Temperature fluctuation of the Iceland mantle plume through time. *Geochemistry, Geophysics, Geosystems* 17 (2):243–254.

Stracke, A., Genske, F., Berndt, J., and Koornneef, J. M. (2019). Ubiquitous ultra-depleted domains in Earth's mantle. *Nature Geoscience* 12 (10):851–855.

Stracke, A., Hofmann, A. W., and Hart, S. R. (2005). FOZO, HIMU, and the rest of the mantle zoo. *Geochemistry, Geophysics, Geosystems* 6 (5).

Tadesse, A. Z., Fontijn, K., Melaku, A. A., Gebru, E. F., Smith, V. C., Tomlinson, E., Barfod, D., Gopon, P., Bégué, F., Caricchi, L., Laha, P., Terryn, H., Gudbrandsson, S., Yirgu, G., and Ayalew, D. (2022). Eruption frequency and magnitude in a geothermally active continental rift: The Bora-Baricha-Tullu Moye volcanic complex, Main Ethiopian Rift. *Journal of Volcanology and Geothermal Research*:107471.

Tadesse, A. Z., Ayalew, D., Pik, R., Yirgu, G., and Fontijn, K. (2019). Magmatic evolution of the Boku Volcanic Complex, Main Ethiopian Rift. *Journal of African Earth Sciences* 149:109–130.

Takahashi, E. (1986). Melting of a dry peridotite KLB-1 up to 14 GPa: Implications on the Origin of peridotitic upper mantle. *Journal of Geophysical Research: Solid Earth* 91 (B9):9367–9382.

Tamburello, G., Pondrelli, S., Chiodini, G., and Rouwet, D. (2018). Global-scale control of extensional tectonics on CO_2 earth degassing. *Nature Communications* 9 (1):4608.

Taracsák, Z., Hartley, M. E., Burgess, R., Edmonds, M., Iddon, F., and Longpré, M.-A. (2019). High fluxes of deep volatiles from ocean island volcanoes: Insights from El Hierro, Canary Islands. *Geochimica et Cosmochimica Acta* 258:19–36.

Tarasewicz, J., White, R. S., Woods, A. W., Brandsdóttir, B., and Gudmundsson, M. T. (2012). Magma mobilization by downward-propagating decompression of the Eyjafjallajökull volcanic plumbing system. *Geophysical Research Letters* 39 (19).

Tefera, M., Chernet, T., and Haro, W. (1996). Explanation of the geological map of Ethiopia. Geological Survey of Ethiopia.

Thomson, A. and Maclennan, J. (2013). The Distribution of Olivine Compositions in Icelandic Basalts and Picrites. *Journal of Petrology* 54 (4):745–768.

Thybo, H. and Nielsen, C. A. (2009). Magma-compensated crustal thinning in continental rift zones. *Nature* 457 (7231):873–876.

Torre, I. de la, Benito-Calvo, A., Mora, R., Martínez-Moreno, J., Morán, N., and Tibebu, D. (2007). Stone Age occurrences in the western bank of the Bilate River (Southern Ethiopia)–Some preliminary results. *Nyame akuma* 67:14–25.

Trela, J., Gazel, E., Sobolev, A. V., Moore, L., Bizimis, M., Jicha, B., and Batanova, V. G. (2017). The hottest lavas of the Phanerozoic and the survival of deep Archaean reservoirs. *Nature Geoscience* 10 (6):451–456.

Trestrail, K. R., Rooney, T. O., Girard, G., Svoboda, C., Yirgu, G., Ayalew, D., and Keppelman, J. (2017). Sub-continental lithospheric mantle deformation in the Yerer-Tullu Wellel Volcanotectonic Lineament: A study of peridotite xenoliths. *Chemical Geology*. The role of intraplate magmas and their inclusions in Earth's mantle evolution 455:249–263.

Trua, T., Deniel, C., and Mazzuoli, R. (1999). Crustal control in the genesis of Plio-Quaternary bimodal magmatism of the Main Ethiopian Rift (MER): geochemical and isotopic (Sr, Nd, Pb) evidence. *Chemical Geology* 155 (3):201–231.

Tucker, J. M., Hauri, E. H., Pietruszka, A. J., Garcia, M. O., Marske, J. P., and Trusdell, F. A. (2019). A high carbon content of the Hawaiian mantle from olivine-hosted melt inclusions. *Geochimica et Cosmochimica Acta* 254:156–172.

Vidal, C. M., Lane, C. S., Asrat, A., Barfod, D. N., Mark, D. F., Tomlinson, E. L., Tadesse, A. Z., Yirgu, G., Deino, A., Hutchison, W., Mounier, A., and Oppenheimer, C. (2022). Age of the oldest known Homo sapiens from eastern Africa. *Nature* 601 (7894):579–583.

Virtanen, P., Gommers, R., Oliphant, T. E., Haberland, M., Reddy, T., Cournapeau, D., Burovski, E., Peterson, P., Weckesser, W., Bright, J., Walt, S. J. van der, Brett, M., Wilson, J., Millman, K. J., Mayorov, N., Nelson, A. R. J., Jones, E., Kern, R., Larson, E., Carey, C. J., Polat, Feng, Y., Moore, E. W., VanderPlas, J., Laxalde, D., Perktold, J., Cimrman, R., Henriksen, I., Quintero, E. A., Harris, C. R., Archibald, A. M., Ribeiro, A. H., Pedregosa, F., and Mulbregt, P. van (2020). SciPy 1.0: fundamental algorithms for scientific computing in Python. *Nature Methods* 17 (3):261–272.

Wadge, G., Biggs, J., Lloyd, R., and Kendall, J.-M. (2016). Historical Volcanism and the State of Stress in the East African Rift System. *Frontiers in Earth Science* 4.

Wallace, P. J. (2005). Volatiles in subduction zone magmas: concentrations and fluxes based on melt inclusion and volcanic gas data. *Journal of Volcanology and Geothermal Research*. Energy and Mass Fluxes in Volcanic Arcs 140 (1):217–240.

Wallace, P. J., Kamenetsky, V. S., and Cervantes, P. (2015). Melt inclusion CO_2 contents, pressures of olivine crystallization, and the problem of shrinkage bubbles. *American Mineralogist* 100 (4):787–794.

Wallace, P. J., Plank, T., Bodnar, R. J., Gaetani, G. A., and Shea, T. (2021). Olivine-Hosted Melt Inclusions: A Microscopic Perspective on a Complex Magmatic World. *Annual Review of Earth and Planetary Sciences* 49 (1):null.

Wan, Z., Coogan, L. A., and Canil, D. (2008). Experimental calibration of aluminum partitioning between olivine and spinel as a geothermometer. *American Mineralogist* 93 (7):1142–1147.

Wang, C. H. and Wright, R. B. (1973). Raman studies of the effect of density of the fermi resonance in CO_2. *Chemical Physics Letters* 23 (2):241–246.

Welsch, B., Faure, F., Famin, V., Baronnet, A., and Bachèlery, P. (2013). Dendritic Crystallization: A Single Process for all the Textures of Olivine in Basalts? *Journal of Petrology* 54 (3):539–574.

Werner, C., Fischer, T. P., Aiuppa, A., Edmonds, M., Cardellini, C., Carn, S., Chiodini, G., Cottrell, E., Burton, M. R., Shinohara, H., and Allard, P. (2019). Carbon Dioxide Emissions from Subaerial Volcanic Regions: Two decades in review. In: *Deep Carbon:*

Past to Present. Ed. by B. Orcutt, R. Dasgupta, and I. Daniel. Cambridge University Press.

Whaler, K. A. and Hautot, S. (2006). The electrical resistivity structure of the crust beneath the northern Main Ethiopian Rift. In: *The Afar Volcanic Province within the East African Rift System*. Ed. by G. Yirgu, C. J. Ebinger, and P. K. H. Maguire. Vol. 259. Geological Society, London, Special Publications, pp. 293–305.

White, R. S., Smith, L. K., Roberts, A. W., Christie, P. a. F., Kusznir, N. J., and the rest of the iSIMM Team (2008). Lower-crustal intrusion on the North Atlantic continental margin. *Nature* 452 (7186):460–464.

White, R. S. and McKenzie, D. P. (1989). Magmatism at rift zones: The generation of volcanic continental margins and flood basalts. *Journal of Geophysical Research: Solid Earth* 94 (B6):7685–7729.

White, R. S., McKenzie, D., and O'Nions, R. K. (1992). Oceanic crustal thickness from seismic measurements and rare earth element inversions. *Journal of Geophysical Research* 97 (B13):19683.

White, T. D., Asfaw, B., Beyene, Y., Haile-Selassie, Y., Lovejoy, C. O., Suwa, G., and WoldeGabriel, G. (2009). Ardipithecus ramidus and the Paleobiology of Early Hominids. *Science* 326 (5949):64–86.

Wieser, P. E., Iacovino, K., Matthews, S., Moore, G., and Allison, C. M. (2022a). VESIcal: 2. A Critical Approach to Volatile Solubility Modeling Using an Open-Source Python3 Engine. *Earth and Space Science* 9 (2):e2021EA001932.

Wieser, P. E., Lamadrid, H., Maclennan, J., Edmonds, M., Matthews, S., Iacovino, K., Jenner, F. E., Gansecki, C., Trusdell, F., Lee, R. L., and Ilyinskaya, E. (2021). Reconstructing Magma Storage Depths for the 2018 Kılauean Eruption From Melt Inclusion CO_2 Contents: The Importance of Vapor Bubbles. *Geochemistry, Geophysics, Geosystems* 22 (2):e2020GC009364.

Wieser, P., Petrelli, M., Lubbers, J., Wieser, E., Ozaydin, S., Kent, A. J., and Till, C. (2022b). Thermobar: An Open-Source Python3 Tool for Thermobarometry and Hygrometry.

Wilson, J. T. (1966). Did the Atlantic close and then re-open? *Nature* (211):676–681.

WoldeGabriel, G., Yemane, T., Suwa, G., White, T., and Asfaw, B. (1991). Age of volcanism and rifting in the Burji-Soyoma area, Amaro Horst, southern Main Ethiopian Rift: geoand biochronologic data. *Journal of African Earth Sciences (and the Middle East)* 13 (3):437–447.

WoldeGabriel, G., Aronson, J. L., and Walter, R. C. (1990). Geology, geochronology, and rift basin development in the central sector of the Main Ethiopia Rift. *Geological Society of America Bulletin* 102 (4):439–458.

Wolfenden, E., Ebinger, C., Yirgu, G., Deino, A., and Ayalew, D. (2004). Evolution of the northern Main Ethiopian rift: birth of a triple junction. *Earth and Planetary Science Letters* 224 (1):213–228.

Wolfenden, E., Ebinger, C., Yirgu, G., Renne, P. R., and Kelley, S. P. (2005). Evolution of a volcanic rifted margin: Southern Red Sea, Ethiopia. *GSA Bulletin* 117 (7-8):846–864.

Wong, K., Mason, E., Brune, S., East, M., Edmonds, M., and Zahirovic, S. (2019). Deep carbon cycling over the past 200 million years: a review of fluxes in different tectonic settings. *Frontiers in Earth Science* 7 (263).

Workman, R. K. and Hart, S. R. (2005). Major and trace element composition of the depleted MORB mantle (DMM). *Earth and Planetary Science Letters* 231 (1-2):53–72.

Wright, T. J., Ayele, A., Ferguson, D. J., Kidane, T., and Vye-Brown, C., eds. (2016). Magmatic Rifting and Active Volcanism. Vol. 420. Geological Society, London, Special Publications.

Wright, T. J., Ebinger, C., Biggs, J., Ayele, A., Yirgu, G., Keir, D., and Stork, A. (2006). Magma-maintained rift segmentation at continental rupture in the 2005 Afar dyking episode. *Nature* 442 (7100):291–294.

Wright, T. J., Sigmundsson, F., Pagli, C., Belachew, M., Hamling, I. J., Brandsdóttir, B., Keir, D., Pedersen, R., Ayele, A., Ebinger, C., Einarsson, P., Lewi, E., and Calais, E. (2012). Geophysical constraints on the dynamics of spreading centres from rifting episodes on land. *Nature Geoscience* 5 (4):242–250.

Xu, R. and Liu, Y. (2016). Al-in-olivine thermometry evidence for the mantle plume origin of the Emeishan large igneous province. *Lithos* 266 (Supplement C):362–366.

Yirgu, G., Ebinger, C. J., and Maguire, P. K. H., eds. (2006). The Afar Volcanic Province within the East African Rift System. Vol. 259. Geological Society, London, Special Publications.

Zhukova, I., O'Neill, H., and Campbell, I. H. (2017). A subsidiary fast-diffusing substitution mechanism of Al in forsterite investigated using diffusion experiments under controlled thermodynamic conditions. *Contributions to Mineralogy and Petrology* 172 (7):53.

Zindler, A. and Hart, S. (1986). Chemical Geodynamics. *Annual Review of Earth and Planetary Sciences* 14 (1):493–571.

Appendix A

Data tables

Data tables are presented in this section. Where data has been published or is available in digital format, a link to the appropriate online repository is provided.

A.1 Chapter 2: collected Main Ethiopian Rift samples

Table A.1 is a table of sample localities visited and material collected during fieldwork in January 2019.

A.2 Chapters 3 and 4: geochemical datasets, pyMelt code availability and inversion results

The analytical data collected for olivine and spinel in Chapters 3 and 4 are archived in a Zenodo repository with DOI 10.5281/zenodo.6786908. This repository includes Datasets S1 (qualitative maps of olivine-spinel pairs), S2 (geochemical analyses of olivine and spinel including secondary standards), and S3 (full inversion outputs).

pyMelt v1.960 and the inversion code used in these chapters are archived in Zenodo repositories with DOI 10.5281/zenodo.6013925 and 10.5281/zenodo.6786875 respectively. The most recent pyMelt version is v2.0 and can be found in Zenodo repository DOI 10.5281/zenodo.7101330.

Posterior probability distribution medians and 95% confidence intervals are presented in Tables A.2 to A.4. Table A.5 shows the melt fractions expected from inversion models, with uncertainties calculated using the 95% confidence interval for mantle T_p while keeping all other variables as the median value. Raw output files from MultiNest are included in Dataset S3. Where KG1 is referenced in the following tables the REE composition is 50:50 DMM:average MORB.

A.3 Chapter 5: geochemical datasets and images of melt inclusions

Geochemical data, standards, secondary standards, and melt inclusion and bubble analyses are archived in a Zenodo repository with DOI 10.5281/zenodo.7106119, alongside high resolution transmitted light and reflected light microscopy images of melt inclusions.

A.4 Chapter 6: geochemical datasets and backscatter electron images

Geochemical data, standards, secondary standards, timescale data and backscatter electron images are archived in a Zenodo repository with DOI 10.5281/zenodo.7236412.

Table A.1: Table detailing localities visited and material collected during fieldwork.

Sample number	**Region**	**Latitude (°N)**	**Longitude (°E)**	**Brief description**
KW-MER19-01	Abaya	6.69523	37.89808	Obsidian
KW-MER19-02	Abaya	6.68678	37.88343	Scoria
KW-MER19-03	Abaya	6.68678	37.88343	Pumice
KW-MER19-04	Abaya	6.68700	37.88164	Vesicular plagioclase-phyric basaltic lava
KW-MER19-05	Abaya	6.69147	37.87717	Vesicular plagioclase-phyric basaltic lava
KW-MER19-06	Abaya	6.66567	37.86422	Scoria (including large piece of splatter)
KW-MER19-07	Abaya	6.75714	37.86066	Flow-banded crystalline rhyolite
KW-MER19-08	Abaya	6.78231	37.92380	Crystalline basaltic lava
KW-MER19-09a	Abaya	6.78286	37.92702	Glassy Scoria chunks (from quarry floor)
KW-MER19-09b	Abaya	6.78286	37.92702	Scoria (from quarry walls)
KW-MER19-10	Abaya	6.78273	37.94859	Basaltic lava (volcanic ejecta)
KW-MER19-11	Abaya	6.77906	37.94541	Vesicular plagioclase-phyric basaltic lava
KW-MER19-12	Abaya	6.77545	37.94087	Glassy, vesicular basaltic lava
KW-MER19-13	Abaya	6.80802	37.94484	Aphyric basaltic lava with elongate vesicles
KW-MER19-14	Abaya	6.79674	37.93701	Scoria
KW-MER19-15	Abaya	6.78609	37.93013	Scoria
KW-MER19-16a	Abaya	6.78473	37.92894	Vesicular plagioclase-phyric basaltic lava
KW-MER19-16b	Abaya	6.78473	37.92894	Scoria
KW-MER19-17	Abaya	6.63314	37.90731	Crystalline ignimbrite
KW-MER19-18a	Abaya	6.61749	37.89989	Plagioclase-rich, glassy basalt
KW-MER19-18b	Abaya	6.61749	37.89989	Weathered ignimbrite
KW-MER19-18c	Abaya	6.61749	37.89989	Welded ignimbrite
KW-MER19-19	Abaya	6.62810	37.89615	Fine-grained aphyric basaltic lava
KW-MER19-20	Abaya	6.62494	37.89014	Vesicular fine-grained crystalline basalt
KW-MER19-21	Abaya	6.62317	37.88619	Fine-grained plagioclase-phyric basaltic lava
KW-MER19-22	Abaya	6.62357	37.87421	Vesicular fine-grained aphyric basalt

Sample localities (continued).

Sample number	**Region**	**Latitude (°N)**	**Longitude (°E)**	**Brief description**
KW-MER19-23	Abaya	6.62414	37.87291	Aphyric basalt with irregular vesicles
KW-MER19-24	Abaya	6.62725	37.86681	Vesicular plagioclase-phyric basalt
KW-MER19-25	Abaya	6.62772	37.86555	Vesicular plagioclase-phyric basalt
KW-MER19-26-0m	Abaya	6.63012	37.86385	Scoria
KW-MER19-26-4m	Abaya	6.63012	37.86385	Scoria
KW-MER19-26-9m	Abaya	6.63012	37.86385	Scoria
KW-MER19-26-13m	Abaya	6.63012	37.86385	Scoria
KW-MER19-26-18m	Abaya	6.63012	37.86385	Scoria
KW-MER19-27	Abaya	6.63412	37.85948	Vesicular plagiolase-phyric partially-altered basaltic lava
KW-MER19-28	Abaya	6.64071	37.85403	Glassy, aphyric basaltic lava
KW-MER19-29	Abaya	6.64699	37.84891	Glassy, aphyric basaltic lava
KW-MER19-30	Abaya	6.64986	37.84708	Plagioclase-phyric finegrained basalt with few vesicles
KW-MER19-31	Abaya	6.65316	37.84542	Plagioclase-phyric finegrained basalt with few vesicles
KW-MER19-32-(-10m)	Abaya	6.65012	37.84255	Scoria
KW-MER19-32-(-7m)	Abaya	6.65012	37.84255	Scoria
KW-MER19-32-(-3m)	Abaya	6.65012	37.84255	Scoria
KW-MER19-32-0m	Abaya	6.65012	37.84255	Scoria
KW-MER19-32-4m	Abaya	6.65012	37.84255	Scoria
KW-MER19-33	Abaya	6.75738	37.91380	Vesicular, plagioclase-phyric basalt
KW-MER19-34	Abaya	6.75654	37.92716	Heavily weathered vesicular, plagioclase-phyric volcanic ejecta
KW-MER19-35	Abaya	6.75570	37.92768	Heavily weathered, vesicular, plagioclase-phyric basaltic lava
KW-MER19-36	Abaya	6.75460	37.92586	Glassy, vesicular, plagioclase-phyric volcanic ejecta
KW-MER19-37	Abaya	6.75471	37.91885	Glassy basalt
KW-MER19-38	Abaya	6.75366	37.91350	Fine-grained volcanic ejecta interiors
KW-MER19-39	Abaya	6.75424	37.91639	Altered volcanic ejecta chunks
KW-MER19-40	Abaya	6.75139	37.91367	Vesicular, glassy, plagioclase-phyric basalt

Sample localities (continued).

Sample number	**Region**	**Latitude (°N)**	**Longitude (°E)**	**Brief description**
KW-MER19-41a	Abaya	6.74729	37.91339	Scoria
KW-MER19-41b	Abaya	6.74729	37.91339	Uncertain lithology (road-building material)
KW-MER19-42	Abaya	6.73678	37.91732	Basaltic lava
KW-MER19-43	Abaya	6.72742	37.90729	Plagioclase-phyric glassy scoria
KW-MER19-44	Abaya	6.71955	37.90713	Crystalline obsidian
KW-MER19-45	Abaya	6.64294	37.95186	Scoria
KW-MER19-46	Abaya	6.63902	37.83577	Vesicular, plagioclase-phyric basalt
KW-MER19-47	Abaya	6.63828	37.83544	Vesicular, plagioclase-phyric basalt
KW-MER19-48-0m	Abaya	6.63828	37.83544	Scoria
KW-MER19-48-4m	Abaya	6.63828	37.83544	Scoria
KW-MER19-48-7m	Abaya	6.63828	37.83544	Scoria
KW-MER19-48-11m	Abaya	6.63828	37.83544	Scoria
KW-MER19-48-15m	Abaya	6.63828	37.83544	Scoria
KW-MER19-48-20m	Abaya	6.63828	37.83544	Scoria
KW-MER19-48-24m	Abaya	6.63828	37.83544	Scoria
KW-MER19-48-28m	Abaya	6.63828	37.83544	Silt and ash
KW-MER19-49	Abaya	6.65842	37.85891	Volcanic ejecta
KW-MER19-50	Abaya	6.65603	37.85835	Partially altered plagioclase-phyric ejecta
KW-MER19-51	Abaya	6.65870	37.85568	Aphyric basaltic lava
KW-MER19-52	Abaya	6.64851	37.85480	Vesicular, plagioclase-phyric basalt
KW-MER19-53-0m	Ziway	7.84955	38.87054	Scoria
KW-MER19-53-5m	Ziway	7.84955	38.87054	Scoria
KW-MER19-53-10m	Ziway	7.84955	38.87054	Scoria
KW-MER19-54	Ziway	7.84834	38.87912	Vesicular plagioclase-phyric basaltic lava
KW-MER19-55a-0m	Ziway	7.85792	38.88076	Scoria
KW-MER19-55a-4m	Ziway	7.85792	38.88076	Scoria

Sample localities (continued).

Sample number	**Region**	**Latitude (°N)**	**Longitude (°E)**	**Brief description**
KW-MER19-55b	Ziway	7.85792	38.88076	Plagioclase-phyric basaltic lava
KW-MER19-56	Ziway	7.85963	38.88017	Heavily weathered ejecta
KW-MER19-57a	Ziway	7.89633	38.89881	Whole-rock ejecta
KW-MER19-57b	Ziway	7.89633	38.89881	Scoria
KW-MER19-58a	Ziway	7.89521	38.89934	Scoria
KW-MER19-58b	Ziway	7.89521	38.89934	Plagioclase- and pyroxene-phyric basaltic lava
KW-MER19-59	Ziway	7.88610	38.89293	Plagioclase- and olivine-phyric basaltic lava
KW-MER19-60	Ziway	7.81958	38.86909	Plagioclase-phyric basalt lava
KW-MER19-61	Ziway	7.80626	38.87271	Aphyrc basalt lava
KW-MER19-62	Ziway	7.80895	38.87767	Olivine-phyric basaltic lava
KW-MER19-63	Ziway	7.81529	38.88472	Vesicular aphyric basalt
KW-MER19-64	Ziway	7.81296	38.88603	Scoria
KW-MER19-65	Ziway	7.81291	38.88665	Altered and amygdalar basalt
KW-MER19-66	Ziway	7.81787	38.88182	Scoria
KW-MER19-67	Ziway	7.81934	38.88109	Ejecta
KW-MER19-68	Ziway	7.81964	38.87905	Silicic ash, affinity with Aluto
KW-MER19-69	Ziway	7.82062	38.87880	Ejecta
KW-MER19-70a	Ziway	7.90926	38.92087	Plagioclase-phyric basaltic lava
KW-MER19-70b	Ziway	7.90926	38.92087	Olivine- and plagioclase-phyric basaltic lava
KW-MER19-71	Ziway	7.92498	38.93879	Olivine- and plagioclase-phyric basaltic lava
KW-MER19-72	Ziway	7.95421	38.90403	Aphyric ejecta
KW-MER19-73	Ziway	7.95197	38.90504	Scoria
KW-MER19-74	Ziway	7.94497	38.91355	Crystal-rich scoria
KW-MER19-75-0m	Ziway	7.94613	38.91148	Scoria
KW-MER19-75-3m	Ziway	7.94613	38.91148	Scoria
KW-MER19-75-6m	Ziway	7.94613	38.91148	Scoria

Sample localities (continued).

Sample number	**Region**	**Latitude (°N)**	**Longitude (°E)**	**Brief description**
KW-MER19-76-0m	Adama	8.44115	39.32137	Scoria
KW-MER19-76-5m	Adama	8.44115	39.32137	Scoria
KW-MER19-76-10m	Adama	8.44115	39.32137	Scoria
KW-MER19-77	Adama	8.42769	39.33536	Basaltic lava
KW-MER19-78a	Adama	8.43793	39.33689	Basaltic lava
KW-MER19-78b	Adama	8.38754	39.32406	Basaltic lava
KW-MER19-79	Adama	8.41255	39.34171	Basaltic lava
KW-MER19-80-(-2m)	Adama	8.47947	39.30506	Scoria
KW-MER19-80-0m	Adama	8.47947	39.30506	Scoria
KW-MER19-80-15m	Adama	8.47947	39.30506	Scoria
KW-MER19-81-0m	Adama	8.48996	39.29378	Scoria
KW-MER19-81-50m	Adama	8.48996	39.29378	Scoria and crystal-rich ejecta
KW-MER19-81-100m	Adama	8.48996	39.29378	Scoria
KW-MER19-82-(-5m)	Adama	8.50330	39.30835	Scoria
KW-MER19-82-0m	Adama	8.50330	39.30835	Scoria
KW-MER19-82-20m	Adama	8.50330	39.30835	Scoria
KW-MER19-82-100m	Adama	8.50330	39.30835	Scoria

Table A.2: Posterior distributions for primary inversion parameters. The median result for each parameter is reported along with the lower and upper uncertainties defining the 95% uncertainty interval (2.5% and 97.5%).

Locality	Upwelling	T_{crys} (° C)	Lz REEs	Px REEs	T_p (° C)	ϕ_{px}	ϕ_{hz}	P_{lith} (GPa)	P_{cryst} (GPa)
MER	Passive	1426±26	PM	KG1	1495^{+31}_{-44}	$0.46^{+0.03}_{-0.02}$	$0.14^{+0.30}_{-0.13}$	$2.47^{+0.13}_{-0.13}$	$0.79^{+0.15}_{-0.14}$
MER	Active	1426±26	PM	KG1	1500^{+31}_{-41}	$0.46^{+0.03}_{-0.02}$	$0.14^{+0.26}_{-0.13}$	$2.49^{+0.14}_{-0.16}$	$0.79^{+0.14}_{-0.14}$
MER	Passive	1426±26	DMM	KG1	1499^{+44}_{-62}	$0.43^{+0.02}_{-0.05}$	$0.68^{+0.17}_{-0.26}$	$2.43^{+0.59}_{-0.48}$	$0.77^{+0.14}_{-0.14}$
Afar	Passive	1339±22	PM	KG1	1507^{+37}_{-32}	$0.64^{+0.04}_{-0.03}$	$0.33^{+0.35}_{-0.28}$	$1.27^{+0.49}_{-0.43}$	$0.64^{+0.10}_{-0.09}$
Afar	Passive	1409±40	PM	KG1	1564^{+48}_{-44}	$0.62^{+0.10}_{-0.07}$	$0.27^{+0.35}_{-0.23}$	$1.92^{+0.66}_{-0.73}$	$0.64^{+0.10}_{-0.10}$
Afar	Passive	1590±33	PM	KG1	1657^{+40}_{-44}	$0.68^{+0.14}_{-0.10}$	$0.66^{+0.19}_{-0.30}$	$2.52^{+0.78}_{-0.76}$	$0.64^{+0.09}_{-0.10}$
Afar	Active	1339±22	PM	KG1	1451^{+69}_{-106}	$0.60^{+0.06}_{-0.02}$	$0.49^{+0.35}_{-0.39}$	$1.32^{+0.42}_{-0.44}$	$0.64^{+0.09}_{-0.09}$
Afar	Active	1409±40	PM	KG1	1550^{+54}_{-64}	$0.63^{+0.12}_{-0.09}$	$0.27^{+0.39}_{-0.24}$	$1.85^{+0.70}_{-0.65}$	$0.64^{+0.09}_{-0.09}$
Afar	Active	1590±33	PM	KG1	1648^{+33}_{-46}	$0.69^{+0.11}_{-0.11}$	$0.67^{+0.20}_{-0.28}$	$2.52^{+0.78}_{-0.74}$	$0.65^{+0.10}_{-0.09}$
Afar	Passive	1339±22	DMM	KG1	1500^{+34}_{-33}	$0.65^{+0.02}_{-0.01}$	$0.53^{+0.21}_{-0.36}$	$1.06^{+0.48}_{-0.36}$	$0.64^{+0.10}_{-0.09}$
Afar	Passive	1409±40	DMM	KG1	1549^{+52}_{-46}	$0.64^{+0.08}_{-0.05}$	$0.47^{+0.29}_{-0.32}$	$1.46^{+0.76}_{-0.55}$	$0.64^{+0.09}_{-0.09}$
Afar	Passive	1590±33	DMM	KG1	1661^{+43}_{-53}	$0.63^{+0.19}_{-0.08}$	$0.77^{+0.10}_{-0.25}$	$2.15^{+0.75}_{-0.74}$	$0.65^{+0.10}_{-0.09}$
MER	Passive	No T_{crys}	PM	KG1	1494^{+36}_{-232}	$0.01^{+0.05}_{-0.01}$	$0.16^{+0.62}_{-0.15}$	$2.46^{+0.17}_{-1.01}$	$0.78^{+0.15}_{-0.14}$
MER	Active	No T_{crys}	PM	KG1	1264^{+32}_{-13}	$0.04^{+0.06}_{-0.03}$	$0.80^{+0.14}_{-0.23}$	$1.45^{+0.09}_{-0.08}$	$0.79^{+0.14}_{-0.14}$
Afar	Passive	No T_{crys}	PM	KG1	1572^{+78}_{-62}	$0.08^{+0.10}_{-0.07}$	$0.45^{+0.34}_{-0.37}$	$1.70^{+0.80}_{-0.70}$	$0.64^{+0.10}_{-0.09}$
Afar	Active	No T_{crys}	PM	KG1	1556^{+74}_{-110}	$0.05^{+0.09}_{-0.04}$	$0.44^{+0.38}_{-0.36}$	$1.70^{+0.87}_{-0.76}$	$0.65^{+0.10}_{-0.09}$

Table A.3: Posterior distributions for buoyancy. This is achieved through comparison with the inversion results for mid-ocean ridge basalt (Matthews et al., 2021). The median result is reported along with the lower and upper uncertainties defining the 95% uncertainty interval (2.5% and 97.5%). Where active upwelling has been considered the wavelength (λ) and amplitude (μ) of the exponential weighting function are also given.

Locality	Geometry	T_{crys} (° C)	Lz REEs	Px REEs	Ambient T_p (° C)	Ambient ϕ_{px}	Ambient ϕ_{hz}	λ	μ
MER	Passive	1426±26	PM	KG1	1364^{+13}_{-12}	$0.02^{+0.02}_{-0.02}$	$0.32^{+0.20}_{-0.21}$	-	-
MER	Active	1426±26	PM	KG1	1364^{+12}_{-13}	$0.02^{+0.02}_{-0.02}$	$0.34^{+0.18}_{-0.24}$	$0.009^{+0.023}_{-0.009}$	$1.62^{+2.23}_{-1.52}$
MER	Passive	1426±26	DMM	KG1	1363^{+11}_{-12}	$0.02^{+0.02}_{-0.02}$	$0.37^{+0.23}_{-0.24}$	-	-
Afar	Passive	1339±22	PM	KG1	1363^{+12}_{-13}	$0.02^{+0.02}_{-0.02}$	$0.27^{+0.18}_{-0.20}$	-	-
Afar	Passive	1409±40	PM	KG1	1364^{+12}_{-14}	$0.02^{+0.02}_{-0.02}$	$0.37^{+0.20}_{-0.24}$	-	-
Afar	Passive	1590±33	PM	KG1	1364^{+13}_{-13}	$0.02^{+0.02}_{-0.02}$	$0.42^{+0.29}_{-0.26}$	-	-
Afar	Active	1339±22	PM	KG1	1362^{+12}_{-12}	$0.02^{+0.02}_{-0.02}$	$0.35^{+0.21}_{-0.25}$	$0.023^{+0.040}_{-0.020}$	$1.49^{+1.99}_{-1.26}$
Afar	Active	1409±40	PM	KG1	1364^{+12}_{-12}	$0.02^{+0.02}_{-0.02}$	$0.38^{+0.23}_{-0.23}$	$0.013^{+0.029}_{-0.012}$	$1.50^{+2.20}_{-1.41}$
Afar	Active	1590±33	PM	KG1	1363^{+12}_{-13}	$0.02^{+0.02}_{-0.02}$	$0.42^{+0.26}_{-0.25}$	$0.011^{+0.025}_{-0.010}$	$1.72^{+2.05}_{-1.58}$
Afar	Passive	1339±22	DMM	KG1	1362^{+13}_{-12}	$0.02^{+0.02}_{-0.02}$	$0.31^{+0.21}_{-0.23}$	-	-
Afar	Passive	1409±40	DMM	KG1	1363^{+13}_{-13}	$0.02^{+0.02}_{-0.02}$	$0.38^{+0.23}_{-0.27}$	-	-
Afar	Passive	1590±33	DMM	KG1	1363^{+12}_{-12}	$0.02^{+0.02}_{-0.02}$	$0.43^{+0.25}_{-0.26}$	-	-
MER	Passive	No T_{crys}	PM	KG1	1364^{+11}_{-13}	$0.02^{+0.02}_{-0.02}$	$0.32^{+0.18}_{-0.23}$	-	-
MER	Active	No T_{crys}	PM	KG1	1363^{+12}_{-12}	$0.02^{+0.02}_{-0.02}$	$0.35^{+0.18}_{-0.21}$	$0.046^{+0.054}_{-0.027}$	$1.63^{+2.01}_{-1.37}$
Afar	Passive	No T_{crys}	PM	KG1	1364^{+12}_{-14}	$0.02^{+0.02}_{-0.02}$	$0.40^{+0.22}_{-0.26}$	-	-
Afar	Active	No T_{crys}	PM	KG1	1364^{+12}_{-12}	$0.02^{+0.02}_{-0.02}$	$0.40^{+0.23}_{-0.25}$	$0.013^{+0.039}_{-0.013}$	$1.60^{+2.17}_{-1.49}$

Table A.4: Posterior distributions for mantle composition parameters. The chosen lherzolite composition and the KG1 pyroxenite compositions are permitted to vary according to a normal distribution with σ of 10%. The median result is reported along with the lower and upper uncertainties defining the 95% uncertainty interval (2.5% and 97.5%). All values are given as ppm.

Locality	Geometry	T_{crys} (° C)	Lz REEs	Px REEs	La_{lz} (ppm)	Dy_{lz} (ppm)	Yb_{lz} (ppm)	La_{px} (ppm)	Dy_{px} (ppm)	Yb_{px} (ppm)
MER	Passive	1426±26	PM	KG1	$0.696^{+0.103}_{-0.091}$	$0.556^{+0.080}_{-0.072}$	$0.474^{+0.060}_{-0.057}$	$2.724^{+0.484}_{-0.443}$	$3.189^{+0.561}_{-0.606}$	$2.020^{+0.355}_{-0.347}$
MER	Active	1426±26	PM	KG1	$0.697^{+0.111}_{-0.096}$	$0.553^{+0.074}_{-0.073}$	$0.480^{+0.062}_{-0.051}$	$2.717^{+0.471}_{-0.467}$	$3.176^{+0.589}_{-0.601}$	$2.031^{+0.355}_{-0.370}$
MER	Passive	1426±26	DMM	KG1	$0.191^{+0.033}_{-0.032}$	$0.504^{+0.080}_{-0.085}$	$0.370^{+0.060}_{-0.060}$	$2.869^{+0.466}_{-0.391}$	$2.248^{+0.244}_{-0.212}$	$2.310^{+0.215}_{-0.189}$
Afar	Passive	1339±22	PM	KG1	$0.657^{+0.112}_{-0.111}$	$0.659^{+0.102}_{-0.112}$	$0.446^{+0.076}_{-0.069}$	$2.759^{+0.476}_{-0.445}$	$3.157^{+0.541}_{-0.549}$	$2.052^{+0.330}_{-0.334}$
Afar	Passive	1409±40	PM	KG1	$0.662^{+0.114}_{-0.101}$	$0.642^{+0.102}_{-0.101}$	$0.459^{+0.068}_{-0.061}$	$2.733^{+0.461}_{-0.468}$	$3.169^{+0.550}_{-0.568}$	$2.020^{+0.376}_{-0.373}$
Afar	Passive	1590±33	PM	KG1	$0.659^{+0.114}_{-0.121}$	$0.677^{+0.108}_{-0.117}$	$0.443^{+0.073}_{-0.066}$	$2.740^{+0.490}_{-0.479}$	$3.251^{+0.553}_{-0.571}$	$2.014^{+0.304}_{-0.325}$
Afar	Active	1339±22	PM	KG1	$0.655^{+0.116}_{-0.103}$	$0.667^{+0.102}_{-0.107}$	$0.446^{+0.070}_{-0.071}$	$2.756^{+0.475}_{-0.455}$	$2.984^{+0.570}_{-0.495}$	$2.111^{+0.350}_{-0.341}$
Afar	Active	1409±40	PM	KG1	$0.663^{+0.116}_{-0.111}$	$0.645^{+0.101}_{-0.111}$	$0.448^{+0.076}_{-0.060}$	$2.752^{+0.435}_{-0.433}$	$3.152^{+0.595}_{-0.559}$	$2.042^{+0.368}_{-0.355}$
Afar	Active	1590±33	PM	KG1	$0.654^{+0.114}_{-0.103}$	$0.679^{+0.112}_{-0.118}$	$0.435^{+0.074}_{-0.074}$	$2.736^{+0.448}_{-0.413}$	$3.264^{+0.556}_{-0.587}$	$2.009^{+0.328}_{-0.338}$
Afar	Passive	1339±22	DMM	KG1	$0.194^{+0.034}_{-0.036}$	$0.497^{+0.089}_{-0.088}$	$0.369^{+0.062}_{-0.064}$	$2.801^{+0.506}_{-0.436}$	$3.103^{+0.528}_{-0.479}$	$2.056^{+0.304}_{-0.334}$
Afar	Passive	1409±40	DMM	KG1	$0.194^{+0.034}_{-0.038}$	$0.493^{+0.081}_{-0.082}$	$0.372^{+0.056}_{-0.060}$	$2.768^{+0.470}_{-0.444}$	$3.076^{+0.577}_{-0.528}$	$2.074^{+0.327}_{-0.309}$
Afar	Passive	1590±33	DMM	KG1	$0.191^{+0.034}_{-0.033}$	$0.509^{+0.084}_{-0.090}$	$0.363^{+0.058}_{-0.058}$	$2.790^{+0.434}_{-0.449}$	$3.262^{+0.538}_{-0.509}$	$1.958^{+0.353}_{-0.293}$
MER	Passive	No T_{crys}	PM	KG1	$0.701^{+0.110}_{-0.092}$	$0.563^{+0.130}_{-0.078}$	$0.473^{+0.063}_{-0.062}$	$2.728^{+0.469}_{-0.448}$	$3.154^{+0.588}_{-0.619}$	$2.058^{+0.328}_{-0.345}$
MER	Active	No T_{crys}	PM	KG1	$0.643^{+0.106}_{-0.121}$	$0.677^{+0.125}_{-0.116}$	$0.446^{+0.072}_{-0.075}$	$2.789^{+0.446}_{-0.407}$	$2.826^{+0.287}_{-0.321}$	$2.182^{+0.251}_{-0.202}$
Afar	Passive	No T_{crys}	PM	KG1	$0.656^{+0.111}_{-0.109}$	$0.660^{+0.105}_{-0.109}$	$0.446^{+0.068}_{-0.066}$	$2.731^{+0.551}_{-0.466}$	$3.183^{+0.565}_{-0.543}$	$2.036^{+0.332}_{-0.353}$
Afar	Active	No T_{crys}	PM	KG1	$0.660^{+0.106}_{-0.109}$	$0.656^{+0.098}_{-0.103}$	$0.450^{+0.070}_{-0.064}$	$2.750^{+0.465}_{-0.429}$	$3.178^{+0.576}_{-0.547}$	$2.023^{+0.333}_{-0.323}$

Table A.5: Melt fractions generated from each inversion. Medians are calculated using median T_p, ϕ_{px} and ϕ_{hz}; uncertainties are determined using the 2.5% and 97.5% T_p percentiles.

Locality	Geometry	T_{crys} (° C)	Lz REEs	Px REEs	F_{tot}	F_{lz}	F_{px}
MER	Passive	1426±26	PM	KG1	$0.09^{+0.02}_{-0.05}$	$0.17^{+0.05}_{-0.10}$	$0.46^{+0.03}_{-0.02}$
MER	Active	1426±26	PM	KG1	$0.09^{+0.02}_{-0.04}$	$0.18^{+0.04}_{-0.09}$	$0.46^{+0.03}_{-0.02}$
MER	Passive	1426±26	DMM	KG1	$0.12^{+0.03}_{-0.02}$	$0.04^{+0.09}_{-0.04}$	$0.43^{+0.02}_{-0.05}$
Afar	Passive	1339±22	PM	KG1	$0.17^{+0.01}_{-0.01}$	$0.26^{+0.02}_{-0.01}$	$0.64^{+0.04}_{-0.03}$
Afar	Passive	1409±40	PM	KG1	$0.15^{+0.03}_{-0.02}$	$0.27^{+0.05}_{-0.03}$	$0.62^{+0.10}_{-0.07}$
Afar	Passive	1590±33	PM	KG1	$0.19^{+0.04}_{-0.03}$	$0.30^{+0.06}_{-0.05}$	$0.68^{+0.14}_{-0.10}$
Afar	Active	1339±22	PM	KG1	$0.14^{+0.02}_{-0.09}$	$0.24^{+0.04}_{-0.20}$	$0.60^{+0.06}_{-0.02}$
Afar	Active	1409±40	PM	KG1	$0.15^{+0.03}_{-0.02}$	$0.27^{+0.06}_{-0.04}$	$0.63^{+0.12}_{-0.09}$
Afar	Active	1590±33	PM	KG1	$0.18^{+0.03}_{-0.03}$	$0.31^{+0.05}_{-0.05}$	$0.69^{+0.11}_{-0.11}$
Afar	Passive	1339±22	DMM	KG1	$0.21^{+0.01}_{-0.02}$	$0.26^{+0.01}_{-0.06}$	$0.65^{+0.02}_{-0.01}$
Afar	Passive	1409±40	DMM	KG1	$0.18^{+0.02}_{-0.01}$	$0.27^{+0.04}_{-0.02}$	$0.64^{+0.08}_{-0.05}$
Afar	Passive	1590±33	DMM	KG1	$0.22^{+0.07}_{-0.03}$	$0.28^{+0.09}_{-0.03}$	$0.63^{+0.19}_{-0.08}$
MER	Passive	No T_{crys}	PM	KG1	$0.09^{+0.02}_{-0.09}$	$0.17^{+0.05}_{-0.17}$	$0.46^{+0.04}_{-0.46}$
MER	Active	No T_{crys}	PM	KG1	$0.02^{+0.01}_{-0.02}$	$0.00^{+0.00}_{-0.00}$	$0.19^{+0.12}_{-0.19}$
Afar	Passive	No T_{crys}	PM	KG1	$0.17^{+0.05}_{-0.02}$	$0.28^{+0.08}_{-0.04}$	$0.66^{+0.17}_{-0.09}$
Afar	Active	No T_{crys}	PM	KG1	$0.16^{+0.04}_{-0.05}$	$0.28^{+0.08}_{-0.11}$	$0.65^{+0.16}_{-0.12}$